TESIS DOCTORAL

UCAM
UNIVERSIDAD CATÓLICA DE MURCIA

ESCUELA INTERNACIONAL DE DOCTORADO

Programa de Doctorado en Tecnologías de la Computación e Ingeniería Ambiental

Spatiotemporal dynamics of groundwater in the Andean Highland in northern Ecuador

Autora:

Lilia Angélica Peñafiel Aguiar

Directores:

Dr. Francisco Javier Alcalá García

Dr. Javier Melchor Senent Aparicio

Murcia, septiembre 2024.

TESIS DOCTORAL

UCAM
UNIVERSIDAD CATÓLICA DE MURCIA

ESCUELA INTERNACIONAL DE DOCTORADO

Programa de Doctorado en Tecnologías de la Computación e Ingeniería Ambiental

---

Spatiotemporal dynamics of groundwater in the Andean Highland in northern Ecuador

Autora:

Lilia Angélica Peñafiel Aguiar

Directores:

Dr. Francisco Javier Alcalá García

Dr Javier Melchor Senent Aparicio

Murcia, septiembre 2024.

AUTORIZACIÓN DEL DIRECTOR DE LA TESIS
PARA SU PRESENTACIÓN

El Dr. D. Francisco Javier Alcalá García y el Dr. D. Javier Melchor Senent Aparicio como Directores[1] de la Tesis Doctoral titulada "Spatiotemporal dynamics of groundwater in the Andean Highland in northern Ecuador" realizada por Dña. Lilia Angélica Peñafiel Aguiar en el Programa de Doctorado en Tecnologías de la Computación e Ingeniería Ambiental, autorizan su presentación a trámite dado que reúne las condiciones necesarias para su defensa.

Lo que firmamos, para dar cumplimiento al Real Decreto 99/2011 de 28 de enero, en Murcia a 20 de septiembre de 2024.

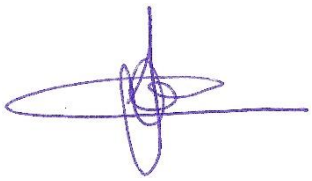

Fdo.: Francisco Javier Alcalá García

Fdo.: Javier Melchor Senent Aparicio

[1] Si la Tesis está dirigida por más de un Director tienen que constar y firmar ambos.

LIST OF PUBLICATIONS

This Doctoral Thesis is presented under the "conventional thesis" modality, although its initial conception was to present it as “compendium of publications”, and hence the included contents adapt the contents published in three JCR articles; Appendix A includes the three articles published in JCR journals. I have made this decision for two reasons. The first is because the journal Geotectonics (Springer Ed.) where one of the articles scheduled for this Thesis was published dropped drastically and unexpectedly in the JCR ranking from Q2 to Q4. The second reason is because the date for the Thesis’ deposit was approaching and I already had all the scientific material that makes up the present document. However, I have finished a fourth article intended that I plan to submit to a Q1 JCR journal once the English revision is finished, and whose content is also an essential part of this Thesis. The following are the publications completed during the development of the Doctoral Program that are the exclusive result of the research associated to this Thesis.

Articles published in JCR journals

Publication 1: Senent-Aparicio, J., Peñafiel, L., Alcalá, F.J., Jimeno-Sáez, P., Pérez-Sánchez, J. Climate change impacts on renewable groundwater resources in the andosol-dominated Andean highlands, Ecuador. *Catena*, 236, 107766. https://doi.org/10.1016/j.catena.2023.107766

Impact Factor 2022 (JCR): 6.200; Category: GEOSCIENCES, MULTIDISCIPLINARY; Ranking: 17/202 (Q1); Date of publication: 2024.

This article analyses the impact of climate change on the renewable groundwater resource. It supports a part of the Sections related to SWAT model (including methods, implementation, results, and discussion) and the entirety of the Sections related to climate change impact on the renewable groundwater resource (including methods, results, and discussion).

Publication 2: Peñafiel, L., Alcalá, F.J., Senent-Aparicio, J. Usefulness of Compiled Geophysical Prospecting Survey in Groundwater Research in the Metropolitan District of Quito in Northern Ecuador. *Applied Sciences*, 11, 11144. https://doi.org/10.3390/app112311144

Impact Factor 2021 (JCR): 2.838; Category: PHYSICS, APPLIED; Ranking: 76/161 (Q2); Date of publication: 2021.

This article analyses the different geophysical research experiences carried out with different techniques and purposes for groundwater research in the Metropolitan District of Quito, Ecuador. None of these experiences reach the basin bedrock and define the aquifer thickness. This publication supports part of the Sections of introduction and geological description, and a part of the Section limitations and future research section.

Publication 3: Peñafiel, L.A., Reyes, P.S., Alcalá F.J., Ramírez, M.R., Cabero, A. Fold-Axis Parallel Extension along the Southern Ending of the Quito (Ecuadorian Andes) Fault System: Implications in River Network and Aquifer Geometry. *Geotectonics*, 54, 256-265. https://doi.org/10.1134/S0016852120020090

Impact Factor 2020 (JCR): 1.121; Category: GEOCHEMISTRY & GEOPHYSICS; Ranking: 75/88 (Q4); Date of publication: 2020.

This article presents an experience of deep geophysical research using magneto-telluric techniques in the southern area of the Metropolitan District of Quito, Ecuador. The exploration does not reach the basin bedrock or fully define the aquifer thickness. This article supports part of the Sections of introduction, geological description, and limitations and future research.

Publication 4 (completed due to lack of English review before submission):

Peñafiel, L., Alcalá F.J., Jimeno-Sáez, P., Senent-Aparicio, J. Groundwater dynamics in the Andean Highland in northern Ecuador.

This article conducts the stationary assessment of renewable groundwater resource and groundwater dynamics. It supports most of the Sections of introduction, justification, description of the studied area, stationarity analysis

(including methods and results), a part of the SWAT model (including methods, implementation, results and discussion) and the entirety of the Sections of chemical and isotopic tracers and physical Darcian-based formulations for groundwater dynamics (including methods, results and discussion).

Articles published in non-indexed journals

Publication 5: Peñafiel, L., Alcalá, F.J., Barragán, E., Larrea. O. 2016. Evaluación del balance hídrico en un área vulcano-sedimentaria de alta montaña poco monitorizada en la Cordillera de Los Andes: acuífero del río Pita, norte de Ecuador. *Revista Latino-Americana de Hidrogeología,* 10, 502–508.

Type of production: Research Article; Format: Journal; Impact: IN-RECS.

This article presents preliminary results of the rainfall-runoff modelling in the Pita River. It supports a small part of the Sections of introduction, justification and SWAT model (including methods, results and discussion).

Publication 6: Peñafiel, L., Alcalá, F.J., Barragán, E., Toro-Espitia, L., Larrea, O. 2016. Uso de trazadores químicos e isotópicos para deducir el funcionamiento del acuífero del río Pita, Cordillera de Los Andes, norte de Ecuador. *Revista Latino-Americana de Hidrogeología,* 10, 495–501.

Type of production: Research Article; Format: Journal; Impact: IN-RECS.

This article presents preliminary results of the groundwater chemical and isotopic tracing in the Pita River Basin. It supports a small part of the Sections of chemical and isotopic tracing (including methods, results and discussion).

Book chapters

Publication 7: Peñafiel, L., Alcalá, F.J., Larrea, O. 2018. Balance neto de agua subterránea en la cuenca alta del río Pita, región alto-andina de Ecuador. In: Aguas subterráneas: Recurso sin fronteras: Hidrogeología Regional, pp. 103-110. Universidad Nacional de Salta, Argentina. ISBN 978-987-633-538-6.

Type of production: Chapter of Book; Format: Book.

Proceedings in international congresses

Publication 8: Alcalá, F.J., Toapanta J., Peñafiel, L., Barragán, E., Yánez, W., Buenaño, M., Larrea, O. 2016. First data on atmospheric chloride mass balance components in the Andean *páramo* in central Ecuador: implications to project climate scenarios of net aquifer recharge and potential groundwater chemical baseline. Session: 6.03-2663, pp. 851-852. International Association of Hydrogeologists. ISBN 978-2-9554864-0-5.

Type of event: Conference; Name: 43th IAH Congress: Groundwater and Society; Organizer: International Association of Hydrogeologists; City: Montpellier, France.

ABSTRACT

Climate change and some adaptive human actions will affect water resource access and availability for environmental requirements and human supply. Hydrological modelling combined with saturated zone routed techniques is an effective strategy for evaluating the renewable water resources under stationary conditions prior forecasting climate and human impacts under plausible scenarios. This methodology has proven to be suitable for sparse-data mountainous basins intended to supply densely populated urban areas. In this context, this Thesis used the SWAT model to evaluate the renewable groundwater resource (RGR) under a stationary condition as a step to assess the impact of climate change on this water component in the Pita River basin (PRB), which is a representative area of the *páramo* ecosystem in the Andean Highland in northern Ecuador proposed to meet a fraction of the future water demand in the Metropolitan District of Quito (MDQ). Tracer techniques and Darcian-based formulations were used to determine the groundwater dynamics by means of some essential variables that SWAT model does not provide.

A SWAT model was configured over the period 2006–2015. A stationarity analysis prior implementing the numerical model was implemented to asseverate that the modelling period is suitable to generate stationary evaluations of the RGR. The SWAT evaluation provided average annual streamflow and aquifer recharge rates around 0.45- and 0.01-fold the average annual precipitation in the area, which is 1,004 mm. The conclusion was that aquifers in the PRB are virtually full, thus repealing most of the infiltration water amount. As in other pristine Andean Highland basins, in the PRB the natural hydrological regime determined by thick, porous andosols over virtually full moderate-permeability volcanic and volcano-sedimentary aquifers induces high streamflow and low aquifer recharge rates.

Five regional climate models (RCMs) based on two Representative Concentration Pathway (RCP) emission scenarios (4.5 and 8.5) were implemented to assess the climate change impact on the RGR for the mid- (2040–2069) and long-term (2070–2099) time horizons. All the RCMs indicated some less aquifer recharge in the mid-term. However, this pattern was softened, and even reversed, in several

scenarios in the long term. Seasonal differences in streamflow and aquifer recharge in the baseline scenario were predicted to increase to + 23 %. Future hydrological regime could place the highly sensitive soil–vegetation dynamics of the *páramo* ecosystem at risk of degradation, with negative consequences for stream water provision. Hence, the RGR fraction seems to be the safest option for water provision in the future, despite that much more knowledge about its dynamics is needed to asseverate that its quantity and quality properties will remain.

Chemical, stable isotope and radioisotope tracer techniques corroborated the existence of shallow and deep aquifers based on the different average groundwater age and sources of salinity associated to each one. The processes controlling the chemical and isotopic baseline of shallow groundwater contributed to baseflow were atmospheric bulk deposition and water-rock interaction. For the deep groundwater discharge, volcanic CO_2 degassing and emanations of halides, lithium and sulphate adds to those above two processes. Based on measurable tritium contents, the contribution of old groundwater was interpreted much minor than modern groundwater. For old groundwater, the renewal time of several millennia agrees with large low-yielding aquifers and low aquifer recharge rates. The low recharge rates estimated with SWAT model corroborates a part of this assertion, the relative one to the assumed high thickness (even some thousand meters) and low specific yielding (lower than 0.01) of deep aquifers remains unknown until conclusive data are available.

Darcian-based formulations provided tentative evaluations of average groundwater residence (renewal) time and total groundwater discharge. Since aquifers are virtually full, groundwater storage is much higher than aquifer recharge, the groundwater residence (renewal) times are typically low (some to dozen years) for shallow groundwater and long to very long, even millennia for deep groundwater. Regarding the RGR, average annual discharge was around 340 mm, which was similar to the sum of baseflow and aquifer recharge calculated with SWAT model. The discharge fraction concerned to average annual subsurface groundwater transmitting through the aquifer to the basin outlet was around 0.28 mm, which was coincident with deep aquifer recharge calculated with SWAT model. Average aquifer thickness and saturated volume were tentatively estimated around 1,350 m and 0.64 km^3, respectively. This volume does not amount to a

significant reserve because the large part is associated to high-mineralized (low quality) old groundwater having a very low renewal.

This Thesis evidences how severe could impact an unplanned exploitation regime on the RGR and especially on the old groundwater reserve; the outlook would worsen if the unplanned exploitation was carried out without considering the additional impact of climate change. Future research will be addressed towards improving the current geological knowledge. This constraint and the low groundwater monitoring prevent implementing coupled surface water-groundwater numerical models for quantitative groundwater assessments. This handicap is similar to that reported in other adjacent basins of the Andean Highland and prevents a sustainable groundwater management.

KEY WORDS

Groundwater, hydrological conceptualization, stationary evaluation, climate change, urban supply, andean highland, Ecuador.

RESUMEN

El cambio climático y algunas acciones humanas adaptativas afectarán al acceso y a la disponibilidad de los recursos hídricos para usos ambientales y suministro humano. La modelización hidrológica, combinada con técnicas de evaluación aplicadas en la zona saturada, es una estrategia eficaz para evaluar los recursos hídricos renovables en condiciones estacionarias, previa predicción de impacto climático y humano bajo escenarios plausibles. Esta metodología ha demostrado ser adecuada en cuencas montañosas con datos dispersos destinadas a abastecer áreas urbanas densamente pobladas. En este contexto, esta Tesis utilizó el modelo SWAT para evaluar el recurso de agua subterránea renovable (RGR) bajo una condición estacionaria como un paso para evaluar el impacto del cambio climático sobre este componente hídrico en la cuenca del río Pita (PRB), que es un área representativa del ecosistema de páramo en el Altiplano Andino en el norte de Ecuador propuesta para satisfacer una fracción de la demanda futura de agua en el Distrito Metropolitano de Quito (MDQ). Se utilizaron técnicas de trazadores y formulaciones basadas en la Ley de Darcy para determinar la dinámica del agua subterránea mediante algunas variables esenciales que el modelo SWAT no proporciona.

Se configuró un modelo SWAT para el periodo 2006-2015. Se implementó un análisis de estacionariedad previo a la implementación del modelo numérico para asegurar que el periodo de modelación es adecuado para generar evaluaciones estacionarias del RGR. La evaluación SWAT proporcionó tasas medias anuales de escorrentía total y de recarga a los acuíferos de 0,45 y 0,01 veces superiores a la precipitación media anual de la zona, que es de 1.004 mm. La conclusión fue que los acuíferos en la PRB están prácticamente llenos, repeliendo la mayor parte del agua infiltrada. Al igual que en otras cuencas prístinas del Altiplano Andino, en la PRB el régimen hidrológico natural determinado por andosoles porosos de gran espesor sobre acuíferos volcánicos y volcano-sedimentarios de permeabilidad moderada prácticamente llenos induce alta tasa de escorrentía total y baja de recarga a los acuíferos.

Se implementaron cinco Modelos Climáticos Regionales (CRMs) basados en dos escenarios de emisiones (4.5 y 8.5) de la Trayectoria de Concentración Representativa (RCP) para evaluar el impacto del cambio climático sobre el RGR para los horizontes temporales de medio (2040-2069) y largo plazo (2070-2099). Todos los CRMs indicaron menor recarga a los acuíferos a medio plazo. Sin embargo, este patrón se suavizó, e incluso se revirtió, en varios escenarios a largo plazo. Se predijo que las diferencias estacionales en la escorrentía total y la recarga a los acuíferos en el escenario de referencia aumentarían a + 23 %. El régimen hidrológico futuro podría poner en riesgo de degradación la dinámica suelo-vegetación altamente sensible del ecosistema del páramo, con consecuencias negativas para la provisión de agua a partir de los cauces. Por lo tanto, la fracción del RGR parece ser la opción más segura para el suministro de agua en el futuro, a pesar de que se necesita mucho más conocimiento sobre su dinámica para afirmar que sus propiedades de cantidad y calidad se mantendrán.

Las técnicas de trazadores químicos, isótopos estables y radioisótopos corroboraron la existencia de acuíferos superficiales y profundos a partir de la diferente edad promedio del agua subterránea y las fuentes de salinidad asociadas a cada uno de ellos. Los procesos que controlan el fondo químico e isotópico del agua subterránea poco profunda que contribuye al flujo base fueron la deposición total atmosférica y la interacción agua-roca. Para la descarga del agua subterránea profunda, la desgasificación volcánica de CO_2 y las emanaciones de haluros, litio y sulfato se suman a los dos procesos anteriores. Sobre la base de contenidos medibles de tritio, la contribución del agua subterránea antigua se interpretó mucho menor que la del agua subterránea moderna. Para el agua subterránea antigua, el tiempo de renovación de varios milenios concuerda con grandes acuíferos de bajo rendimiento y baja tasa de recarga. La baja tasa de recarga estimada con el modelo SWAT corrobora una parte de esta afirmación, la relativa al gran espesor (incluso algunos miles de metros) y bajo rendimiento específico (inferior a 0,01) de los acuíferos profundos sigue siendo desconocida hasta que no se disponga de datos concluyentes.

Las formulaciones basadas en la Ley de Darcy proporcionaron evaluaciones tentativas del tiempo promedio de residencia (renovación) del agua subterránea y la descarga total de agua subterránea. Dado que los acuíferos están virtualmente llenos, el almacenamiento de agua subterránea es mucho mayor que la recarga a

los acuíferos, lo que induce que los tiempos de residencia (renovación) del agua subterránea poco profunda suelan ser bajos (de algunos a decenas años) y largos a muy largos, incluso milenios para el agua subterránea profunda. En cuanto al RGR, la descarga media anual fue en torno a 340 mm, similar a la suma del flujo base y la recarga a los acuíferos calculados con el modelo SWAT. La fracción de descarga asociada al agua subterránea media anual que se transmite a través del acuífero hasta la salida de la cuenca fue 0,28 mm, que coincide con la recarga del acuífero profundo calculada con el modelo SWAT. El espesor medio y el volumen saturado del acuífero se estimaron tentativamente en torno a 1.350 m y 0,64 km^3, respectivamente. Este volumen no representa una reserva significativa debido a que la mayor parte está asociada a agua subterránea antigua de alta mineralización (baja calidad) que tiene una renovación muy baja.

Esta Tesis evidencia la gravedad con la que podría impactar un régimen de explotación no planificado sobre el RGR y especialmente sobre la reserva de agua subterránea antigua; las perspectivas empeorarían si la explotación no planificada se llevara a cabo sin considerar el impacto adicional del cambio climático. Las investigaciones futuras se orientarán a mejorar el conocimiento geológico actual. Esta limitación y la baja monitorización del agua subterránea impiden la implementación de modelos numéricos acoplados de agua superficial-subterránea para evaluaciones cuantitativas del agua subterránea. Este obstáculo es similar al reportado en otras cuencas adyacentes del Altiplano Andino e impide un manejo sostenible del agua subterránea.

PALABRAS CLAVE

Agua subterránea, conceptualización hidrológica, evaluación estacionaria, cambio climático, suministro urbano, altiplano andino, Ecuador.

ACKNOWLEDGEMENTS

From a formal point of view, I will express my gratitude to the support of the research projects ECU/7/006 through the International Atomic Energy Agency, PROMETEO-CEB-014-2015 and PII-DG-02-2016 funded by the Government of Ecuador, PID2020-117825GB-C21 and PID2020-117825GB-C22 funded by the Spanish Ministry of Economy and Competitiveness, P20_00016 funded by the Andalusian Ministry of Economy, Innovation, Science and Employment, and the EU HORIZON project CiROCCO under Grant Agreement No 101086497 funded by the European Commision. I'm also grateful to the authorities and technical staff of the Quito's Public Water Supply Company, Institute for Meteorology and Hydrology, Ecuador Water Authority, Fund for the Protection of Water, Ecuadorian Space Institute, and National Polytechnic School in Quito of Ecuador, for the valuable information and suggestions provided.

From a personal point of view, I would like to thank my supervisors Dr. Francisco Javier Alcalá for his patience and invaluable help in the successful completion of this Thesis, as well as Dr. Javier Senent for his dedication and generosity in sharing his knowledge during the development of this work.

Finally, I would like to express my affection to my husband Pedro and my children Darío, Amanda and Santiago for their love and motivation to complete this Thesis.

‘Knowledge rests not only on truth but also on error’ Carl Jung.

GENERAL TABLE OF CONTENTS

LIST OF PUBLICATIONS **7**

ABSTRACT **11**

RESUMEN **14**

ACKNOWLEDGEMENTS **17**

ACRONYMS AND ABBREVIATIONS **24**

LIST OF FIGURES **28**

LIST OF TABLES **33**

I - INTRODUCTION **37**

1.1. GLOBAL WATER ISSUE **37**

1.2. Justification of the research **38**

1.3. Objective **41**

1.4. Structure of the thesis **42**

II - JUSTIFICATION **47**

2.1. Andean Highland **47**

2.2. Hydrological modelling tools **48**

2.3. Hydrological modelling strategies and experiences **49**

III - STUDY AREA **55**

3.1. Location and climate **55**

3.2. Geology and hydrogeology **59**

3.3. Soils, land use, and water-dependent economy **61**

IV - RESEARCH METHODOLOGY **67**

4.1. Long-term representativeness of the water balance components **67**

4.2. SWAT model **69**

4.2.1. Basic description 69

4.2.2. Calibration and validation of model predictions....72
4.2.3. Input data and model set-up....75
4.3. Future climate scenarios....75
4.4. Groundwater dynamics....77
4.4.1. Basic rationale....77
4.4.2. Tracer techniques....77
4.4.3. Sampling and analytical methods....80
4.4.4. Darcian-based formulations....82
V - RESULTS AND DISCUSSION....87
5.1. Stationarity of the modelling period....87
5.1.1. Stationarity analysis....87
5.2. Modelling of stationary streamflow....91
5.2.1. SWAT model setup....91
5.2.2. SWAT model output, calibration and validation....99
5.2.3. Stationary water balance components....106
5.3. Modelling of future scenarios streamflow....110
5.3.1. Selection of climate change models....110
5.3.2. Changes in projected precipitation and temperature....111
5.3.3. Response of renewable groundwater resource to climate change....116
5.3.4. Impact of climate change on magnitude, variability and seasonality of the RGR 124
5.4. Hydrogeological functioning and groundwater dynamics in the PRB 131
5.4.1. Findings from chemical, stable isotope and radioisotope tracing....131
5.4.2. Findings from Darcian based formulations....141
VI - LIMITATIONS AND FUTURE WORK....147
6.1. Overall exposition....147

6.2. Hydrogeological conceptualization of regions with active tectonics and volcanism 148

6.3. Surface water - groundwater coupled modelling 153

VII - CONCLUSIONS 157

VIII - BIBLIOGRAPHICAL REFERENCES 163

IX - APPENDIXES 203

APPENDIX A. Articles published in JCR journals 203

A1. Publication 1 203

A2. Publication 2 223

A3. Publication 3 242

APPENDIX B. Brief description of SWAT model 253

B1. SWAT model performance statistics 253

B2. Brief description of SWAT model calibration parameters 255

B3. Parameters used for daily SWAT model calibration 258

B4. Additional remarks on the interpretation of calibrated parameters 259

ACRONYMS AND ABBREVIATIONS

AMS, Accelerator Mass Spectrometer

AW, Atlantic watershed

CCT, Climate Change Toolkit

CHV, Chalupas Volcano

CHVS, Chalupas Volcano Sequence

COV, Cotopaxi Volcano

COVS, Cotopaxi Volcano Sequence

CSIC, Spanish National Research Council

CV, Coefficient of variation

DEM, Digital Elevation Model

DIC, Dissolved inorganic carbon (DIC)

EAC, Eastern Andean Cordillera

EPN, National Polytechnic School

ENSO, El Niño–Southern Oscillation index

EPMAPS, Quito's Public Water Supply Company

ERW, Esmeraldas River watershed

FONAG, Fund for the Protection of Water, Ecuador

GCM, Global Climate Model

HRU, Hydrologic Response Unit

HRU, Hydrological Response Unit

HWSD, Harmonized World Soil Database

HPWCA, High Pita Water Conservation Area

IAEA, International Atomic Energy Agency

IAV, Inter-Andean Valley

IGME, Geological and Mining Institute of Spain

INAMHI, Institute for Meteorology and Hydrology of Ecuador

IRMS, Isotope Radio Mass Spectometer

KGE, Kling–Gupta efficiency

lnNSE, Logarithmic Nash-Sutcliffe coefficient efficiency

MA, Moving average

MAAE, Ministry of Environment, Water and Ecological Transition of Ecuador

MINTUR, Ministry of Tourism of Ecuador

MDQ, Metropolitan District of Quito city

N, critical number of years for a variable to attain stationarity

NSE, Nash-Sutcliffe efficiency

PBIAS, Percent bias

PBIAS, Percent bias

PRB, Pita River basin

PW, Pacific watershed

R2, Coefficient of determination

RCM, Regional Climate Model

RCP, Representative Concentration Pathway

RGR, Renewable groundwater resource

RMSE, Root mean squared error

RSR, RMSE relative to the standard deviation of the observations

RSR, Root mean square error to the standard deviation ratio

SENAGUA, Ecuador Water Authority

SIV, Sincholagua Volcano

SIVS, Sincholagua Volcano Sequence

SUFI-2, Sequential Uncertainty Fitting version 2 of SWAT

SWAT, Soil and Water Assessment Tool

SWAT-CUP, Calibration and Uncertainty Procedure Software of SWAT

TU, Tritio units

V-SMOW, Vienna Standard Mean Ocean Water

V-PDB, Vienna Peedee belemnite standard

WAC, Western Andean Cordillera

WRC, Water retention capacity

LIST OF FIGURES AND TABLES

LIST OF FIGURES

Figure 1. (a) Central and northern sectors of the Andean Highland dominated by the *páramo* ecosystem from Costa Rica to Peru (base map modified from Buytaert et al., 2006), showing the location of the PRB and the long-term Izobamba weather station (W5) in northern Ecuador, and other sites cited in the text. (b) The PRB over a 30-m-resolution Digital Elevation Model (DEM) from SavGIS [http://www.savgis.org/ecuador.htm], showing location of weather and stream-gauging stations as in Table 2, Bocatoma (S1) and Salitre (S2) permanent baseflow springs, Chilcahuayco (S3) permanent thermal spring, and location of some illustrative views displayed in Figure 2. (c) Hydrogeological map (scale 1:50,000) of the PRB after literature data (Malo et al., 1980; Clapperton, 1993; Hall and Mothes, 2008) and direct field observations, showing the location of S1, S2 and S3 springs, boreholes W1 and W2 used for pumping tests, regional piezometry, and hydrogeological cross-sections A–A′ and B–B′. (d) Soil map (scale 1:200,000) of the PRB after Mejía et al. (1978) and direct field observations, showing the location of sites T1 to T8 used for soil hydraulic tests as in Table 3. (e) Land-use Units of the PRB (scale 1:25,000) after FONAG (2018), aerial photographs and direct field observations, showing the Cotopaxi National Park (CNP) and the High Pita Water Conservation Area (HPWCA). IAV—Inter-Andean Valley; EAC—Eastern Andean Cordillera; WAC—Western Andean Cordillera; PW—Pacific watershed; AW—Atlantic watershed; ERW—Esmeraldas River watershed; WRC—water retention capacity at saturation in $cm^3\ cm^{-3}$ 57

Figure 2. Some illustrative views of the PRB. (a) Northern flank of the Cotopaxi Volcano (COV). (b) Southern flank of the Sincholagua Volcano (SIV). (c) Bocatoma gauging station (Q5) and andesitic lavas from the Cotopaxi Volcano Sequence (COVS) at the PRB outlet. (d) Ash flows from Chalupas Volcano Sequence (CHVS). (e) Thermal permanent spring S3 discharging old groundwater. (f) Typical andosol

of the *páramo* ecosystem over pyroclastic flows from the CHVS. See location and orientation of views in Figure 1b. 58

Figure 3. Schematic of surface and subsurface water balance components implemented in SWAT model, modified from Luo et al. (2012). Notation for variables used (all in mm H_2O per day) as (1) P is precipitation; (2) E_A is actual evapotranspiration; (3) Q denotes streamflow components, where subscript T is total streamflow, U is surface and interflow runoff, S is surface runoff, L is lateral flow (interflow) from unsaturated soil, D is drainage from tiles, BT is baseflow from shallow aquifer and deep aquifer discharges, BS is baseflow from shallow aquifer discharge, and BD is baseflow from deep aquifer discharge; (4) W denotes transferable amount of water between two ground layers (hydrological zones), where subscript SS is seepage percolation from unsaturated zone to shallow aquifer, SD is seepage percolation from shallow aquifer to deep aquifer, RS is shallow aquifer recharge, and RD is deep aquifer recharge; and (5) S denotes water storage in a ground layer (hydrological zone), where subscript W is unsaturated (soil-root and vadose) zone, S is shallow aquifer (fluctuating saturated zone), and D is deep aquifer (permanent saturated zone). Notation for parameters used as (1) δ denotes delay time or drainage time (days) between two ground layers (hydrological zones), where subscript rs is in-transit W_{SS} to W_{RS} and rd is in-transit W_{SD} to W_{RD}; and (2) α denotes baseflow recession parameter (days), where subscript bs is shallow aquifer and bd is deep aquifer. 71

Figure 4. Results from the n-year moving average (MA) analysis of yearly precipitation (P) and temperature (T) time series from the 54-year long Izobamba weather station (see basic statistics in Table 2 in next section), with n≤nX for series of averages and n≤nX-1 for series of coefficients of variation (CVs); nX = elements series. (a) Average value of the MA series of averages, mX: mP and mT, mm year-1. (b) Dimensionless average value of the MA series of CVs, mCVX: mCVP and mCVT. (c) Dimensionless error (coefficient of variation) of the MA mX series, cvX: cvP and cvT. (d) Dimensionless error (coefficient of variation) of the MA mCVX series, cvCVX: cvCVP and cvCVT. N = N-year period for stationarity. 88

Figure 5. For years 1964–2017 in the PRB area, (a) Normalized El Niño–Southern Oscillation (ENSO) index [ENSO website: https://origin.cpc.ncep.noaa.gov/products/analysis_monitoring/ensostuff/ONI_v5.php]; (b) yearly precipitation (P) time series from Izobamba weather station and

cumulative deviation (CD) from its average yearly P, mm year^{-1}; (c) yearly temperature (T) time series from Izobamba weather station and CD from its average yearly T, ºC. For (a) and (b), 0.2 percentile, average (0.5 percentile), and 0.8 percentile of yearly data series are indicated. Vertical grey shading indicates the entire modelling period 2003–2015, including the 2003–2005 warm-up (WU), 2006–2010 calibration (CA), and 2011–2015 validation (VA) periods implemented in SWAT model. 90

Figure 6. For SWAT model in the PRB, (a) daily precipitation at Izobamba weather station (W5; Figure 1b; Table 2); (b) observed and predicted daily streamflow (QT) at Bocatoma gauging station (Q5; Figure 1b; Table 2) for the 2004–2005 warm-up, 2006–2010 calibration, and 2011–2015 validation periods; (c) predicted (z*) vs. observed (z) daily streamflow data for the calibration and validation periods, RE=(z–z*)/z is the relative difference; (d) predicted daily baseflow (QBT) at Q5 gauging station; (e) observed vs. predicted monthly streamflow (QT) at Q5 gauging station for the 2004–2015 simulation period; (f) RE=(z–z*)/z for the calibration and validation periods; and (g) predicted monthly baseflow (QBT) at Q5 gauging station..... 106

Figure 7. In each of the seven PRB sub-basins (SB) over the period 2006–2015, average yearly value (a through e), coefficient of variation (CV) (f through j), and yearly time series (k through o) of precipitation (P), total streamflow (Q_T), baseflow (Q_{BT}), shallow aquifer recharge (W_{RS}), and deep aquifer recharge (W_{RD}). 107

Figure 8. Distribution of the mean values and standard deviations of monthly temperature and precipitation of the three RCM-RCP 4.5 ensembles for the baseline period (1976–2005) and the mid- (2040–2069) and long-term (2070–2099) future horizons. Figure modified and updated from Senent-Aparicio et al. (2024)..... 113

Figure 9. Distribution of the mean values and standard deviations of monthly temperature and precipitation of the three RCM-RCP 8.5 ensembles for the baseline period (1976–2005) and the mid- (2040–2069) and long-term (2070–2099) future horizons. Figure modified and updated from Senent-Aparicio et al. (2024)..... 114

Figure 10. Distribution of the monthly mean values of the main water balance components predicted by the three RCM-RCP 4.5 ensembles in the PRB for the baseline period (1976–2005) and the mid- (2040–2069) and long-term (2070–2099) future horizons. P—precipitation in mm; E_A (here denoted as ET)—actual

evapotranspiration in mm; EA:P (here denoted as ET/P)—evaporative fraction of P as a dimensionless fraction; 1–(EA:P) (here denoted as 1–[ET/P])—non-evaporative fraction of P as a dimensionless fraction; WYLD—maximum amount of water that can contribute to streamflow and aquifer recharge after discounting transmission losses in mm; and WR (here denoted as TA_RCHG)—total aquifer recharge in mm. Figure modified and updated from Senent-Aparicio et al. (2024).....122

Figure 11. Distribution of the monthly mean values of the main water balance components predicted by the three RCM-RCP 8.5 ensembles in the PRB for the baseline period (1976–2005) and the mid- (2040–2069) and long-term (2070–2099) future horizons. P—precipitation in mm; EA (here denoted as ET)—actual evapotranspiration in mm; EA:P (here denoted as ET/P)—evaporative fraction of P as a dimensionless fraction; 1–(EA:P) (here denoted as 1–[ET/P])—non-evaporative fraction of P as a dimensionless fraction; WYLD—maximum amount of water that can contribute to streamflow and aquifer recharge after discounting transmission losses in mm; and WR (here denoted as TA_RCHG)—total aquifer recharge in mm. Figure modified and updated from Senent-Aparicio et al. (2024).....124

Figure 12. (a) Classification and location of the selected water points over a 30-m-resolution DEM of the PRB (Figure 1b) with the main geological structures overlapped (Figure 1c). (b) rCl/rBr molar ratio vs. chloride content in mg L–1; 1—water points with predominant atmospheric chloride, 2—water points with volcanic contribution of halides, and 3—streamflow revealing a mixture of chloride from atmospheric sources and volcanic halides. (c) δ18O referred to the V-SMOW standard in ‰ vs. elevation in m a.s.l.; MAL—meteoric altitudinal line, SAL—streamflow altitudinal line, and 1—high-elevation recharge water points. (d) 3H content in tritium units (TU) vs. calculated water age (GA) in year. (e) δ13CDIC referred to the V-PDB standard in ‰ vs. HCO3 (DIC) in mg L–1, indicating sources of CO2 after Mook (2001); 1—in-transit recharge usually contributing to interflow runoff, 2—water points with volcanic CO2, and 3—shallow discharge contributing to streamflow. (f) Non-normalized 14C activity (A14C) in percent modern carbon (pmc) vs. calculated conventional age (GA) in kiloyear (kyr). For (b) throughout (f), the values correspond to the average weighed hydrochemistry and isotope content calculated over the control period February–August 2015, as reported in Table 17. 133

Figure 13. Two-dimensional geothermal modelling in the northern versant of the Cotopaxi Volcano (southern part of the PRB), modified and updated from Hemmings et al. (2016), including water (liquid) saturation (background colours), temperature (coloured contours), and heat flux (streamlines and arrows; logarithmic scale) dynamics at the end of the initial model simulation (3,500 years). 151

LIST OF TABLES

Table 1. Equations, ranges and optimal values for SWAT model performance statistics, after Moriasi et al., (2007, 2012). 74

Table 2. Description of weather (W) and streamflow gauging (Q) stations used in this research. 94

Table 3. Description of the essential weather (E) and stream-gauging (A) stations in the PRB used to build the stationary SWAT model. 95

Table 4. Hydraulic properties of different soil typologies surveyed at the PRB, after literature data. 96

Table 5. The Harmonized World Soil Database (FAO / UNESCO, 1988) soil data used in the SWAT model and andosol experimental data obtained from Lahuette and Recalde (2015) in the PRB. 97

Table 6. Hydraulic properties of different geological formations surveyed at the PRB. 98

Table 7. The thirteen parameters used in the first-step monthly SWAT model calibration in the PRB. 102

Table 8. The additional eight parameters used in the second-phase daily SWAT model calibration in the PRB. 103

Table 9. SWAT model performance statistics for daily and monthly simulations in the PRB. Author's elaboration. 104

Table 10. For the period 2006–2015, average yearly value and coefficient of variation of the water balance components in each sub-basin (SB) and the entire PRB. 108

Table 11. Id index of each RCM model for precipitation and temperature monthly series 110

Table 12. Changes in the average values and standard deviations of annual precipitation and temperature predicted by the implemented RCM-RCP ensembles relative to the corresponding values for each RCM baseline scenario. 112

Table 13. Average annual SWAT water balance components in the PRB after implementing the RCM-RCP 4.5 and 8.5 ensembles for mid- (2040–2069) and long-term (2070–2099) future horizons. 119

Table 14. Seasonal distribution of predicted total aquifer recharge (W_R) in the PRB after implementing the RCM-RCP 4.5 and 8.5 ensembles for mid- (2040–2069) and long-term (2070–2099) future horizons..... 127

Table 15. Quantification of the impact of climate change on the magnitude and variability..... 128

Table 16. Quantification of the impact of climate change on the seasonality..... 129

Table 17. Hydrochemistry and isotope data from representative water points selected to identify the sources of groundwater salinity, identify the existence of shallow and deep aquifers, and calculate average groundwater ages in the PRB. Data are expressed as average weighed values over the control period February–August 2015. 139

Table 18. Input data and results of the binary mixing model implemented to calculate the baseflow fraction contributed to streamflow over the control period February–August 2015..... 141

Table 19. Scenarios of average groundwater-turnover time and total groundwater discharge in the PRB attending to plausible aquifer saturated thickness ranges and other aquifer variables and parameters..... 152

I – INTRODUCTION

I - INTRODUCTION

1.1. GLOBAL WATER ISSUE

Mountain regions in tropical latitudes play an important role in global freshwater supply and are highly sensitive to climate change (Barnett et al., 2005; Bradley et al., 2006; Viviroli et al., 2007; 2011; Rangwala and Miller, 2012). Most of high-mountain basins in these latitudes, including those partially headed by glacier patches with a base at melting point (Cuffey and Paterson, 2010; Koboltschnig et al., 2011; Van Vliet-Lanoë, 2014), have preferably been studied for surface hydrology purposes. However, the groundwater resource was hardly considered and more effort in the assessment of the aquifer functioning (recharge, discharge, and storage capacity) and river–aquifer interactions is required to forecast the evolution of freshwater resources due to global driving forces and adaptive human actions (Vincent et al., 2019).

Climate change, coupled with adaptive human actions, will introduce a variety of physical and biological effects that directly impact hydrological processes and indirectly affect water availability for human and environmental requirements (Holman, 2006; Green et al., 2007; Kovalevskii, 2007; Kundzewicz et al., 2008; Bovolo et al., 2009; Green et al., 2011). In mountainous regions, climate change is expected to strongly modify temporal and spatial temperature and precipitation, with important consequences for freshwater provision in low-lying areas (Kilsby et al., 2007; Woodward et al., 2010; López-Moreno et al., 2011). According to projected climate scenarios, changes in long-term precipitation and temperature regimes are likely to increase the frequency and intensity of extreme rainfall events and droughts (Buytaert et al., 2010; Green et al., 2011; Pulido-Velázquez et al., 2018). Both global driving forces and adaptive human actions are expected to strongly affect the magnitude and natural variability of streamflow, soil moisture, and aquifer recharge (Dettinger and Earman, 2007; Kløve et al., 2014; Mishra et al., 2018; Blanco-Gómez et al., 2019), with repercussions for food provision, hydropower generation, and preservation of dependent ecosystems. Assessing the renewable groundwater resource (hereafter RGR) in the Andean

Highland is the first step for sustainable policies aimed at attenuating the consequences of climate change and adaptive human actions on water supply.

The Andean Highland constitute one of the most extensive and distinctive landscape of South America. It is dominated by the wet alpine meadow (locally named *páramo*) ecosystem in the central and northern sectors (Buytaert et al., 2006). This ecoregion roughly extends between latitudes 11ºN and 8ºS from Costa Rica to northern Peru over 3,000 meters above sea level (m a.s.l.), play a crucial role in global freshwater supply, and is highly sensitive to climate change and human pressures (Barnett et al., 2005; Bradley et al., 2006; Buytaert et al., 2006; Viviroli et al., 2007; 2011; López-Moreno et al., 2011). As in other high-mountain areas, in the Andean Highland many of ecosystem typologies are groundwater dependent, including the *páramo* ecosystem (Bradley et al., 2006; Buytaert et al., 2006; Urrutia and Vuille, 2009; Ochoa-Tocachi et al., 2016; Zulkafli et al., 2016). In this region, the combined influence of global driving forces and some human actions (e.g., deforestation, overgrazing, soil degradation, and water overdevelopment) is altering the natural regimes of river flow, soil moisture and aquifer recharge, with negative consequences for dependent ecosystems and human water provision in low-lying areas (Urrutia and Vuille, 2009; Alves and Marengo, 2010; Buytaert et al., 2006; 2010; Flores-López et al., 2016; López et al., 2017; Gonzales-Zeas et al., 2019). As a consequence, most rivers and streams traditionally considered the main freshwater source to meet the water demand of densely-populated urban areas have ceased to represent a guarantee of permanent water supply, and the groundwater resource is increasingly exploited (Buytaert, et al, 2005a, 2006; Vergara et al., 2007; Alcalá et al., 2016; Minga-Leon et al., 2018). However, the spatial and temporal coverage of hydrological information in these regions is typically low (Célleri et al., 2010; Ochoa-Tocachi et al., 2016, 2018), and only a reduced number of basins enables to make confident assessments of the RGR, including (i) stationary evaluations and (ii) predictions under climate change scenarios for different time horizons.

1.2. JUSTIFICATION OF THE RESEARCH

As the standard of living in developing countries rises, the population growing and new habits for water consumption adopted could upset the

groundwater resource sustainability (Alcalá et al., 2015; 2018; Ibáñez et al., 2022), with additional negative consequences for water provision in the future. Increased demand in many densely populated Andean urban areas has driven Authorities water source diversification to alleviate pressure on traditional ones (Bradley et al., 2006; Buytaert, et al, 2006; López et al., 2017; Minga-Leon et al., 2018). This is also the case in the Metropolitan District of Quito city (MDQ) in northern Ecuador, where groundwater from the Andean Highland and surface water transferred from the Amazonian watershed supplement traditional sources from local rivers and streams (Gonzales-Zeas et al., 2019; Minga-Leon et al., 2018). As in other Andean capitals, internal migration since the 1990s has produced rapid population growth in the MDQ. The current 2.7 million inhabitants will undoubtedly increase due to the noticeable population increase foreseen for the period 2020–2040, leading to new water source diversification (Larrea, 2016).

The Ecuador water authority is the Ministry of Environment, Water and Ecological Transition (MAAE), before SENAGUA, and Quito's Public Water Supply Company (EPMAPS) are not immune to this problem. EPMAPS is responsible for prospecting, developing, distributing, and managing potable water in the MDQ, and promotes groundwater research to improve general hydrogeological knowledge as a prerequisite for a sustainable water supply. The water supply system currently covers about 99% of the inhabitants, making the MDQ one of the best served urban areas in South America. Groundwater meets around 16% of the total urban water demand, although this figure will increase because population is growing and new caught areas in the Andean Highland are planned to be included in the water supply system. The Pita River basin (hereafter PRB) is one of these areas intended to supply the most populated southern urban districts of the MDQ.

A question arises, how the increasing groundwater extraction will affect reserves and dependent ecosystems in the Andean Highland and compromising future water provision? Applied research aimed at defining the aquifer functioning needed to assess the RGR is yet incipient to answer this question accurately in most of this region (Peñafiel et al., 2016a; 2016b). The first step in making sustainable groundwater policies departs from basic research aimed at identifying the essential features of the aquifer functioning. The second step is choosing a representative

basin having the required spatial and temporal data coverage to implement (i) robust techniques to evaluate the RGR, and (ii) procedures to verify that the evaluation represents the stationarity condition of the system prior implementing tools to assess impacts of climate change.

Different techniques can be used to evaluate the RGR (Lerner et al., 1990; De Vries and Simmers, 2002; Batelaan and De Smedt, 2007; Alcalá and Custodio, 2014). In the Andean Highland, systematic monitoring of saturated and vadose zones over large areas is quite limited, and seldom the datasets are long and unbiased enough to implement groundwater numerical modelling (Hojberg and Refsgaard, 2005; Poeter and Anderson, 2005; Beven, 2007), Darcian physical techniques based on aquifer hydraulic data, or tracer techniques (Lerner et al., 1990; Scanlon et al., 2002; Alcalá and Custodio, 2014), including stable isotopes and radioisotopes for groundwater characterization and dating. The PRB is one of these areas having long enough streamflow data series to make confident evaluations of RGR. These data must be further combined with specific monitoring of certain variables to enlarge the confidence of stationary and near-future evaluations.

Since 2003, EPMAPS is monitoring the most representative streams in the PRB (Muñoz, 2016; Minga-León et al., 2018; Gonzales-Zeas et al., 2019), and the groundwater resource to a lesser extent due to its limited access (Peñafiel et al., 2016a, 2016b, 2020, 2021). Apart from the interest for urban water supply, the PRB is a representative area to document the hydrological functioning of the Andean Highland, which makes this pilot quite suitable for implementing rainfall–runoff numerical models and some saturated-zone routed physical and tracer techniques for representative groundwater evaluations.

Since 2003, EPMAPS is monitoring the most representative streams in the PRB (Muñoz, 2016; Minga-León et al., 2018; Gonzales-Zeas et al., 2019), and the groundwater resource to a lesser extent due to its limited access (Peñafiel et al., 2016a, 2016b, 2020, 2021). Apart from the interest for urban water supply, the PRB is a representative area to document the hydrological functioning of the Andean Highland, which makes this pilot quite suitable for implementing rainfall–runoff numerical models and some saturated-zone routed physical and tracer techniques for representative groundwater evaluations.

For rainfall–runoff models, the required weather, soil, land-use, and streamflow input data are available, and the predictions can be later calibrated and validated. Streamflow hydrograph filtering techniques to separate the baseflow component as a reliable proxy of the RGR can also be applied in this pristine basin with gaining streams (Lerner et al., 1990; Scanlon et al., 2002; Paniconi et al., 2003; Hilberts et al., 2004), since aquifer recharge and discharge can be equated because groundwater transference and abstraction are nil, and direct evapotranspiration from shallow aquifers and underflow to deep aquifers can be assumed negligible (Peñafiel et al., 2016a; 2016b). For additional evaluations based on saturated zone routed physical and tracer techniques, some data concerning to aquifer hydraulic parameters and specific groundwater and rainfall chemical and isotopic data series gained in former field campaigns are available. Additionally, the critical balance period for variables to reach a comparable stationary condition can be defined, as prerequisite for the confident long-term representativeness of the evaluation obtained from suboptimal temporal and spatial data coverages (Alcalá and Custodio, 2015; Alcalá et al., 2018), which is the common in the region.

1.3. OBJECTIVE

The objective of Thesis is modelling of the spatiotemporal dynamics of the RGR in the Andean Highland, with special focus on the existing condition in northern Ecuador. This objective involved two spatial and temporal scales. Regarding the two spatial scales, this Thesis was aimed at evaluating the groundwater resource in the PRB for sustainable water use in the MDQ and enhancing the groundwater dynamics knowledge in the northern Andean Highland in general. Otherwise, the two temporal scales involved the initial conceptualization and stationary evaluation of the RGR, prior the prediction of the RGR under climate change scenarios for different time horizons.

For the stationary evaluation of the RGR, this Thesis has employed three kinds of methodologies. First, the Soil and Water Assessment Tool (SWAT) semi-distributed rainfall–runoff model was implemented to evaluate daily the surface-water and groundwater balance components from shallow and deep aquifers over the period 2003–2015, including the warm-up (2003–2005), calibration (2006–2010), and validation (2011–2015) periods. Next, tracer techniques (including chemical,

stable isotopes and radioisotopes) were used to elucidate the atmospheric and endogenous sources of salinity, calculate the baseflow fraction contributed to streamflow, and dating groundwater. The last was some Darcian-based formulations to deduce the hydrological functioning through the aquifer discharge, groundwater residence (renewal) times, and aquifer exhaustion under groundwater exploitation. Most of SWAT model input data were generated in the framework of this investigation. The input data concerning to chemical and isotope tracers and hydraulics parameters came from the EPMAPS periodical monitoring, different surveys performed in the area, official reports, scientific documents, and global repositories hosted in different websites, all of them cited in the specific chapters of this Thesis.

In addition, this Thesis evaluated the impact of climate change on the RGR in the PRB, which serves as a proxy of the expected near-future condition in many areas of the northern Andean Highland. The results intended to illustrate how climate change could modify the regime of this barely known resource, which is destined to meet most future water demand. The methodological route to achieving this aim included two stages. First, the semi-distributed rainfall–runoff SWAT model (Arnold et al., 1998) was implemented and operated over the period 2003–2015. Next, the variables of a climate change prediction ensemble consisting of five Regional Climate Models (hereafter RCMs) (ESM2M, HadGEM2-ES, IPSL-CM5A-LR, MIROC and NoerESM1-M) using the Representative Concentration Pathways (hereafter RCPs) 4.5 and 8.5 emission scenarios for the mid- (2040–2069) and long-term (2070–2099) future horizons were implemented into the SWAT model to generate future streamflow series, from which the impacts of climate change on the RGR were assessed.

1.4. STRUCTURE OF THE THESIS

The structure of this Thesis was divided into eight chapters and two appendixes. Following the brief introduction, **Chapter I** introduced the significance of the research in the northern Andean Highland in general and the MDQ in particular, as well as the objective of the study. **Chapter II** overviewed research background and latest studies in hydrological models and physical and tracer techniques used to assess some groundwater properties that SWAT model cannot

calculate. **Chapter III** described the study area. **Chapter IV** described the research methodologies, including SWAT model, tracer techniques and Darcian-based formulations aimed at enhancing the groundwater hydrological meaning and timing under stationary conditions, as well as the implemented methodology to evaluate the impacts of climate change on the RGR for different future horizons. **Chapter V** described the main results and proposed to discuss some implications for current and future use of the RGR under sustainable criteria. **Chapter VI** presented the limitations to carry out this study and determined future research directions. **Chapter VIII** contained a bibliography of references cited in this Thesis. **Appendix A** included the articles published in JCR journals. Finally, the **Appendix B** included additional information concerning to SWAT model implementation and results.

II – JUSTIFICATION

II - JUSTIFICATION

This chapter complements the literature review that frames the conceptual and theoretical framework on which this thesis is based. On the one hand, the most recent and representative hydrological modelling research was included. In addition, the state of the art of research methods on hydrologic evaluation in sparse-data mountainous regions was inquired. Additional to the general literature included in this chapter, a huge number of scientific publications and technical reports have been compiled. The compiled information served to support the exposition of the contents included in the chapters of this Thesis, as well as provide essential data.

2.1. ANDEAN HIGHLAND

Hydrological literature about the Andean Highland, as in other mountainous regions, primarily refers to surface hydrology processes preferentially studied in small catchments over short monitoring periods (Buytaert et al., 2004, 2005b, 2006; Célleri and Feyen, 2009; Tovar et al., 2013; Crespo et al., 2011, 2014; Ponce-Vega, 2015; Muñoz, 2016; Minga-Leon et al., 2018). Applied studies concerning to the stationary characterization of the RGR component (aquifer recharge, discharge and storage) or more advanced studies focused on the impact of climate change on this resource in large basins are insignificant in number or virtually non-existent (Mark et al., 2010; Favier et al., 2008; Baraer et al., 2012, 2015; Hemmings et al., 2016; Peñafiel et al., 2016a, 2016b, 2021; Vuille et al., 2018; Ruiz-Pico et al., 2019). The scant knowledge about groundwater systems in the Andean Highland derives from limited groundwater accessibility, few operational weather and stream-gauging stations, a lack of detailed geological and soil maps and sparse hydraulic and soil-vegetation data. In recent decades, climate records for the Andean Highland have also revealed perturbing changes in precipitation and temperature regimes (Espinoza-Villar et al., 2009), the consequences of which for soil moisture, streamflow and RGR remain largely unidentified. However, geological knowledge determining the capability for advanced hydrogeological conceptualization is by far the most important handicap for reliable conceptualization prior confident

evaluation of groundwater (Peñafiel et al., 2020, 2021). This constraint determines a severe limitation for suitable water policies aimed at warranty the resource sustainability, as will be explained in the discussion chapter.

2.2. HYDROLOGICAL MODELLING TOOLS

For the water (and groundwater) resource evaluation in semi-gauged basins, different rainfall-runoff numerical models exist, including statistical or mechanistic, and lumped or distributed ones (Huber et al., 1998; Cambien, 2017). In sparse-data areas such as most of the hydrological basins in the Andean Highland, a compromise between the above options is semi-distributed, mechanistic models which subdivide the area into several, homogeneous (lumped) regions with similar hydrological response (Kumar et al., 2009; Cao et al., 2006; Harmel, 2006; Jajarmizadeh et al., 2012).

The semi-distributed SWAT rainfall–runoff model (Arnold et al., 1993, 1995, 1998) was selected based on the rationales described below. SWAT model operates on a daily time step and uses spatially derived data on topography, land use, soil, and weather for stream-routed hydrology and water quality modelling (Arnold and Fohrer, 2005; Gamble and Babbar-Sebens, 2012; Izady et al., 2015). SWAT also includes different statistical tools for measuring the quality of model predictions (Neitsch et al., 2005). For model variables and parameters distribution over space, SWAT divides the studied basin into several sub-basins, which are in turn subdivided into Hydrologic Response Units (HRUs) with homogeneous land use, management, and soil properties. SWAT simulates the hydrological output of each sub-basin (Gassman et al., 2007, 2014) and enables to evaluate shallow aquifer recharge as a soil water balance component in each HRU of the different sub-basins in which a basin can be divided. However, deep aquifer recharge is a water balance closure component since SWAT model is lumped itself and does not admit distributed aquifer parameters such as bedrock hydraulic information nor additional data of the saturated zone to evaluate the magnitude and spatial distribution of this component. The sum of shallow and deep aquifer recharge, hereafter named total aquifer recharge, is the RGR. However, the rough evaluation of the deep aquifer recharge makes the RGR evaluation quite uncertainty and additional evaluations are needed to verify its magnitude, especially in areas with

thicker, productive regional aquifers contributing to streamflow. This limitation has usually been solved by using specific saturated-zone routed techniques and numerical models to characterize the groundwater components (Han et al., 2015; Jin et al., 2015; Devi at al., 2015; Stehr et al., 2009; Abiodun et al., 2018; Tobin and Bennett, 2019; Obuobie, 2008; Rahayuningtyas et al., 2014; Senent-Aparicio et al., 2020; Lee et al., 2018).

2.3. HYDROLOGICAL MODELLING STRATEGIES AND EXPERIENCES

The consulted literature shows how both shallow and deep aquifer recharge components were indistinctly used to evaluate the RGR, following four typical strategies. The first strategy used shallow aquifer recharge as a reliable proxy of the RGR in unconfined aquifers having shallow piezometry where the expected difference between shallow and total aquifer recharge is low, despite that no external verifications were always implemented to verify this assumption, as reported in basins in Australia (Sun and Cornish, 2005), India (Awana and Ismaeel, 2014), New Zealand (Me et al., 2015), Spain (Raposo et al., 2013), Iran (Izady et al., 2015), and South Africa (Gyamfi et al., 2017).

The second strategy used shallow aquifer recharge by SWAT to refine the total aquifer recharge input in groundwater numerical models. Because groundwater numerical models often overlook the required accuracy of aquifer recharge (Kim et al., 2008), assumed accurate shallow aquifer recharge by SWAT was once used in low-steep areas with enough data coverage. The different hydrological meaning and timing of shallow and deep aquifer recharge could not always be verified. Most of cases combined SWAT and MODFLOW (McDonald and Harbaugh, 1988) as in basins in USA (Sophocleous and Perkins, 2000; Menking et al., 2003), France (Conan et al., 2003), South Korea (Kim et al., 2008), Spain (Pulido-Velázquez et al., 2015, 2015b), and Iran (Ehtiat et al., 2016).

The third strategy used streamflow hydrograph filtering techniques to separate the baseflow component. These techniques were preferably used in steep basins with gaining streams and null groundwater transference and abstraction, which allows to equal total aquifer recharge to baseflow discharge (Rutledge and Mesko, 1996; Lim et al., 2005; Plesca et al., 2012; Lee et al., 2018). Among the techniques identified as the top performers with the lowest data requirements from

more than 40 different techniques of baseflow separation (Nejadhashemi et al., 2008), was the BFLOW program used in SWAT model (Nathan and McMahon, 1990; Arnold et al., 1995; Arnold and Allen, 1999) the most recursive digital filter technique in basins in USA (Chu and Shirmohammadi, 2004; Eckhardt, 2008), in western Africa (Obuobie, 2008), South Korea (Chung et al., 2010), China (Luo et al., 2012), Canada (Stadnyk et al., 2014), South Korea (Jung et al., 2016), and Nepal (Bastola et al., 2018).

The fourth strategy applied specific recharge techniques based on vadose-zone and saturated-zone studies to refine shallow and deep aquifer recharge components by SWAT, respectively. The procedure was to refine the SWAT parameters that govern shallow and deep aquifer recharge. There are many examples in the scientific literature concerning to the shallow aquifer recharge by SWAT refinement in basins in China (Han et al., 2015), Japan (Jin et al., 2015), Chile (Stehr et al., 2009), South Australia (Abiodun et al., 2018), and USA (Tobin and Bennett, 2019), western Africa (Obuobie, 2008), Indonesia (Rahayuningtyas et al., 2014), Spain (Senent-Aparicio et al., 2020), and South Korea (Lee et al., 2018).

The available data type and density and the limited capability for additional data acquisition on the field, restrict feasible strategies in the PRB to the first and fourth. When additional hydrogeological data are available, other widely-used saturated-zone routed techniques can be implemented to evaluate crucial groundwater features that cannot be calculated with SWAT and similar other rainfall–runoff models (Lerner et al., 1990; De Vries and Simmers, 2002; Batelaan and De Smedt, 2007; Nolan et al., 2007; Coes et al., 2007; Alcalá and Custodio, 2014; Senent-Aparicio et al., 2020). Based on available information on piezometry and aquifer hydraulics parameters, Darcian-based formulations additional to those included in SWAT model can be implemented for average groundwater-turnover time and total aquifer discharge, which includes the fraction of groundwater discharged as baseflow and that one is underground transmitted towards the aquifer outlet (Healy and Cook, 2002; Hojberg and Refsgaard, 2005; Poeter and Anderson, 2005; Beven, 2007); SWAT model does not evaluate this latest fraction. Based on available information on chemical solutes in spring and river water, and the stable and radioactive isotopes of water oxygen, hydrogen and dissolved inorganic carbon, tracer techniques can be used to elucidate the origin and

distribution of groundwater and estimate the average groundwater turnover time (Lerner et al., 1990; Scanlon et al., 2002; Alcalá and Custodio, 2014).

Regarding experiences in similar contexts, SWAT model has been successfully applied in many non-homogeneous high-mountain areas (Ahl et al., 2008; Bruijnzeel et al., 2011; Luo et al., 2012; Palazón et al., 2014; Senent-Aparicio et al., 2017, 2020; Jain et al., 2017), including some applications in the Andean Highland in general (Quintero et al., 2009; Stehr et al., 2009, 2010; Barrios and Uribarri, 2010; Silva, 2010; Uribe and Quintero, 2011; Schwank et al., 2014; Francesconi et al., 2016, 2018; Khosravi et al., 2018; Uribe et al., 2018), and in the Ecuadorian Andean Highland in particular (Quintero et al., 2009; Crespo et al., 2006; Plesca et al., 2012; Velasco-Argüello, 2014; Oñate-Valdivieso and Bosque-Sendra, 2014; Oñate-Valdivieso et al., 2016; Espinosa and Rivera, 2016; Hasan and Wyseure, 2018; Salmoral et al., 2018). These SWAT applications mostly contributed to conceptualize surface hydrology processes and paid less attention to the groundwater resource, so they provided scarcely checked evaluations of shallow and deep aquifer recharge. Only few exceptional cases in favourable contexts used additional techniques to evaluate (and validate) the RGR. In the most complex cases, especially those related to basins with thick, productive aquifers whose discharge contributes significantly to streamflow, important simplifications (often ambiguous) were introduced. As far as the findings of this literature review reached, only a handful of papers pointed out the relevance of the RGR through the baseflow component deduced from streamflow hydrograph filtering techniques (Plesca et al., 2012; Oñate-Valdivieso and Bosque-Sendra, 2014; Oñate-Valdivieso et al., 2016). In the PRB, available data meets with data requirements for streamflow hydrograph filtering techniques.

III – STUDY AREA

III - STUDY AREA

Chapter III was divided into three sections. Section 3.1 described the geography and climate of the study area. Section 3.2 presented the geological and hydrogeological. Section 3.3 described soils, land use, and water-dependent economy.

3.1. LOCATION AND CLIMATE

The Pita River basin (PRB) is a representative area of the páramo ecosystem in the northern Andean Highland in Ecuador with relatively high data density and null groundwater abstraction and where the natural state of soils, streams and aquifers is well preserved. This pristine basin was selected to evaluate the status and the impact of climate change on the RGR due to its representativeness, minimum data coverage requirement to make hydrological evaluations and potential to supply approximately 400,000 inhabitants in the MDQ in the future. Hence, this basin is significant for future water resource assessment and management by local water authorities. This situation is like that reported in other large urban areas in the Andean Highland due to the expected reduction in renewable water resources and the increasing population's water use habits.

The Pita River basin (PRB) is located 50 km southeast from Quito city (0°29′–0°41′ S and 78°19′–78°26′ W) in northern Ecuador (Figure 1a). This basin covers an area of 184.5 km^2, is bounded by the north-eastern flank of the Cotopaxi Volcano and the south-western flank of the Sincholagua Volcano (Figure 1b), has a mean elevation of 4,008 m a.s.l. (outlet is 3,361 m a.s.l. at the north and peak elevation is 5,897 m a.s.l. at the south), and lies in the Inter-Andean Valley (IAV) between the Western Andean Cordillera (WAC) and Eastern Andean Cordillera (EAC). The Pita River flows northward through the IAV and is tributary of the Esmeraldas River in the Pacific Ocean watershed (Figure 1a) (Erazo et al., 2018; González-Zeas et al., 2019; Peñafiel et al., 2021). Some illustrative views of representative features of the PRB are in Figure 2.

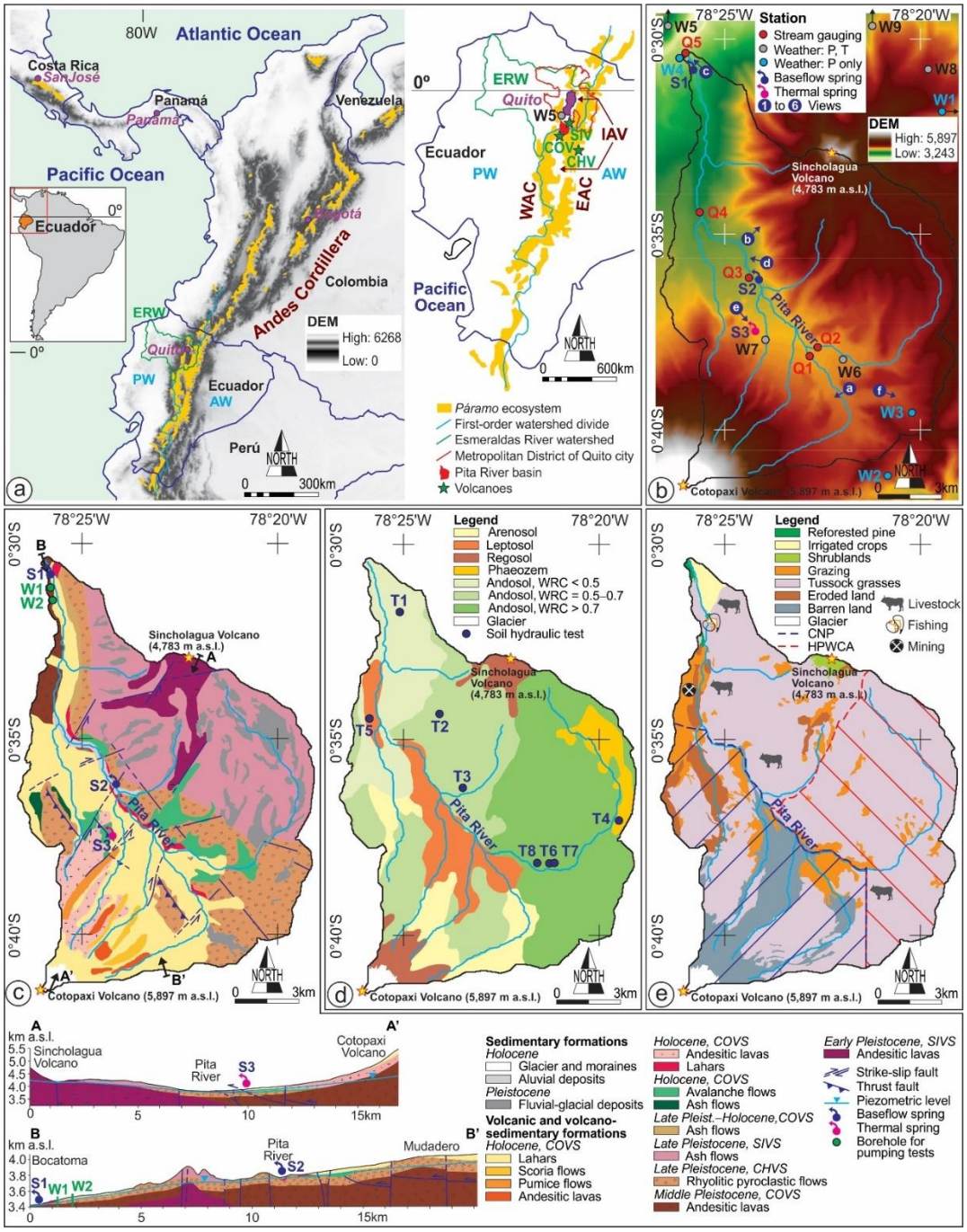

Figure caption on next page.

Figure 1. (a) Central and northern sectors of the Andean Highland dominated by the *páramo* ecosystem from Costa Rica to Peru (base map modified from Buytaert et al., 2006), showing the location of the PRB and the long-term Izobamba weather station (W5) in northern Ecuador, and other sites cited in the text. (b) The PRB over a 30-m-resolution Digital Elevation Model (DEM) from SavGIS [http://www.savgis.org/ecuador.htm], showing location of weather and stream-gauging stations as in Table 2, Bocatoma (S1) and Salitre (S2) permanent baseflow springs, Chilcahuayco (S3) permanent thermal spring, and location of some illustrative views displayed in Figure 2. (c) Hydrogeological map (scale 1:50,000) of the PRB after literature data (Malo et al., 1980; Clapperton, 1993; Hall and Mothes, 2008) and direct field observations, showing the location of S1, S2 and S3 springs, boreholes W1 and W2 used for pumping tests, regional piezometry, and hydrogeological cross-sections A–A′ and B–B′. (d) Soil map (scale 1:200,000) of the PRB after Mejía et al. (1978) and direct field observations, showing the location of sites T1 to T8 used for soil hydraulic tests as in Table 3. (e) Land-use Units of the PRB (scale 1:25,000) after FONAG (2018), aerial photographs and direct field observations, showing the Cotopaxi National Park (CNP) and the High Pita Water Conservation Area (HPWCA). IAV—Inter-Andean Valley; EAC—Eastern Andean Cordillera; WAC—Western Andean Cordillera; PW—Pacific watershed; AW—Atlantic watershed; ERW—Esmeraldas River watershed; WRC—water retention capacity at saturation in $cm^3\ cm^{-3}$

Figure caption on next page.

Figure 2. Some illustrative views of the PRB. (a) Northern flank of the Cotopaxi Volcano (COV). (b) Southern flank of the Sincholagua Volcano (SIV). (c) Bocatoma gauging station (Q5) and andesitic lavas from the Cotopaxi Volcano Sequence (COVS) at the PRB outlet. (d) Ash flows from Chalupas Volcano Sequence (CHVS). (e) Thermal permanent spring S3 discharging old groundwater. (f) Typical andosol of the *páramo* ecosystem over pyroclastic flows from the CHVS. See location and orientation of views in Figure 1b.

As other IAV basins, the PRB exhibits a neo-tropical high-mountain climate determined by the El Niño–Southern Oscillation oceanographic phenomena and the Humboldt current, and the steep orography (Kumar et al., 2000; Bendix, 2000; Bendix et al., 2004; Minga-León et al., 2018; González-Zeas et al., 2019). Both global climatic forces and orographic features determine a marked distribution of biozones at different elevations, including tropical mountain rainforests at low-lying areas, the *páramo* ecosystem in mid-slope areas, dry and cold scrublands in the highlands, and permanent snow covers at volcanoes peaks (Buytaert et al., 2006). In the PRB, the *páramo* ecosystem dominates the landscape. It consists in steep, mostly glacier formed valleys and plains with lakes, peat bogs, and wet grasslands intermingled with scrublands and low-bearing forest patches (Buytaert et al., 2006).

Precipitation (*P*) follows a bimodal distribution (Buytaert et al., 2006; Makowski Giannoni et al., 2016; Minga-León et al., 2018). Most of *P* occurs in February–May whereas the lowest amount is recorded in July–September (Rollenbeck et al., 2006). Annual mean *P* is around 1,100 mm, with a coefficient of variation of 0.21 over the period 1964–2017. Precipitation follows a decreasing gradient from east to west controlled by the incoming Atlantic cloud fronts and elevation (Garreaud and Falvey, 2009; Makowski Giannoni et al., 2016) and exhibits a positive gradient from low-lying areas up to around 3,500 m a.s.l. and a negative one above that elevation (Bendix, 2000; Bendix et al., 2004). Extreme rainfall events over 50 mm per day have been documented. Snow events are restricted to volcanoes peaks, which cover less than 1% of the PRB surface (González-Zeas et al., 2019).

Annual mean temperature (*T*) is around 7.5 °C, with daily minimums in June–September and maximums in February–April. The daily *T* amplitude may be as high as 19 °C in the Highland and around 10 ºC in low-lying areas. The decreasing *T* gradient with elevation (lapse rate) is around 0.6–0.7 ºC per 100 m

elevation (Van der Hammen and Hooghiemstra, 2000; Castaño-Uribe, 2002). Higher air humidity rates may decrease the lapse rate around 0.5 ºC per 100 m of elevation (Bacuilima et al., 1999) and the daily *T* amplitude below 10 ºC (Buytaert et al., 2006). Average daily sunshine is around 12 hours. Average daily solar radiation is 8.3 MJ m^{-2}; the lowest values occurring in wet season (February–May) and the highest ones in dry season (July–September), respectively. Insolation increases from low-lying to summit areas due to cloudiness induced by the Foehn effect in valleys from incoming Atlantic cloud fronts (Rollenbeck et al., 2006). Annual mean potential evapotranspiration is around 1,000 mm.

3.2. GEOLOGY AND HYDROGEOLOGY

The study area belongs to the Pacific Ring of Fire, a highly active belt of volcanism and seismic activity originating from the subduction of the oceanic Nazca Plate beneath the South American Plate, which is the source of the compressive tectonics and arc magmatism of the Andes Cordillera (Trenkamp et al., 2002; Tamay et al., 2016). The PRB is in the westernmost part of the NNE-trending fault-bounded Andean compressive structure, which includes the IAV between the WAC and EAC (Figure 1a).

The PRB lies in the IAV (Figure 1c). In the study area, subparallel belts of Palaeozoic metapelitic form the western metamorphic basement of the EAC (Litherland et al., 1994), which does not outcrop directly but is assumed the basement of the PRB (Malo et al., 1980). At present, the basement depth and structure in the PRB area remain unknown (EPMAPS, 2012; Peñafiel et al., 2021), thus making it undefinable the thickness of overlying formations. A variety of Quaternary volcanic and volcano-sedimentary formations from the Sincholagua, Cotopaxi, and Chalupas volcanoes is unconformable deposited over the basement (Malo et al., 1980; Spikings et al., 2000; Garrison et al., 2011), with the following synthetic succession from bottom to top (Hall and Wood, 1985; Hall and Mothes, 2008) (Figure 1c): (1) early Pleistocene andesitic lavas from the Sincholagua Volcano Sequence (SIVS) (Malo et al., 1980); (2) middle Pleistocene andesitic lavas from the Cotopaxi Volcano Sequence (COVS); (3) late Pleistocene rhyolitic pyroclastic flows from the Chalupas Volcano Sequence (CHVS) overlying andesitic lavas from SIVS and COVS (Beate, 1989; Hammersley et al., 2000; Hall and Mothes, 2008); (4) late

Pleistocene ash flows from SIVS (Malo et al., 1980); (5) late Pleistocene to Holocene ash flows from COVS; (6) Holocene ash flows and extensive avalanche flows from COVS; (7) Holocene lahars and andesitic lavas from COVS (Smyth and Clapperton, 1986; Mothes et al., 1998); and (8) Holocene andesitic lavas, pumice flows, scoria flows, and lahars from COVS (Mothes et al., 2004; Garrison et al., 2011). The Quaternary sedimentary formations (Clapperton, 1993; Rose, 1996) comprise (1) Pleistocene to Holocene fluvial-glacial deposits, (2) Holocene alluvial deposits filling the Pita River valley, and (3) current glacier and moraines at the Cotopaxi Volcano peak.

The PRB occupies a large portion of the Cayambe-Rumiñahui Hydrogeological Unit and a small part of the Quito-Machachi Hydrogeological Unit (Burbano et al., 2015). In hydrogeological terms, the above geological formations can be classified into six groups attending to the permeability type and specific yield reported in the consulted literature (PETROECUADOR, 2005; EPMAPS, 2006a, 2006b, 2012; Burbano et al., 2015); Hemmings et al. (2016); Ruiz-Pico et al. (2019): (1) the Palaeozoic metapelitic basement is a low-permeability formation representing the impervious lower boundary of the regional aquifers; (2) the Pleistocene and Holocene andesitic lavas from the SIVS and COVS and pyroclastic flows from the CHVS form deep thick regional compartmentalized aquifers of moderately permeability, with probable (currently unknown) thickness higher than 1,000 m in some sectors and yield dependent upon the degree of fracturing and fissuring; (3) the Pleistocene and Holocene ash flows from the SIVS and COVS are low-permeability formations, often confining the above Pleistocene and Holocene andesitic lavas and pyroclastic flow formations; (4) Holocene lahars from the COVS are low- to moderately-permeability formations catalogued as aquitard with thickness up to 100 m (Peñafiel et al., 2021); (5) Holocene avalanche flows, andesitic lavas, pumice flows, and scoria flows from the COVS are moderate- to high-permeability shallow thin aquifers; and (6) Pleistocene to Holocene fluvial-glacial deposits, alluvial deposits in the Pita River valley, and glacier and moraines in the Cotopaxi Volcano peak are moderate- to high-permeability unconfined aquifers of intergranular porosity with thickness up to 50 m (Figure 1c).

Hydrogeological functioning in the PRB depends on: (1) the low permeability of the Palaeozoic metapelitic impervious basement; (2) the compartmentalization,

great thickness and extend, and degree of fracturing and fissuring in Pleistocene andesitic lavas from SIVS and COVS and pyroclastic flows from CHVS, determining a noticeable but unassessed storage capacity for these aquifers; (3) the extent and thickness of low-permeability Pleistocene and Holocene ash flows from SIVS and COVS, forming aquitards; (4) the hydraulic connectivity between Pleistocene and Holocene aquifers and aquitards, favouring the deep percolation of aquifer recharge and localized aquifer discharge; and (5) the thickness and extent of avalanche flows from COVS and coarse-grained sediments for draining interflow runoff and shallow aquifer discharge (Burbano et al., 2015; EPMAPS, 2012; Muñoz, 2016; Peñafiel et al., 2009, 2016a, 2016b, 2021).

In spite that the permeability contrast between thick porous soils and volcanic and volcano-sedimentary rocks favours the noticeable interflow runoff rates (Buytaert et al., 2005a, 2006; Célleri and Feyen, 2009; Flores-López et al., 2016), recharge to deep thick aquifers is possible from (1) direct rainfall and interflow runoff infiltration (and de-icing in a very minor extent) in mid-slopes and summits where these aquifers are unconfined (Hemmings et al., 2016; Muñoz, 2016; Vuille et al., 2018), and (2) percolation from lahars and ash flows to deep thick aquifers where fracturing and fissuring is dense enough (Changkuon et al., 1989; Alcalá et al., 2016). Typically, most of aquifer discharge takes place just where the incisive valleys topography intersects the piezometry of regional aquifers and/or through fault systems reaching surface, producing permanent baseflow springs that contributes significantly to streamflow (Figure 1c).

3.3. SOILS, LAND USE, AND WATER-DEPENDENT ECONOMY

In the Andean Highland, cold and wet climate favour organic-matter-rich soils. This is the case in the PRB where dark, humic, and allophane-rich andosols with a porous structure and bulk density in the 0.13–0.95 g cm^{-3} range predominates (Fontes et al 2004; Crespo et al., 2010; Lahuatte and Recalde, 2015). These features together with the clay mineral assemblages and organic-matter contents between 10% (degraded state) and 40% (natural state) determine high organic-carbon contents in the 1–44% range, high water-holding capacities, and water retention capacity (WRC) near to 0.9 cm^3 cm^{-3} at saturation for natural states, thus inducing soil infiltration capacity in the 20–60 mm h^{-1} range higher than

typical rainfall intensities (Buytaert et al, 2004, 2005b, 2006; Célleri and Feyen, 2009; Crespo et al., 2010).

In the PRB, the soil typologies include 74.40% organic-matter rich andosols, 20.65% regosol in northern slopes of the Cotopaxi Volcano having organic-matter content less than 1%, 1.43% gleysol in summit areas including the Sincholagua and Cotopaxi volcano glacier, 3.52% phaeozems with weathered organic matter over fluvial-glacial sediments above 4,000 m a.s.l., (Figure 1d) (Mejía et al., 1978). In the study area, Mejía et al. (1978) classified the andosols into three groups, attending to the WRC as a proxy of the conservation state as (1) 14.3% at low-lying areas with <0.5 cm^3 cm^{-3}, (2) 24.6% at mid-slope areas with 0.5–0.7 cm^3 cm^{-3}, and (3) 32.2% at high-slope areas with >0.7 cm^3 cm^{-3} (Figure 1d). These figures agree with the experimental soil hydraulic data measured in the area (Peñafiel, 2009; Lahuatte and Recalde, 2015).

Regarding land use, the PRB is covered 74.1% by xerophytic tussock grasses over andosols, phaeozems, and regosols, 14.0% by barren and eroded lands over regosols and gleysols, 9.3% by grazing over regosols at low-lying areas and andosols at mid-slope areas, 0.8% by shrublands and small natural low-bearing forest patches over regosols, 1.0% by sparse irrigated crops over degraded andosols in northern areas, 0.1% by reforested pine in the basin outlet, and 0.7% is the glacier of the Cotopaxi Volcano (FONAG, 2018) (Figure 1e). The PRB hosts two environmentally protected areas, the Cotopaxi National Park (CNP) and the High Pita Water Conservation Area (HPWCA) (Figure 1e). The CNP was created in 1975 by the Government of Ecuador to protect the wildlife and covers 333.9 km^2, from which 68.7 km^2 are in the PRB (MAE, 2014). The HPWCA was declared in 2016 by the EPMAPS and the Fund for the Protection of Water (FONAG) to preserve the *páramo* ecosystem in the PRB as source of water and covers 66.2 km^2.

Water-dependent economy in the area includes extensive livestock and traditional irrigated crops in small farms. Irrigated crops such as cereals (corn, barley, and wheat), potatoes, and vegetables and small rainfed crops are devoted to family consumption. Irrigation water is collected from headwater springs in lateral catchments and distributed thought a network of ancestral ditches which favour permanent water losses and soil saturation (Somers et al., 2018). Water irrigation demand is around 5,000 m^3 per hectare and year (FONAG, 2018). The

traditional livestock is devoted to milk (cows) and wool (alpacas) production. Milk production is about 50 m^3 per day and wool production is about 10.6 tons per year (FONAG, 2018). Other activities are some sportive fishing centres and quarries for stone production (Figure 1e).

This area had 200 inhabitants censured in 2010, according to the National Institute of Statistics and Census of Ecuador (INEC, 2018a; 2018b). Most of inhabitants live in disseminated farms in low-lying areas, so human impact is very low in the protected CNP and HPWCA areas. The CNP attracted about 60,700 national and international visitors per year over the period 2000–2003 (MINTUR, 2014; 2017). Tourism is restricted to accessible areas and tourists do not overnight in the area because there are not facilities for lodging.

IV – RESEARCH METHODOLOGY

IV -RESEARCH METHODOLOGY

Chapter IV was divided into four sections. Section **4.1** described the stationarity analysis required to implement numerical models. Section **4.2** presented the SWAT model, including used input data and calibration and validation analysis for the stationary evaluation of the RGR. Section **4.3** described the analysis of climate scenarios implemented to deduce the RGR in future time horizons. Finally, Section **4.4** presented the tracer techniques and Darcian-based formulations used to deduce other essential variables for the groundwater dynamics that SWAT model does not provide.

4.1. LONG-TERM REPRESENTATIVENESS OF THE WATER BALANCE COMPONENTS

Stationarity (stable conditions over many years) is a prerequisite for defining the minimum, critical modelling period needed for a confident long-term prediction on the water balance components (Stahl et al., 2010). This initial verification is especially important in sparse-data areas having variable-length data series (Alcalá et al., 2018). The stationary evaluation of a given environmental variable consists of an average value and a range of its natural (inherent, background) uncertainty, which can be characterized by the coefficient of variation (*CV*) of its yearly time series. For the stationary evaluation of the variables involved in the long-term streamflow modelling, the critical period for confident averages and their *CV*s must be defined.

Based on the statistical study of available long data series, the method defined by Alcalá and Custodio (2015) was used to determine the desirable length of yearly time series to reach stationarity. This method uses the moving average (MA) series analysis (Brockwell and Davis, 1991) to screen the long-term behaviour of averages and their *CV*s. For a subset i of n consecutive time-equispaced data X_{i+j} of the nx elements series ($n \leq nx$) of a given variable X (for instance precipitation or temperature, the average is:

$$X_i^{MA} = \frac{1}{n} + \sum_{j=0}^{n-1} X_{i+j} \quad (1)$$

The X_i^{MA} values of each *n*-year MA series provide an average value and a standard deviation. For increasing *n*, this average tends to a given value while the *CV* generally decreases, even when the number of MA series decreases and finally there is only one, with $n=n_X$ for the average and $n=n_X-1$ for the *CV* (Brockwell and Davis, 1991; Tesfaye et al., 2006).

The average value of each *n*-year set of X_i^{MA} values is:

$$mX = \frac{1}{n} + \sum_{i=1}^{n} X_i^{MA} \quad (2)$$

whose coefficient of variation is *cvX*.

The average value of the CVs of each n-year set of X_i^{MA} values is:

$$mCV_x = \frac{1}{n} + \sum_{i=1}^{n} (CV_{Xi}^{MA}) \quad , n \leq n_X - 1 \quad (3)$$

whose coefficient of variation is $cvCV_X$.

The stationary values of *mX* and mCV_X can be deduced for longer time series when the decreasing trend of *cvX* and $cvCV_X$ reaches a critical lower asymptotic limit (Brockwell and Davis, 1991; Simpson et al., 2013). Increasing values of *n* are required in order to identify the full temporal variability of the variables, and therefore the critical *n*-value to attain stationarity, hereafter denoted *N*. Averages and *CV*s for a common *N*-year period are needed to make a confident stationary evaluation of the variables determining streamflow (Simpson et al., 2013; Alcalá and Custodio, 2015; Alcalá et al., 2018).

4.2. SWAT MODEL

4.2.1. Basic description

Once stationarity for representative long-term streamflow predictions was verified, the hydrological modelling of the PRB was performed using the semi-distributed SWAT rainfall–runoff model extension (Arnold et al., 1993, 1995, 1998) for the QGIS interface, called QSWAT (Dile et al., 2016) [QSAWT website: https://swat.tamu.edu/software/qswat/]. SWAT is a continuous-time, semi-distributed, and physically based hydrological model that operates on a daily or hourly time step and uses spatially derived data on topography, land use, soil, and weather for stream-routed hydrology and water quality modelling (Arnold and Fohrer, 2005; Izady et al., 2015). SWAT is designed to predict and quantify surface and subsurface water flows through rivers and landscapes in basins with different climatic conditions, soil properties, land uses, and topography (Arnold et al., 1998). The hydrological routines within SWAT account for unsaturated zone processes (e.g., soil infiltration, evaporation, plants uptake, and lateral flow), groundwater flows (e.g., shallow and deep aquifer recharge), and snow accumulation and melt (Zhang et al., 2007). SWAT includes different statistical tools for measuring the quality of model predictions (Neitsch et al., 2005).

SWAT includes the spatial heterogeneity by dividing the basin surface into multiple sub-basins attending to the river network and topography. The sub-basins are in turn subdivided into Hydrologic Response Units (HRUs) with homogeneous land use, management, and soil properties that produce homogeneous hydrologic responses not identified spatially within a SWAT simulation (Narsimlu et al., 2013).

SWAT simulates the hydrological output of each sub-basin but does not discriminate the specific output from each HRU (Gassman et al., 2007, 2014). Streamflow generated in each HRU adds to the streamflow at the sub-basin outlet which in turn contributes to the observed streamflow at a given reference gauging station. From groundwater purposes, SWAT evaluates shallow aquifer recharge as a soil water balance component in each HRU of the different sub-basins. However, deep aquifer recharge is a water balance closure component since SWAT model is lumped itself and does not admit distributed aquifer parameters such as hydraulic conductivity, specific yield or piezometry.

For the hydrological cycle simulation, SWAT establishes two major operative components. The first one is the land phase, which determines the water balance in each sub-basin as response of climate, soil moisture, and energy inputs (Abbaspour et al., 2015). For a daily step, the dynamics of the water balance components can be expressed as:

$$S_{WF} = S_{WI} + \sum_{j=1}^{t} (P - E_A - Q_U - W_{SS} - Q_{BT})_i \quad (4)$$

where t is the simulation period in days in which S_{WF} is final soil-water content and S_{WI} is initial soil-water content for plants uptake, and i is a given day (24-h) in which P is precipitation, E_A is actual evapotranspiration, Q_U is surface and interflow runoff, W_{SS} is percolation below the unsaturated zone, and Q_{BT} is baseflow, i.e., groundwater discharge from shallow (Q_{BS}) and deep (Q_{BD}) aquifers to streamflow (Q_T), all of them in mm H_2O per day.

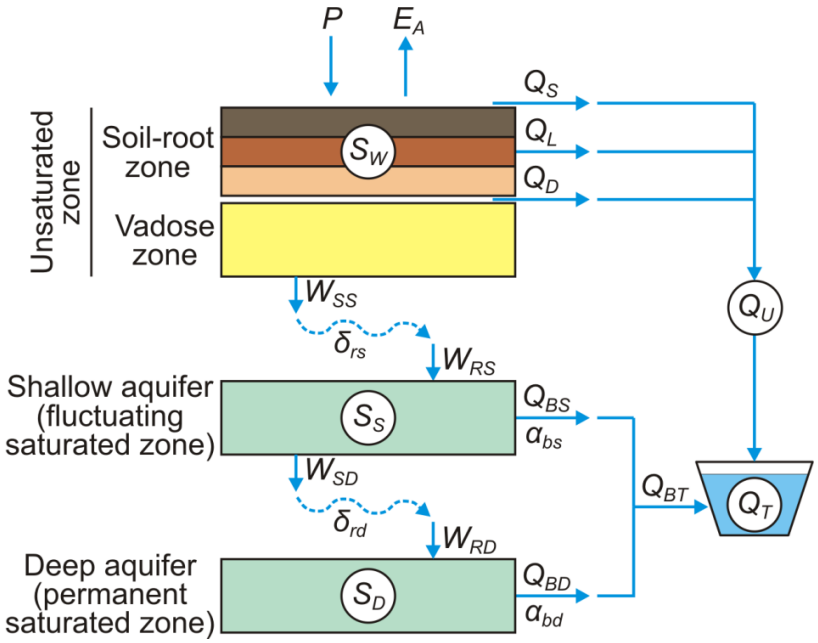

Figure caption on next page.

Figure 3. Schematic of surface and subsurface water balance components implemented in SWAT model, modified from Luo et al. (2012). Notation for variables used (all in mm H_2O per day) as (1) P is precipitation; (2) E_A is actual evapotranspiration; (3) Q denotes streamflow components, where subscript T is total streamflow, U is surface and interflow runoff, S is surface runoff, L is lateral flow (interflow) from unsaturated soil, D is drainage from tiles, BT is baseflow from shallow aquifer and deep aquifer discharges, BS is baseflow from shallow aquifer discharge, and BD is baseflow from deep aquifer discharge; (4) W denotes transferable amount of water between two ground layers (hydrological zones), where subscript SS is seepage percolation from unsaturated zone to shallow aquifer, SD is seepage percolation from shallow aquifer to deep aquifer, RS is shallow aquifer recharge, and RD is deep aquifer recharge; and (5) S denotes water storage in a ground layer (hydrological zone), where subscript W is unsaturated (soil-root and vadose) zone, S is shallow aquifer (fluctuating saturated zone), and D is deep aquifer (permanent saturated zone). Notation for parameters used as (1) δ denotes delay time or drainage time (days) between two ground layers (hydrological zones), where subscript rs is in-transit W_{SS} to W_{RS} and rd is in-transit W_{SD} to W_{RD}; and (2) α denotes baseflow recession parameter (days), where subscript bs is shallow aquifer and bd is deep aquifer.

The detailed simulation of the water balance components is described in SWAT manuals (Di Luzio et al., 2002; Neitsch et al., 2005; Winchell et al., 2010) and its description has been omitted. The Figure 3 shows the schematic of surface and subsurface water balance components implemented in SWAT model, and notation for variables and parameters used in this Thesis.

Once SWAT model has implemented the land phase, the following step is the routing phase in which the movement of the streamflow components Q_U and Q_{BT} through the channel system towards the reference gauging station is defined (Neitsch et al., 2005). This research has integrated the 24-h predictions to provide monthly values.

The baseflow component is a reliable proxy of the RGR in pristine basins with gaining streams (Lerner et al., 1990; Scanlon et al., 2002) when aquifer recharge and discharge can be equated because groundwater abstraction is nil, and direct evapotranspiration from shallow aquifers and underflow to deep aquifers is negligible. Originally developed for SWAT, the BFLOW program [BFLOW website: http://swatmodel.tamu.edu/software/baseflow-filter-program,2011] was used to separate the baseflow component from predicted streamflow by recursively passing a digital filter over an observed daily streamflow record (Nathan and McMahon, 1990; Arnold et al., 1995; Arnold and Allen, 1999; Szilagyi, 2003, 2004). The recursive digital filter of BFLOW uses the signal analysis and processing

developed by Lyne and Hollick (1979) to automatically separate low-frequency baseflow from high-frequency quick flow (Nathan and McMahon 1990). This procedure is, in fact, arbitrary and has no physical basis in groundwater flow theory (Arnold and Allen, 1999), despite that it provides easily automated, subjective, and repeatable baseflow estimations (Nathan and McMahon, 1990). The original filter given by Lyne and Hollick (1979) is expressed as:

$$Q_{U,i} = \gamma . Q_{U,i-1} + \frac{1+\gamma}{2} (Q_{T,i} - Q_{T,j-1}) \quad (5)$$

where variables Q_U and Q_T (Figure 3) are in mm H_2O per day, γ is the dimensionless filter parameter, and i is a 24-h streamflow record. Baseflow (Q_{BT}) is calculated as:

$$Q_{BT,i} = Q_{T,i} - Q_{U,i} \quad (6)$$

A γ value in the 0.90–0.95 range determines the baseflow attenuation; optimally γ being 0.925 (Nathan and McMahon, 1990; Arnold et al., 1998). This research integrates the 24-h Q_{BT} predictions to provide monthly values.

4.2.2. Calibration and validation of model predictions

Calibration was aimed at optimizing predictability of SWAT model through the comparison of observed and simulated streamflow data at the reference gauging station, searching for the best optimization of an objective function (Nash and Sutcliffe, 1970; Moriasi et al., 2007). Validation was aimed at testing the robustness of the model by using a period in which climatic conditions and subsequent streamflow records are different from those recorded during the calibration period. The validation used the values of the calibrated parameters.

During the setting up, different uncertainties may cause the malfunction of the model. According to Bastin et al., (2013), Refsgaard et al. (2007) and Schuol et al. (2008), uncertainties may be introduced at (1) the input data stage by missing, error data, and adopted spatial and temporal scales; and (2) the model operation

level due to parameterization and formalisms used. The model performance must be improved to confirm its reliability by studying the difference between observed and simulated streamflow (Rollo, 2012). The free Calibration and Uncertainty Procedure (SWAT-CUP) Software integrates various calibration/uncertainty analysis algorithms for SWAT model (Abbaspour, 2015), such as Sequential Uncertainty Fitting version 2 (SUFI-2) (Abbaspour et al., 2004; 2007), Generalized Likelihood Uncertainty Estimation (GLUE) (Beven and Binley, 1992), Particle Swarm Optimization (PSO) (Eberhart and Kennedy, 1995), Parameter Solution (PARASOL) (Van Grinsven and Meixner, 2006), and Markov Chain Monte Carlo (MCMC) (Kuczera and Parent, 1998).

The SUFI-2 algorithm was chosen in this Thesis for model calibration and validation because all sources of uncertainty introduced by the inputs and parameters can be mapped (Yang et al., 2008, 2011), and many parameters and data recorded in many weather and gauging stations can be simultaneously managed. Further documentation of the SUFI-2 algorithm can be found in Abbaspour et al. (2004). SUFI-2 assumes a large parameter uncertainty within the 95% prediction uncertainty (95PPU) that gradually decreases and offers different objective functions to assess the model performance in terms of water flows and absolute deviations (Bioteau et al., 2002; Moriasi et al., 2007). For model efficiency criteria, the following performance statistics were used: Nash–Sutcliffe efficiency (NSE), logarithm form of the NSE (ln NSE), coefficient of determination (R^2), percent bias (PBIAS), root-mean-square error relative to standard deviation ratio (RSR), and Kling–Gupta efficiency (KGE) (Table 1). Validation uses the values of the calibrated parameters for a monthly time-step simulation. The ranges for the model performance statistics in the validation period indicated in Table 1 refers to the values proposed by Gupta et al. (1999), Santhi et al. (2001), and Moriasi et al. (2007, 2012, 2015) for monthly time-step simulations. Section B.1 in Appendix B includes a detailed description of these model performance statistics (Di Luzio et al., 2002; Neitsch et al., 2005; Winchell et al., 2010).

Table 1. Equations, ranges and optimal values for SWAT model performance statistics, after Moriasi et al., (2007, 2012).

Statistic and Equation [a]	Description
NSE: Nash–Sutcliffe efficiency coefficient $= 1 - \frac{\sum_{i=1}^{n}(O_i - S_i)^2}{\sum_{i=1}^{n}(O_i - \bar{O})^2}$	NSE indicates a perfect match between observed and simulated data. NSE ranges from −∞ to 1. Values higher than 0.5 are considered satisfactory.
lnNSE: logarithmic form of NSE $= 1 - \frac{\sum_{i=1}^{n}(\ln O_i - \ln S_i)^2}{\sum_{i=1}^{n}\left(\ln O_i - \overline{\ln O}\right)^2}$	lnNSE emphasizes the low flows whereas NSE emphasizes the high flows.
R^2: coefficient of determination $= \left[\frac{\sum_{i=1}^{n}(O_i - \bar{O}) \cdot (S_i - \bar{S})}{\left[\sum_{i=1}^{n}(O_i - \bar{O})^2\right]^{0.5} \cdot \left[\sum_{i=1}^{n}(S_i - \bar{S})^2\right]^{0.5}}\right]^2$	R^2 indicates the degree of linear relationship between observed and simulated data. R^2 ranges from 0 to 1. Values higher than 0.5 are considered satisfactory.
PBIAS: percent bias $= \frac{\sum_{i=1}^{n}(O_i - S_i) \cdot 100}{\sum_{i=1}^{n}(O_i)}$	PBIAS calculates the average tendency of the simulated data to be higher or lower than their observed counterparts. Perfect match is 0. Acceptable values are in the ±25% range.
RSR: root-mean-square error relative to standard deviation of observed data $= \frac{\sqrt{\sum_{i=1}^{n}(O_i - S_i)^2}}{\sqrt{\sum_{i=1}^{n}(O_i - \bar{S})^2}}$	RSR ranges from 0 to ∞. The lower the RSR, the lower the RMSE and the better the model performance. Values lower than 0.7 are considered acceptable.
KGE: Kling–Gupta efficiency $= 1 - \sqrt{(r-1)^2 + \left(\frac{\sigma_S}{\sigma_O} - 1\right)^2 + \left(\frac{\bar{S}}{\bar{O}} - 1\right)^2}$	KGE establishes equal weighting of the correlation, bias, and relative variability of observed and simulated data. KGE ranges from −∞ to 1. Values higher than 0.5 are considered satisfactory.

[a] n is the number of observations, O_i is the ith observed data, $\bar{O}$ is the mean of the n observed data, S_i is the ith simulated data, $\bar{S}$ is the mean of the n simulated data, r is the coefficient of correlation of the O_i and S_i data pairs, and σ_S and σ_O are the standard deviation of the n O_i and S_i data, respectively.

4.2.3. Input data and model set-up

SWAT model requires the following inputs: digital elevation model, land use map, hydraulic and physical soil data, vegetation cover, and meteorological data such as daily precipitation, maximum and minimum air temperature, solar radiation, relative humidity, and wind speed.

4.3. FUTURE CLIMATE SCENARIOS

The calibrated and validated SWAT model for current hydrological conditions can be used to predict streamflow and the subsequent baseflow component for future climate scenarios. Data for the different climate change scenarios were collected from the Climate Change Toolkit (CCT) outlined by Vaghefi et al. (2017). Available at the Water Weather Energy Ecosystems website [http://www.2w2e.com], the CCT enables data extraction and set-up for climate change studies and hydrological applications. Precipitation and temperature data were extracted from the five Global Climate Models (GCMs) available in the CCT (GFDL-ESM2M, HadGEM2-ES, IPSL-CM5A-LR, MIROC, and NoerESM1-M) for the historical baseline (1975–2005) and the future (2006–2099). In this Thesis, the Representative Concentration Pathways (RCPs) 4.5 and 8.5 emission scenarios were used to assess the potential changes in hydrological response in the PRB in the mid- (2040–2069) and long-term (2070–2099) future time horizons.

Climate change scenarios were modelled in four steps. First, historical baseline and future GCM climate data was extracted from GFDL-ESM2M, HadGEM2-ES, IPSL-CM5A-LR, MIROC, and NoerESM1-M models. Next, the GCM products were regionalized to a specific area to obtain a meaningful interpretation of the impacts of climate change on a local scale. In addition, climatic data was corrected to eliminate potential biases (Chen et al., 2013). Statistical downscaling was used to bias-correct the future GCM data against the observed data. Different hydro-climatological studies (Vaghefi et al., 2019) have considered this statistical bias correction method satisfactory for downscaling the precipitation and temperature variables from the GCMs. The CCT software was used for data downloading, spatial downscaling and correcting the GCMs for bias.

The third step was to select GCMs according to their ability to reproduce historical baseline climatology in the study area. A comparative analysis of GCM products, previously downscaled and bias corrected, was performed. This task was completed using the methodology developed for aquifer recharge projections under future climate change scenarios introduced by Pulido-Velazquez et al. (2015a). This method compares the monthly means and standard deviations for an average year of historical and GCM (hereafter Regional Climate Model, RCM) precipitation and temperature series over the same period. For this purpose, the index *Id* was used to measure the goodness-of-fit obtained for each RCM by adding the changes (increases) in the means and standard deviations of the control series over the historical period 1980–2004 for both climatic variables, as:

$$Id_i = \sum_{n,m=1}^{2} Id_i(V_n S_m)$$
$$Id_i(V_n S_m) = \sum_{j=1}^{12} \left[(V_n S_m)_i^j - (V_n S_m)_H^j\right] \Big/ (V_n S_m)_H^j, \quad (7)$$

where the subscript i denotes a specific RCM, the subscript H denotes historical, the superscript j represents the months of a mean year, V_1 is mean precipitation, V_2 is mean temperature, and S_1 and S_2 are the monthly mean value and monthly standard deviation for a specific RCMi, respectively.

Once the four *Id* indexes for each RCM were obtained, each corresponding to the mean value and standard deviation of the precipitation and temperature series, the superior models in terms of goodness-of-fit to the observed time series were selected. Finally, the simulation results from the selected RCMs, such as daily precipitation and maximum and minimum air temperature data for both scenarios, were used as SWAT model inputs to generate the streamflow responses and subsequent baseflow predictions in the mid- and long-term future time horizons.

4.4. GROUNDWATER DYNAMICS

4.4.1. Basic rationale

The correct use of any numerical simulation model as decision-support tool requires an additional effort to conceptualize the hydrological functioning of the modelled system to improve evaluations and predictions. In scarcely monitored areas, the groundwater dynamics deduced from SWAT model (and other rainfall–runoff numerical models) can be unsatisfactory in what concerns to the essential features of the groundwater resource. So, additional techniques to those included in SWAT were used to assess (i) the baseflow faction of streamflow over a control period, (ii) the resource renewability via different average groundwater age from different hydraulically-connected aquifers (different spatiotemporal dynamics) contributing to streamflow, and (iii) other essential groundwater parameters for sustainable management based on a better knowledge of the aquifer functioning (Freeze and Cherry, 1979; Edmunds, 2012). Next two sections describe the saturated zone routed techniques used to achieve these targets.

4.4.2. Tracer techniques

Some chemical and isotope tracers can be used to quantify the atmospheric bulk deposition (precipitation, dust, aerosols, …) control on the chemical and isotopic background (baseline) of groundwater, as well as to identify how certain endogenous sources may contribute to groundwater modifying its initial atmospheric baseline. Other tracer applications based on the chemistry of dissolved inorganic carbon (DIC) are of special interest to interpret groundwater radiocarbon data.

In this Thesis, hydrochemistry and isotope data generated in the framework of two international R&D projects (Larrea et al., 2016; Alcalá, 2016) were used. This information included major and some minor dissolved components in mg/L (Cl^-, SO_4^{-2}, DIC —HCO_3^- being the main DIC species—, Br^-, Li^+, Na^+, K^+, Ca^{+2}, and Mg^{+2}), stable isotopes in ‰ ($\delta^{18}O$ and $\delta^{2}H$ referred to the V-SMOW standard, and $\delta^{13}C_{DIC}$ referred to the V-PDB standard), and radioisotopes tritium (^3H) as tritium units (TU) and radiocarbon ($^{14}C_{DIC}$) activity ($A^{14}C$) as percent modern carbon (pmc). For

simplicity, the ion charge of chemical species is not indicated, except when needed. When the ion symbol is preceded by 'r', it means that the value is expressed in meq/L.

The interpretative basis included (i) hydrochemical discretization of water types; (ii) molar ratios rCl/rBr, rCl/rSO_4, rNa/rK, rNa/rLi, rMg/rCa and rCl/rHCO_3 to identify sources of salinity modifying the original atmospheric baseline of groundwater (Davis et al., 2004; Alcalá and Custodio, 2008a; Custodio and Jódar, 2016; Horner et al., 2017; Urrutia et al., 2022); (iii) water-stable isotopes $\delta^{18}O$ and $\delta^{2}H$ to identify conditions for aquifer recharge (Cartwright et al., 2006; Vengosh et al., 2007; Urrutia et al., 2022); (iv) ^{3}H to date modern groundwater and surface-water (Cook et al., 2005; Herrera and Custodio, 2014); and (v) $\delta^{13}C_{DIC}$ to elucidate the atmospheric and sub-surface sources of DIC as a prerequisite to use $A^{14}C$ to date old groundwater (Vengosh et al., 2007; Burg et al., 2013; Huang et al., 2017; Han and Wassensaar, 2021).

Chemical and isotope tracers behaving a quite conservative behaviour during the hydrogeological processes are useful to implement a binary mixing model of the two end members that contribute to streamflow (Q_T), both baseflow (Q_{BT}) and surface and interflow runoff (Q_U). The selected conservative tracers were rCl/rBr molar ratio, water-stable isotope $\delta^{18}O$ and radioisotope ^{3}H. The water and tracer mass balances were expressed as:

$$Q_T = Q_{BT} + Q_U \tag{8a}$$

$$Q_T R_{QT} = Q_{BT} R_{QBT} + Q_U R_{QU} \tag{8b}$$

or alternatively in relative terms as:

$$1 = x + y \tag{9a}$$

$$R_{QT} = x Q_{QBT} + (1 - x) R_{QU} \tag{9b}$$

The Q_{BT} fraction x contributed to Q_T is:

$$x = \frac{R_{QT} - R_{QU}}{R_{QBT} - R_{QU}} \tag{10}$$

where Q_T, Q_{BT} and Q_U are in mm H_2O [L^2 T^{-1}] over a control period, and R is the tracer content of the balance component identified by the subscript.

Radioisotopes ^3H and ^{14}C were used to calculate average groundwater age. Because hydrodynamic dispersion is small in many aquifers, groundwater ages using radioisotopes closely approximate hydraulic ages (sub-surface residence times) of the water (Ekwurzel et al., 1994; Cook et al., 2005). The assumption of constant atmospheric contents of a given radioisotope allows average groundwater age (G_A) to be calculated from the measured concentration (activity) of the radioisotope (C_m) in water using the decay equation (Clark and Fritz, 1997; Cartwright et al., 2020; Han and Wassenaar, 2021):

$$G_A = -\frac{t_{1/2}}{\ln(2)} ln\left(\frac{C_m}{C_i \cdot f}\right) \tag{11}$$

where G_A is in T (typically in year), C_i is the initial concentration (activity in pmc) of the radioisotope in the recharging water, in which the atmospheric concentration of the radioisotope is diminished by the disintegration during the transit time through the unsaturated and saturated zones, assumed constant, and f is a dimensionless correction factor to account for other non-atmospheric sources of the radioisotope affecting C_i; for ^3H, the half-life ($t_{1/2}$) is 12.32±0.02 year, and for ^{14}C, $t_{1/2}$ is 5700±30 year.

For reported ^3H data, no correction was considered, thus f =1. For reported ^{14}C data, $f = f' \cdot f''$ and additional correction was needed. The calculation of the dimensionless correction factors f' and f'' was based on measurable or deducible ^{13}C and ^{14}C data. Factor f' reverts the reported normalized ^{14}C values to non-normalized ones (Clark and Fritz, 1997; Han and Wassenaar, 2021). Factor f'' implies a ^{13}C and ^{14}C binary mixing of two inorganic carbon reservoirs contributing $^{13}C_{DIC}$ and $^{14}C_{DIC}$ to groundwater, for instance biogenic soil CO_2 (S) and dead carbon volcanic CO_2 (M) (Atkinson et al., 2014; Han and Wassenaar, 2021).

$$f' = \left(\frac{1 + \frac{\delta^{13}C_m}{1000}}{0.975}\right)^2 \tag{12}$$

$$f'' = 1 - \frac{^{14}C_S - {}^{14}C_M}{^{14}C_M} \cdot \frac{\delta^{13}C_S - \delta^{13}C_m}{\delta^{13}C_S - \delta^{13}C_M} \quad (13)$$

where $^{14}C_S$ and $^{14}C_M$ are the $A^{14}C_{DIC}$ of the end members S and M in pmc, $\delta^{13}C_S$ and $\delta^{13}C_M$ are the $^{13}C_{DIC}$ content of the end members S and M in ‰, and $\delta^{13}C_m$ is the measured $^{13}C_{DIC}$ content in the water sample in ‰.

No further correction referred to pass atmospheric 3H and 14C contents was applied. Thus, the calculated ages are conventional instead of corrected or actual ones (Han and Wassenaar, 2021).

4.4.3. Sampling and analytical methods

Representative water points concerning to the Pita River course and groundwater discharge from shallow and deep aquifers were sampled over a control period. Water samples were initially preserved in a cold box and later transferred to a refrigerator in the laboratory. Field work included measurements of temperature, pH, and conductivity. Water samples were filtered immediately upon reaching the laboratory. They were delivered to national and international laboratories upon refrigerating conditions. Numerical treatment of atmospheric bulk deposition and spring discharge data following procedures described by Alcalá and Custodio (2008b) and Alcalá et al. (2011), respectively.

The following analytical remarks refer to the samples reported by Larrea et al. (2016) and Alcalá (2016). The physicochemical analyses carried out in the EPMAPS Laboratory in Quito (Larrea et al., 2016) were (i) temperature (T), pH, and electric conductivity (EC) by means of electrometric techniques, with precision of ±0.1°C, ±0.1, and ±1µS/cm for T, pH, and EC, respectively; (ii) Na, K and Li by atomic emission spectrometry (AES), using a Varian Vista MPX® inductively coupled plasma (ICP) spectrophotometer with argon emission detection; and (iii) SO_4, Cl, HCO_3, Ca, and Mg by flame atomic absorption spectrophotometry, using a Varian SF 330® spectrophotofluorometer with continuous flow auto-analysers. The detection limits in mg/L were 1 for Na, K, Ca and Mg, 3 for SO_4 and HCO_3, and 0.2 for Li. In the Geological Survey of Spain (IGME–CSIC) Laboratory in Madrid, SO_4, Cl and Br were additionally analysed, using a DIONEX 600® high-performance liquid (anionic) chromatograph (Alcalá, 2016). The detection limits in µg/L were

180 for SO_4, 100 for Cl, and 1 for Br. The analytical determinations followed the US EPA 300.1 method (Hautman and Munch, 1997) on filtered unacidified samples. The average precision of the analysis carried out in the EPMAPS and IGME–CSIC Laboratories was better than ±5% (±1σ).

Stable isotopes ($\delta^{18}O$, $\delta^{2}H$, and $\delta^{13}C_{DIC}$) and radioisotopes (^{3}H and $^{14}C_{DIC}$) were determined in the IAEA Isotope Laboratory in Vienna. Water-stable isotopes ($\delta^{18}O$ and $\delta^{2}H$) were measured using a gas-source Isotope Ratio Mass Spectrometer Finnigan Delta S. Hydrogen samples were reacted at 750 °C with Cr metal using a Finnigan H/Device coupled to a mass spectrometer. For oxygen, the samples were equilibrated with CO_2 gas at approximately 15 °C in an automated equilibration device coupled to a mass spectrometer. The measurement standard deviations were ± 0.1‰ for $\delta^{18}O$ and ± 1‰ for $\delta^{2}H$ (±1σ). Isotopic ratios for $\delta^{2}H$ and $\delta^{18}O$ were reported for the V-SMOW standard.

Liquid Scintillation Counting was used to determine tritium (^{3}H). The results of ^{3}H were reported in tritium units (TU) and the analytical error was ±0.09 TU.

As reported in Larrea et al. (2016) and Alcalá (2016), dissolved inorganic carbon (DIC) was measured in the laboratory because the influence regarding its measurement in the field is often small when HCO_3^- is the main DIC species, as corroborated previously. CO_2 was extracted from the water sample by addition of phosphoric acid in a vacuum pumped system. An aliquot of this CO_2 was combusted at around 800 °C under a 100% oxygen atmosphere, first dried with methanol/dry ice, and measured on a gas-source isotope ratio mass spectrometer. $\delta^{13}C$ was measured on a gas-source Isotope Ratio Mass Spectrometer (IRMS) and referred to the V-PDB standard, and its measurement error was better than ±0.06‰ (±1σ). The rest of the obtained CO_2 in the water sample was subjected to graphitization to measure ^{12}C, ^{13}C and ^{14}C by using an Accelerator Mass Spectrometer (AMS) on graphite produced by hydrogen reduction of the CO_2 sample over a cobalt catalyst. The results of ^{14}C (radiocarbon) activity ($A^{14}C$) were reported in pmc (percent modern carbon), and they are relative to the normalized (standardized) ^{14}C amount in the calibration standard as a combination of $\delta^{13}C$ AMS and $\delta^{13}C$ IRMS values. The reported error of the normalized $A^{14}C$ data was in the range of 0.04–0.36 pmc.

4.4.4. Darcian-based formulations

Some Darcian-based formulations were used to assess groundwater residence (renewal) time and total groundwater discharge; these variables are not evaluated by SWAT model. These variables can not only assess the renewability of the resource, but also provide sound evidence to show that the groundwater resource is generated by modern or old recharge (Kazemi et al., 2006; Suckow, A., 2014; Cartwright et al., 2020; Li et al., 2022).

Groundwater residence (renewal) time (G_T) is the time it takes for particles of water to travel from the recharge area to the discharge area of the aquifer (Modica et al., 1998; Kazemi et al., 2006; Li et al., 2022). Average one- and three-dimensional G_T were roughly calculated from aquifer hydraulics data by assuming a predominant piston (plug) flow condition (Custodio and Llamas, 1983; Alcalá et al., 2011; 2015; 2018) as:

$$G_T \approx \frac{H}{R} \tag{14a}$$

$$G_T \approx \frac{V}{F} \approx \frac{H \cdot A_A}{R \cdot A_B} \tag{14b}$$

where G_T is in T (typically in year), R is the one-dimensional steady aquifer recharge in $L \cdot T^{-1}$, F is the three-dimensional steady water flow input in $L^3 \cdot T^{-1}$, H is the aquifer saturated thickness in L, V is the aquifer saturated volume in L^3, A_A is the two-dimensional aquifer extension (the product of width and length) in L^2, and A_B is the two-dimensional basin surface receiving recharge and contributing to aquifer storage in L^2.

G_T is distinguished from groundwater age (G_A), which is the elapsed time since a given water molecule was recharged until it reaches a specific location in the system where is evaluated (Kazemi et al., 2006; Suckow, 2014). Thus, G_A and G_T are equivalent at the aquifer discharge point or at the basin outlet when the basin surface roughly coincides with the boundary of an aquifer whose main contribution to streamflow occurs at the basin outlet or close to it (Alcalá et al., 2015; 2018). In this circumstance, Equations 14a and 14b were combined to express average G_T (Herrera and Custodio, 2014) as:

$$G_T \approx \frac{H}{R} \approx \frac{1}{\lambda}\left(\frac{C_{i\cdot f}}{C_m} - 1\right) \quad (15a)$$

$$G_T \approx \frac{V}{F} \approx \frac{1}{\lambda}\left(\frac{C_i \cdot f}{C_m} - 1\right) \quad (15b)$$

where $\lambda = \ln(2)/t_{1/2}$, being $5.62 \cdot 10^{-2}$ year for ^{3}H and $1.21 \cdot 10^{-4}$ year for ^{14}C.

The Coutagne (1948) formulation was used for subsurface groundwater discharge transmitting through the aquifer to the basin outlet (Q_A). No thresholds for Q_A due to aquifer geometry and hydraulic-head limitations were imposed. One- and three-dimensional S_T were expressed as:

$$Q_A = \frac{(H \cdot S)^b}{G_T} \quad (16a)$$

$$Q_A = \frac{(H \cdot A_A \cdot S)^b}{G_T} \quad (16b)$$

where Q_A is in $L \cdot T^{-1}$ (1D; Equation 16a) or $L^3 \cdot T^{-1}$ (3D; Equation 16b), b is a dimensionless flow-path form parameter determined by the aquifer geometry used to capture the effect of the aquifer geometry on groundwater discharge flow paths (Chapman, 1999), and S is the dimensionless aquifer specific yield or drainable porosity for unconfined aquifers. In Equation 16a, G_T was derived from Equations 14a or 15a. In Equation 16b, G_T was derived from Equations 14b or 15b.

Total groundwater discharge (D_T) includes Q_A and the baseflow fraction contributed to streamflow (B_{BT}); the latter is evaluated by SWAT model. D_T was expressed as:

$$D_T = Q_A + Q_{BT} \quad (17)$$

where D_T, Q_A and Q_{BT} are in $L \cdot T^{-1}$ (1D, typically in mm H_2O per year) or $L^3 \cdot T^{-1}$ (3D, typically in m^3 H_2O per year). Average yearly values of D_T, Q_A and Q_{BT} were evaluated over the entire modelling period instead of from yearly time series.

Average G_T and/or G_A are a part of the necessary data for optimal groundwater evaluation prior further exploitation. Groundwater exploitation

implies exhaustion. The rate of groundwater reserve exhaustion is assumed exponential and was estimated as:

$$E = \frac{4T}{L^2 \cdot S} \tag{18}$$

where T is the aquifer transmissibility in $L^2 \cdot T^{-1}$ (typically in $m^2\ day^{-1}$), which is the product of aquifer hydraulic conductivity (K) in $L \cdot T^{-1}$ (typically in $m\ day^{-1}$) and H in L (m), and L is the aquifer dimension (width) in L (in m).

The time to exhaust half the groundwater reserve was expressed as:

$$E_T = \frac{\ln (2)}{E} \tag{19}$$

where E_T is in T (typically in year).

V – RESULTS AND DISCUSSION

V - RESULTS AND DISCUSSION

Chapter V was divided into four sections. Section **5.1** provided the critical stationarity period for a confidence modelling. Section **5.2** presented the SWAT model results concerning the modelling of current, stationary streamflow, including used input data and calibration and validation analysis. Section **5.3** presented the SWAT model results concerning the modelling of future streamflow scenarios, including data sources and climate scenarios implemented. Finally, Section **5.4** described the results provided by the tracer techniques and Darcian-based formulations in relation to the essential variables for deducing groundwater dynamics in the PRB.

5.1. STATIONARITY OF THE MODELLING PERIOD

5.1.1. Stationarity analysis

Determining the stationary condition of a water balance based on short, biased or incomplete time series of key variables is a crucial step not sufficiently documented in the scientific literature (Alcalá and Custodio, 2015; Alcalá et al., 2018). An illusory low uncertainty of the evaluation may hide an insufficient temporal representativeness of the balance period. As will be described in Section 5.2, available model input data in the PRB area could be short for a reliable long-term evaluation, so it's necessary to ensure the stationarity condition of the modelling period prior using SWAT model as decision-support tool.

Considering that dynamics of precipitation (P) and temperature (T) is inferred by global climatic forces, and they ultimately determine streamflow (Q_T), the 54-year P and T time series (period 1964–2017) from Izobamba weather station (Figure 1b) were used to define the critical balance period for variables to reach a comparable stationary condition needed for long-term representativeness; basic statistics of P and T time series from Izobamba weather station are in next section (Table 2). In the PRB area, the critical N-year period was defined by studying the n-year MA mX and mCV_X series built for yearly P and T time series (Figure 4). The

wide range for 1-year MA *mX* series quickly narrowed with increasing *n*. However, the averaging interval (the subset length) does not significantly influence the *mX* values (Figure 4a). The wide range for 2-year MA mCV_X series also narrowed with increasing *n* (Figure 4b), albeit the mCV_X values slightly increased with *n* (periodicity effect) from 0.01–0.39 and 0–0.06 for *n*=2 MA series of *P* and *T* variables, respectively, up to 0.17 and 0.03 for *n*≥40 MA series of *P* and *T* variables, respectively. These results explain why a short modelling period must has produced a poor evaluation of Q_T, since their natural uncertainties may vary from illusory accuracy (low *CV*s) to excessive uncertainty (high *CV*s), and more so the shorter the series is.

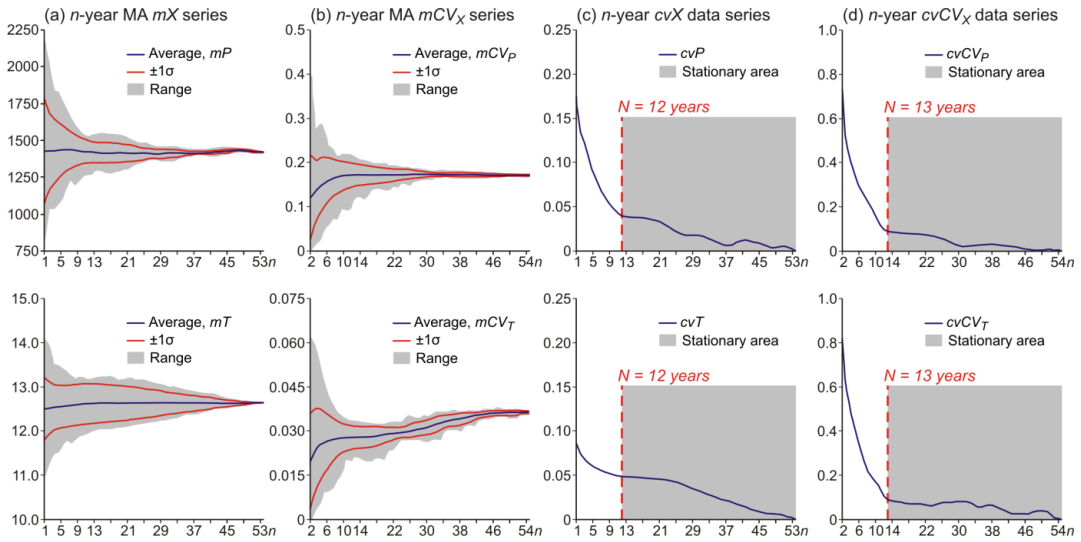

Figure 4. Results from the n-year moving average (MA) analysis of yearly precipitation (P) and temperature (T) time series from the 54-year long Izobamba weather station (see basic statistics in Table 2 in next section), with n≤nX for series of averages and n≤nX-1 for series of coefficients of variation (CVs); nX = elements series. (a) Average value of the MA series of averages, mX: mP and mT, mm year-1. (b) Dimensionless average value of the MA series of CVs, mCVX: mCVP and mCVT. (c) Dimensionless error (coefficient of variation) of the MA mX series, cvX: cvP and cvT. (d) Dimensionless error (coefficient of variation) of the MA mCVX series, cvCVX: cvCVP and cvCVT. N = N-year period for stationarity.

As *n* increased, the number of MA series decreased, and the estimation of dimensionless errors (*cv*) became impaired. However, even under this circumstance, *cvX* reached a lower asymptotic limit below 0.05 and 0.03 after 12-year MA series for *P* and *T* variables, respectively (Figure 4c), whereas $cvCV_X$

reached that asymptotic limit below 0.05 after 28-year and 22-year MA series for *P* and *T* variables, respectively (Figure 4d). Thus, *N*=12-year seems a critical modelling period for the stationary evaluation of Q_T in the PRB area, to be biased by assumable values of < 0.05 and < 0.1 after 12 years for averages and *CV*s, respectively. SWAT model was operated over the period 2003–2015 (Figure 5), which lightly surpasses the *N*=12-year critical modelling period for the stationary evaluation of Q_T in the PRB area. Long-term significance for these thirteen years was evaluated from the cyclicity analysis of the global El Niño–Southern Oscillation (ENSO) index [ENSO website: https://origin.cpc.ncep.noaa.gov/products/precip/CWlink/MJO/enso.shtml] (Figure 5a). The ENSO index controls long-term *P* (Figure 5b) and *T* (Figure 5c) regimes in the pacific versant of the Andean Highland in northern Ecuador (Kumar al., 2000; Bendix, 2000; Bendix et al., 2004; IPCC, 2007; Makowski Giannoni et al., 2016).

The oscillating trend of yearly *P* and *T* time series from Izobamba weather station (Figure 5) corroborates the existence of irregular 4–14-year long cycles with imperfect 2–7-year positive and negative phases that follow the ENSO cyclicity. The modelling period 2003–2015 covers one of these cycles with average *P* of 1,452±277 mm year^{-1} and *T* of 12.2±0.4 ºC that almost match those average values deduced from the 54-year long *P* and *T* records. So, the 13-year modelling period is considered representative enough for a stationary evaluation of Q_T using SWAT model.

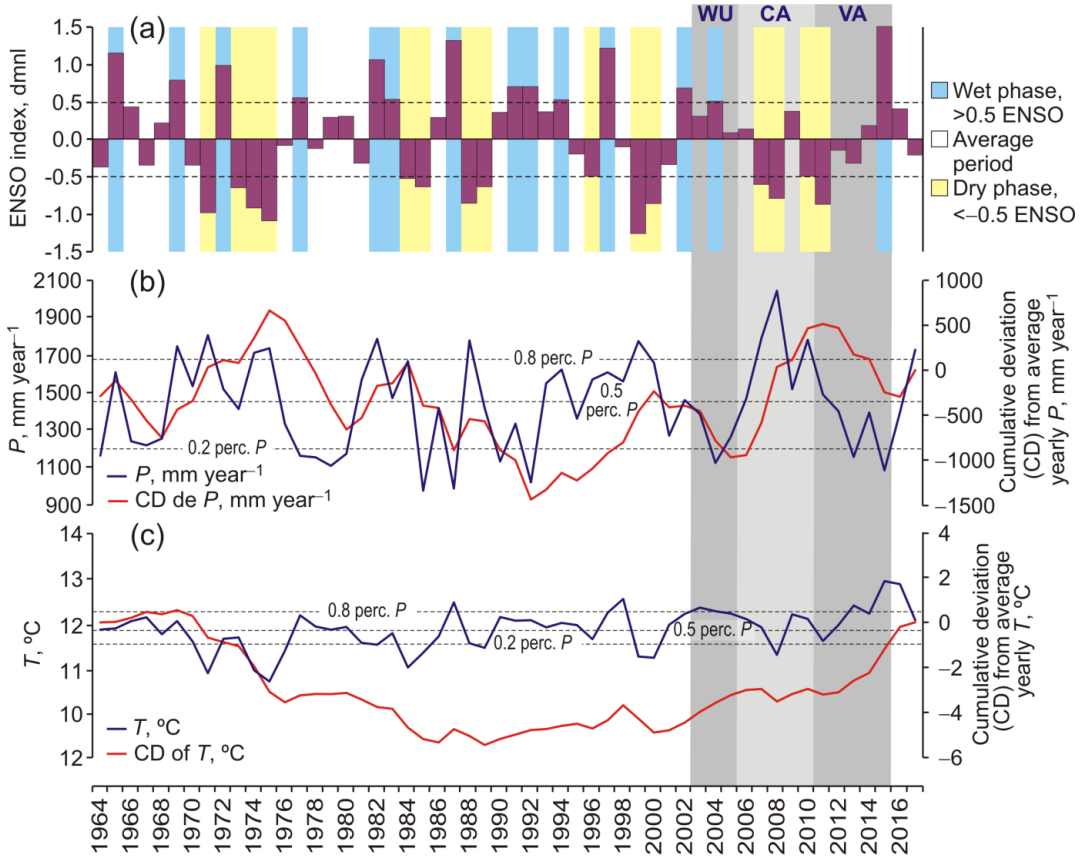

Figure 5. For years 1964–2017 in the PRB area, (a) Normalized El Niño–Southern Oscillation (ENSO) index [ENSO website: https://origin.cpc.ncep.noaa.gov/products/analysis_monitoring/ensostuff/ONI_v5.php]; (b) yearly precipitation (P) time series from Izobamba weather station and cumulative deviation (CD) from its average yearly P, mm year^{-1}; (c) yearly temperature (T) time series from Izobamba weather station and CD from its average yearly T, ºC. For (a) and (b), 0.2 percentile, average (0.5 percentile), and 0.8 percentile of yearly data series are indicated. Vertical grey shading indicates the entire modelling period 2003–2015, including the 2003–2005 warm-up (WU), 2006–2010 calibration (CA), and 2011–2015 validation (VA) periods implemented in SWAT model.

5.2. MODELLING OF STATIONARY STREAMFLOW

5.2.1. SWAT model setup

After verifying that the modelling period 2003–2015 enables a stationary evaluation of Q_T, SWAT model was first required to adapt the standardized databases for the USA to the local weather, land and soil conditions of the PRB. For this data treatment, SWAT includes the Weather Generator (WGEN) program (Sharpley and Williams, 1990; Neitsch et al. (2011). The model setup used five groups of input data, as follows:

1. The 30-m-resolution Digital Elevation Model (DEM) of Ecuador (Datum PSA56) from SavGIS website [http://www.savgis.org/ecuador.htm] was used to define the basin and sub-basins boundaries (Figure 1b). No further data treatment was required.
2. Daily records of precipitation and maximum and minimum air temperature from weather stations located in and around the PRB (Figure 1b) were used for spatial discretization of precipitation and temperature by using the daily weather generator algorithm dGen (Schuol and Abbaspour, 2007). These data were compiled from the public repositories of EPMAPS (EPMAPS, 2017), Institute for Meteorology and Hydrology of Ecuador (INAMHI) (INAMHI, 2017), and Fund for the Protection of Water of Ecuador (FONAG) over the period 1964–2017 (Figure 1b; Table 2). After a first analysis of data goodness, only some precipitation and temperature data series in the PRB (see location in Figure 1b) were selected to build the SWAT model; these selected stations are indicated in Table 3.
3. Soil data typologies deduced from the Quito Soil Map (scale 1:200,000) after Mejía et al. (1978) and MAG-ORSTOM (1978) (Figure 1d) and experimental soil data from the PRB compiled from Peñafiel (2009) and Lahuette and Recalde (2015) (Table 4) were updated attending to the Harmonized World Soil Database v.1.2 (HWSD) classification (FAO/UNESCO, 1988; FAO, 2015). A first comparison of andosol parameters from HWSD and Lahuette and Recalde (2015) revealed relative error in the range of ±0.05 (Table 5). Given this low relative error, HWSD was used to characterize the soil types in the

study area from information on soil texture, hydraulic conductivity and water content, among others for two layers depths (0–0.3 m and 0.3–1 m) (Nachtergaele et al., 2008). There are four soil types in the study area: andosol, gleysol, phaeozem y regosol (Table 5).

4. Digital land-use map (scale 1:25,000) from FONAG (2018) [FONAG website: http://infoagua-guayllabamba.ec/repositorio/web/documento/index] and additional information from CLIRSEN-EMAAP-Q (2006) were used to define the land-use Units of the PRB (Figure 1e), where 70% of the main land use in the PRB is páramo grassland, followed by 15% barren land (Figure 1e).
5. Daily streamflow records from gauging station Q5 at the PRB outlet and monthly streamflow records from gauging stations Q1 through Q4 at the outlet of some sub-basins were compiled from the EPMAPS repository (EPMAPS, 2017). These data were used to compare with simulated streamflow (Figure 1b; Table 2).

SWAT offers three options to calculate potential evapotranspiration (E_P) through the Priestley–Taylor, Hargreaves, and Penman–Monteith models. Because only daily records of precipitation and maximum and minimum temperature are available in the PRB area, the non-global Hargreaves model was used to estimate potential evapotranspiration (E_P) (Hargreaves, 1994; Nachtergaele et al., 2008). In temperate, humid regions, Oudin et al., (2005) proved that parsimonious precipitation- and temperature-based models estimate similarly well E_P to other more data-requiring global models. Actual evapotranspiration (E_A) was calculated as the sum of actual plant-canopy interception, plant transpiration, and soil evaporation by using an approach similar to that reported by Ritchie (1972). See details in SWAT manuals (Di Luzio et al., 2002; Neitsch et al., 2005; Winchell et al., 2010).

In spite that SWAT model does not uses hydrogeological information to calculate the baseflow component, lithology (scale 1:50,000) (Malo et al., 1980; Clapperton, 1993; Hall and Mothes, 2008) (Figure 1c), hydraulic conductivity (permeability) and specific yield of the geological formations (PETROECUADOR, 2005; EPMAPS, 2006a, 2006b, 2012), as well as piezometry and hydraulic gradients deduced from direct observation and geothermal

modelling (Hemmings et al., 2016) were compiled (Table 6). These data constituted the inputs of the tracer and Darcian-based techniques selected to deduce basic groundwater parameters, which complements the SWAT model evaluation, as will be described in Section 5.2.

Table 2. Description of weather (W) and streamflow gauging (Q) stations used in this research.

ID	Name	Network	Variable	Coordinates		Elevation	Sampling period		Years	% Gap	P [a]	σ_P [a]	T [b]	σ_T [b]	Q_T [c]	σ_{QT} [c]
				Latitude	Longitude	(m a.s.l.)	From	To								
W1	La Mica	EPMAPS	*P*	0° 31' 26" S	78° 13' 34" W	3922	01-01-1988	31-12-2017	30	8	762	224				
W2	Maucatambo	EPMAPS	*P*	0° 40' 30" S	78° 20' 60" W	3840	01-01-2003	31-12-2017	15	13	1049	365				
W3	Yangahuagra	EPMAPS	*P*	0° 38' 53" S	78° 20' 24" W	3972	01-01-2004	31-12-2017	14	8	1053	155				
W4	Bocatoma	EPMAPS	*P*	0° 29' 49" S	78° 26' 17" W	3387	01-01-2003	31-12-2017	15	15	1217	436				
W5	Izobamba	INAMHI	*P*,*T*	0° 21' 57" S	78° 33' 18" W	3058	01-01-1964	31-12-2017	54	0	1442	246	11.9	0.4		
W6	Mudadero	FONAG	*P*,*T*	0° 37' 01" S	78° 24' 07" W	3866	07-02-2012	31-12-2017	6	3	721	224	6.3	0.3		
W7	Cotopaxi	FONAG	*P*,*T*	0° 33' 50" S	78° 26' 35" W	3670	01-01-2008	31-12-2017	10	6	941	212	7.2	1.2		
W8	El Carmen	FONAG	*T*	0° 30' 07" S	78° 19' 59" W	4100	29-11-2009	31-12-2017	8	1			4.8	0.5		
W9	Gordillo	FONAG	*T*	0° 25' 05" S	78° 21' 25" W	3248	08-02-2010	31-12-2017	8	1			11.5	0.6		
Q1	Pita	EPMAPS	Q_T	0° 37' 28" S	78° 22' 56" W	3895	01-01-2003	31-12-2015	13	98					0.7	0.3
Q2	Mudadero 2	EPMAPS	Q_T	0° 37' 19" S	78° 22' 60" W	3877	01-01-2003	31-12-2015	13	98					0.6	0.4
Q3	Salitre	EPMAPS	Q_T	0° 35' 32" S	78° 24' 24" W	3760	01-01-2003	31-12-2015	13	98					2.2	0.8
Q4	Proaño	EPMAPS	Q_T	0° 33' 60" S	78° 25' 44" W	3641	01-01-2003	31-12-2015	13	98					2.5	1.1
Q5	Bocatoma	EPMAPS	Q_T	0° 29' 48" S	78° 26' 08" W	3361	01-01-2005	31-12-2017	13	16					2.6	1.4

ID and location as in Figure 1b.

[a] P—average annual precipitation and its standard deviation (σP) in mm year^{-1}.

[b] T—average daily temperature and its standard deviation (σT) in ºC.

[c] Q_T—average daily streamflow and its standard deviation (σQ_T) in m^3 s^{-1}

Table 3. Description of the essential weather (E) and stream-gauging (A) stations in the PRB used to build the stationary SWAT model.

ID	Name	Latitude	Longitude	Elevation (m a.s.l.)	Variable	P [a]	T [a]	Q [a]
E1	Maucatambo	0°40'30" S	78°20'60" W	3,845	P	1,049		
E2	Yangahuagra	0°38'53" S	78°20'24" W	4,040	P	1,053		
E3	Mudadero	0°37'01" S	78°24'07" W	3,866	P, T	721	6.3	
E4	Cotopaxi	0°33'50" S	78°26'35" W	3,670	P, T	941	7.2	
E6	Bocatoma	0°29'49" S	78°26'17" W	3,360	P	1,217		
E7	El Carmen	0°30'07" S	78°19'59" W	4,100	T		4.8	
E9	Gordillo	0°25'05" S	78°21'25" W	3,248	T		11.5	
A1	Bocatoma	0°29'49" S	78°26'08" W	3,380	Q			2.6

ID as in Figure 1b.

[a] Average annual values of P—precipitation in mm, T—temperature in ºC, and Q—streamflow in m s–1 over the period 2003–2015.

Table 4. Hydraulic properties of different soil typologies surveyed at the PRB, after literature data.

ID	Name	Soil type	Coordinates		Elevation	Date	WRC [a]	AIR [b]	FC [c]	Reference
			Latitude	Longitude	(m a.s.l.)					
T1	Panzapamba	Andosol 1	0°30'55"S	78°25'24"W	3551	22-Mar-2007	0.39	29.6		Peñafiel (2009)
T2	Derrumbopungo	Andosol 2	0°34'06"S	78°24'18"W	3915	19-Mar-2007	0.51	42.5		Peñafiel (2009)
T3	Salitre	Andosol 2	0°35'41"S	78°23'48"W	3875	23-Mar-2007	0.52	40.1		Peñafiel (2009)
T4	Carcelén	Phaeozem	0°36'56"S	78°20'11"W	4048	21-Mar-2007	0.35	0.42		Peñafiel (2009)
T5	Norte Cotopaxi	Leptosol	0°33'56"S	78°26'06"W	3666	20-Mar-2007	0.69	119.2		Peñafiel (2009)
T6	Mudadero 2	Andosol 3	0°37'36"S	78°21'27"W	3939	09-Jun-2013	0.69		0.46	Lahuatte and Recalde (2015)
T7	Mudadero 3	Andosol 3	0°37'36"S	78°21'24"W	3941	09-Jun-2013	0.72		0.50	Lahuatte and Recalde (2015)
T8	Mudadero 5	Andosol 3	0°37'36"S	78°21'49"W	3915	09-Jun-2013	0.71		0.47	Lahuatte and Recalde (2015)

ID and location as in Figure 1d.

[a] WRC—Water retention capacity in $cm^3\ cm^{-3}$.

[b] AIR—Average infiltration rate in $mm\ d^{-1}$.

[c] FC—Field capacity as a dimensionless fraction.

Table 5. The Harmonized World Soil Database (FAO / UNESCO, 1988) soil data used in the SWAT model and andosol experimental data obtained from Lahuette and Recalde (2015) in the PRB.

	Andosol						Gleysol	Phaeozem	Regosol
Parameter	HWSD	Experimental data [a]					HWSD	HWSD	HWSD
HWSD code [b] / sample ID [c]	16206	s1	s2	s3	s4	RE [d]	16207	16197	16201
Depth, m	0.30	0.40	0.17	0.40	0.36	0.10	0.30	0.30	0.30
Field capacity (FC), mm H_2O	150.0	185.6	84.2	198.3	169.7	0.06	150.0	150.0	150.0
Wilting point (WP), mm H_2O		134.8	61.1	136.0	147.6				
Saturation (SA), mm H_2O		317.2	135.3	289.0	290.7				
pH, H_2O	5.1	5.8	5.6	5.7	5.71	0.11		6.20	8.50
Organic carbon, % weight	13.1	15.3	14.5	13.0	14.5	0.08	0.80	0.88	0.34
Bulk density, g cm^3	0.7	0.85	0.76	0.74	0.76	0.13	1.29	1.36	1.29
Sand fraction, %	27	38	40	38	34	0.28	8	60	48
Silt fraction, %	56	43	43	47	55	-0.19	57	31	49
Clay fraction, %	17	19	17	15	11	-0.10	35	9	3

[a] Andosol experimental data (ED) obtained from Lahuette and Recalde (2015).

[b] Harmonized World Soil Database (HWSD) codes.

[c] Sample ID and location as in Figure 1d.

[d] For andosol, relative error is expressed as RE = (ED–HWSD)/ED, where ED is the average value of the available data.

Table 6. Hydraulic properties of different geological formations surveyed at the PRB.

Lithology [a]	Age [a]	Hydraulic conductivity [b]		Transmissivity [c]	Specific yield [d]	Reference
		Magnitude	Type			
Glacier and moraines	Holocene	0.15–8.2 (1.39)	ip	233.3 (80)	0.02–0.11	PETROECUADOR (2005), EPMAPS (2012)
Alluvial deposits	Holocene	0.18–12.1 (2.92)	ip		0.05–0.15	PETROECUADOR (2005), EPMAPS (2012)
Fluvial–glacial deposits	Pleistocene	0.07–7.9 (1.25)	fi,ip		0.04–0.13	PETROECUADOR (2005), EPMAPS (2012)
Lahars, COVS	Holocene	10^{-3}–10^{-2} (0.01)	fr,fi		<0.01–0.02	EPMAPS (2006a, 2006b, 2012)
Scoria and pumice flows, COVS	Holocene	10^{-2}–10^{-1} (0.04)	fr,fi			PETROECUADOR (2005), EPMAPS (2012)
Andesitic lavas, COVS	Holocene	0.13–2.85 (1.73)	fr,fi		<0.01–0.05	EPMAPS (2006a, 2006b, 2012)
Lahars, COVS	Holocene	10^{-3}–10^{-2} (0.01)	fr,fi		<0.01–0.02	EPMAPS (2006a, 2006b, 2012)
Avalanche flows, COVS	Holocene	10^{-2}–10^{-1} (0.95)	fr,fi	39.8 (40)		PETROECUADOR (2005), EPMAPS (2012)
Ash flows, COVS	Holocene	10^{-3}–10^{-1} (0.02)	fr,fi			PETROECUADOR (2005), EPMAPS (2012)
Ash flows, COVS	Late Pleistocene	10^{-3}–10^{-1} (0.05)	fr,fi	0.3 (5)	<0.01	EPMAPS (2006a, 2006b, 2012)
Ash flows, SIVS	Late Pleistocene	10^{-3}–10^{-1} (0.03)	fr,fi			PETROECUADOR (2005), EPMAPS (2012)
Rhyolitic pyroclastic flows, CHVS	Late Pleistocene	0.04–1.26 (0.66)	fr,fi	49.3 (70)	<0.01–0.05	PETROECUADOR (2005), EPMAPS (2012)
Andesitic lavas, COVS	Middle Pleistocene	0.03–1.65 (0.79)	fr,fi	60.5 (50)	<0.01–0.04	EPMAPS (2006a, 2006b, 2012)
Andesitic lavas, SIVS	Early Pleistocene	0.02–1.45 (0.71)	fr,fi	12.2 (14)	<0.01–0.04	EPMAPS (2012)

[a] Lithology and age as in Figure 1c. COVS—Cotopaxi Volcano Sequence, SIVS—Sincholagua Volcano Sequence, CHVS—Chalupas Volcano Sequence.

[b] Hydraulic conductivity in m d^{-1}; the range refers to theoretical data or experimental data after pumping tests with average values into parenthesis; fr—fracturation, fi—fissuration, and ip—intergranular porosity.

[c] Transmissivity in m^2 d^{-1}; the value refers to single experimental data after pumping tests surveyed for a given saturated thickness in m into parenthesis.

[d] Specific yield as a dimensionless fraction; the range refers to experimental data after pumping tests surveying with average values into parenthesis.

5.2.2. SWAT model output, calibration and validation

Aimed at facilitating model processing, the PRB was divided into seven sub-basins. The subdivision of sub-basins into HRUs was based on land-use, soil, and slope maps using internal options of SWAT model. No thresholds to remove minor land uses, soil typologies, and slope classes were imposed to calculate the HRUs in each sub-basin. Four slope classes were done as 0–5, 5–20, 20–35 and >35. The SWAT interface identified 215 HRUs in the PRB. The available daily streamflow record for the observation period 2003–2015 was divided into a warm-up period (2003–2005) to allow the model parameters to reach equilibrium, a calibration period (2006–2010) to minimize the distance between predicted and observed streamflow values, and a validation period (2011–2015) (Figure 5). The other actions are described below.

The sensitivity analysis and automatic calibration was done by using the SUFI-2 algorithm of the Calibration and Uncertainty Programs from SWAT (SWAT-CUP) (Abbaspour, 2007; Abbaspour et al., 2012). The choice for parameters selection was based on previous SWAT experiences in the Andean Highland (Oñate-Valdivieso and Bosque-Sendra, 2014; Oñate-Valdivieso et al., 2016; Salmoral et al., 2018; Quintero et al., 2009; Crespo et al., 2006; Plesca et al., 2012; Velasco-Arguello 2014; Espinosa and Rivera, 2016; Hasan and Wyseure, 2018), experiences gained by the supervisors of this Thesis in similar neotropical mountainous areas in the Americas (Jimeno-Sáez et al., 2021, 2018; Senent-Aparicio et al., 2021c), other many examples available in the scientific literature, giving relevance to those associated to groundwater flow, runoff and soil data, as well as on the combination of the Latin hypercube and one-factor-at-a-time sampling strategies (Van Griensven and Meixner, 2006; Schoul et al., 2008b). These SWAT experiences allowed to select twenty-one calibration parameters and their ranges among the existing 629 ones for sensitivity analysis, as described below. The full description of calibration parameters can be found in SWAT manuals (Di Luzio et al., 2022; Neitch et al., 2005; Winchell et al., 2010).

The calibration methodology was based on two steps according to Castellanos-Osorio et al. (2023). First, a global monthly scale calibration was performed to better adjust the volume of water components. This global sensitivity

analysis allowed to identify the most influential parameters governing streamflow, with special focus on those governing surface and interflow runoff, surface and deep percolation, and baseflow. Table 7 includes the thirteen parameters used to match predicted and observed monthly streamflow data pairs. The second step consisted of a daily scale calibration to improve the temporality of the model flow rates. This step used eight additional parameters (Table 8) to the above described thirteen ones to match predicted and observed daily streamflow data pairs.

Three iterations (each iteration represented 500 simulations) were performed to achieve an acceptable calibration. Each parameter range was updated after each iteration. Flow data from gauging station Q5 for the periods 2006-2010 (calibration) and 2011-2015 (validation) were used. It is important for reliable model calibration and validation that both periods include dry, wet and usual values (Arnold et al., 2012; Gan et al., 1997). This investigation considered wet and dry years the 80th and 20th percentiles of annual cumulative precipitation, respectively, which resulted in 1,228 mm (80) and 1,033 mm (20). The calibration period (2006-2010) ranged from 1,484 mm to 1,025 mm, and the validation values (2011-2015) ranged from 1,334 mm to 990 mm. A ranking of parameter sensitivities was obtained after 500 model runs to identify the impact of each one on the objective function (Abbaspour et al., 2018). The parameters ranges were updated after each iteration. The stopping of iterations was dictated by values of model performance statistics below the standardized ranges proposed in the SWAT literature (Bastin et al., 2013; Refsgaard et al., 2007; Schuol et al., 2008).

The ranges of calibrated parameters showed in Table 7 and Table 8 are found physically realistic (Eckhardt et al., 2005). So, the model could be employed for assessing the current stationary regime as well as the impact of climate change in streamflow in the PRB after the performance metrics analysis, as will be described in Section 5.3. The parameters average slope length (SLSUBBSN) and average slope steepness (HRU_SLP) varied in the 12.92–172.35 m and 0.01–0.81 m m^{-1} range in the seven sub-basins, with average surface-weighed values of 130 m and 0.05 m m^{-1}, respectively. These figures were corroborated by additional analysis on GIS. The parameter Manning's 'n' value for overland flow (OV_N) was 0.99, the parameter average slope of the tributary channels (CH_N1) was 2.08 m m^{-1}, and the parameter Manning's 'n' value for the main channel (CH_N2) was 0.13. The parameters

average slope of the tributary channels (CH_S1) and average slope of the main channel along the channel length (CH_S2) varied in the 0.02–0.09 m m^{-1} and 0.01–0.03 m m^{-1} range in the seven sub-basins, with average surface-weighed values of 0.023 m m^{-1} and 0.017 m m^{-1}, respectively. The parameter surface runoff lag coefficient (SURLAG) was 3.74. The magnitude of these last three parameters agrees with the typical high roughness and slope of high mountain riverbeds. Sections B.2 and B.3 in Appendix B describe the calibration parameters used in the monthly and daily model, respectively. Section B.4 in Appendix B widens the description of the magnitude, range and hydrological meaning of these parameters.

Table 7. The thirteen parameters used in the first-step monthly SWAT model calibration in the PRB.

Parameter [a]	Description and units [a]	Range used in calibration	Fitted value	Final Value
r_CN2.mgt	Soil Conservation Service (SCS) runoff curve number, [–]	–0.1 to 0.1	0.02	70.64 to 96.23 [b]
v_ALPHA_BF.gw	Baseflow alpha factor, day^{-1}	0 to 0.8	0.63	0.63
a_GW_DELAY.gw	Groundwater delay time, day	–10 to 70	58.60	89.6
a_GWQMN.gw	Threshold groundwater depth in the shallow aquifer for return flow to occur, mm	–200 to 200	129.50	1129.50
v_GW_REVAP.gw	Groundwater revap coefficient, [–]	0.02 to 0.2	0.10	0.10
a_RCHRG_DP.gw	Deep aquifer percolation fraction, [–]	–0.01 to 0.03	–0.004	0.05
a_REVAPMN.gw	Threshold groundwater depth in the shallow aquifer for revap or percolation to the deep aquifer to occur, mm	–250 to 250	185.60	935.60
v_CANMX.hru	Maximum canopy storage, mm	0 to 5	0.15	0.15
v_LAT_TTIME.hru	Lateral flow travel time, day	10 to 150	104.01	104.01
v_SLSOIL.hru	Slope length for lateral subsurface flow, m	0 to 50	0.28	0.28
v_EPCO.bsn	Plant uptake compensation factor, [–]	0.3 to 1	0.45	0.45
v_ESCO.bsn	Soil evaporation compensation factor, [–]	0.3 to 0.8	0.71	0.71
r_SOL_AWC.sol	Available water capacity of the soil layer, mm $H_2O \cdot mm\ soil^{-1}$	–0.02 to 0.02	–0.01	0.099 to 0.165 [c]

[–] — dimensionless.

[a] Parameter notation, description and units as they appear in SWAT manuals (Di Luzio et al., 2022; Neitch et al., 2005; Winchell et al., 2010). (r_) refers to relative change, i.e., the current parameter must be multiplied by (1 + the value obtained in calibration); (v_) means that the existing parameter value must be replaced by the value obtained in calibration; and (a_) refers to absolute change, i.e., the fitted value must be added to the existing parameter value.

[b] Range for all the 215 HRUs.

[c] Range for all soil typologies and soil layer thickness.

Table 8. The additional eight parameters used in the second-phase daily SWAT model calibration in the PRB.

Parameter [a]	Description and units [a]	Range used in calibration	Fitted value	Final Value
r_SLSUBBSN.hru	Average slope length, m	–0.1 to 0.5	0.41	12.92–172.35 [b]
r_HRU_SLP.hru	Average slope steepness, m m^{-1}	–0.5 to 0.2	0.04	0.01–0.81 [b]
v_OV_N.hru	Manning's 'n' value for overland flow, [–]	0.1 to 1	0.99	0.99
r_CH_S1.sub	Average slope of the tributary channels, m m^{-1}	–0.5 to 0.2	–0.48	0.02–0.09 [b]
v_CH_N1.sub	Manning's 'n' value for the tributary channels, [–]	0.01 to 30	2.08	2.08
r_CH_S2.rte	Average slope of the main channel along the channel length, m m^{-1}	–0.5 to 0.3	–0.21	0.01–0.03 [b]
v_CH_N2.rte	Manning's 'n' value for the main channel, [–]	0.02 to 0.2	0.13	0.13
v_SURLAG.bsn	Surface runoff lag coefficient, [–]	0.05 to 15	3.74	3.74

[–] — dimensionless.

[a] Parameter notation, description and units as they appear in SWAT manuals (Di Luzio et al., 2022; Neitch et al., 2005; Winchell et al., 2010). (r_) and (v_) as in Table 7.

[b] Range for all the 215 HRUs

The Kling–Gupta efficiency (KGE) (Gupta et al. 2009) was chosen as the primary objective function to evaluate the SWAT model performance on monthly (first step) and daily (second step) scales (Table 9). Further efficiency criteria used to measure the model's goodness-of-fit included the logarithmic Nash-Sutcliffe coefficient efficiency (lnNSE) (Nash and Sutcliffe, 1970), the coefficient of determination (R^2), percent bias (PBIAS), root mean squared error (RMSE) and RMSE relative to the standard deviation of the observations (RSR) (Table 9). The description of these statistics is in Section B.1 in Appendix B after Moriasi et al. (2007). Krause et al. (2005) advise against using the NSE to evaluate low flow conditions. To better evaluate the behaviour of low flows, lnNSE was adopted as alternative indicator to NSE. The lnNSE has the advantage of providing a more balanced approach at both extremely low and peak values. Previous studies have successfully applied this lnNSE index (Castellanos-Osorio et al. 2023; Chen et al., 2018; Osuch et al., 2018; Parra et al., 2019; Senent-Aparicio et al., 2021a, 2021b). Focusing on the KGE and lnNSE statistics (Krause et al., 2005), daily SWAT model showed acceptable values –good performance– for the calibration and validation periods.

The observed and predicted streamflow values in the warm-up, calibration and validation periods are displayed in the Figure 6a. The predicted (z^*) and observed (z) streamflow data pairs (Q_T) were compared for calibration and validation periods only (Figure 6b). The relative difference, $RE=(z-z^*)/z$, averages –0.03±0.34, i.e., the daily SWAT model lightly underestimate streamflow, especially peak flows as a typical expected behaviour. *RE* typically varies in the ±0.2 range, with 38% in the ±0.5 range, 5.5% in the ±0.75 range, and 1.5% below –1 (Figure 6b).

Table 9. SWAT model performance statistics for daily and monthly simulations in the PRB. Author's elaboration.

Model evaluation statistic	Daily streamflow		Monthly streamflow	
	Calibration	Validation	Calibration	Validation
KGE	0.48	0.60	0.73	0.65
lnNSE	0.44	0.52	0.67	0.65
R^2	0.31	0.45	0.66	0.67
PBIAS	1.96	7.43	1.75	7.36
RMSE	1.25	0.95	0.51	0.58
RSR	0.85	0.77	0.58	0.62

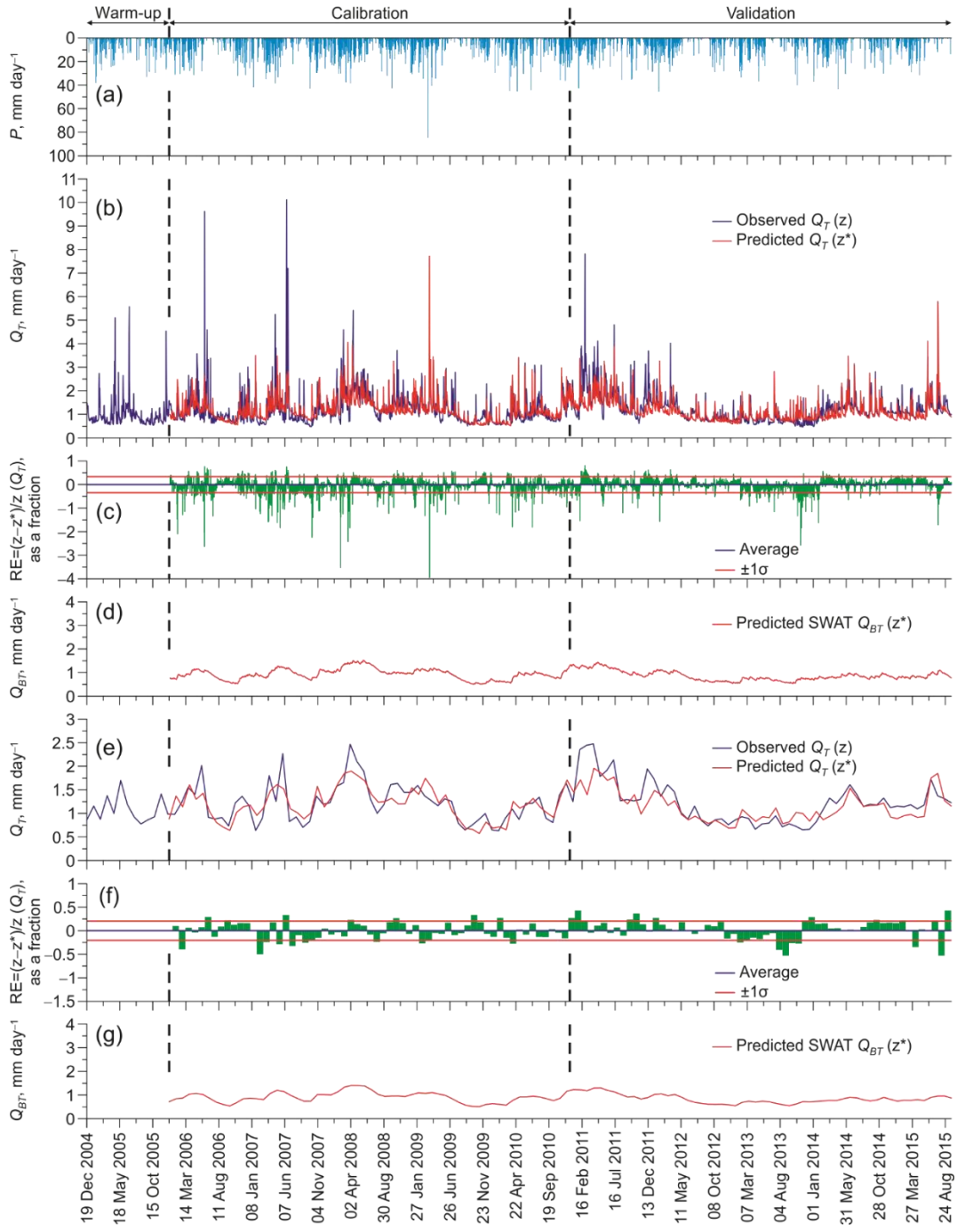

Figure caption on next page.

Figure 6. For SWAT model in the PRB, (a) daily precipitation at Izobamba weather station (W5; Figure 1b; Table 2); (b) observed and predicted daily streamflow (QT) at Bocatoma gauging station (Q5; Figure 1b; Table 2) for the 2004–2005 warm-up, 2006–2010 calibration, and 2011–2015 validation periods; (c) predicted (z*) vs. observed (z) daily streamflow data for the calibration and validation periods, RE=(z–z*)/z is the relative difference; (d) predicted daily baseflow (QBT) at Q5 gauging station; (e) observed vs. predicted monthly streamflow (QT) at Q5 gauging station for the 2004–2015 simulation period; (f) RE=(z–z*)/z for the calibration and validation periods; and (g) predicted monthly baseflow (QBT) at Q5 gauging station.

5.2.3. Stationary water balance components

In Section 5.1, the stationarity condition of the water balance components over the modelling period 2003–2015 was checked. The subsequent hydrograph analysis described in Section 5.2.2 was aimed at splitting precipitation (P) into actual evapotranspiration (E_A) and total streamflow (Q_T), as well as into other water balance subcomponents such as surface and interflow runoff (Q_U), baseflow (Q_{BT}), shallow aquifer recharge (W_{RS}), and deep aquifer recharge (W_{RD}). In each of the seven PRB sub-basins over the period 2006–2015, the spatial distribution of the average yearly value and coefficient of variation (CV) of the water balance components P, Q_T, Q_{BT}, W_{RS} and W_{RD} in displayed in Figure 7. Table 10 summarizes the results.

In the PRB over the period 2006–2015, predicted average yearly values of P, E_A, Q_T, Q_U, Q_{BT}, W_{RS}, and W_{RD} were 1,004.6, 559.1, 445.5, 92.8, 341.3, 11.1, and 0.3 mm year^{-1}, respectively, whereas their coefficients of variation CV_P, CV_{EA}, CV_{QT}, CV_{QU}, CV_{QBT}, CV_{WRS}, CV_{WRD} were 0.26, 0.58, 0.57, 0.39, 0.48, 0.68, and 0.53, respectively (Table 10). The yearly average values mean 0.56-, 0.44-, 0.09-, 0.34-, 0.01-, and <0.01-fold average yearly P. These magnitudes are like those reported in other Andean Highland basins with analogous geology, geography, land use, and vegetation cover (Buytaert et al., 2006; Minga-Leon et al., 2018; Ochoa-Sánchez, et al., 2019).

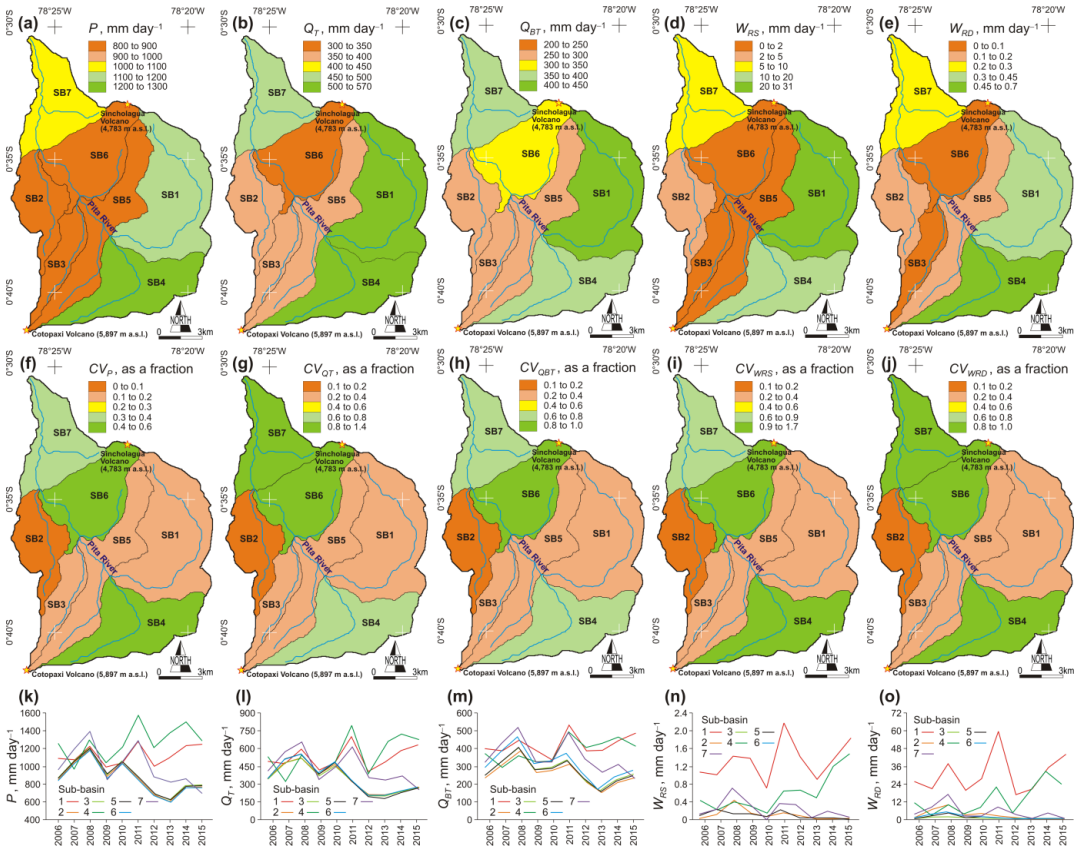

Figure 7. In each of the seven PRB sub-basins (SB) over the period 2006–2015, average yearly value (a through e), coefficient of variation (CV) (f through j), and yearly time series (k through o) of precipitation (P), total streamflow (Q_T), baseflow (Q_{BT}), shallow aquifer recharge (W_{RS}), and deep aquifer recharge (W_{RD}).

Regarding Q_{BT}, it means 0.76-fold Q_T and 0.34-fold P, thus being Q_{BT} the predominant streamflow fraction and showing also the relevance of groundwater discharge as the prime water resource in the PRB. Similar magnitude of Q_{BT} was reported in other analogous northern Andean Highland basins (Oñate-Valdivieso and Bosque-Sendra, 2014; Oñate-Valdivieso et al., 2016; Quintero et al., 2009; Crespo et al., 2006; Plesca et al., 2012; Velasco-Arguello 2014; Espinosa and Rivera, 2016; Hasan and Wyseure, 2018). Conversely, W_{RS} and W_{RD} mean 0.01- and <0.01-fold P, respectively. These figures are consistent with observed high piezometric levels in shallow and deep aquifers, and deep aquifer discharge (including thermal springs) determining permanent baseflow (Peñafiel et al., 2016a; 2016b). Attending to these findings and for practical conceptualization, these aquifers may be

considered full in its current unexploited state, thus favouring that a noticeable fraction of each recharge event could be added to the baseflow as aquifer discharge rather than contributing to aquifer storage.

Table 10. For the period 2006–2015, average yearly value and coefficient of variation of the water balance components in each sub-basin (SB) and the entire PRB.

Variable [a]	SB 1	SB 2	SB 3	SB 4	SB 5	SB 6	SB 7	PRB
Surface, km^2	44.0	17.4	11.4	31.1	28.8	27.5	24.3	184.5
Average elevation, m a.s.l.	4105	3839	4127	4059	4113	3998	3715	4007
P	1126.6	862.2	862.2	1216.3	862.2	862.2	1011.3	1004.6
E_A	599.7	507.9	488.4	655.0	493.1	516.4	559.3	559.1
Q_T	527.0	354.3	373.8	561.3	369.1	345.8	451.9	445.5
Q_U	75.7	92.4	104.0	164.2	99.7	38.4	80.5	92.8
Q_{BT}	420.0	259.0	269.5	382.7	267.7	306.0	365.8	341.3
W_{RS}	30.9	2.8	0.3	13.9	1.6	1.4	5.4	11.1
W_{RD}	0.41	0.13	0.04	0.64	0.13	0.05	0.26	0.28
CV_P	0.10	0.04	0.19	0.53	0.14	0.44	0.33	0.26
CV_{EA}	0.21	0.14	0.33	0.75	0.26	1.16	1.17	0.58
CV_{QT}	0.21	0.14	0.32	0.75	0.25	1.38	0.89	0.57
CV_{QU}	0.16	0.09	0.28	0.61	0.17	0.70	0.71	0.39
CV_{QBT}	0.21	0.13	0.32	0.77	0.25	0.98	0.64	0.48
CV_{WRS}	0.21	0.14	0.32	1.64	0.27	1.07	0.88	0.68
CV_{WRD}	0.26	0.19	0.35	0.88	0.25	0.92	0.82	0.53

[a] Notation and description for variables as in Figure 1. P, E_A, Q_T, Q_U, Q_{BT}, W_{RS} and W_{RD} in mm year^{-1}; CVs as dimensionless fractions.

As shown in Figure 7, the magnitude of the water balance components varies over space and time. In what follows, the description will refer to the groundwater components only, also including precipitation and total streamflow as governing reference components.

Average yearly P is higher than 1,000 mm year^{-1} in the south-eastern (sub-basin 1) and north-western (sub-basin 7) sectors of the PRB, as well as on the western versant of the Eastern Andean Cordillera (sub-basin 4) (Figure 7a). In the central sector of the PRB (sub-basins 2, 3, 5 and 6), average annual P is slightly higher than 850 mm year^{-1}. This lower magnitude of P is associated with the orographic shadow that Cotopaxi and Sincholagua volcanoes impose on incoming Atlantic and Pacific cloud fronts (Pourrut, 1995; Garreaud, 2009). This orographic

shadow also produces a more irregular rainfall pattern and subsequent higher CV_P values in sub-basins 4 and 6 (Figure 7f).

Average yearly Q_T is higher than 500 mm year^{-1} in sub-basins 1 and 4, where average yearly P is also higher, and in sub-basin 7 since it receives streamflow generated in the entire PRB area (Figure 7b). In sub-basins 3 and 5, which drain the northern slope of the Cotopaxi Volcano, and in the centre of the PRB (sub-basins 2, 3, 5 and 6), average yearly Q_T is somewhat less than 400 mm year^{-1}. This general behaviour shows how Q_T tends to decrease from upstream to mid-slope areas, as was also identified by Muñoz, (2016). Average yearly Q_{BT} narrowly follows the spatial distribution of average yearly Q_T, with values higher than 350 mm year^{-1} in sub-basins 1, 4 and 7 (Figure 7c). The higher CV_P values induce the higher CV_{QT} (Figure 7g) and CV_{QBT} (Figure 7h) values in sub-basins 4, 6 and 7.

Average yearly W_{RS} (Figure 7d) and W_{RD} (Figure 7e) follow a similar spatial distribution, with higher values in in sub-basins 1 and 4, moderate in sub-basin 7, and lower in the other sub-basins. Higher values in sub-basins 1, 4 and 7 are attributed to a combination of higher average yearly P values, presence of well-preserved andosols admitting downward percolation of infiltration events, and the existence of deeper piezometric levels and thicker unsaturated zones favouring vertical transmission of water to underlying andesitic lavas formations (the aquifer). Lower values in sub-basins 2, 3, 5 and 6 are attributed to lower average yearly P values, poorly developed soils over lahar deposits in the versants of the Cotopaxi and Sincholagua volcanoes, thin unsaturated zones and shallow piezometric levels repealing infiltration of recharge events (Figure 7a). The higher CV_P values induce the higher CV_{WRS} (Figure 7i) and CV_{WRD} (Figure 7j) values in sub-basins 4, 6 and 7.

Regarding the temporal evolution of the water balance components, in dry years like 2007 and 2008 (Figure 5a), yearly P is higher in sub-basin 7 in the northwest sector of the PRB (Figure 7k–o), while in average years like 2013 and 2014 and wet years like 2015 (Figure 5a), yearly P is higher in the high-elevation sub-basins 1 and 4 (Figure 7k–o). In all sub-basins, the yearly time series of Q_T, Q_{BT}, W_{RS} and W_{RD} roughly follows the temporal evolution of yearly P values (Figure 7k–o).

5.3. MODELLING OF FUTURE SCENARIOS STREAMFLOW

5.3.1. Selection of climate change models

The calibrated and validated SWAT model for the PRB described in the previous section was run to evaluate the impact of climate change on streamflow (Q_T) and actual evapotranspiration (E_A) and other subcomponents such as surface and interflow runoff (Q_U), baseflow (Q_{BT}), shallow aquifer recharge (W_{RS}), deep aquifer recharge (W_{RD}), and total aquifer recharge (W_R) expressed as the sum of W_{RS} and W_{RD}. As described in Section IV.3, the five RMC models available in the CCT (GFDL-ESM2M, HadGEM2-ES, IPSL-CM5A-LR, MIROC, and NoerESM1- M) were analysed to identify those that best reproduce the average year from the mean values and standard deviations. The selection was based on the *Id* index, which is the sum of the absolute value of the relative differences in the historical and control series statistics during the 12 months of an average year. Table 11 presents the *Id* values obtained for the 2006–2015 study period. The higher the *Id*, the worse the goodness-of-fit. Except for the HadGEM2-ES model, the RCM models achieved similar mean *Id* values, *Id*(Δx), for precipitation and temperature. However, greater differences in standard deviations, *Id*(Δσ), were observed among the RCM models, especially for temperature, which ranged from 18.78 (model IPSL-CM5A-LR) to 55.64 (model GFDL-ESM2M). The IPSL-CM5A-LR, MIROC, and NoerESM1-M models achieved lower *Id* values. This issue is in line with previous similar works (Pulido-Velazquez et al., 2015b; Urrutia and Vuille, 2009). Hence, these three RCM models were selected to assess the impact of climate change on the RGR in the PRB.

Table 11. Id index of each RCM model for precipitation and temperature monthly series.

RCM model	Precipitation		Temperature		*Id* [a]
	Id(Δx)	*Id*(Δσ)	*Id*(Δx)	*Id*(Δσ)	
GFDL-ESM2M	0.87	11.6	0.61	55.64	68.72
HadGEM2-ES	7.97	12.24	7.47	23.12	50.8
IPSL-CM5A-LR	0.8	5.92	0.61	18.78	26.11
MIROC	1.22	6.1	0.57	30.32	38.21
NoerESM1-M	0.92	8.38	0.59	22.65	32.54

[a] Id—sum of the absolute values of the mean values, denoted as Id(Δx), and standard deviations, denoted as Id(Δσ), of precipitation and temperature monthly series.

5.3.2. Changes in projected precipitation and temperature

The implemented ensembles consisted of three RCM models (IPSL-CM5A-LR, MIROC, and NoerESM1-M) and RCP emission scenarios 4.5 and 8.5. Table 12 summarizes the changes in the average values and standard deviations of the temperature and precipitation (the climate variables) annual series from the implemented ensembles relative to the corresponding values of each RCM baseline period (1976–2005). The changes refer to the mid- (2040–2069) and long-term (2070–2099) future horizons. In addition, the distributions of monthly mean values and standard deviations of temperature and precipitation for the three RCM-RCP 4.5 ensembles and the three RCM-RCP 8.5 ensembles over the baseline period in the mid- and long-term future horizons are displayed in Figure 8 and Figure 9, respectively.

Regarding average annual temperature (Table 12), the three RCMs predicted increases from +1.4 °C, in the mid-term, to +2.5 °C, in the long term, for RCP 4.5 and from +1.9 °C, in the mid-term, to 4.7 °C, in the long term, for RCP 8.5. These figures indicate increases of +20–35 % for RCP 4.5 and +30–65 % for RCP 8.5 regarding the baseline. The NoerESM1-M model predicted lower temperature increases regarding the baseline, with values 10–20 % (depending on the RCP) lower than those obtained in the other two RCMs. This increase in temperature is a proven historical fact corroborated by the 0.1–0.2 °C increase per decade recorded in the last 70–100 years (Buytaert et al., 2014; Sklenár et al., 2021; Vuille et al., 2015), which exceeds the threshold of natural climate variation (Gutiérrez-Salazar and Medrano-Vizcaíno, 2019). These results concur with the average temperature increases of 2 °C and 5 °C predicted in the coastal versant of the WAC (Ilbay-Yupa et al., 2021; Rivadeneira-Vera et al., 2020) and the Andean Highland of Ecuador (Herzog et al., 2012), respectively. Regarding the average annual temperature standard deviations, the IPSL-CM5A-LR and NoerESM1-M models revealed changes lower than the baseline for RCP. 4.5, whereas the MIROC model predicted increases of more than 100 % for RCP 4.5. The RCP 8.5 ensembles predicted an increase in temperature in the 20–90 % range, depending on the RCM.

Table 12. Changes in the average values and standard deviations of annual precipitation and temperature predicted by the implemented RCM-RCP ensembles relative to the corresponding values for each RCM baseline scenario.

RCM model	Emission scenario	Period	Annual precipitation, mm				Annual temperature, °C			
			Mean value	Change relative to baseline [a]	Standard deviation	Change relative to baseline [a]	Mean value	Change relative to baseline [a]	Standard deviation	Change relative to baseline [a]
IPSL-CM5A-LR	Baseline	1976–2005	1091.29	–	91.2	–	7.12	–	0.45	–
	RCP 4.5	2040–2069	1124.11	+ 32.82(+3%)	95.06	+3.88(+4%)	9.08	+1.96(+28%)	0.31	–0.14(–31%)
		2070–2099	1143.73	+52.45(+5%)	71.50	–19.68(–22%)	9.55	+2.43(+34%)	0.27	–0.18(–39%)
	RCP 8.5	2040–2069	1141.76	+50.47(+5%)	84.40	–6.78(–7%)	9.82	+2.71 (+38%)	0.53	+0.08(+18%)
		2070–2099	1309.72	+218.43 (+20%)	104.57	+13.39(+15%)	11.82	+4.70 (+66%)	0.69	+0.24(+54%)
MIROC	Baseline	1976–2005	945.32	–	49.18	–	8.20	–	0.47	–
	RCP 4.5	2040–2069	923.21	–22.12 (–2%)	44.34	–4.84(–10%)	10.03	+1.83 (+22%)	1.00	+0.53(+111%)
		2070–2099	932.08	–13.24 (–1%)	46.16	–3.02(–6%)	10.67	+2.47 (+30%)	0.67	+0.20(+41%)
	RCP 8.5	2040–2069	948.82	+3.50 (+0.4%)	66.72	+17.54(36%)	10.69	+2.48 (+30%)	0.61	+0.14(+29%)
		2070–2099	1052.05	+106.73 (+11%)	39.27	–9.91(–20%)	12.70	+4.50 (+55%)	0.89	+0.42(+88%)
NoerESM1-M	Baseline	1976–2005	970.43	–	70.20	–	7.16	–	0.33	–
	RCP 4.5	2040–2069	1160.21	+189.79(+20%)	89.38	+19.18(+27%)	8.53	+1.37 (+19%)	0.29	–0.04(–13%)
		2070–2099	1149.02	+178.59 (+18%)	86.31	+16.11(+23%)	8.84	+1.68 (+23%)	0.27	–0.06(–19%)
	RCP 8.5	2040–2069	1197.85	+227.42 (+23%)	89.81	+19.61(+28%)	9.02	+1.86 (+26%)	0.40	+0.07(+22%)
		2070–2099	1371.91	+401.48 (+41%)	92.55	+22.34(+32%)	10.28	+3.12 (+44%)	0.46	+0.13(+40%)

[a] Changes are expressed as positive or negative absolute (in the same unit as the variable) and relative (percentages in parentheses) differences.

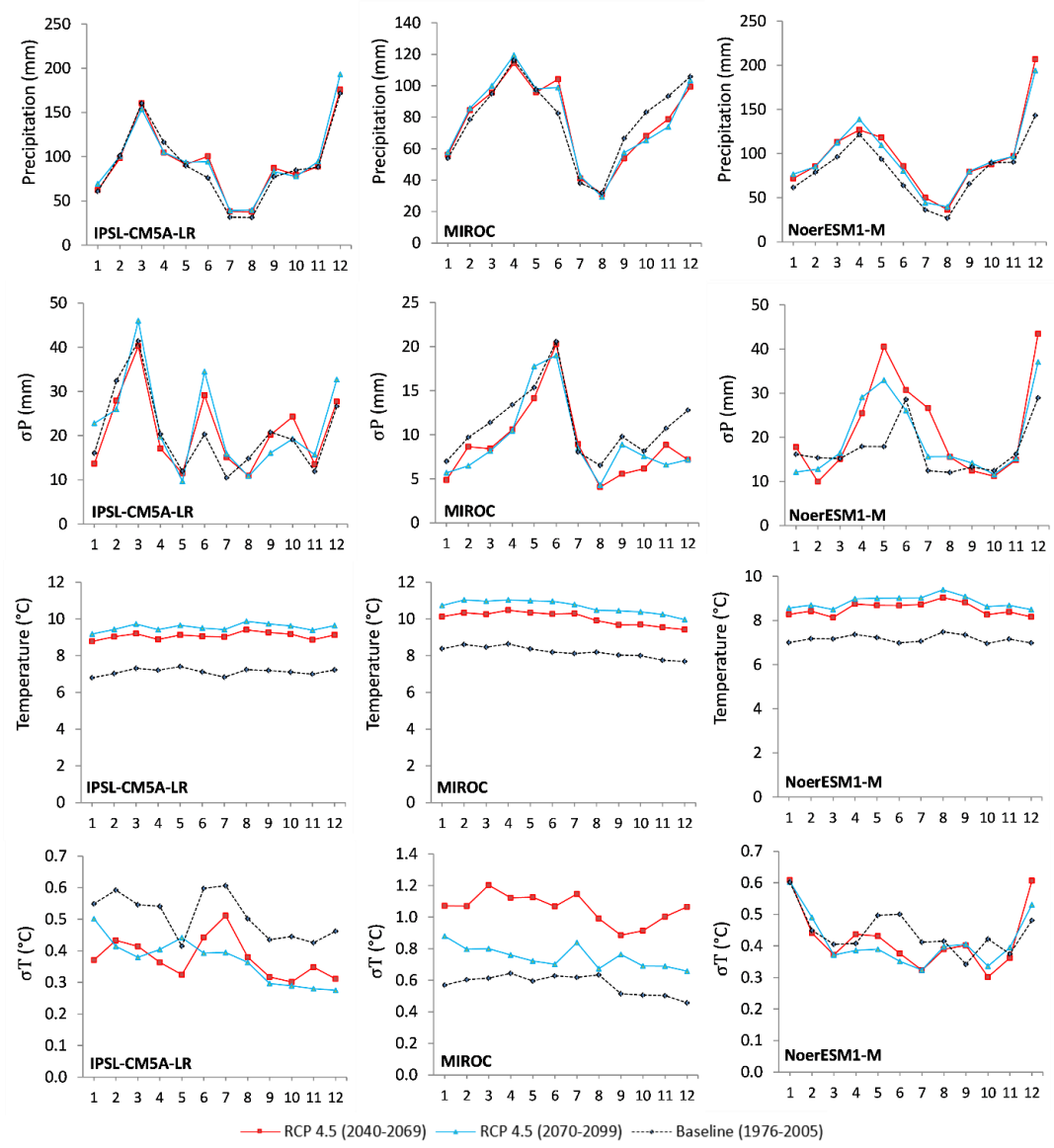

Figure 8. Distribution of the mean values and standard deviations of monthly temperature and precipitation of the three RCM-RCP 4.5 ensembles for the baseline period (1976–2005) and the mid- (2040–2069) and long-term (2070–2099) future horizons. Figure modified and updated from Senent-Aparicio et al. (2024).

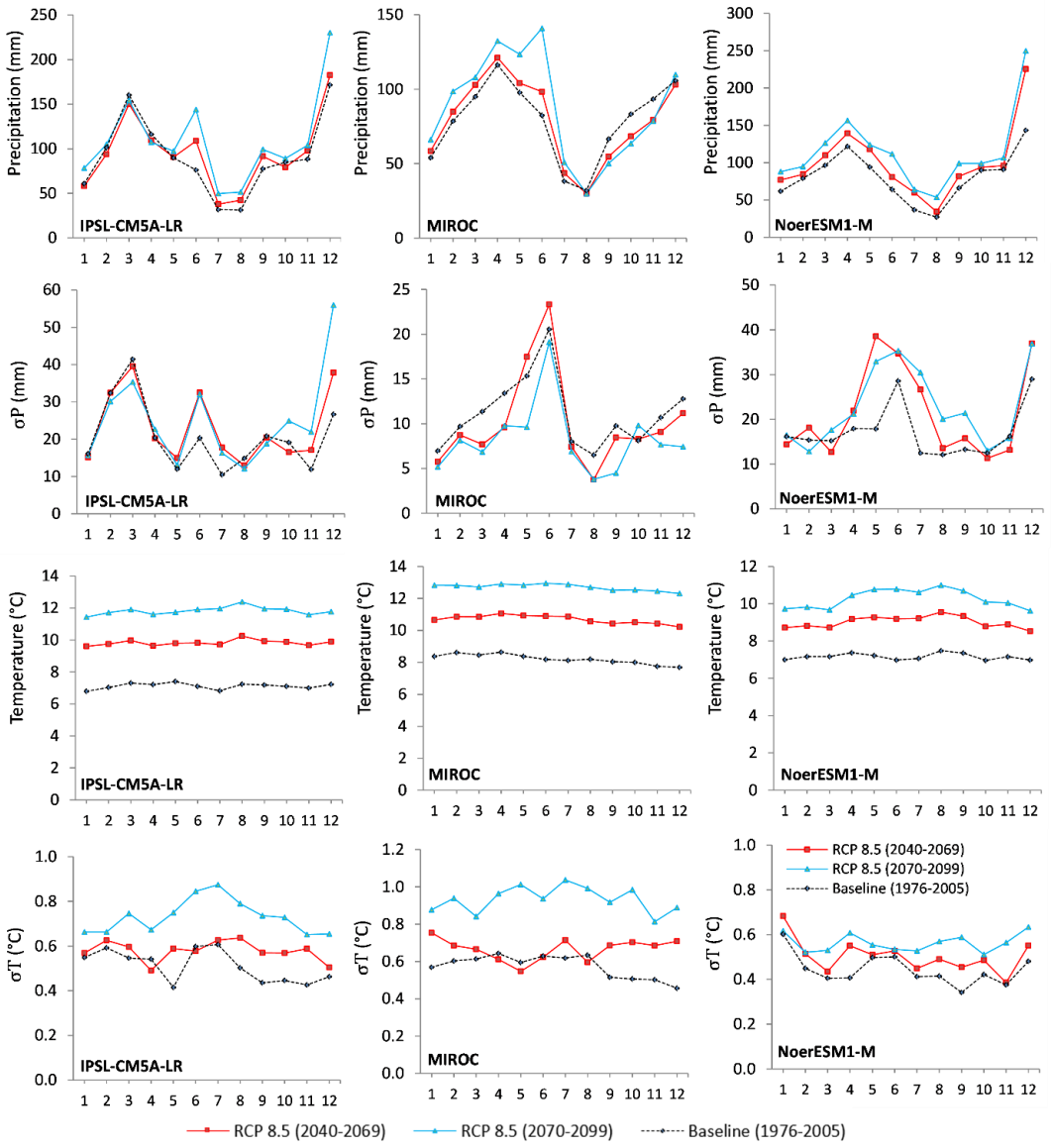

Figure 9. Distribution of the mean values and standard deviations of monthly temperature and precipitation of the three RCM-RCP 8.5 ensembles for the baseline period (1976–2005) and the mid- (2040–2069) and long-term (2070–2099) future horizons. Figure modified and updated from Senent-Aparicio et al. (2024)

At the monthly scale, for RCP 4.5 (Figure 8) and RCP 8.5 (Figure 9), the mid- and long-term mean temperature trends are similar to the baseline, regardless of the RCM considered. Only the NoerESM1-M model predicted more pronounced variation between April and July for RCP 8.5 in the long term, with higher

temperature increases for the rest of the year. However, the standard deviations for monthly temperature changed significantly depending on the RCM-RCP ensemble. While the baseline remained unvaried in the mid- and long-term RCP 4.5 scenarios, except for the MIROC model, RCP 8.5 revealed an apparent increase in standard deviations for all the RCMs, especially in the long term. Moreover, the dry season exhibited the highest values, except in the NoerESM1-M model. Furthermore, the change in temperature for RCP 4.5 is much greater in the mid-term than in the long term, inversely compared to the RCP 8.5 results. Generally, these projections are consistent with the results previously assessed in similar regions studied (Buytaert et al., 2011; Cresso et al., 2020; Flores-López et al., 2016).

Regarding average annual precipitation (Table 12), the MIROC–RCP 4.5 ensemble revealed slight decreases of –2% and –1% in the mid- and long-term horizons, respectively, compared to the baseline. Conversely, the ensembles generated from the other two RCMs predicted increases. Unlike the temperature trend, precipitation covered a wide range of changes regarding the baseline, varying from +0.4 % to +41 % depending on the RCM-RCP ensemble, although RCP 8.5 generally demonstrated greater increases. Recent studies agree that regional warming is more evident than future variations in precipitation. For example, several authors have demonstrated a decrease of nearly 15 % in the IAV region (Kirtman et al., 2013; Vuille et al., 2008), while others have suggested increases of around 10 % in the eastern and western flanks (Ilbay-Yupa et al., 2021). Historical precipitation over the last 50 years does not display a definitive trend (Vuille et al., 2003), only a slight reduction at most (Martínez et al., 2011), as also showed in Figure 5, with few impacts on water resource availability. Regarding the average annual precipitation standard deviation, the changes vary between –20 % and +35 %, in contrast to the wide variation between –30 % and +110 % in the average annual temperature standard deviation. Notwithstanding, each RCM-RCP ensemble differs significantly. The IPSL-CM5A-LR model demonstrated a significant decrease (–22 %) for RCP 4.5 in the long term but the opposite (an increase of +15 %) for RCP 8.5. The NoerESM1-M model achieved increases of approximately 20 % for all the scenarios, whereas the MIROC model revealed precipitation increases and decreases depending on the RCP and time horizon considered.

At the monthly scale, for RCP 4.5 (Figure 8) and RCP 8.5 (Figure 9), mean precipitation also exhibits slight seasonal differences. For all RCMs, mean monthly precipitation is similar to the baseline, except in June. This finding is especially relevant for RCP 8.5 in the long term, where the increase reached +100 % in the IPSL-CM5A-LR and MIROC models. No clear trends are evident concerning the monthly precipitation standard deviation since variations are indistinctly positive or negative depending on the RCM-RCP ensemble, which appear not to be in line with Zhiña et al. (2019) whose study in the southern Ecuadorian Andes points to a higher increase in monthly precipitation, especially in the long-term period.

In the mid- and long-term future, the increase in average temperature combined with the slight increase in average precipitation obtained in most of the RCM-RCP ensembles should result in higher actual evapotranspiration (i.e., the evaporative fraction of precipitation that returns to the atmosphere) and, therefore, a decrease in the available water for ecosystems and human uses (i.e., the non-evaporative fraction of precipitation or the water amount that could contribute to streamflow and aquifer recharge after discounting transmission losses), as presented in Table 12. This plausible framework could also be accompanied by changes in the fire regime (Kitzberger et al., 2022) due to warmer temperatures and soil degradation resulting from subsequent low- vegetated patches and changes in the frequency and intensity of rainfall events (Muñoz et al., 2021) and dry spells. This combination could worsen the current hydraulic state of andosols (Young et al., 2011), altering or degrading the *páramo* ecosystem's hydrological functioning and temporal water storage capacity. This alpine ecosystem's sensitivity to climate change (Cuesta et al., 2017) implies a high risk of habitat loss and unsafe water provision, as identified by Anderson et al. (2011).

5.3.3. Response of renewable groundwater resource to climate change

This section analyses and discusses the response of main water balance components to each RCM-RCP ensemble in the mid- (2040–2069) and long-term (2070–2099) future horizons. The results are summarized in Table 13. The changes in the baseline scenario indicate the expected magnitude of the RGR and its hydrological significance in the future. Different experimental relationships for aquifer recharge predictions under different precipitation fields associated to

current and future climate frameworks can be found in the scientific literature (Alcalá et al., 2018, 2011; Ross et al., 2005). For example, Taylor et al. (2013) observed a positive relationship between projected changes in precipitation and subsequent aquifer recharge responses. In the PRB, although increased precipitation typically implies increased streamflow, it does not always correspond with increased aquifer recharge, as presented in Table 13. Therefore, precipitation (P) and total aquifer recharge (W_R = W_{RS} (shallow aquifer recharge) + W_{RD} (deep aquifer recharge)) did not follow a linear relationship, and more interdisciplinary information to conceptualize the soil–aquifer relationships is needed to interpret the changes in lower aquifer recharge rates obtained as differences in P and other significant water balance components such as actual evapotranspiration (E_A). In most ungauged mountainous areas, E_A is typically one of the less certain water balance components, especially when only non-global models, such as Hargreaves (1994) and similar, can be used for potential evapotranspiration due to data scarcity (Alcalá et al., 2011; España et al., 2013, 2011; Gerrits et al., 2009; Were et al., 2007). This is the case in the PRB, where uncertainty in E_A propagates through the model equations to reveal relatively uncertain W_R rates, which can be uninterpretable when attempting to draw conclusions. Therefore, comparisons of aquifer recharge with the evaporative fraction of P (E_A:P ratio) or the non-evaporative fraction of P (1–[E_A:P] ratio) instead of P or E_A were preferred to analyze changes in streamflow and aquifer recharge. Likewise, other authors (Pool et al., 2021; Seddon et al., 2021) have used similar indices to provide more accurate relationships between the parameters implied in the aquifer recharge. When the E_A:P and 1–(E_A:P) ratios were compared with W_R, interpretable negative and positive relationships were obtained, respectively, as expected.

After this conceptualization, the IPSL-CM5A-LR model produced increases lower than 6 % in P and E_A for the two RCPs. The exception is RCP 8.5 in the long term, which reached increases of +20 % and +15 % in P and E_A, respectively. Similar P and E_A magnitudes resulted in slight increases in the E_A:P ratio below +2 %, contributing to a gradual increase in Q_T due to the increase in P but a sharp decrease in W_R of between –14 % and –17 %. In the long term, RCP 8.5 significantly increased P (+20 %) and E_A (+15 %). However, the greater difference in P and E_A increased the 1–(E_A:P) ratio by +6 %, resulting in significant increases in Q_T (+27 %) and W_R (+15 %). The NoerESM1-M model produced higher increases in P and E_A, significantly

increasing the 1–(E_A:P) ratio compared with the other two RCMs, reaching +25 % for RCP 8.5 in the long term. Moreover, the NoerESM1-M model increased W_R; the observed W_R increase is two-fold higher than the observed Q_T increase. In fact, the increase in Q_T and W_R for RCP 8.5 in the long term is +76 % and +173 %, respectively. The MIROC model illustrates how the water balance components adjust when P decreases and E_A increases. Regarding the IPSL-CM5A-LR model, the E_A:P ratios are also positive (in the 1–2 % range), but the other water balance components differ substantially. The decrease in P caused a slight decrease in Q_T (between –3% and –6%), but the diminution of W_R was significant at approximately –40 % for RCP 4.5 in the long term.

Table 13. Average annual SWAT water balance components in the PRB after implementing the RCM-RCP 4.5 and 8.5 ensembles for mid- (2040–2069) and long-term (2070–2099) future horizons.

RCM model	Emission scenario	Period	P [a]	E_A [a]	E_A:P [a]	1–(E_A:P) [a]	WYLD [a]	W_R [a]
IPSL-CM5A-LR	Baseline	1976–2005	1091.29	663.57	0.61	0.39	412.23	17.54
	RCP 4.5	2040–2069	1124.11 (+3%)	695.19 (+5%)	0.62 (+2%)	0.38 (-3%)	414.31 (+1%)	14.59 (–17%)
		2070–2099	1143.73 (+5%)	701.92 (+6%)	0.61 (+1%)	0.39 (-1%)	427.89 (+4%)	14.98 (–15%)
	RCP 8.5	2040–2069	1141.76 (+5%)	701.21 (+6%)	0.61 (+1%)	0.39 (-2%)	428.34 (+4%)	15.05 (–14%)
		2070–2099	1309.72 (+20%)	765.56 (+15%)	0.58 (–4%)	0.42 (+6%)	523.92 (+27%)	20.11 (+15%)
MIROC	Baseline	1976–2005	945.32	657.08	0.70	0.30	283.64	4.05
	RCP 4.5	2040–2069	923.21 (–2%)	651.27 (–1%)	0.71 (+1%)	0.29 (-3%)	267.72 (–6%)	3.08 (–24%)
		2070–2099	932.08 (–1%)	660.99 (+1%)	0.71 (+2%)	0.29 (-5%)	267.93 (–6%)	2.44 (–40%)
	RCP 8.5	2040–2069	948.82 (+0.4%)	669.39 (+2%)	0.71 (+1%)	0.29 (-3%)	275.03 (–3%)	2.86 (–29%)
		2070–2099	1052.05 (+11%)	719.31 (+9%)	0.68 (–2%)	0.32 (+4%)	327.44 (+15%)	4.70 (+16%)
NoerESM1-M	Baseline	1976–2005	970.43	628.23	0.65	0.35	332.88	8.62
	RCP 4.5	2040–2069	1160.21 (+20%)	693.67 (+10%)	0.60 (–8%)	0.40 (+14%)	452.19 (+36%)	15.72 (+82%)
		2070–2099	1149.02 (+18%)	697.14 (+11%)	0.61 (–6%)	0.39 (+12%)	436.94 (+31%)	14.09 (+63%)
	RCP 8.5	2040–2069	1197.85 (+23%)	711.10 (+13%)	0.59 (–8%)	0.41 (+15%)	469.32 (+41%)	16.06 (+86%)
		2070–2099	1371.91 (+41%)	765.57 (+22%)	0.56 (–14%)	0.44 (+25%)	585.90 (+76%)	23.54 (+173%)

[a] P—average annual precipitation in mm; E_A—average annual evapotranspiration in mm; E_A:P—evaporative fraction of P as a dimensionless fraction; 1–(E_A:P)—non-evaporative fraction of P as a dimensionless fraction; WYLD—average annual maximum amount of water that can contribute to streamflow and aquifer recharge after discounting transmission losses in mm; and W_R—average annual total aquifer recharge in mm. The percentages of the relative changes in the variables and/or ratios to the corresponding baseline scenarios are given in parentheses.

The distributions of the monthly mean values of the water balance components for the three RCM-RCP 4.5 ensembles and the three RCM- RCP 8.5 ensembles, over the baseline period and the mid- and long- term future horizons, are displayed in Figure 10 and Figure 11, respectively. The variations in monthly W_R are highly dependent on the RCP. For RCP 4.5, W_R decreased conspicuously in the mid and long term, except in the NoerESM1-M model. However, RCP 8.5 revealed a significant increase, especially in the second half of the year. The differences in Q_T and W_R in the NoerESM1-M model increased significantly, especially in the long term. Notwithstanding, the yearly pattern does not differ significantly from the baseline, except in June and July (dry season), as previously identified in monthly variations in temperature and precipitation (climate variables). No significant differences were observed in the average monthly E_A:P and 1–(E_A:P) ratios.

These findings demonstrate a strong positive relationship between P and Q_T. However, W_R variations are predominantly related to the E_A:P and 1–(E_A:P) ratios. This observation supports the rationale that W_R highly depends on the water available after soil and vegetation water demands have been satisfied (Bhunia, 2020); in the case of local soils is high as described above. The logical increases in Q_T for low (below +10 %) increases in P are also corroborated by Q_T increases in the 1–3 % range for every +1 % change in P, as reported globally by Chiew et al. (2006). However, uncertainty propagation in model projections has induced a wide range of aquifer recharge changes, as discussed above and observed by Döll (2009). Notably, small changes in W_R forecasted by Buytaert et al. (2010) in equivalent humid Andean Highland with similar predominant andosols do not align with our results indicating changes ranging from 40 % to +173 %. This disparity is not definitive since it can be attributed to a number of factors, such as the different observation scales used, improvability of RCM models over time, and inadequate W_R estimation as differences in P and E_A when data scarcity prevents E_A estimation using global models (Alcalá et al., 2011; España et al., 2013, 2011; Were et al., 2007).

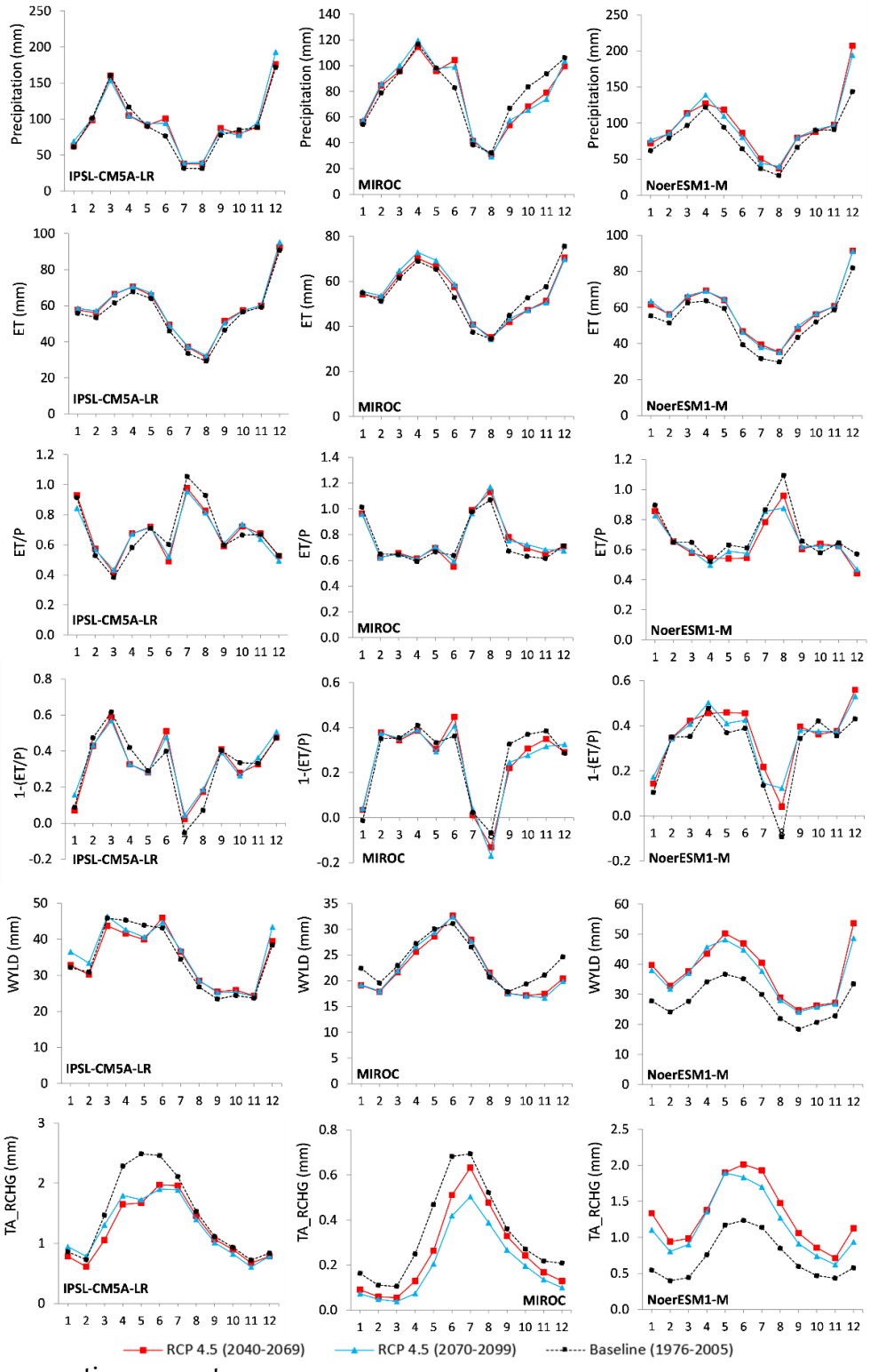

Figure caption on next page.

Figure 10. Distribution of the monthly mean values of the main water balance components predicted by the three RCM-RCP 4.5 ensembles in the PRB for the baseline period (1976–2005) and the mid- (2040–2069) and long-term (2070–2099) future horizons. P—precipitation in mm; E_A (here denoted as ET)—actual evapotranspiration in mm; EA:P (here denoted as ET/P)—evaporative fraction of P as a dimensionless fraction; 1–(E_A:P) (here denoted as 1–[ET/P])—non-evaporative fraction of P as a dimensionless fraction; WYLD—maximum amount of water that can contribute to streamflow and aquifer recharge after discounting transmission losses in mm; and W_R (here denoted as TA_RCHG)—total aquifer recharge in mm. Figure modified and updated from Senent-Aparicio et al. (2024).

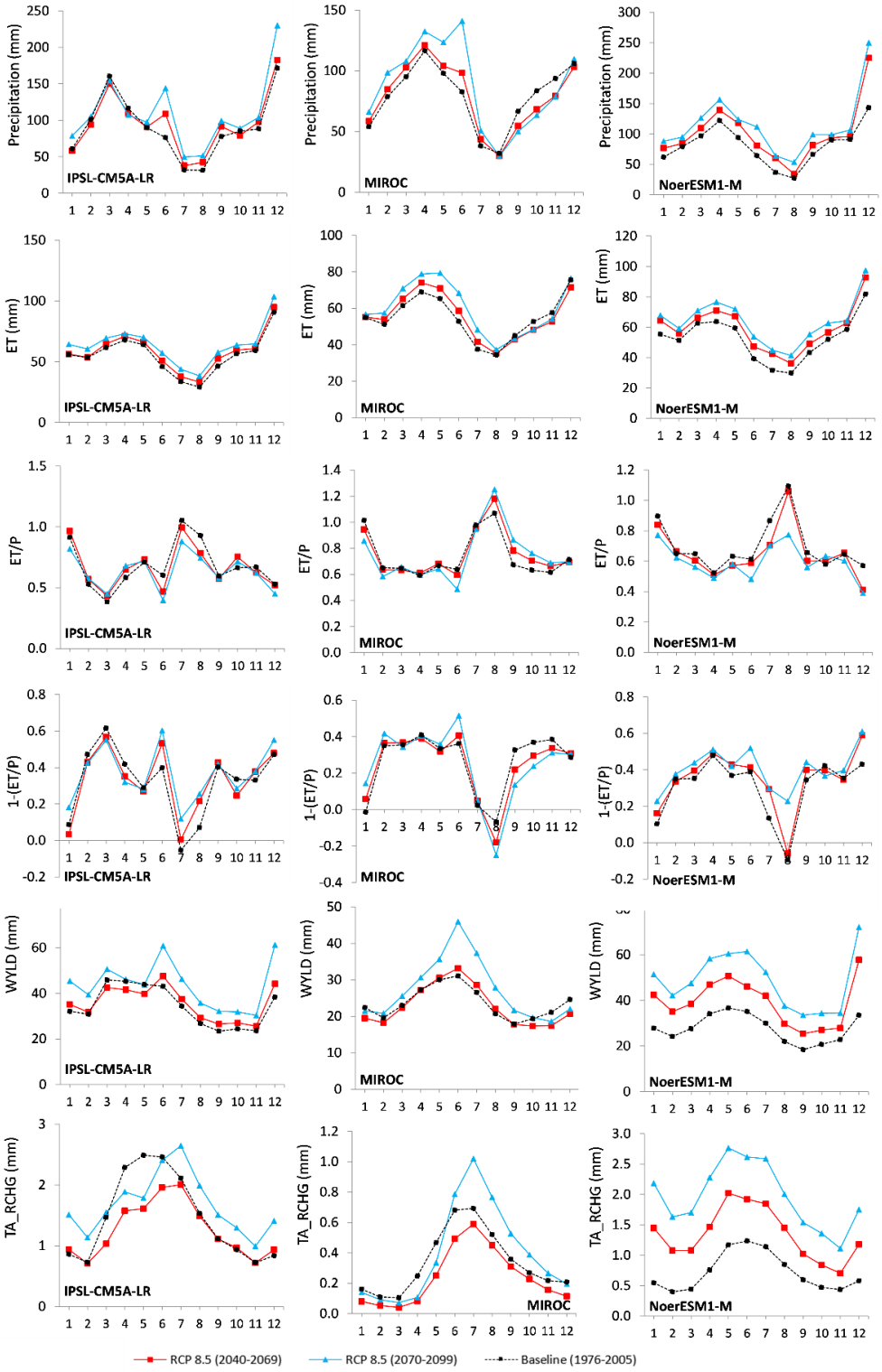

Figure caption on next page.

Figure 11. Distribution of the monthly mean values of the main water balance components predicted by the three RCM-RCP 8.5 ensembles in the PRB for the baseline period (1976–2005) and the mid- (2040–2069) and long-term (2070–2099) future horizons. P—precipitation in mm; E_A (here denoted as ET)—actual evapotranspiration in mm; EA:P (here denoted as ET/P)—evaporative fraction of P as a dimensionless fraction; 1–(E_A:P) (here denoted as 1–[ET/P])—non-evaporative fraction of P as a dimensionless fraction; WYLD—maximum amount of water that can contribute to streamflow and aquifer recharge after discounting transmission losses in mm; and W_R (here denoted as TA_RCHG)—total aquifer recharge in mm. Figure modified and updated from Senent-Aparicio et al. (2024).

5.3.4. Impact of climate change on magnitude, variability and seasonality of the RGR

As indicated in Table 14, Figure 10 and Figure 11, variation in W_R is greater in the wet season (February to May) than in the dry season (July to September), except in the MIROC model. In the IPSL-CM5A-LR and NoerESM1-M models, W_R in the dry season is around 0.7–0.9-fold the observations during the wet season. However, the magnitude of the relative change in W_R in wet and dry seasons differs; the change in the wet season is usually greater than that observed in the dry season. This typical W_R behavior depends on available soil water, as has been documented in other mountainous areas (Alcalá et al., 2011; Were et al., 2007). However, a discrepancy is observed in the MIROC model: the change is between 15 % and 54 % in the wet season and between 9% and +47 % in the dry season. Similarly, the sharp increases in W_R in the NoerESM1-M model are much higher in the wet season than in the dry season. W_R rates are typically low, in the 0.43–8.38 mm range. As described above, null groundwater exploitation in the moderate-permeability volcanic and volcano-sedimentary aquifers in the PRB favors high piezometric levels. Hence the shallow and deep aquifers can be considered virtually full, repelling most recharge events, while most soil water excess percolates downwards and contributes interflow runoff to streamflow in the wet season. Consequently, only a minor fraction of the soil water excess during the wet season produces W_R, delayed, to some extent, when the aquifer marginally empties during the dry season.

Previous studies conducted over a large territory including soils with worse hydraulic conditions (less water storage capacity) in nearby regions (Carvajal et al., 2017) highlight the apparent differences between wet and dry seasons. However,

the results in the PRB (where andosols with better hydraulic conditions predominate) do not diverge as much by season. In fact, soil hydraulics tests performed on degraded and well-preserved andosols (Boulanger et al., 2007; Buytaert et al., 2009) also provide different W_R responses, which diverge from the more similar responses obtained in the implemented RCM-RCP 4.5 and 8.5 ensemble projections. The exception is the NoerESM1-M model projections, which could depend more on specific soil, vegetation cover and climate data for improved results. However, this additional work has been considered beyond the scope of this Thesis.

The influence of the soil preservation state on W_R response appears evident. Alcalá, (2016) used tracer (chemical, stable isotopes and radioisotopes) and physical techniques to evaluate W_R in a close IAV catchment with equivalent binomial of well-preserved andosols over moderate-permeability volcano-sedimentary geological formations (the typical *páramo* ecosystem landscape) to that existing in the PRB. This author demonstrated W_R responses in the three–four-month range after the wet season had ended. Therefore, the soil preservation degree is a determinant for the E_A:P and 1–(E_A:P) ratios and, thus, controls the magnitude and duration of W_R events. Climate change could alter (deteriorate) soil hydraulic properties, as reported by Kumar et al. (2022) and, therefore, current surface water–groundwater dynamics in the andosol-dominated Andean Highland, resulting in less soil water storage capacity, more rapid runoff responses and prolonged water-deficit periods.

The magnitude and variability of water resources are critical for conserving natural biodiversity and the stability of aquatic environments (Pérez-Sánchez et al., 2020). The indicators of hydrological alteration included in the IAHRIS (IndicAtors of Hydrological alteration in RIverS) software (Fernández et al., 2012), specific for the evaluation of the alteration of the natural regime of a river in non-coetaneous series, have been used to evaluate the impact of climate change on the magnitude, variability and seasonality of the RGR in the PRB. These indexes are (1) Mean value of the annual volumes (Mean); (2) Extreme variability (EV), which is calculated as the average value of the difference between the maximum and minimum monthly discharge for each year; (3) Difference between the daily mean flows corresponding to the 10th (Q10) and 90th (Q90) percentiles; and (4) Maximum/minimum relative

frequency of the month (MaxRF/MinRF). As shown in Table 15, there is no significant overall increase in annual flows except in the long term and under the scenario RCP 8.5. Only the RCM Model NoerESM1-M estimates significant increases in annual flows in the short and long terms and for RCP 4.5 and 8.5. However, there is a wider consensus in estimating an increase in flow variability. For example, all models estimate that the extreme variability may almost double in the long term and under the RCP 8.5 scenario. It is important to note that this increase in variability can significantly affect the geomorphological and ecological dynamics of the river and thus the diversity of the river (López-Ballesteros et al., 2020). Accordingly, variability based on the 10th and 90th percentiles will also increase, although to a more limited extent than extreme variability.

The seasonality in which maximum and minimum flows occur in a river is an aspect that is closely and synchronously linked to the life cycles of the species (Ngor et al., 2018). As can be seen in Table 16, climate change can significantly affect these life cycles. A delay is observed in the MaxRF, with respect to the maximums that tend to occur in the month of May and which in the future will occur more frequently in June. An increase in the frequency of these MaxRFs is also observed in December. Regarding the MinRFs, all models coincide in concentrating these MinRFs during the months of September-November. There is a clear tendency to delay the occurrence of these minimum values from September to November.

Table 14. Seasonal distribution of predicted total aquifer recharge (W_R) in the PRB after implementing the RCM-RCP 4.5 and 8.5 ensembles for mid- (2040–2069) and long-term (2070–2099) future horizons.

RCM model	Emission scenario	Period	W_R [a]	W_R, wet season fraction [a]	W_R, dry season fraction [a]
IPSL-CM5A-LR	Baseline	1976–2005	17.54	6.97	4.76
	RCP 4.5	2040–2069	14.59 (–17%)	4.99 (–28%)	4.49 (–6%)
		2070–2099	14.98 (–15%)	5.61 (–19%)	4.30 (–10%)
	RCP 8.5	2040–2069	15.05 (–14%)	4.93 (–29%)	4.61 (–3%)
		2070–2099	20.11 (+15%)	6.35 (–9%)	6.14 (+29%)
MIROC	Baseline	1976–2005	4.05	0.93	1.57
	RCP 4.5	2040–2069	3.08 (–24%)	0.51 (–46%)	1.44 (–9%)
		2070–2099	2.44 (–40%)	0.79 (–15%)	1.16 (–26%)
	RCP 8.5	2040–2069	2.86 (–29%)	0.43 (–54%)	1.35 (–14%)
		2070–2099	4.70 (+16%)	0.61 (–35%)	2.31 (+47%)
NoerESM1-M	Baseline	1976–2005	8.62	2.77	2.58
	RCP 4.5	2040–2069	15.72 (+82%)	5.21 (+88%)	4.47 (+73%)
		2070–2099	14.09 (+63%)	4.96 (+79%)	3.88 (+50%)
	RCP 8.5	2040–2069	16.06 (+86%)	5.65 (+104%)	4.32 (+67%)
		2070–2099	23.54 (+173%)	8.38 (+203%)	6.13 (+137%)

[a] Values of W_R in mm. Changes are expressed as positive or negative absolute (in the same unit as the variable) and relative (percentages in parentheses) differences.

Table 15. Quantification of the impact of climate change on the magnitude and variability.

Parameter	RCM model	Baseline (1976–2005)	RCP 4.5 (2040–2069)	RCP 4.5 (2070–2099)	RCP 8.5 (2040–2069)	RCP 8.5 (2070–2099)
Mean, Mm^3	IPSL-CM5A-LR	74.37	74.01	76.47	76.88	93.23
	MIROC	50.57	47.63	47.88	48.79	58.47
	NoerESM1-M	59.51	81.23	78.39	83.60	105.51
EV, Mm^3	IPSL-CM5A-LR	5.13	4.94	5.58	5.15	7.74
	MIROC	2.66	2.92	3.06	3.07	4.98
	NoerESM1-M	4.36	6.84	5.90	6.88	8.26
Q10%, $m^3\ s^{-1}$	IPSL-CM5A-LR	3.33	3.15	3.33	3.31	4.08
	MIROC	2.05	2.03	2.07	2.10	2.67
	NoerESM1-M	2.52	3.60	3.48	3.71	4.75
Q90%, $m^3\ s^{-1}$	IPSL-CM5A-LR	1.53	1.63	1.63	1.71	2.03
	MIROC	1.22	1.13	1.11	1.14	1.28
	NoerESM1-M	1.29	1.67	1.65	1.71	2.19

Table 16. Quantification of the impact of climate change on the seasonality.

Parameter	RCM model	Emission scenario	Jan	Feb	Mar	Apr	May	Jun	Jul	Aug	Sep	Oct	Nov	Dec
Max RF	IPSL-CM5A-LR	Baseline (1976-2005)	0.00	0.00	0.38	0.10	0.14	0.21	0.00	0.00	0.00	0.00	0.00	0.17
		RCP 4.5 (2040-2069)	0.03	0.00	0.21	0.07	0.00	0.45	0.00	0.00	0.00	0.00	0.00	0.24
		RCP 4.5 (2070-2099)	0.00	0.00	0.38	0.03	0.00	0.24	0.00	0.00	0.00	0.00	0.00	0.34
		RCP 8.5 (2040-2069)	0.00	0.03	0.10	0.14	0.03	0.45	0.00	0.00	0.00	0.00	0.00	0.24
		RCP 8.5 (2070-2099)	0.03	0.03	0.14	0.00	0.00	0.45	0.00	0.00	0.00	0.00	0.00	0.34
	MIROC	Baseline (1976-2005)	0.00	0.00	0.00	0.00	0.38	0.59	0.03	0.00	0.00	0.00	0.00	0.00
		RCP 4.5 (2040-2069)	0.00	0.00	0.00	0.00	0.10	0.90	0.00	0.00	0.00	0.00	0.00	0.00
		RCP 4.5 (2070-2099)	0.00	0.00	0.00	0.00	0.24	0.76	0.00	0.00	0.00	0.00	0.00	0.00
		RCP 8.5 (2040-2069)	0.00	0.00	0.00	0.00	0.28	0.72	0.00	0.00	0.00	0.00	0.00	0.00
		RCP 8.5 (2070-2099)	0.00	0.00	0.00	0.00	0.38	0.59	0.03	0.00	0.00	0.00	0.00	0.00
	NoerESM1-M	Baseline (1976-2005)	0.00	0.00	0.00	0.14	0.41	0.21	0.07	0.00	0.00	0.00	0.00	0.17
		RCP 4.5 (2040-2069)	0.07	0.00	0.00	0.03	0.28	0.14	0.00	0.00	0.00	0.00	0.00	0.48
		RCP 4.5 (2070-2099)	0.03	0.00	0.00	0.24	0.17	0.21	0.00	0.00	0.00	0.00	0.00	0.34
		RCP 8.5 (2040-2069)	0.03	0.00	0.00	0.10	0.21	0.10	0.07	0.00	0.00	0.00	0.00	0.48
		RCP 8.5 (2070-2099)	0.00	0.00	0.00	0.07	0.07	0.21	0.03	0.00	0.00	0.00	0.00	0.62
Min RF	IPSL-CM5A-LR	Baseline (1976-2005)	0.03	0.14	0.00	0.00	0.00	0.00	0.00	0.03	0.28	0.21	0.31	0.00
		RCP 4.5 (2040-2069)	0.07	0.10	0.00	0.00	0.00	0.00	0.00	0.03	0.10	0.14	0.55	0.00
		RCP 4.5 (2070-2099)	0.03	0.03	0.00	0.00	0.00	0.00	0.00	0.00	0.31	0.21	0.41	0.00
		RCP 8.5 (2040-2069)	0.03	0.10	0.00	0.00	0.03	0.00	0.00	0.03	0.31	0.07	0.41	0.00
		RCP 8.5 (2070-2099)	0.03	0.07	0.00	0.07	0.00	0.00	0.00	0.03	0.10	0.24	0.45	0.00
	MIROC	Baseline (1976-2005)	0.00	0.28	0.00	0.00	0.00	0.00	0.00	0.00	0.66	0.03	0.03	0.00
		RCP 4.5 (2040-2069)	0.00	0.28	0.00	0.00	0.00	0.00	0.00	0.00	0.24	0.24	0.24	0.00
		RCP 4.5 (2070-2099)	0.00	0.17	0.00	0.00	0.00	0.00	0.00	0.00	0.10	0.31	0.41	0.00
		RCP 8.5 (2040-2069)	0.07	0.17	0.00	0.00	0.00	0.00	0.00	0.00	0.21	0.28	0.28	0.00
		RCP 8.5 (2070-2099)	0.00	0.28	0.00	0.00	0.00	0.00	0.00	0.00	0.66	0.03	0.03	0.00

Continued on next page.

NoerESM1-M	Baseline (1976-2005)	0.00	0.03	0.00	0.00	0.00	0.00	0.00	0.00	0.90	0.07	0.00	0.00
	RCP 4.5 (2040-2069)	0.00	0.07	0.00	0.00	0.00	0.00	0.00	0.00	0.69	0.10	0.14	0.00
	RCP 4.5 (2070-2099)	0.00	0.07	0.00	0.00	0.00	0.00	0.00	0.03	0.76	0.03	0.10	0.00
	RCP 8.5 (2040-2069)	0.00	0.03	0.00	0.00	0.00	0.00	0.00	0.07	0.66	0.10	0.14	0.00
	RCP 8.5 (2070-2099)	0.00	0.00	0.00	0.00	0.00	0.00	0.00	0.17	0.28	0.21	0.34	0.00

5.4. HYDROGEOLOGICAL FUNCTIONING AND GROUNDWATER DYNAMICS IN THE PRB

5.4.1. Findings from chemical, stable isotope and radioisotope tracing

This section used hydrochemistry and isotope data generated in two international R&D projects (Larrea et al., 2016; Alcalá, 2016) developed in 2014–2015. Hydrochemistry and isotope data from selected water points were expressed as average weighed values over the control period February–August 2015, which was chosen based on having suitable spatial data density and covering the main hydrogeological processes. Weighting was done by (i) precipitation volume of the atmospheric bulk deposition samples collected in two open collectors installed at Bocatoma (W4) and Mudadero (W6) weather stations, (ii) groundwater discharge flow measured in springs S1 to S4 from the shallow aquifer and springs D1 to D7 from the deep aquifer, and (iii) streamflow measured along the Pita River at Bocatoma (Q5), Proaño (Q4) and Mudadero (Q2) stream-gauging stations (Figure 12a). All water points were bimonthly sampled. Table 17 summarizes the average weighed hydrochemistry and isotope results.

The waters initially associated to the current renewable dynamic from atmospheric bulk deposition, Pita River course (surface-water) and shallow springs are mainly of the Ca-Mg-HCO_3 type; the waters initially associated to a low to very low renewability from deep springs being of the Ca-Mg-Cl-SO_4 type. Below, the description of results is focused on the rCl/rBr molar ratio, water-stable isotope $\delta^{18}O$, radioisotope ^{3}H, stable isotope $\delta^{13}C$, and radioisotope ^{14}C, with additional remarks on DIC and molar ratios rCl/rSO_4, rNa/rK, rNa/rLi, rMg/rCa and rCl/rHCO_3.

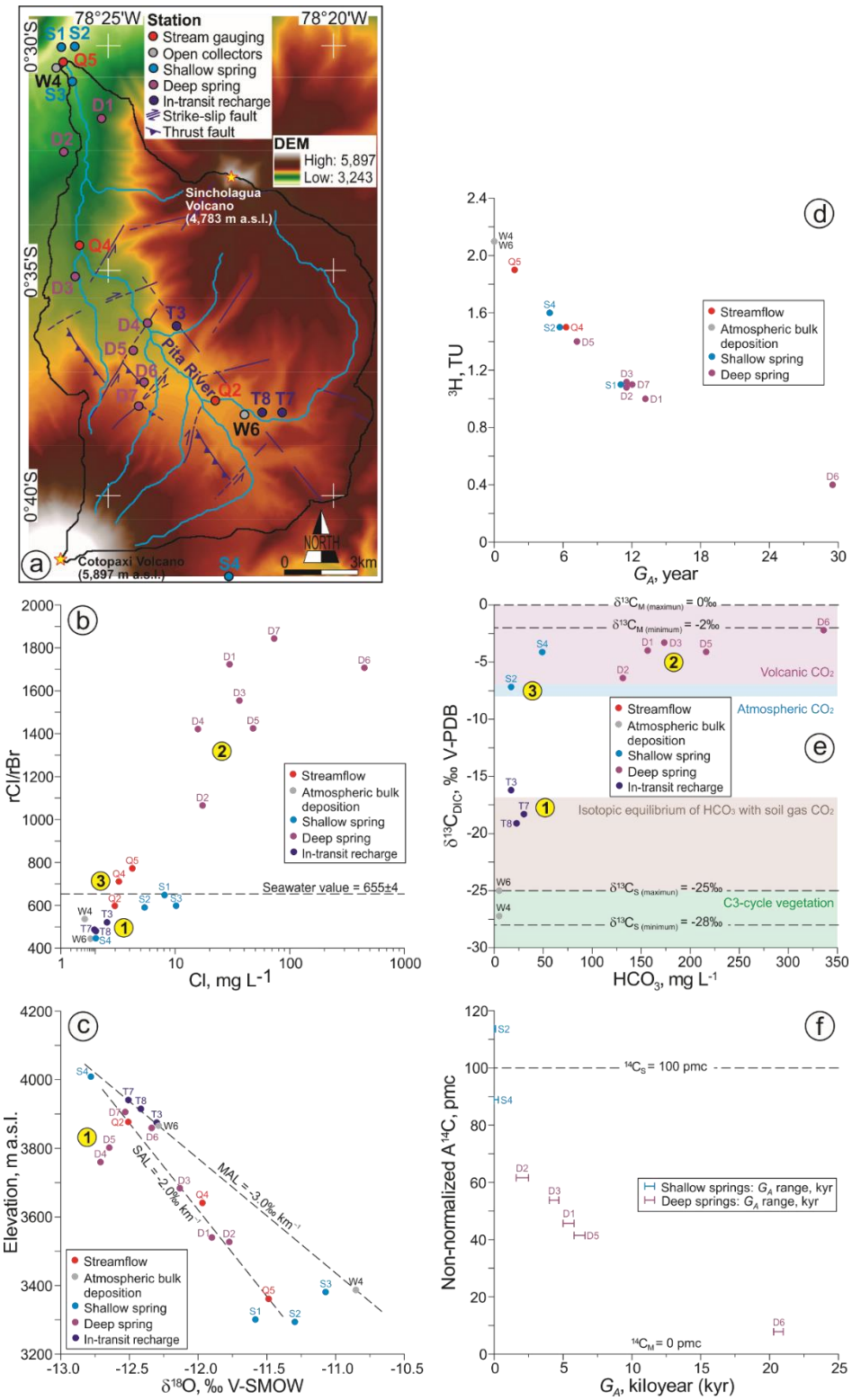

Figure caption on next page.

Figure 12. (a) Classification and location of the selected water points over a 30-m-resolution DEM of the PRB (Figure 1b) with the main geological structures overlapped (Figure 1c). (b) rCl/rBr molar ratio vs. chloride content in mg L–1; 1—water points with predominant atmospheric chloride, 2—water points with volcanic contribution of halides, and 3—streamflow revealing a mixture of chloride from atmospheric sources and volcanic halides. (c) δ18O referred to the V-SMOW standard in ‰ vs. elevation in m a.s.l.; MAL—meteoric altitudinal line, SAL—streamflow altitudinal line, and 1—high-elevation recharge water points. (d) 3H content in tritium units (TU) vs. calculated water age (GA) in year. (e) δ13CDIC referred to the V-PDB standard in ‰ vs. HCO3 (DIC) in mg L–1, indicating sources of CO2 after Mook (2001); 1—in-transit recharge usually contributing to interflow runoff, 2—water points with volcanic CO2, and 3—shallow discharge contributing to streamflow. (f) Non-normalized 14C activity (A14C) in percent modern carbon (pmc) vs. calculated conventional age (GA) in kiloyear (kyr). For (b) throughout (f), the values correspond to the average weighed hydrochemistry and isotope content calculated over the control period February–August 2015, as reported in Table 17.

The rCl/rBr ratio was used to identify the origin of salinity in groundwater and surface-water. This ratio is quite conservative during the hydrogeological processes, so it behaves an ideal chemical tracer (Davis et al., 2004; Alcalá and Custodio, 2008a). In the ocean, wind-generated aerosols preserve the seawater rCl/rBr ratio around 655±5, and decreases in continental atmospheric bulk deposition in the range of 100–600, with a decreasing trend along the wind path (Butler et al., 2007; Alcalá and Custodio, 2008a; Alcalá et al., 2015). Volcanism is a source of halide emissions to the atmosphere and directly into groundwater. The volcanic degassing produces volatile Cl and Br compounds. In general Cl is released more easily than Br, thus being able to increase the rCl/rBr ratio up to 2000 (Aiuppa et al., 2005; Schaefer and Fegley, 2005; Alcalá and Custodio, 2008a; Marrero et al., 2015). In the PRB (Figure 12b; Table 17), the rCl/rBr ratio in atmospheric bulk deposition lightly decreased with elevation from 536 at W4 (3,387 m a.s.l.) to 445 at W6 (3,866 m a.s.l.). This decreasing trend was also observed in shallow springs, passing from 648 in S1 (3,301 m a.s.l.) to 447 in S4 (4,009 m a.s.l.), thus showing that shallow springs discharge is associated to local recharge areas. The rCl/rBr ratio was in the 1066–1844 range in deep springs D1 to D7. The deep springs integrate shallow and deep groundwater flow paths, so their discharges represent a variable mixture of modern (recent, contemporaneous) shallow groundwater with low (but not always negligible) volcanic influence and old deep groundwater with prolonged water-rock interaction and evident contribution of

volcanic halides, as described below. The progressive discharge of deep groundwater to the baseflow tends to increase the rCl/rBr ratio in streamflow from 598 at Q2 (Highland) to 773 at Q5 (PRB outlet) (Figure 12b).

The molar ratios rCl/rSO_4, rNa/rK, rNa/rLi and rMg/rCa (Table 17) corroborated the sources of salinity identified with the rCl/rBr molar ratio. Shallow springs S1 to S4 showed similar ratios to that of the atmospheric bulk deposition, evidencing low volcanic influence and low-temperature weathering of volcanic rocks. Regarding the atmospheric values, deep springs showed lower rCl/rSO_4, rNa/rLi and rMg/rCa ratios, and higher rNa/rK ratios. These values are associated to a variable influence of volcanic SO_4 emanations and volcanic rock weathering over a prolonged water-rock interaction in deep high-temperature layers, thus inducing neoformation of Ca- and K-rich minerals and excess of Na, Li and Mg (Schaefer and Fegley, 2005; Vengosh et al., 2007; Urrutia et al., 2022).

In atmospheric bulk deposition, $\delta^{18}O$ decreased with elevation from -10.9‰ at W4 to -12.5‰ at W6, with an altitudinal $\delta^{18}O$ gradient of -3.0‰ km^{-1} (Figure 12c). The associated meteoric altitudinal line (MAL) allowed to identify the specific elevation for recharge contributing to local springs, as well as those springs whose discharge integrates high- and low-elevation recharge (Figure 12c). In the PRB, local springs are located at summit areas and provided $\delta^{18}O$ signatures close to the MAL, whereas the $\delta^{18}O$ signatures of large springs discharging at mid-slope and low-lying areas appeared variably deviated toward more negative values (lighter $\delta^{18}O$ signatures) (Figure 12c). This behaviour is more evident in the shallow springs D2 and D3 and deep springs D4 and D5, whose discharge integrates high- and low-elevation recharge produced along the north-western versant of the Sincholagua Volcano and the northern versant of the Cotopaxi Volcano, respectively (Figure 12a). The $\delta^{18}O$ signature in streamflow decreased with elevation from -11.5‰ at Q5 to -12.6‰ at Q2, with an altitudinal $\delta^{18}O$ gradient of -2.3‰ km^{-1} (Figure 12c). The streamflow altitudinal line is located between the MAL and the lighter $\delta^{18}O$ signatures of those shallow and deep springs that integrates high- and low-elevation recharge, thus verifying the contribution of Q_u with a meteoric $\delta^{18}O$ signature and groundwater discharge with lighter $\delta^{18}O$ signatures.

The deuterium excess (d) was used to discern the atmospheric water vapor sources in the PRB. It is well known the good linear correlation between $\delta^{2}H$ and

$\delta^{18}O$ for meteoric water, which can be expressed as $\delta^{2}H=a\delta^{18}O+b$ (Araguás-Araguás et al., 2000; Rozanski et al., 1993; Cartwright et al., 2006). For values in ‰, the classic a=8.0 and b=10‰ for modern average global precipitation were considered to define $d=\delta^{2}H-8\delta^{18}O$, which enables to identify the atmospheric water vapor sources from the Atlantic Ocean with d > 10‰ and Pacific Ocean with d < 10‰ (Mook, 2001). In atmospheric bulk deposition d values increased with elevation from 9.7‰ at W4 to 10.2‰ at W6 (Table 17). One shallow (S1) and five deep springs (D1, D2, D3 and D7) showed d values in the 8.7–10.1‰ range, and three shallow (S2, S3 and S4) and two deep (D4 and D5) springs showed d values in the 10.8–12.8‰ range due to higher influence of Atlantic Ocean sources at high-elevation recharge areas. The d values increased in streamflow with elevation from 10.2‰ at Q5 to 11.0‰ at Q2. At station Q5, d values can be explained through the double contribution of Q_U with meteoric d values and groundwater discharge with higher d values.

All water points sampled to determine tritium had ^{3}H contents in the 0.4–2.1 TU range (Figure 12d). The ^{3}H content in atmospheric bulk deposition was 2.1 TU at W4 and W6 (Figure 12d). The measured ^{3}H content (C_m) was 1.4–1.6 TU in shallow springs S2 and S4 and deep spring D5, 1.0–1.1 TU in shallow spring S1 and deep springs D1, D2, D3 and D7, and 0.4 TU in deep spring D6, thus giving average groundwater ages (G_A) of 4.8–7.2 years, 11.5–13.2 years, and 29.5 years, respectively. Thus, discharge from shallow and deep springs includes a fraction of modern groundwater recharged after the thermonuclear bomb pulse in the 1950s and 1960s (Mook, 2001). In the PRB, in-transit diffuse aquifer recharge percolates through an unsaturated zone several tens of meters thick before reaching the saturated zone. Thus, a fraction of the ^{3}H decreasing content can be explained by simple decay after several months to some years of transit time through the unsaturated zone. In the saturated zone, the groundwater moves towards the discharge points, increasing its age. Groundwater discharge consists of a mixture of flow paths with a wide range of transit times in macroscopically unconfined aquifers. In streamflow, the ^{3}H content was 1.9 TU (1.8 years) at station Q5 and 1.5 TU (6.0 years) at station Q4, which is similar to the 1.4 TU (7.2 years) measured in deep spring D5. According to the SWAT model evaluation described in Section V.2 and the additional remarks on calibrated parameters included in Sections B.2 and B.3 in Appendix B, the circulation time of Q_U through the main channel is 1–2 months, so the ^{3}H content in Q_U would decay 0.01–0.02 TU at most. This range is

less than the determination error of ±0.1 TU. Therefore, the mixing of Q_U (with similar ^3H content to that of atmospheric bulk deposition) and groundwater discharge (with ^3H content similar to that of deep spring D5) can justify the ^3H content in streamflow at station Q5. These findings corroborated the existence of two water sources: modern RGR associated with current climate cycles and old groundwater not generated nor substantially influenced by these cycles.

In atmospheric bulk deposition, $\delta^{13}C_{DIC}$ increased with elevation from -27.2‰ at station W4 to -25.0‰ at station W6 (Figure 12e; Table 17), with an altitudinal $\delta^{13}C_{DIC}$ gradient of -4.0‰ km^{-1}. These $\delta^{13}C_{DIC}$ signatures differed from the atmospheric CO_2 (around -8‰) but agreed with the signature of biogenic soil gas CO_2 derived from C3-cycle vegetation (Bender, 1971; Deines, 1980). The $\delta^{13}C_S$ range adopted for ^{14}C data correction was -28‰ to -25‰. The $\delta^{13}C_{DIC}$ values of some in-transit recharge water sampled at the boundary between natural andosols and volcanic formations near to the sites T3, T7 and T8 used for soil hydraulic tests (Figure 1d; Table 4; Table 5) ranged from -19‰ to -16‰ (Alcalá, 2006). These values showed an apparent isotopic equilibrium of HCO_3 with biogenic soil CO_2. The only six analysed shallow and deep springs showed $\delta^{13}C_{DIC}$ values ($^{13}C_m$) ranging from -7.2‰ to -2.2‰ (Figure 12e; Table 17). These values indicated that DIC is enriched (become heavier) in $\delta^{13}C$ regarding the expected values for isotopic equilibriums of sole biogenic soil CO_2 and dissolved HCO_3. Since outcropping volcanic formations do not include carbonate minerals, the explanation is a mixture of biogenic soil CO_2 and volcanic CO_2 influenced by remobilization and high-temperature decomposition of crustal carbon, as other authors (Tassi et al., 2010, 2011); Mason et al., 2017; de Moor et al., 2017; Battaglia et al., 2018) suggested to explain $\delta^{13}C_{DIC}$ values ranging from -9‰ to -1‰ in equivalent arc volcanic areas. In the IAV, deep Cretaceous limestones underlying the Pliocene to Quaternary volcanic and volcano-sedimentary formations have been documented (Feininger and Seguin, 1983; Litherland et al., 1994; Hughes and Pilatasig, 2002; Burbano et al., 2015). $\delta^{13}C_M$ range adopted for ^{14}C data correction was -2‰ to 0‰.

The $rCl/rHCO_3$ molar ratio was used to discriminate the dominant species of DIC in this active volcanic area. In the ocean and coastal areas, the $rCl/rHCO_3$ ratio is 235±15 and decrease in continental areas according to the decreasing trend of Cl in atmospheric bulk deposition along the wind path and natural sources of HCO_3.

Lithology and volcanism degassing determine pH and dissolved CO_2 in groundwater (Mook, 2001; Urrutia et al., 2022). In general, HCO_3 is the dominant species of DIC in fresh groundwater with pH in the 7.0–8.5 range, thus giving $rCl/rHCO_3$ ratios around or lower than the atmospheric values. Volcanism is a source of Cl emanations and CO_2 degassing into groundwater. This means that the $rCl/rHCO_3$ ratio can increase regarding the atmospheric values when the Cl emanations are significant. In the PRB, the $rCl/rHCO_3$ ratio in atmospheric bulk deposition increased with elevation from 0.29 at W4 to 0.36 at W6 (Table 17). The shallow aquifer springs S1 to S4 showed $rCl/rHCO_3$ ratios in the 0.04–0.20 range, pH of 6.5–8.1, and DIC of 20–120 mg L^{-1} originated mostly from atmospheric CO_2 dissolution in equilibrium with water. Deep springs showed $rCl/rHCO_3$ ratios in the 0.23–0.36 (D1 to D4) and 0.56–1.24 (D5 to D7) ranges, pH of 6.4–8.6, and DIC of 140–250 mg L^{-1} in D1–D4 and 220–630 mg L^{-1} in D5–D7, the latest ones more clearly affected by additional CO_2 sources, such as magma degassing. The progressive groundwater discharge tends to increase the $rCl/rHCO_3$ ratio in streamflow from 0.58 at station Q2 to 0.85 at station Q5. As found for ^3H, these figures also identified the DIC of 85 mg L^{-1} at Q5 as the result of a mixture of Q_U and groundwater discharge.

Radiocarbon (^{14}C) activity ($A^{14}C$) was measured in two shallow and four deep spring waters to calculate G_A. For ^{14}C data correction, (i) the factor f' was applied to revert the reported normalized $A^{14}C$ values into non-normalized ones; and (ii) the correction factor f'' was used to solve the binary mixing model with end members $\delta^{13}C_S$ ranging from -28‰ to -25‰, $\delta^{13}C_M$ ranging from -2‰ to 0‰, $^{14}C_S$ = 100 pmc, and $^{14}C_M$ = 0 pmc; the last two as reported by Mook (2001). Since past atmospheric ^{14}C was not considered in correction, the G_A values corresponded to conventional ages instead of corrected ones. In what follows, $A^{14}C$ data and G_A are referred to non-normalized activities and conventional ages, respectively. The $A^{14}C$ values were in the 88.9–113.7 pmc range in shallow springs and between 7.8 and 61.6 pmc in deep springs (Figure 12f; Table 17). The volcanic CO_2 degassing was reflected in water points with low $A^{14}C$ and high DIC, such as in deep springs D5 (41.5 pmc $A^{14}C$ and 220.6 mg L^{-1} DIC) and D6 (7.8 pmc $A^{14}C$ and 336.0 mg L^{-1} DIC). A typical negative relationship between DIC and $A^{14}C$ was observed (Figure 12f). The other shallow and deep springs showed higher $A^{14}C$ and lower DIC values, thus identifying less contribution of volcanic CO_2. Cretaceous limestones underlying the

Pliocene to Quaternary volcanic and volcano-sedimentary formations (Feininger and Seguin, 1983; Litherland et al., 1994; Hughes and Pilatasig, 2002; Burbano et al., 2015) was considered the prime source of dead carbon in volcanic CO_2. Discharge from shallow springs D2 (113.7 pmc $A^{14}C$, 17.1 mg L^{-1} DIC, and 7.5 pH), located at the northern versant of the inactive Sincholagua Volcano, and D4 (88.9 pmc $A^{14}C$, 49.0 mg L^{-1} DIC, and 8.2 pH), located at the eastern versant of the active Cotopaxi Volcano, was considered modern water with G_A of 0–0.1 kiloyears (kyr) and 0–0.3 kyr, respectively. In deep springs, G_A was 1.6–5.8 kyr in D1–D3, 5.8–6.6 kyr in D5, and 20.3–21.0 kyr in D6 (Figure 12f). These waters are clearly disconnected from current climate cycles. Normalized and non-normalized $A^{14}C$ data, correction factors f' and f'', and G_A values are included in Table 17.

The multiple processes affecting the sampled waters in a heterogeneous system make the estimation of G_A a difficult and uncertain task to find additional trends and features. However, these figures corroborate that spring discharge integrates modern (current) and old groundwater. Thus, they are likely explained by the mixing of waters from different depths and ages. Since all sampled water points have measurable ^3H contents, the contribution of old groundwater can be assumed much minor than modern groundwater. Old groundwater with renewal time of several millennia agrees with large low-yielding aquifers and low recharge rates. The low recharge rates estimated with SWAT model (Table 8) corroborates a part of this assertion, the relative ones to thickness and yielding of deep aquifers remain unknown, although they can be supposed high (hundreds of meters, even some thousands) and low (lower than 0.01), respectively, as deduced in next section.

Table 17. Hydrochemistry and isotope data from representative water points selected to identify the sources of groundwater salinity, identify the existence of shallow and deep aquifers, and calculate average groundwater ages in the PRB. Data are expressed as average weighed values over the control period February–August 2015.

ID	Name	Coordinates		Elevation, m a.s.l.	Water flow [a]			Chemicals [b]								Stable isotopes [c]				Radioisotopes and groundwater age [d]						
		Latitude	Longitude		*P*	*Q*	*D*	Cl	DIC	rCl/rBr	rCl/rSO_4	$rCl/rHCO_3$	rNa/rLi	rNa/rK	rCa/rMg	$\delta^{18}O$	$\delta^{2}H$	d-excess	$\delta^{13}C$	^{3}H	G_A (^{3}H)	$A^{14}Cn$	*f'*	*f''*	$A^{14}Cnn$	G_A (^{14}C)
W4	Bocatoma	0°29'49"S	78°26'17"W	3387	856			1.4	5.0	536	0.84	0.29		6.60	2.99	-10.9	-77.1	9.7	-27.2	2.1						
W6	Mudadero	0°37'01"S	78°24'07"W	3866	425			1.8	5.0	445	1.11	0.36		3.65	1.37	-12.3	-87.9	10.5	-25.0	2.1						
Q2	Mudadero 2	0°37'19"S	78°22'60"W	3877		2.56		3.0	61.0	598	1.27	0.58	159.5	4.74	0.81	-12.5	-89.1	10.9								
Q4	Proaño	0°33'60"S	78°25'44"W	3641		2.28		3.2	76.3	711	0.58	0.72	191.5	6.74	1.67	-12.0	-85.2	10.5		1.5	6.0					
Q5	Bocatoma	0°29'48"S	78°26'08"W	3361		0.89		4.2	73.1	773	0.54	0.85	296.2	7.02	2.78	-11.5	-81.7	10.2		1.9	1.8					
S1	El Salto	0°29'02"S	78°26'17"W	3301			3.0	8.1	124.0	648	0.64	0.11	401.7	7.30	1.47	-11.6	-82.5	10.1		1.1	11.5					
S2	Santa Rita	0°29'02"S	78°25'60"W	3294			0.5	5.4	17.3	590	0.73	0.04	127.8	5.36	1.21	-11.3	-79.6	10.8	-7.2	1.5	6.0	109.6	1.04	0.19–0.29	113.7	0–0.1
S3	Bocatoma	0°29'49"S	78°26'09"W	3381			0.5	10.2	101.4	598	1.09	0.20	316.7	6.36	1.30	-11.1	-76.9	11.6								
S4	Chirimachay	0°41'27"S	78°2228"W	4009			450.1	2.0	49.0	447	1.01	0.08	150.2	5.75	1.08	-12.8	-90.2	12.1	-4.1	1.6	4.8	85.2	1.04	0.08–0.16	88.9	0–0.3
D1	Panzapamba	0°31'03"S	78°25'18"W	3540			1.5	29.8	156.5	1723	0.52	0.33	277.8	11.82	0.84	-11.9	-86.3	8.9	-4.0	1.0	13.2	43.8	1.04	0.08–0.16	45.7	5.0–5.8
D2	Panzatilin	0°31'47"S	78°26'13"W	3527			2.7	17.3	131.2	1066	0.47	0.23	371.7	9.11	1.98	-11.8	-85.1	9.0	-6.4	1.1	11.5	59.3	1.04	0.17–0.26	61.6	1.6–2.5
D3	Proaño	0°34'31"S	78°25'55"W	3683			0.4	36.4	173.4	1555	0.48	0.36	280.9	25.95	0.80	-12.1	-88.4	8.7	-3.3	1.1	11.5	51.4	1.05	0.05–0.13	53.8	4.0–4.7
D4	Salitre	0°35'32"S	78°24'24"W	3760			0.5	15.8	243.1	1422	0.57	0.28	263.4	15.57	1.00	-12.7	-89.0	12.7								
D5	Chilcahuaico	0°36'13"S	78°24'30"W	3802			462.3	47.8	216.1	1425	0.49	0.56	130.1	17.90	0.69	-12.6	-88.4	12.8	-4.1	1.4	7.2	39.8	1.04	0.08–0.16	41.5	5.8–6.6
D6	Lindoloma	0°36'38"S	78°24'26"W	3859			0.4	447.8	336.0	1707	0.62	1.74	173.7	26.59	0.06	-12.3	-89.5	9.2	-2.2	0.4	29.5	7.5	1.05	0.01–0.09	7.8	20.3–21.0
D7	Rinconada	0°37'16"S	78°24'29"W	3906			3.2	73.1	278.0	1844	0.45	0.83	136.5	18.58	0.49	-12.5	-90.8	9.4		1.1	11.5					
T3	ITR	0°35'41"S	78°23'48"W	3875				2.5	17.3	521	0.79	0.27		8.73	1.40	-12.3	-88.4	10.1	-16.2							
T7	ITR	0°37'36"S	78°21'24"W	3941				2.0	30.3	487	1.02	0.11		6.21	1.74	-12.5	-89.4	10.6	-18.3							
T8	ITR	0°37'36"S	78°21'49"W	3915				2.1	22.8	479	0.97	0.08		5.62	1.83	-12.4	-88.7	10.6	-19.1							

ID and location of atmospheric bulk deposition collectors W4 and W6, stream gauging stations Q2, Q4 and Q5, shallow springs S1–S4 and deep springs D1–D7, and in-transit recharge (ITR) measured at sites T3, T7 and T8 as in Figure 12a.

[a] P—precipitation in mm $year^{-1}$, Q—average streamflow in m^3 s^{-1}, and D—average spring discharge flow in L s^{-1}.

[b] Cl and DIC in mg L^{-1}; the molar ratios are dimensionless.

[c] $\delta^{18}O$, $\delta^{2}H$, d-excess and $\delta^{13}C$ in ‰.

[d] ^{3}H in TU, $A^{14}Cn$—normalized $A^{14}C$ and $A^{14}Cnn$—non-normalized $A^{14}C$ (the product of $A^{14}Cn$ and f') in pmc, correction factors f' and f'' are dimensionless, and GA—groundwater age of modern (recent, contemporaneous) water thought ^{3}H (^{3}H) and old water thought ^{14}C (^{14}C) in year and kiloyear, respectively.

Baseflow (Q_{BT}) and surface and interflow runoff (Q_U) were used as end members of a binary mixing model implemented to calculate the Q_{BT} fraction contributed to streamflow (Q_T) over the control period February–August 2015. As indicated in previous sections, the Q_{BT} fraction corresponds to a mixing of RGR (modern discharge) associated with current climate cycles and old groundwater not influenced by these cycles. As described in Section IV.4.4, *R* denoted the tracer content of the mass balance component identified in the subscript. For the conservative tracers rCl/rBr, $\delta^{18}O$ and ^{3}H (i) R_{QT} was the average-weighted tracer value measured at gauging station Q5; (ii) R_{QU} adopted the precipitation-weighed atmospheric bulk deposition tracer value measured at collectors W4 and W6; and (iii) R_{QBT} adopted the discharge-weighed tracer value measured at Chilcahuaico deep spring (D5), which is the most representative spring in terms of groundwater discharge flow (460 L s^{-1}; Table 17), i.e., 0.52-fold average Q_{BT} = 0.88 m^3 s^{-1} (0.41 mm day^{-1}) calculated with SWAT over the same control period February–August 2015 (Figure 6d). See Table 17 for further information. Table 18 shows the input data and results of the implemented binary mixing model. The Q_{BT} fraction calculated with tracer techniques varied in the 0.26–0.30 range. This range was almost identical to the Q_T fraction of 0.28±0.05 calculated with SWAT model over the same control period February–August 2015; average Q_T being 3.17 m^3 s^{-1} (1.48 mm day^{-1}) as displayed in Figure 6d. The relative difference was ±0.07 (Table 18). This figure allows the tracer mass balance to be proposed as a robust procedure for external validation of Q_{BT} calculated with SWAT model.

Hydrochemistry and isotope tracing corroborated the existence of shallow and deep aquifers in the PRB, which is a prerequisite for a standard implementation of SWAT model, such as carried out in this Thesis. The corroboration of two aquifers is based on the different average groundwater age and sources of salinity associated to each one. Processes controlling the chemical and isotope baseline of the groundwater discharge contributed to the baseflow fraction of streamflow are atmospheric bulk deposition and water-rock interaction. This is the case for groundwater discharge from shallow aquifer. For groundwater discharge from deep aquifer, volcanic CO2 degassing and emanations of halides, Li and SO4 adds to the above described two processes. The consequence is a relatively easy tracing of modern (recent, contemporaneous) shallow and old deep

groundwater contributions to streamflow that corroborates the above asseverations.

Table 18. Input data and results of the binary mixing model implemented to calculate the baseflow fraction contributed to streamflow over the control period February–August 2015.

Selected tracer	R_{QT}	R_{QU}	R_{QBT}	Q_{BT} fraction	RE [a]
rCl/rBr, [–]	773	490	1425	0.30	-0.07
$\delta^{18}O$, ‰ V-SMOW	-11.5	-11.1	-12.6	0.27	0.04
^{3}H, TU	1.9	2.1	1.4	0.26	0.07

R denotes the tracer content of the mass balance component identified in the subscript, as Q_T—streamflow, Q_U—surface and interflow runoff, and Q_{BT}—baseflow; [–] — dimensionless.

[a] Comparison of the calculated Q_{BT} fraction with tracers (z*) and SWAT model (z), RE = (z – z*)/z is the relative difference.

5.4.2. Findings from Darcian based formulations

Shallow and deep aquifers are hydraulically connected, as deduced from hydrochemistry and isotope tracing described in Section V.4.1. The rCl/rBr ratio and radioisotope data evidenced how deep spring discharge integrates variable fractions of modern and old groundwater, thus indicating a mixing of waters from different depths and ages. All sampled water points had measurable ^{3}H contents, so the old groundwater fraction contributed to baseflow can be assumed much minor than the modern one. This system conceptualization involves macroscopically unconfined flow conditions, despite that both shallow and deep aquifers (i) include fluctuating saturated zones at high-elevation unconfined recharge areas and some confined sectors with permanent saturated thickness at mid-slope and low-lying discharge areas due to the existence of confining lahar formations (Figure 1c); and (ii) show differences in the magnitude of hydraulic conductivity and specific yield, which are somewhat higher in the case of the shallow aquifer (Table 6).

After these remarks, average groundwater residence (renewal) time (G_T) and total groundwater discharge (D_T) were calculated using the Darcian-based formulations described in Section 4.4.4. Input data included the previous information generated and/or compiled in the area (Table 6) and findings deduced from hydrochemistry and isotope tracing of Section 4.4.1. G_T and D_T were evaluated

separately for the shallow aquifer, which is formed by Holocene andesitic lavas and avalanche flows from COVS and late Pleistocene Rhyolitic pyroclastic flows from CHVS, and the deep aquifer, which is formed by middle Pleistocene andesitic lavas from COVS and early Pleistocene andesitic lavas from SIVS (Figure 1c); see geological and hydrogeological descriptions of Section 3.2.

Other additional remark was necessary for conceptualization. Aquifer recharge includes two fractions, one that effectively contributes to the aquifer storage from shallow and deep aquifers (respectively named W_{RS} and W_{RD} in SWAT model) and other that discharges quickly and contributes to the baseflow (Q_{BT}). This consideration implies that the microscopically unconfined system is virtually full, which is plausible since groundwater exploitation is nil. Thus, total potential recharge from precipitation can be expressed as summation of Q_{BT}, W_{RS}, and W_{RD}. This assertion required an external evaluation of aquifer recharge using an alternative technique. For this purpose, the atmospheric chloride mass balance technique (Nolan et al., 2007; Coes et al., 2007; Alcalá and Custodio, 2014; 2015) expressed as $R \equiv P(C_P/C_R)$ was implemented at the headwater of the PRB (subbasin 4; Figure 7), where R = 389 mm year^{-1} is total potential recharge, P = 425 mm year^{-1} is yearly precipitation at weather station W6, C_P = 1.84 mg L^{-1} is average precipitation-weighted chloride content from atmospheric bulk deposition collected at W6, and C_R = 2.01 mg L^{-1} is average discharge-weighted chloride content monitored at the shallow spring S4 (Figure 12b; Table 17). R was quite similar to $Q_{BT}+W_{RS}+W_{RD}$ = 397 mm year^{-1} calculated with SWAT model at subbasin 4 (Table 10). The similarity of the rCl/rBr ratio found in W6 (445) and S4 (447) corroborated the atmospheric origin of chloride needed to propose this aquifer recharge estimation reliable enough (Figure 12b), whereas G_A = 4.8 year calculated with ^{3}H (Figure 12d) and G_A = 0–0.3 kyr calculated with ^{14}C (Figure 12f) identified modern (recent) groundwater comparable to the current groundwater components evaluated with SWAT model. This calculation serves as additional external validation of SWAT model.

Using in Equation 15a average $R = Q_{BT}+W_{RS}+W_{RD}$ = 353 mm year^{-1} calculated with SWAT model for the entire PRB (Table 10) and average $G_T \approx G_A$ = 11.5 year (1.1 TU) calculated from the selected deep springs D1 to D7 (Figure 12d), the saturated thickness (H) was 4.06 m. Using the average aquifer specific yield (S) of 0.003 after

experimental values (Table 6) and pumping tests performed in pumping wells W1 and W2 (Figure 1c), aquifer thickness was around 1350 m. The parameter specific yield was quite uncertain because aquifer information was available up to 300 m depth. Specific yield is around 0.01 in the uppermost 50–100 m of the shallow aquifer (Table 6) and may be 0.001 or less in the lowermost part of the deep aquifer due to fissure infilling associated to clay neoformation and carbonates precipitation at high-temperature rock weathering that could justify the groundwater transit times of several millennia calculated with ^{14}C. Using in Equation 15b the above R, G_T and H values, and considering a two-dimensional basin surface receiving recharge and contributing to aquifer storage (A_B) of 156.4 km^2 (Figure 1c), the aquifer saturated volume (V) was tentatively estimated to be around 0.64 km^3.

The subsurface groundwater discharge transmitting through the entire aquifer system to the basin outlet (Q_A) was also calculated. The 1D (Equation 17a) calculation used the above G_T, H and S values, and $b = 1.3$, as pointed out by Chapman (1999) for macroscopically unconfined aquifers having longitudinal flow paths with certain convergent (radial) component. $Q_A = 0.28$ mm year^{-1}. This figure coincided with deep aquifer recharge ($W_{RD} = 0.28$ mm year^{-1}) calculated with SWAT model (Table 10). The 3D (Equation 17b) calculation used the above G_T, H, S, b and A_A values. $Q_A = 0.013$ km^3 year^{-1}. Total groundwater discharge (D_T) includes Q_A and Q_{BT}. In the PRB, $D_T = 0.28+341.3 = 341.6$ mm year^{-1}. Since the aquifer is virtually full, Q_A coarsely corresponds to the groundwater discharge fraction from the deep aquifer, since the groundwater discharge fraction from the shallow aquifer contributes almost entirely to the baseflow. Therefore, the hydrological system functioning follows a stationary regime, where long-term recharge and discharge tend to be equal for periods coinciding with a natural groundwater renewal cycle of around 11.5 year long, as also was corroborated by the 12-year critical balance period for stationary evaluations calculated in Section 5.1 for the PRB area.

As a part of the necessary data for optimal groundwater evaluation prior exploitation, the rate of groundwater reserve exhaustion after exploitation (E) was calculated. As described above, aquifer information was available up to 300 m depth, so average aquifer transmissivity (T) data can be assumed quite uncertain and biased for deeper depths. Thus, T was replaced in Equation 19 by the product

of average hydraulic conductivity (K) and H. $E = 0.009$, considering the above H and S values, average $K = 0.19$ m^2 day^{-1} after weighting of experimental values (Table 6) and pumping tests performed in pumping wells W1 and W2 (Figure 1c), and an average aquifer dimension $L = 5.5$ km (Figure 1c). Using Equation 19 and assuming constant E and other aquifer form parameters, the time to exhaust half the groundwater reserve (E_T) associated to a given exploitation regime was around 55 years. This tentative evaluation shows how severe could impact an unplanned exploitation on the groundwater reserve; the outlook would worsen if this unplanned exploitation were carried out without considering the additional impact of climate change. In the current climate context, an unplanned exploitation regime could have irreversible consequences on the current baseflow regime, the water quality level required for the environment and urban supply, and the yielding of the pumping wells themselves. The evaluation of these multivariant impacts and consequences is out the scope of this Thesis.

The above figures obtained from basic Darcian-based formulations were supported with probably biased input data, which are the only ones available. A sound uncertainty must affect this evaluation. However, uncertainty was not evaluated since the full range of error of the variables and parameters involved is unknown, thus the uncertainty evaluation should also be biased. Therefore, the reported groundwater evaluation is highly interpretable. In a study area with such a scarcity of hydrogeological data, the order of magnitude of the aquifer variables and parameters is what matters. Regarding the significance of the RGR in the PRB, and in the Andean Highland in general, future research should aim to refine future predictions based on necessary groundwater monitoring to support specific groundwater modelling tools. For example, coupled SWAT–MODFLOW models have proven satisfactory solutions, provided piezometry can be long-term monitored and hydraulic parameters for aquifers and their hydraulically connected aquitards can be surveyed accurately. However, these tools could be restricted to some areas since data availability in many Andean Highland sites is similar or even worse than existing in the PRB (Alcalá, 2006).

VI – LIMITATIONS AND FUTURE WORK

VI -LIMITATIONS AND FUTURE WORK

6.1. OVERALL EXPOSITION

The main limitation to correctly conceptualize the hydrogeological functioning of the PRB is the insufficient geological definition. This problem is shared by most of the Andean Highland basins, except in some exceptions where the oil industry has carried out detailed geological explorations in accordance with its exploration needs prior to drilling and extraction operations. The insufficient geological definition generates two important problems. The first is the insecurity of the proposed hydrogeological conceptualization. The second, which depends on the first, is the inability to implement numerical models to simulate groundwater flow, since these models need to incorporate the geometry of the aquifers and aquitards. In turn, this second limitation evidences another type of deficiency to characterize the groundwater resource, which is the practical absence of networks for monitoring groundwater, and pumping wells and piezometers to measure hydraulic properties of the geological formations and record time series of the variables, such as piezometry. This basic information requires operating networks for monitoring piezometry, spring discharge flow and other similar ones, in addition to those typically associated with the control of the hydrochemical dynamics of the different groundwater flow paths. In short, implementing numerical groundwater simulation tools with a minimum resolution and predictive capability in the PRB and in most of the Andean Highland basins is unfeasible. These needs lead to other first-rate limitations, such as the budgetary and financial capacity of governmental water agencies and public water supply companies to undertake this type of research and the time interval necessary to achieve correctly validated products.

The following two sections are devoted to describe additional scientific remarks of the two general limitations: the insufficient geological definition and the inability to numerical models to simulate groundwater flow, emphasizing that this second limitation depends on a confident definition of subsurface geology, and also on the existence of input data series long enough to guarantee a correct

stationary evaluation and hydraulic parameters of aquifers and associated aquitards by means of pumping tests surveyed in spatially distributed pumping wells, which also do not exist in the PRB. In the PRB, none of these conditions exist, and there is no known basin in the Andean Highland in northern Ecuador that fully meets them. This clear limitation to carry out an orderly evaluation of the groundwater resource is the reason that has driven the design of the methodological strategy proposed in this Thesis to evaluate the RGR and the dynamics of the groundwater resource. The following two sections also describe research in progress to advance our understanding of these important limitations.

6.2. HYDROGEOLOGICAL CONCEPTUALIZATION OF REGIONS WITH ACTIVE TECTONICS AND VOLCANISM

In the Andean Highland in northern Ecuador, high precipitation rates, low evapotranspiration rates, and favourable physicochemical properties of soils determine annual streamflow-to-precipitation ratios in the 0.6–0.8 range (Buytaert et al., 2006; Tobón and Arroyave, 2007; Crespo et al., 2014). In general, this behaviour favours high interflow rates, low to moderate shallow aquifer recharge rates, and low to very low deep aquifer recharge rates (Alcalá et al., 2016; Peñafiel et al., 2016a). From a hydrogeological point of view, Mesozoic carbonate formations and Neogene to Quaternary volcanic and volcano-sedimentary formations form moderately permeable regional aquifers of more than 1,000 m thick (Peñafiel et al., 2020, 2021). The high compartmentalization of these geological formations induced by active tectonics and volcanism determines different hydraulic and physicochemical behaviours along the flow paths and complex interactions between aquifers and rivers, lakes and streams (Hemmings et al., 2016; Muñoz, 2016; Vuille et al., 2018; Vincent et al., 2019). Aquifer recharge is mostly produced in summit areas where these formations outcrop, whereas aquifer discharge occurs through valleys downstream where the incisive topography interests the regional piezometry and occasionally through faults forming permanent springs (Peñafiel et al., 2016a, 2016b; Ruiz-Pico et al., 2019). Quaternary alluvial and fluvial-glacial formations form small, highly permeable aquifers that collect regional aquifer discharge (Hall and Motes, 2008; Mark et al., 2010; Favier et al., 2008; Baraer et al., 2012, 2015; Hemmings et al., 2016; Peñafiel et al., 2016a, 2016b; Vuille et al., 2018;

Ruiz-Pico et al., 2019). The typical hydrological functioning is basins with losing streams in summits and gaining streams in mid-slope and low-lying areas (Alcalá et al., 2016). This general hydrogeological functioning is perfectly observed in the PRB.

The hydrogeological functioning of most Andean Highland basins in combination with habits for water consumption of population have determined the capability for using and monitoring the groundwater resource. In natural mid-slope and summit areas, groundwater is deeper, human use is low or negligible, aquifer discharge equals to aquifer recharge, average groundwater turnover time is in the range of some years (Peñafiel et al., 2016a; 2016b), and the general lack of observation networks has prevented to implement saturated-zone routed techniques or numerical models for groundwater evaluation (Célleri and Feyen, 2009). In mid-slope and low-lying areas, groundwater is often shallower and better monitored, human pressure is high, aquifer discharge is higher than local aquifer recharge, average turnover time varies in the range of decades or more (Peñafiel et al., 2016a; 2016b), and the increasing exploitation has introduced disturbances that put severe pressure on the groundwater resource (Buytaert and De Bievre, 2012; Ochoa-Tocachi et al., 2018). This is the case of most IAV aquifers, where the PRB becomes an excellent case study for natural mid-slope and summit areas.

In the PRB, the magnitude of the RGR obtained with SWAT model (Table 10) and the conceptualization gained from tracer techniques and Darcian-based formulations agree the above overall synthesis, but with particularities associated to the fact that aquifers are virtually full determining low shallow aquifer recharge and very low deep aquifer recharge. Therefore, the hydrogeological functioning of the PRB can be considered a guide for initial conceptualizations of other similar basins, saving the logical expected differences in magnitude and renewal of the groundwater balance components according to their geographical, climatological, geological and dimensional features.

Thickness and specific yield of shallow and deep aquifers are crucial pieces of information in groundwater exploration that requires further discussion (and caution) when derived indirectly from Darcian-based formulations. In Section V.4.2 aquifer thickness around 1,350 m was deduced. As shown in Figure 1c, the shallow aquifer average thickness is around 150 m. For the deep aquifer, this

information is unknown. In Figure 1c, aquifer thickness was drawn around 500 m, although no specific geological or geophysical research aimed at defining the position of the impervious lower boundary of the deep aquifer and therefore its saturated thickness is available. Fortunately, there is other type of information from which this hydrogeological information can be corroborated. Hemmings et al. (2016) inferred aquifer thickness over 1,000 m at least (the model did not report results below this depth) in the northern versant of the Cotopaxi Volcano (southern part of the PRB) after two-dimensional geothermal modelling, whereas Peñafiel et al. (2020; 2021) reported aquifer thickness around 1,500 m for the equivalent geological formations in the nearest Quito basin after electromagnetic (Magnetotelluric Soundings) geophysical surveys. The work of Hemmings et al. (2016) is of especial interest because it corroborates the aquifer thickness magnitude approached in the PRB and provides a validated heat flow model based on several combinations of aquifer hydraulic conductivity (K) and specific yield (S). The validated average K and S were in the 0.15–0.25 m^2 day^{-1} and 0.002–0.005 ranges, i.e., they have the same magnitude that the average values used in this Thesis.

Many other findings of hydrogeological interest can be deduced when a combined analysis of the two-dimensional geothermal model of Hemmings et al. (2016) (Figure 13) and findings deduced from SWAT model, tracer techniques and Darcian-based formulations is performed. First, the geothermal model identifies two heat layers, a thin shallow cold layer derived from current recharge floating over a thick deep hot layer subjected to hydrothermal processes equivalent to the deep aquifer defined in this Thesis (Figure 13). The second is the heat flow paths system, where shallow groundwater is transmitted horizontally near surface and discharges where topography intersects piezometry. However, deep groundwater is slowly transmitted throughout the aquifer and discharges in favourable sites such regional fault systems, as also was evidenced by the low electrical resistivity (high electrical conductivity) longitudinal fields recorded with electromagnetic geophysical techniques in the vicinity of active faults in Quito basin (Peñafiel et al., 2020; 2021). The consequence is shallow groundwater discharge showing low to very low volcanic influence and deep groundwater discharge being a variable mixture of shallow and deep groundwater, as was deduced from chemical and isotope tracing in Section 4.4.1. Thus, the hydrogeological conceptualization in the PRB must also include the presence of regional active faults to justify deep

groundwater contributing to streamflow (Figure 13). In the PRB, the two-dimensional geothermal model also corroborates that the aquifer is virtually full, thus the effective recharge contributing to the aquifer storage is quite low as SWAT model evaluated and chemical and isotope tracing corroborated.

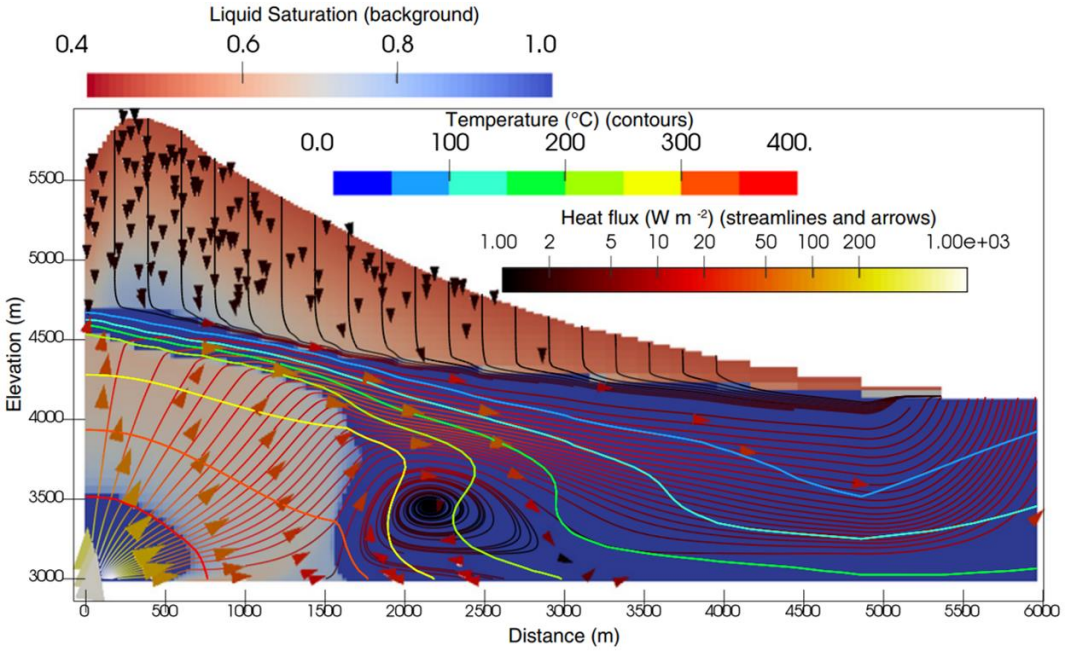

Figure 13. Two-dimensional geothermal modelling in the northern versant of the Cotopaxi Volcano (southern part of the PRB), modified and updated from Hemmings et al. (2016), including water (liquid) saturation (background colours), temperature (coloured contours), and heat flux (streamlines and arrows; logarithmic scale) dynamics at the end of the initial model simulation (3,500 years).

The most important parameters to characterize the dynamics of the RGR were aquifer recharge (shallow and deep aquifer recharge), aquifer discharge (groundwater transmitting to the basin/aquifer outlet and baseflow fraction of streamflow) and groundwater turnover time (renewal time). These variables depend on and allows calculate the aquifer thickness (H) magnitude obtained in the PRB. However, the evaluation of these variables for H = 1350 m or higher values could be unrealistic because it is unknown if all the deep geological formations is saturated or there are low-permeability geological formations forming aquitards or aquicludes of unknown thickness, as could easily be expected. What it seems evident is that the magnitudes of these variables are consistent with the geometry

and hydraulic properties of the explored aquifer sectors, including indirect deductions from two-dimensional geothermal models and geophysical surveys. Since the saturated thickness of these aquifers is unknown, a theoretical calculation of aquifer discharge (G_T) and groundwater turnover time (D_T) is provided, using H = 150 m for shallow aquifer (a proved condition; Figure 1c; Figure 13) and two options (H = 500 m and H = 1,000 m) for deep aquifer. Table 19 summarizes these theoretical results, which are aimed at providing basic hydrological criteria for sustainable groundwater exploitation.

Table 19. Scenarios of average groundwater-turnover time and total groundwater discharge in the PRB attending to plausible aquifer saturated thickness ranges and other aquifer variables and parameters.

Variable/parameter	Shallow aquifer [a]	Deep aquifer [a]	Deep aquifer [a]
b, [–]	1.2	1.2	1.2
A, km²	24.8	36.8	36.8
S min, [–] [a]	0.008	0.009	0.009
S avg, [–] [a]	0.015	0.012	0.012
S max, [–] [a]	0.051	0.048	0.048
K min, m day^{-1} [a]	0.123	0.110	0.110
K avg, m day^{-1} [a]	0.288	0.205	0.205
K max, m day^{-1} [a]	0.877	0.658	0.658
H, m [b]	150	500	1000
G_T min, year [c]	106.0	19.9	8.8
G_T avg, year [c]	28.4	14.1	5.9
G_T max, year [c]	15.8	17.7	11.8
D_T min, mm year^{-1} [c]	35.2	305.9	1794.5
D_T avg, mm year^{-1} [c]	93.2	607.6	2691.7
D_T max, mm year^{-1} [c]	362.9	2565.5	7103.5

[–] — dimensionless.

[a] For S and K, experimental range as in Table 6 and average surface-weighted value (into parenthesis) after data from each geological formation forming the corresponding aquifer.

[b] For the shallow aquifer, average H value after geological cross-sections as in Figure 1c. For the deep aquifer, H = 500 m and H = 1,000 m are two options adopted for calculations.

[c] For the shallow aquifer, experimental range and average value (into parenthesis) of G_T and D_T after experimental values of S and K. For the deep aquifer, ranges and average values of G_T and D_T after experimental values of S and K for H = 500 m and H = 1,000 m.

Finally, under the auspice of public funds from Ecuadorian authorities and academic institutions, an electromagnetic (Magnetotelluric Soundings) geophysical survey will be performed in the PRB in coming months. This scientific research is aimed at defining aquifer geometry (thickness and extension) and identifying geological structures (active faults) determining preferential flow paths of the deep aquifer.

6.3. SURFACE WATER - GROUNDWATER COUPLED MODELLING

Surface water and groundwater numerical models, including the rainfall–runoff SWAT model, allows evaluations over the modelling period that may differ from the expected long-term stationary condition when using short, variable-length time series. Usually, the modelling period is constrained to the length of the shorter input model variable, usually observed streamflow record in rainfall–runoff models and piezometry in groundwater models. Rarely, the long-term stationary representativeness of the evaluation (of the water balance components) is evaluated, so results can only be considered representative for the condition monitored during the modelling period. Model uncertainty and performance may be unreal, varying from illusory low values to unmanageable high values, which are unpractical for water resources management.

This Thesis has put attention in this issue and has implemented a procedure to analyse the temporal representativeness of the governing water balance components before proposing a given numerical model and using the model estimates as support for decision making. This initial analysis is especially important in the Andean Highland, where the short, variable-length time series predominate, and the water resources evaluation can be suboptimal, even unpractical.

As described in Section II.3, the consulted SWAT literature indistinctly used both shallow and deep aquifer recharge components to evaluate the RGR, following four typical strategies. This Thesis used the third and fourth strategies. The third strategy used streamflow hydrograph filtering techniques to separate the baseflow component, after experiences gained in similar steep basins with gaining streams and null groundwater transference and abstraction, which allows to equal total aquifer recharge to aquifer discharge contributed to the baseflow component

(Rutledge and Mesko, 1996; Lim et al., 2005; Plesca et al., 2012; Lee et al., 2018). The fourth strategy applied in the PRB used specific recharge techniques based on saturated zone routed physical and tracer techniques to refine shallow and deep aquifer recharge components by SWAT model. The procedure was to complement the SWAT model evaluation in what concern to the groundwater components, as has been documented in the scientific literature (Han et al., 2015; Jin et al., 2015; Stehr et al., 2009; Abiodun et al., 2018; Tobin and Bennett, 2019; Senent-Aparicio et al., 2020, 2021b; Lee et al., 2018). The other two strategies are constrained in the PRB and in most of the Andean Highland basins because of the scarcity of aquifer data, as described in previous sections. In fact, the first strategy, which is based on direct groundwater monitoring, is a part needed for a correct implementation of the second one.

Scientific research ahead is aimed at coupling groundwater numerical models like MODFLOW with SWAT model. This second strategy will use the RGR evaluated by SWAT model to refine the aquifer recharge/discharge function used in MODFLOW. Because groundwater numerical models often overlook the required accuracy for aquifer recharge (Kim et al., 2008), assumed accurate shallow aquifer recharge by SWAT model and deep groundwater dynamics by tracer techniques and Darcian-based formulations will be crucial pieces of information. The different hydrological meaning and timing of shallow and deep aquifer recharge would be quantified. This future research will start when the geological/geophysical research described in the previous section will end. However, a first analysis has already been initiated to assess the coupling capability of SWAT and MODFLOW models in the PRB, which will include the tentative values of aquifer thickness, total discharge and average groundwater turnover time (renewal) obtained in this Thesis.

VII – CONCLUSIONS

VII - CONCLUSIONS

The conclusions of the Thesis have been drawn from findings reached in the three published high-impact articles, and other one about to be published, all of them prepared in the exclusive research framework that has led to this work. See the initial Publications Section for details.

Hydrological modelling combined with saturated zone routed techniques is an effective strategy for evaluating the renewable water resources under stationary conditions prior forecasting climate and human impacts under plausible scenarios. This methodology is suitable for sparse-data mountainous basins intended to supply densely populated urban areas. This Thesis used the SWAT model to evaluate the renewable groundwater resource (RGR) under a stationary condition as a step to assess the impact of climate change on this water component in the Pita River basin (PRB), which is a representative area of the *páramo* ecosystem in the northern Andean Highland in northern Ecuador proposed to meet the future water demand of approximately 400,000 inhabitants in the Metropolitan District of Quito (MDQ). Tracer techniques and Darcian-based formulations were also used to determine the groundwater dynamics by means of some essential variables that SWAT model does not provide.

A SWAT model was configured over the period 2006–2015. A stationarity analysis prior implementing the numerical model was implemented to asseverate that the modelling period is suitable to generate stationary evaluations of the RGR. The SWAT evaluation provided average annual streamflow and aquifer recharge rates around 0.45- and 0.01-fold the average annual precipitation in the area, which is 1,004 mm. The conclusion was that aquifers in the PRB are virtually full, thus repealing most of the infiltration water amount. As in other pristine Andean Highland basins, in the PRB the natural hydrological regime determined by thick, porous andosols over virtually full moderate-permeability volcanic and volcano-sedimentary aquifers induces high streamflow (high baseflow and surface and interflow runoff) and low aquifer recharge (shallow and deep fractions) rates.

Regarding the climate change impact on the RGR, five Regional Climate Models (RCMs) based on two Representative Concentration Pathway (RCP)

emission scenarios (4.5 and 8.5) for the mid- (2040–2069) and long-term (2070–2099) time horizons were implemented. Hydrological modelling demonstrated increases in average temperature and precipitation of + 2 °C and + 3 % in the mid-term and + 4.5 °C and + 20 % in the long term, respectively. All the RCMs indicated some less aquifer recharge in the mid-term. However, this pattern was softened, and even reversed, in several scenarios in the long term. Seasonal differences in streamflow and aquifer recharge in the baseline scenario were predicted to increase to + 23 %. Future hydrological regime could place the highly sensitive soil–vegetation dynamics of the *páramo* ecosystem at risk of degradation, with negative consequences for stream water provision. Hence, the RGR fraction seems to be the safest option for water provision in the future, despite that much more knowledge about its dynamics is needed to asseverate that its quantity and quality properties will remain.

Chemical, stable isotope and radioisotope tracer techniques corroborated the existence of shallow and deep aquifers based on the different average groundwater age and sources of salinity associated to each one. The processes controlling the chemical and isotopic baseline of shallow groundwater contributed to baseflow were atmospheric bulk deposition and water-rock interaction. For the deep groundwater discharge, volcanic CO_2 degassing and emanations of halides, lithium and sulphate adds to those above two processes. Based on measurable tritium contents, the contribution of old groundwater was interpreted much minor than modern groundwater; experimental data showed average groundwater renewal around 11.5 years for modern groundwater after tritium data up to millennia for old groundwater after radiocarbon data. For old groundwater, the renewal time of several millennia agrees with large low-yielding aquifers and low aquifer recharge rates. The low recharge rates estimated with SWAT model corroborates a part of this assertion, the relative one to thickness and specific yielding of deep aquifers remains unknown, although they were assumed high (even some thousand meters) and low (lower than 0.01), respectively, until conclusive data are available.

Darcian-based formulations provided tentative evaluations of average groundwater residence (renewal) time and total groundwater discharge. Since aquifers are virtually full, groundwater storage is much higher than aquifer recharge and groundwater residence (renewal) times were typically low (some to dozen years) for shallow groundwater and long to very long, even millennia for

deep groundwater, thus corroborating estimates from radioisotope tracing. Regarding the RGR, average annual discharge was around 340 mm, which was similar to the sum of baseflow and aquifer recharge calculated with SWAT model. The discharge fraction concerned to average annual subsurface groundwater transmitting through the aquifer to the basin outlet was around 0.28 mm, which was coincident with deep aquifer recharge calculated with SWAT model. Average aquifer thickness and saturated volume were tentatively estimated around 1,350 m and 0.64 km^3, respectively. This volume does not amount to a significant reserve because the large part is associated to high-mineralized (low quality) old groundwater having a very low renewal.

This Thesis evidences how severe could impact an unplanned exploitation regime on the RGR and especially on the old groundwater reserve; the outlook would worsen if the unplanned exploitation was carried out without considering the additional impact of climate change. In the current climate context, unplanned exploitation regimes could have irreversible consequences on the baseflow regime, water quality level required for the environment and urban supply, and yielding of the pumping wells themselves. Regarding the significance of the RGR in the PRB, and in the Andean Highland in general, future research should aim to refine future predictions based on necessary groundwater monitoring to support specific groundwater modelling tools. For example, coupled SWAT–MODFLOW models have proven satisfactory solutions. Future research is aimed at improving the deficient geological knowledge. This constraint and the low level of groundwater monitoring prevent implementing the coupled numerical models for quantitative groundwater assessments. This handicap is similar to that reported in other adjacent basins of the Andean Highland and prevents a sustainable groundwater management.

VIII – BIBLIOGRAPHICAL REFERENCES

VIII - BIBLIOGRAPHICAL REFERENCES

Abbaspour, K.C. (2007). User Manual for SWAT-CUP, SWAT Calibration and Uncertainty Analysis Programs. Swiss Federal Institute of Aquatic Science and Technology, Eawag, Duebendorf, Switzerland.

Abbaspour, K.C. (2012). SWAT Calibration and Uncertainty Program—A User Manual; SWAT-CUP-2012; Swiss Federal Institute of Aquatic Science and Technology: Dubendorf, Switzerland.

Abbaspour, K.C. (2015). SWAT-CUP 2012: SWAT calibration and uncertainty programs – A User Manual. Available at https://swat.tamu.edu/media/114860/usermanual_swatcup.pdf

Abbaspour, K.C., Johnson. C.A., Van Genuchten, MTh. (2004). Estimating Uncertain Flow and Transport Parameters Using a Sequential Uncertainty Fitting Procedure. Vadose Zone Journal, 3, 1340–1352.

Abbaspour, K.C., Yang, J., Maximov, I., Siber, R., Bogner, K., Mieleitner, J., Zobrist, J., Srinivasan, R. (2007). Modelling hydrology and water quality in the pre-alpine/alpine Thur watershed using SWAT. *Journal of Hydrology*, 333, 413–430.

Abbaspour, K.C., Rouholahnejad, E., Vaghefi, S., Srinivasan, R., Yang, H., Klove, B. (2015). A continental-scale hydrology and water quality model for Europe: Calibration and uncertainty of a high-resolution large-scale SWAT model. *Journal of Hydrology.* 524, 733–752.

Abbaspour, K.C., Vaghefi, S., Srinivasan, R. (2018). A guideline for successful calibration and uncertainty analysis for soil and water assessment: A review of papers from the 2016 International SWAT Conference. *Water*, 10, 6.

Abiodun, O.O., Guan, H., Post, V.E.A., Batelaan, O. (2018). Comparison of MODIS and SWAT evapotranspiration over a complex terrain at different spatial scales. *Hydrology and Earth System Sciences*, 22, 2775–2794.

Ahl, R.S., Scott, W.W., Zuuring, H.R. (2008). Hydrologic Calibration and Validation of SWAT in a Snow-Dominated Rocky Mountain Watershed, Montana, U.S.A. *Journal of the American Water Resources Association*, 44, 1411–1430.

Aiuppa, A., Federico, C., Franco, A., Giudice, G., Gurrieri, S., Inguaggiato, S., Liuzzo, M., McGonigle, A.J.S., Valenza, M., (2005). Emission of bromine and iodine from Mount Etna volcano. Geochemistry, Geophysics and Geosystems 6, Q08008. doi: 10.1029/2005GC000965.

Alcalá, F.J. (2016). Optimization of methods to evaluate the groundwater quantity and quality dynamics in basins of the province of Tungurahua in Ecuador. Ed. Secretary for Higher Education, Science, Technology and Innovation of Ecuador. SENESCYT Repository. Scientific Report PROMETEO-CEB-014-2015. Quito, Ecuador. 38 pp.

Alcalá, F.J., Custodio, E. (2008a). Using the Cl/Br ratio as a tracer to identify the origin of salinity in aquifers in Spain and Portugal, *Journal of. Hydrology*., 359, 189–207.

Alcalá, F.J., Custodio, E. (2008b). Atmospheric chloride deposition in continental Spain. Hydrological Processes 22, 3636-3650. DOI: 10.1002/hyp.6965.

Alcalá, F.J., Custodio, E. (2014). Spatial average aquifer recharge through atmospheric chloride mass balance and its uncertainty in continental Spain. *Hydrological Processes*, 28, 218–236.

Alcalá, F.J., Custodio, E. (2015). Natural uncertainty of spatial average aquifer recharge through atmospheric chloride mass balance in continental Spain. *Journal of Hydrology*, 524, 642–661.

Alcalá, F.J., Cantón, Y., Contreras, S., Were, A., Serrano-Ortiz, P., Puigdefábregas, J., Solé-Benet, A., Custodio, E., Domingo, F. (2011). Diffuse and concentrated recharge evaluation using physical and tracer techniques: results from a semiarid carbonate massif aquifer in southeastern Spain. Environ. Earth Sci. 62, 541–557. https://doi.org/10.1007/s12665-010-0546-y

Alcalá, F.J., Martínez-Valderrama, J., Robles-Marín, P., Guerrera, F., Martín-Martín, M., Raffaelli, G., Tejera de León, J., Asebriy, L. (2015). A hydrological-economic model for sustainable groundwater use in sparse-data drylands: Application to the Amtoudi Oasis in southern Morocco, northern Sahara. *Science of the Total Environment*, 537, 309–322.

Alcalá, F.J., Toapanta, J., Peñafiel, L., Barragán, E., Yánez, W., Buenaño, M., Larrea, O. (2016). First data on atmospheric chloride mass balance components in the

Andean páramo in central Ecuador: implications to project climate scenarios of net aquifer recharge and potential groundwater chemical baseline. In: 43rd IAH Congress: Groundwater and society. Montpellier, France, 851–852.

Alcalá, F.J., Martín-Martín, M., Guerrera, F., Martínez-Valderrama, J., Robles-Marín, P. (2018). A feasible methodology for groundwater resource modelling for sustainable use in sparse-data drylands: Application to the Amtoudi Oasis in the northern Sahara. Sci. Total Environ. 630, 1246–1257. https://doi.org/10.1016/j.scitotenv.2018.02.294

Alves, L.M., Marengo, J. (2010). Assessment of regional seasonal predictability using the PRECIS regional climate modelling system over South America. *Theoretical and Applied Climatology*, 100, 337–350.

Anderson, E.P., Marengo, J., Villalba, R., Halloy, S., Young, B., Cordero, D., Gast, F., Jaimes, E., Ruiz, D. (2011). Consequences of climate change for ecosystems and ecosystem services in the tropical Andes, in: Climate Change and Biodiversity in the Tropical Andes. Inter-American Institute for Global Change Research (IAI) and Scientific Committee on Problems of the Environment (SCOPE), pp. 1–18.

Araguás-Araguás, L., Froehlich, K., Rozanski, K. (2000) Deuterium and oxygen-18 isotope composition of precipitation and atmospheric moisture. *Hydrological Processes*, 14(8), 1341–1355.

Arnold, J.G., Allen, P.M. (1999). Automated methods for estimating baseflow and ground water recharge from streamflow records. *Journal of the American Water Resources Association,* 35, 411–424.

Arnold, J.G., Fohrer, N. (2005). SWAT2000: current capabilities and research opportunities in applied watershed modelling. *Hydrological Processes,* 19, 563–572.

Arnold, J.G., Allen, P.M., Bernhardt, G. (1993). A comprehensive surface-groundwater flow model. *Journal of Hydrology*, 142, 47–69.

Arnold, J.G., Allen, P.M., Muttiah, R., Bernhardt, G. (1995). Automated base flow separation and recession analysis techniques. *Ground Water*, 33, 1010–1018.

Arnold, J.G., Srinivasan, R., Muttiah, R.S., Williams, J.R. (1998). Large area hydrologic modeling and assessment. Part I: model development. *Journal of the*

American Water Resources Association, 34, 73–89. https://doi.org/10.1111/j.1752-1688.1998.tb05961.x

Arnold, J.G., Moriasi, D.N., Gassman, P.W., Abbaspour, K.C., White, M.J., Srinivasan, R., Santhi, C., Harmel, R. D., van Griensven, A., Van Liew, M. W., Kannan, N., Jha, M. K. (2012). SWAT: Model Use, Calibration, and Validation. Trans. ASABE 55, 1491–1508. https://doi.org/10.13031/2013.42256

Athira, P., Sudheer, K.P., (2021). Calibration of distributed hydrological models considering the heterogeneity of the parameters across the basin: a case study of SWAT model. *Environmental Earth Sciences*. 80, 131. https://doi.org/10.1007/s12665-021-09434-8

Awana, U.K., Ismaeel, A. (2014). A new technique to map groundwater recharge in irrigated areas using a SWAT model under changing climate. *Journal of Hydrology*, 519, 1368–1382.

Bacuilima, F.L., Bacuilima, J.C, Bermeo, W.A. (1999). Caracterización 38 de clima por microcuencas en el Austro Ecuatoriano. MSc Thesis, Universidad de Cuenca, Ecuador.

Baraer, M., Mark, B.G., McKenzie, J.M., Condom, T., Bury, J., Huh, K., Portocarrero, C., Gomez, J., Rathay, S. (2012). Glacier recession and water resources in Peru's Cordillera Blanca. *Journal of Glaciology*, 58, 134–150.

Baraer, M., McKenzie, J., Mark, B., Gordon, R., Bury, J., Condom, T., Gómez, J., Knox, S., Fortner, S. (2015). Contribution of groundwater to the outflow from ungauged glacierized catchments: a multi-site study in the tropical Cordillera Blanca, Peru. *Hydrological Processes,* 29, 2561–2581.

Barnett, T.P., Adam, J.C., Lettenmaier, D.P. (2005). Potential impacts of a warming climate on water availability in snow-dominated regions. Nature, 438, 303–309. https://doi.org/10.1038/nature04141

Barrios, A.G., Uribarri, L.A. (2010). Application of SWAT model in the Venezuelan Andes high Chama River Basin. *Revista Geográfica Venezolana,* 51, 11–29.

Bastin, L., Cornford, D., Jones, R., Heuvelink, G., Pebesma, E., Stasch, C., Nativi, S., Mazzetti, P., Williams, M. (2013). Managing uncertainty in integrated environmental modelling: The UncertWeb framework. *Environmental Modelling & Software,* 39, 116–134.

Bastola, S., Seong, Y., Lee, D., Youn, I., Oh, S., Jung, Y., Choi, G., Jang, D. (2018). Contribution of Baseflow to River Streamflow: Study on Nepal's Bagmati and Koshi Basins. *KSCE. Journal of Civil Engineering*, 22, 4710–4718.

Batelaan, O., De Smedt, F., (2007). GIS based recharge estimation by coupling surface- subsurface water balances. *Journal of Hydrology*, 337, 337–355.

Battaglia, A., Bitetto, M., Aiuppa, A., Rizzo, A.L., Chigna, G., Watson, I.M., D'Aleo, R., Juárez Cacao, F. J., de Moor, M.J. (2018). The Magmatic Gas Signature of Pacaya Volcano, With Implications for the Volcanic CO_2 Flux from Guatemala. *Geochemistry*, *Geophysics*, *Geosystems*, 19, 667–692.

Beate, B. (1989). The Chalupas ignimbrite. In: IAVCEI General Assembly, New Mexico. *New Mexico Bureau of Mines and Mineral Resources,* 131, 18.

Bender, M.M. (1971). Variations in the $^{13}C/^{12}C$ ratios of plants in relation to the pathway of photosynthetic carbon dioxide fixation. *Phytochemistry*,10, 1239–1244.

Bendix, J. (2000). Precipitation dynamics in Ecuador and northern Peru during the 1991/92 El Nino: A remote sensing perspective. Int. J. Remote Sens. 21, 533–548. https://doi.org/10.1080/014311600210731

Bendix, J., Rollenbeck, R., Palacios, W.E. (2004). Cloud detection in the Tropics – a suitable tool for climate-ecological studies in the high mountains of Ecuador. *International Journal of Remote Sensing,* 25, 4521–4540. https://doi.org/10.1080/01431160410001709967

Beven, K. (2007). Towards integrated environmental models of everywhere: uncertainty, data and modelling as a learning process. *Hydrology Earth System Sciences*, 11, 460–467.

Beven, K., Binley, A. (1992). The future of distributed models – model calibration and uncertainty prediction. *Hydrological Processes,* 6, 279–298.

Bhunia, G.S. (2020). An approach to demarcate groundwater recharge potential zone using geospatial technology. *Applied Water Science* 10, 138. https://doi.org/10.1007/s13201-020-01231-1

Bioteau, T., Bordenave, P., Laurent, F., Ruelland, D. (2002). Evaluation des risques de pollution agricole à l'échelle de bassins versants: intérêts d'une approche par modélisation hydrologique avec SWAT. *Ingénieries-EAT,* 32, 3–13.

Blanco-Gómez, P., Jimeno-Sáez, P., Senent-Aparicio, J., Pérez-Sánchez, J. (2019). Impact of Climate Change on Water Balance Components and Droughts in the Guajoyo River Basin (El Salvador). Water 11, 2360. https://doi.org/10.3390/w11112360

Boulanger, J.-P., Martinez, F., Segura, E.C. (2007). Projection of future climate change conditions using IPCC simulations, neural networks and Bayesian statistics. Part 2: Precipitation mean state and seasonal cycle in South America. Clim. Dyn. 28, 255–271. https://doi.org/10.1007/s00382-006-0182-0

Bovolo, C.I., Parkin, G., Sophocleous, M. (2009). Groundwater resources, climate and vulnerability. Environmental Research Letters, 4, 035001. https://doi.org/10.1088/1748-9326/4/3/035001

Bradley, R.S., Vuille, M., Diaz, H.F., Vergara, W. (2006). Threats to Water Supplies in the Tropical Andes. Science 312, 1755–1756. https://doi.org/10.1126/science.1128087

Brockwell, P.J., Davis, R.A. (1991). Time Series: Theory and Methods. 2nd Ed. Springer, New York, USA. 520 pp.

Bruijnzeel, L.A., Mulligan, M., Scatena, F.N. (2011). Hydrometeorology of tropical montane cloud forests: emerging patterns. *Hydrological Processes,* 25, 465–498.

Burbano, N., Becerra, S., Pasquel, E. (2015). Introduction to the Hydrogeology of Ecuador. National Institute for Meteorology and Hydrology (INAMHI). Technical Report. Government of Ecuador, Quito. 121 pp (in Spanish).

Burg, A., Zilberbrand, M., Yechieli, Y. (2013). Radiocarbon variability in groundwater in an extremely arid zone-the Arava Valley, Israel. *Radiocarbon*, 55, 963–978.

Butler., J.H., King, D.B., Lobert, J.M., Montzka, S.A., Yvon-Lewis, S.A., Hall, B.D., Warwick, N.J., Mondeel, D.J., Aydin, M., Elkins, J.W. (2007). Oceanic distributions and emissions of short-lived halocarbons. *Global Biogeochemistry Cycles 21*, GB1023. doi: 10.1029/2006GB002732.

Buytaert, W., De Bièvre, B., Wyseure, G., Deckers, J. (2004). The use of the linear reservoir concept to quantify the impact of land use changes on the hydrology of catchments in the Ecuadorian Andes. *Hydrology and Earth System Science*s, 8, 108–114. https://doi.org/10.5194/hess-8-108-2004

Buytaert, W., Wyseure, G., De Bièvre, B., Deckers, J. (2005a). The effects of land-use changes on the hydrological behaviour of Histic Andosols in south Ecuador. *Hydrological Processes,* 19, 3985–3997.

Buytaert, W., Sevink, J., Leeuw, B.D., Deckers, J. (2005b). Clay mineralogy of the soils in the south Ecuadorian paramo region. *Geoderma*, 127, 114–129. https://doi.org/10.1002/hyp.5867

Buytaert, W., Célleri, R., De Bièvre, B., Cisneros, F., Wyseure, G., Deckers, J., Hofstede, R. (2006). Human impact on the hydrology of the Andean páramos. *Earth-Science Reviews,* 79, 53–72. https://doi.org/10.1016/j.earscirev.2006.06.002

Buytaert, W., Célleri, R., Timbe, L. (2009). Predicting climate change impacts on water resources in the tropical Andes: Effects of GCM uncertainty. *Geophysical Research Letters*, 36. https://doi.org/10.1029/2008GL037048

Buytaert, W., Vuille, M., Dewulf, A., Urrutia, R., Karmalkar, A., Célleri, R. (2010). Uncertainties in climate change projections and regional downscaling in the tropical Andes: Implications for water resources management. *Hydrology and Earth System Science*s, 14, 1247–1258. https://doi.org/10.5194/hess-14-1247-2010

Buytaert, W., Cuesta-Camacho, F., Tobón, C. (2011). Potential impacts of climate change on the environmental services of humid tropical alpine regions: Climate change and environmental services. *Global Ecology and Biogeography*, 20, 19–33. https://doi.org/10.1111/j.1466-8238.2010.00585.x

Buytaert, W., De Bièvre, B. (2012). Water for cities: The impacts of climate change and demographic growth in the tropical Andes. *Water Resources Rresearch,* 48: W08503, doi:10.1029/2011WR011755

Buytaert, W., Sevink, J., Cuesta, F., LLambi, L., Posner, J. (2014). Cambio climático: la nueva amenaza para los páramos, in: Avances En Investigación Para La Conservación de Los Páramos Andinos. Condesan, Lima, Peru.

Cao, W., Bowden, W.B., Davie, T., & Fenemor, A. (2006). Multi-variable and multi-site calibration and validation of SWAT in a large mountainous catchment with high spatial variability. *Hydrological Processes,* 20, 1057–1073.

Cartwright, I., Weaver, T.R., Fifield, L.K. (2006). Cl/Br ratios and environmental isotopes as indicators of recharge variability and groundwater flow: an example from the southeast Murray Basin, Australia, Chemical. Geology, 231, 38–56.

Cartwright, I., Currell, M.J., Cendón, D.I., Meredith, K.T. (2020). A review of the use of radiocarbon to estimate groundwater residence times in semi-arid and arid areas. *Journal of. Hydrology*, 580, 124247.

Carvajal, P.E., Anandarajah, G., Mulugetta, Y., Dessens, O. (2017). Assessing uncertainty of climate change impacts on long-term hydropower generation using the CMIP5 ensemble—the case of Ecuador. Climatic Change 144, 611–624. https://doi.org/10.1007/s10584-017-2055-4

Castaño-Uribe, C. (2002). Páramos y ecosistemas alto andinos de Colombia en condición de hotspot y global climatic tensor. Ed. IDEAM, Bogotá, Colombia. 387 pp. (in Spanish)

Castellanos-Osorio, G., López-Ballesteros, A., Pérez-Sánchez, J., Senent-Aparicio, J. (2023). Disaggregated monthly SWAT+ model versus daily SWAT+ model for estimating environmental flows in Peninsular Spain. Journal Hydrology, 623, 129837. https://doi.org/10.1016/j.jhydrol.2023.129837

Célleri, R., Feyen, J. (2009). The Hydrology of Tropical Andean Ecosystems: Importance, Knowledge Status, and Perspectives. *Mointain Research and Development*, 29, 350–355. https://doi.org/10.1659/mrd.00007

Célleri, R., Buytaert, W., De Bièvre, B., Tobón, C., Crespo, P., Molina, J., Feyen, J. (2010). Understanding the hydrology of tropical Andean ecosystems through an Andean Network of Basins. Status and Perspectives of Hydrology in Small Basins. *IAHS-AISH Publication*, 336, 209–212.

Changkuon, L., Aranyossy, J.F., Oleas, M., Lopoukine, M. (1989). Determination of the geothermal model of the Chillos Valley (Ecuador), based on environmental isotopes, In: Isotope Hydrology investigations in Latin America (IAEA, Ed.), Vienna, Austria, 291–303 (in Spanish with abstract in English).

Chen, Z., Grasby, S.E., Osadetz, K.G. (2004). Relation between climate variability and groundwater levels in the upper carbonate aquifer, southern Manitoba, Canada. *Journal of Hydrology*, 290, 43–62.

Chen, J., Brissette, F.P., Chaumont, D., Braun, M. (2013). Performance and uncertainty evaluation of empirical downscaling methods in quantifying the climate change impacts on hydrology over two North American river basins. *Journal of Hydrology*. 479, 200–214. https://doi.org/10.1016/j.jhydrol.2012.11.062

Chen, Y., Chen, X., Xu, C.Y., Zhang, M., Liu, M., Gao, L. (2018). Toward improved calibration of SWAT using season-based multi-objective optimization: a case study in the Jinjiang Basin in southeastern China. Water Resources Management, 32 (4), 1193–1207. https://doi.org/10.1007/s11269-017-1862-8.

Chiew, F.H.S., Peel, M.C., McMahon, T.A., Siriwardena, L.W. (2006). Precipitation elasticity of streamflow in catchments across the world, in: Climate Variability and Change: Hydrological Impacts, IAHS Publication. Presented at the 5th FRIEND World Conference, IAHS Press, Havana, CUBA, pp, 256–262.

Chu, T.W., Shirmohammadi, A. (2004). Evaluation of the SWAT model's hydrology component in the Piedmont physiographic region of Maryland. *Transactions of the ASAE,* 47, 1057–1073.

Chung, I.M., Kim, N.W., Lee, J., & Sophocleous, M. (2010). Assessing distributed groundwater recharge rate using integrated surface water-groundwater modelling: application to Mihocheon watershed, South Korea. *Hydrogeology Journal,* 18, 1253–1264.

Clapperton, C.M. (1993). Quaternary Geology and Geomorphology of South America. Elsevier, Amsterdam, 796 pp.

Clark, I.D., Fritz, P. (1997). Environmental Isotopes in Hydrogeology. CRC Press.

CLIRSEN-EMAAP-Q, (2006). Diagnóstico Ambiental de la Cuenca del Río Pita. Memoria Técnica. Quito.

Conan, C., Bouraoui, F., Turpin, N., De Marsily, G., & Bidoglio, G. (2003). Modeling flow and nitrate fate at catchment scale in Brittany (France). *Journal of. Environmental Quality,* 32, 2026–2032.

Cook, P.G., Love, A.J., Robinson, N.I., Simmons, C.T. (2005). Groundwater ages in fractured rock aquifers. *Journal of Hydrology,* 308, 284–301.

Crespo, P., Cisneros, F., Torres, P., Célleri, R., & Feyen, J. (2006). Efecto de la escala de información sobre el desempeño del modelo SWAT en una microcuenca de montaña. In: X Congreso Ecuatoriano de la Ciencia del Suelo. Guayaquil, Ecuador, 1–47.

Crespo, P., Célleri, R., Buytaert, W., Feyen, J., Iñiguez, V., Borja, P., De Bievre, B. (2010). Land use change impacts on the hydrology of wet Andean páramo ecosystems. *International Association of Hydrological Sciences,* 336, 71–76.

Crespo, P., Feyen, J., Buytaert, W., Bucker, A., Breuer, L., Frede, H., Ramírez, M. (2011). Identifying controls of the rainfall-runoff response of small catchments in the tropical Andes (Ecuador). Journal of Hydrology, 407, 164-174.

Crespo, P., Célleri, R., Buytaert, W., Ochoa, B., Cárdenas, I., Íñiguez, V., Borja, P., De Bièvre, B. (2014). Impactos del cambio de uso de la tierra sobre la hidrología de los páramos húmedos andinos. In: Avances en investigación para la conservación de los páramos andinos (Cuesta F et al.), CODESAN Ed, 287–304.

Cresso, M., Clerici, N., Sanchez, A., Jaramillo, F. (2020). Future Climate Change Renders Unsuitable Conditions for Paramo Ecosystems in Colombia. Sustainability 12, 8373. https://doi.org/10.3390/su12208373

Cuesta, F., Muriel, P., Llambí, L.D., Halloy, S., Aguirre, N., Beck, S., Carilla, J., Meneses, R.I., Cuello, S., Grau, A., Gámez, L.E., Irazábal, J., Jácome, J., Jaramillo, R., Ramírez, L., Samaniego, N., Suárez-Duque, D., Thompson, N., Tupayachi, A., Viñas, P., Yager, K., Becerra, M.T., Pauli, H., Gosling, W.D. (2017). Latitudinal and altitudinal patterns of plant community diversity on mountain summits across the tropical Andes. Ecography 40, 1381–1394. https://doi.org/10.1111/ecog.02567

Cuffey, K., Paterson, W.S.B. (2010). The Physics of Glaciers, 4th Ed., Academic Press, Burlington and Oxford, 704 pp.

Custodio, E., Jódar, J. (2016). Simple solutions for steady-state diffuse recharge evaluation in sloping homogeneous unconfined aquifers by means of atmospheric tracers. *Journal of. Hydrology*, 540, 287–305. https://doi.org/10.1016/j.jhydrol.2016.06.035.

Davis, S.N., Fabryka-Martin, J., Wolfsberg, L.E. (2004). Variations of bromide in potable ground water in the United States. Ground Water, 42, 902–909.

de Moor, J. M., Kern, C., Avard, G., Muller, C., Aiuppa, A., Saballos, A., Ibarra, M., LaFemina, P., Protti, M., Fischer, T.P. (2017). A new sulfur and carbon degassing inventory for the Southern Central American Volcanic Arc: The importance of accurate time-series data sets and possible tectonic processes responsible for temporal variations in arc-scale volatile emissions. *Geochemistry, Geophysics, Geosystems*, 18, 4437–4468.

De Vries, J.J., Simmers, I. (2002). Groundwater recharge: an overview of processes and challenges. Hydrogeology Journal, 10, 5–17.

Deines, P. (1980). The isotopic composition of reduced organic carbon. In: P. Fritz and J.C. Fontes (Eds.), Hand book of Environmental Isotope Geochemistry. Elsevier, Amsterdam, pp. 329-406.

Dettinger, M.D., Earman, S. (2007). Western ground water and climate change-pivotal to supply sustainability or vulnerable in its own right?. *Ground Water*, 4, 4–5.

Devi, G.K, Ganasri, B.P., & Dwarakish, G.S. (2015). A review on hydrological models. *Aquatic Procedia*, 4, 1001–1007.

Di Luzio, M., Srinivasan, R., Arnold, J.G., & Neitsch, S.L. (2002). ArcView interface for SWAT 2000, user's guide. Grassland soil and water research laboratory and USDA agricultural research service, Blackland research center, Texas agricultural experiment station. Texas water resources institute, College station, Texas TWRI Report TR, 193, 351.

Digital Elevation Model (DEM), 30-m resolution. Available from: http://www.savgis.org/ecuador.htm

Dile, Y.T., Daggupati, P., George, C., Srinivasan, R., Arnold, J. (2016). Introducing a new open source GIS user interface for the SWAT model. *Environmental Modelling & Software*, 85, 129–138. https://doi.org/10.1016/j.envsoft.2016.08.004

Döll, P. (2009). Vulnerability to the impact of climate change on renewable groundwater resources: a global-scale assessment. *Environmental Research Letters*, 4, 035006. https://doi.org/10.1088/1748-9326/4/3/035006

Eberhart, R.C., Kennedy, J. (1995). A new optimizer using particle swarm theory. Proceedings of the sixth international symposium on micro machine and human science. Nagoya, Japan, August, 39–43.

Eckhardt, K., Fohrer, N., Frede, H.-G. (2005). Automatic model calibration. Hydrology Processes, 19, 651–658. https://doi.org/10.1002/hyp.5613

Eckhardt, K. (2008). A comparison of baseflow indices, which were calculated with seven different baseflow separation methods. *Journal of Hydrology*, 352, 168–173.

Edmunds, W.M. (2012). Limits to the availability of groundwater in Africa. *Environmental. Research. Letter*, 7, 021003.

Ehtiat, M., Mousavi, S.J., Vaghefi, S.A., Ghaheri, A. (2016). Analysis of recharge conceptualization in inverse groundwater modelling. *Hydrological Sciences Journal,* 61, 2789–2801.

Ekwurzel, B., Schlosser, P., Smethie, W.M., Plummer, L.N., Busenberg, E., Michel, R.L., Weppernig, R., Stute, M. (1994). Dating of shallow groundwater: comparison of the transient tracers $^{3}H/^{3}He$, chlorofluorocarbons, and ^{85}Kr. *Water Resources Research,* 30, 1693–1708.

EPMAPS. (2006a). CAP-1 borehole drilling report: The Pita aquifer. Technical Report. EPMAPS Repository (in Spanish).

EPMAPS. (2006b). CAP-2 borehole drilling report: The Pita aquifer. Technical Report. EPMAPS Repository (in Spanish).

EPMAPS. (2012). Hydrogeological map of the metropolitan district of Quito (scale 1:250,000). Ed. International Association of Hydrogeologists - Ecuadorian Group 2, 25–30 (in Spanish).

EPMAPS. (2017). Public Water Supply Company of Quito database repository (accessed on 15 June 2017).

Erazo, B., Bourrel, L., Frappart, F., Chimborazo, O., Labat, D., Domínguez-Granda, L., Matamoros, D., Mejía, R. (2018). Validation of Satellite Estimates (Tropical Rainfall Measuring Mission, TRMM) for Rainfall Variability over the Pacific Slope and Coast of Ecuador, *Water,* 10, 213, doi:10.3390/w10020213.

España, S., Alcalá, F.J., Vallejos, Á., Pulido-Bosch, A., (2011). ArcE: A GIS tool for modelling actual evapotranspiration. Computer & Geosciences, 37, 1468–1475. https://doi.org/10.1016/j.cageo.2011.03.008

España, S., Alcalá, F.J., Vallejos, A., Pulido-Bosch, A. (2013). A GIS tool for modelling annual diffuse infiltration on a plot scale. *Computers & Geosciences*, 54, 318-325. https://doi.org/10.1016/j.cageo.2013.01.017

Espinosa, J., Rivera, D. (2016). Variations in water resources availability at the Ecuadorian páramo due to land-use changes. *Environmental Earth Sciences,* 75, 1173. https://doi.org/10.1007/s12665-016-5962-1

Espinoza-Villar, J.C., Ronchail, J., Guyot, J.L., Cochonneau, G., Naziano, F., Lavado, W., De Oliveira, E., Pombosa, R., Vauchel, P. (2009). Spatio-temporal rainfall variability in the Amazon basin countries (Brazil, Peru, Bolivia, Colombia, and

Ecuador). *International Journal of Climatology*, 29, 1574–1594. https://doi.org/10.1002/joc.1791

FAO / UNESCO, (1988). Soil Map of the World: Revised Legend; FAO World Resources Report 60; Food and Agricultural Organization of the United Nations. Rome, Italy.

FAO, (2015). World Reference Base for Soil Resources. World Soil Resources Reports Nº 106. United Nations, Rome, Italy, 192 pp.

FAO, IIASA, ISRIC, ISSCAS y JRC. (2012). Harmonized World Soil Database (vs 1.2), FAO, Rome, Italy and IIASA. Laxenburg, Austria.

Favier, V., Coudrain, A., Cadier, E., Francou, B., Ayabaca, E., Maisincho, L., Pradeiro, E., Villacís, M., Wagnon, P. (2008). Evidence of groundwater flow on Antizana ice-covered volcano, Ecuador / Mise en évidence d'écoulements souterrains sur le volcan englacé Antizana, Equateur. *Hydrological Sciences Journal*, 53, 278–291. https://doi.org/10.1623/hysj.53.1.278

Feininger, T., Seguin, M.K. (1983). Simple Bouguer gravity anomaly field and the inferred crustal structure of continental Ecuador. *Geology*, 11, 40–44.

Fernández, J.A., Martínez, C., Magdaleno, F. (2012). Application of indicators of hydrologic alterations in the designation of heavily modified water bodies in Spain. Environmental Science & Policy 16, 31–43. https://doi.org/10.1016/j.envsci.2011.10.004

Flores-López, F., Galaitsi, S., Escobar, M., Purkey, D. (2016). Modeling of Andean Páramo Ecosystems' Hydrological Response to Environmental Change. *Water*, 8, 94. https://doi.org/10.3390/w8030094

FONAG, (2018). Diagnosis and action plans for integrated protection of water resources in areas of water interest: High Pita and eastern water units. Technical Report. Fund for the Protection of Water. Quito - Ecuador, 89 pp (in Spanish)

FONAG, (2022). Fondo para la protección del agua [WWW Document]. URL https://www.fonag.org.ec/web/ (accessed 6.12.22).

Fontes, J.C., Gonçalves, M.C., Pereira, L.S. (2004). Andosols of Terceira, Azores: measurement and significance of soil hydraulic properties. *Catena,* 56, 145–154

Francesconi, W., Srinivasan, R., Pérez-Miñana, E., Willcock, S.P., Quintero, M. (2016). Using the Soil and Water Assessment Tool (SWAT) to model ecosystem services: A systematic review. *Journal of Hydrology,* 535, 625–636.

Francesconi, W., Uribe, N., Valencia, J., Quintero, M. (2018). *Modeling for management a case study of the Cañete watershed, Peru*. In: Andean Hydrology (Rivera DA, Godoy-Faundez A, Lillo-Saavedra M., eds.). CRC Press, Boca Raton, FL, 84–101.

Freeze, R.A., Cherry, J.A. (1979). Groundwater, Prentice Hall, Inc., Upper Saddle River, NJ.

Gamble, A., Babbar-Sebens, M. (2012). On the use of multivariate statistical methods for combining in-stream monitoring data and spatial analysis to characterize water quality conditions in the White River Basin, Indiana, USA. *Environmental Monitoring and Assessment,* 184, 845–875.

Gan, T.Y., Dlamini, E.M., Biftu, G.F. (1997). Effects of model complexity and structure, data quality, and objective functions on hydrologic modeling. *Journal of Hydrology*, 192, 81–103. https://doi.org/10.1016/S0022-1694(96)03114-9

Garreaud, R.D. (2009). The Andes climate and weather. Advances in Geosciences. 22, 3-11.

Garreaud, R., Falvey, M. (2009). The coastal winds off western subtropical South America in future climate scenarios, *International Journal of Climatology*, 29, 543–554, doi:10.1002/joc.1716, 2009.

Garrison, J.M., Davidson, J.P., Hall, M., Mothes, P. (2011). Geochemistry and Petrology of the Most Recent Deposits from Cotopaxi Volcano, Northern Volcanic Zone, Ecuador. *Journal of Petrology*, 52, 1641–1678. https://doi.org/10.1093/petrology/egr023

Gassman, P.W., Reyes, M.R., Green, C.H., Arnold, J.G. (2007). The soil and water assessment tool: historical development, applications and future research directions. *American Society of Agricultural and Biological Engineers,* 50, 1211–1250. https://doi.org/10.13031/2013.23637

Gassman, P.W., Sadeghi, A.M., Srinivasan, R. (2014). Applications of the SWAT model special section: Overview and insights. *Journal of Environmental Quality,* 43, 1–8. https://doi.org/10.2134/jeq2013.11.0466

Gerrits, A.M.J., Savenije, H.H.G., Veling, E.J.M., & Pfister, L. (2009). Analytical derivation of the Budyko curve based on rainfall characteristics and a simple evaporation model. *Water Resources Research,* 45, W04403. doi:10.1029/2008WR007308.

Gonzales-Zeas, D., Erazo, B., Lloret, P., De Bièvre, B.D, Steinchneider, S., Dangles, O. (2019). Linking global climate change to local water availability: Limitations and prospects for a tropical mountain watershed. *Science of the Total Environment,* 650, 2577-2586. https://doi.org/10.1016/j.scitotenv.2018.09.309

Green, T.R., Taniguchi, M., Kooi, H. (2007). Potential impacts of climate change and human activity on subsurface water resources. *Vadose Zone Journal*, 6, 531–532. https://doi.org/10.2136/vzj2007.0098

Green, T., Taniguchi, M., Kooi, H., Gurdak, J., Allen, D., Hiscock, K., Treidel, H., Aureli, A. (2011). Beneath the surface of global change: impacts of climate change on groundwater. *Journal of Hydrology,* 405, 532-560. https://doi.org/10.1016/j.jhydrol.2011.05.002

Gupta, H.V., Sorooshian, S., Yapo, P.O. (1999). Status of automatic calibration for hydrologic models: Comparison with multilevel expert calibration. *Journal of Hydrologic Engineering,* 4, 135–143. https://doi.org/10.1061/(ASCE)1084-0699(1999)4:2(135)

Gupta, H.V., Kling, H., Yilmaz, K.K., Martinez, G.F. (2009). Decomposition of the mean squared error and NSE performance criteria: Implications for improving hydrological modelling. *Journal of Hydrology*, 377, 80–91. https://doi.org/10.1016/j.jhydrol.2009.08.003

Gutiérrez-Salazar, P., Medrano-Vizcaíno, P. (2019). The effects of climate change on decomposition processes in Andean paramo ecosystem–synthesis, a systematic review. *Applied Ecology and Envonmental Research*, 17, 4957–4970. https://doi.org/10.15666/aeer/1702_49574970

Gyamfi, C., Ndambuki, J.M., Anornu, G.K., Kifanyi, G.E. (2017). Groundwater recharge modelling in a large scale basin: an example using the SWAT hydrologic model. *Modeling Earth Systems and Environment,* 3, 1361–1369.

Hall, M.L., Wood, C.A. (1985). Volcano-tectonic segmentation of the northern Andes. *Geology*, 13, 203–207. https://doi.org/10.1130/0091-7613(1985)13<203:VSOTNA>2.0.CO;2

Hall, M., Mothes, P. (2008). The rhyolitic-andesitic eruptive history of Cotopaxi volcano, Ecuador. *Bulletin of Volcanology*, 70, 675–702. https://doi.org/10.1007/s00445-007-0161-2

Hammersley, L., De Paolo, D.J., Beate, B. (2000). Chalupas Caldera, Ecuador: A study of the development of a large volume rhyolite system in the northern Andes. IAVCEI General Assembly, Bali, Indonesia.

Han, M., Zhao, C., Šimůnek, J., Feng, G. (2015). Evaluating the impact of groundwater on cotton growth and root zone water balance using Hydrus-1D coupled with a crop growth model. *Agricultural Water Management,* 160, 64–75.

Han, L.F., Wassenaar, L.I., (2021). Principles and uncertainties of 14C age estimations for groundwater transport and resource evaluation. *Isotopes in Environmental and Health Studies*, 57, 111–141.

Hargreaves, G.H. (1994). Defining and Using Reference Evapotranspiration. *Journal of Irrigation and Drainage Engineering-ASCE* 120, 1132–1139. https://doi.org/10.1061/(ASCE)0733-9437(1994)120:6(1132)

Harmel, R.D., Cooper, R.J., Slade, R.M., Haney, R.L, Arnold, J.G. (2006). Cumulative uncertainty in measured stream flow and water quality data for small watersheds. *Transactions of the ASAE*, 49, 689–701.

Hasan, M.M., Wyseure, G. (2018). Impact of climate change on hydropower generation in Rio Jubones Basin, Ecuador. *Water Science and Engineering,* 11, 157–166.

Hautman, D.P., Munch, D.J. (1997). EPA 300 1. Determination of Inorganic Anions in Drinking Water by Ion Chromatography. Revision 1.0. USEPA, Office of Water. EPA, Cincinnati, Ohio, 40 pp.

Healy, R.W., Cook, P.G. (2002). Using groundwater levels to estimate recharge. *Hydrogeology Journal,* 10, 91–109.

Hemmings, B., Whitaker, F., Gottsmann, J., Hawes, M.C. (2016). Non-eruptive ice melt driven by internal heat at glaciated stratovolcanoes. *Journal Volcanology*

Geothermal Research, 327, 385–397. https://doi.org/10.1016/j.jvolgeores.2016.09.004

Herrera, C., Custodio, E. (2014). Origin of waters from small springs located at the northern coast of Chile, in the vicinity of Antofagasta. *Andean Geology*, 41, 314–341.

Herzog, S.K., Martinez, R., Jørgensen, P.M., Tiessen, H. (2012). Climate Change and Biodiversity in the Tropical Andes [Spanish]. – Inter–American Institute for Global Change Research (IAI), Montevideo and Scientific Committee on Problems of the Environment (SCOPE).

Hilberts, A.G.J, van Loon, E.E., Troch, P.A., Paniconi, C. (2004). The hillslope-storage Boussinesq model for non-constant bedrock slope. *Journal of Hydrology*, 291, 160–173.

Hojberg, A.L., Refsgaard, J.C. (2005). Model uncertainty-parameter uncertainty versus conceptual models. *Water Science and Technology*, 52, 177–186.

Holman, I.P. (2006). Climate change impacts on groundwater recharge-uncertainty, shortcomings, and the way forward? *Hydrogeology Journal,* 14, 637–647.

Horner, K.N., Short, M.A., McPhail, D.C. (2017). Chloride and bromide sources in water: quantitative model use and uncertainty., Journal of. Hydrology, 549, 571–580.

Huang, T., Pang, Z., Liu, J., Yin, L., Edmunds, W.M. (2017). Groundwater recharge in an arid grassland as indicated by soil chloride profile and multiple tracers. *Hydrology Processes*. 31, 1047–1057.

Huber, A., Bach, M., Frede, H.G. (1998). Modeling pesticide losses with surface runoff in Germany. *Science of the Total Environment,* 223, 177–191.

Hughes, R.A., Pilatasig, L.F. (2002). Cretaceous and Tertiary terrane accretion in the Cordillera Occidental of the Ecuadorian Andes. *Tectonophysics*, 345, 29–48.

Ibáñez, J., Gartzia, R., Alcalá, F.J., Martínez-Valderrama, J. (2022). The importance of prevention in tackling desertification: an approach to anticipate risks of degradation in coastal aquifers. *Land,* 11, 1626.

Ilbay-Yupa, M., Ilbay, F., Zubieta, R., García-Mora, M., Chasi, P. (2021). Impacts of Climate Change on the Precipitation and Streamflow Regimes in Equatorial Regions: Guayas River Basin. *Water,* 13, 3138. https://doi.org/10.3390/w13213138

INAMHI, (2017). National Institute for Meteorology and Hydrology database repository (accessed on 15 June 2017).

INEC, (2018a). Census of population and housing 2010: Province of Pichincha. Technical Report. National Institute of Statistics and Census. Government of Ecuador, Quito 8 pp (in Spanish)

INEC, (2018b). Census of population and housing 2010: Province of Napo. Technical Report. National Institute of Statistics and Census. Government of Ecuador, Quito 8 pp (in Spanish)

IPCC, (2007). Climate Change 2007: Impacts, Adaptation and Vulnerability. In: Contribution of Working Group II to the Fourth Assessment Report of the Intergovernmental Panel on Climate Change, Cambridge University Press.

Izady, A., Davary, K., Alizadeh, A., Ziaei, A.N., Akhavan, S., Alipoor, A., Joodavi, A., Brusseau, M.L. (2015). Groundwater conceptualization and modeling using distributed SWAT based recharge for the semi-arid agricultural Neishaboor plain, Iran. *Hydrogeology Journal*, 23, 47–68.

Jain, S.K., Jain, S.K., Jain, N., Xu, C.Y. (2017). Hydrologic modeling of a Himalayan mountain basin by using the SWAT model. *Hydrology an Earth System Sciences*. 1-26. https://doi.org/10.5194/hess-2017-100

Jajarmizadeh, M., Harun, S., Salarpour, M. (2012). A review on theoretical consideration and types of models in hydrology. *Journal of Environmental Science and Technology*, 5, 249–261.

Jimeno-Sáez, P., Senent-Aparicio, J., Pérez-Sánchez, J., Pulido-Velazquez, D. (2018). A Comparison of SWAT and ANN Models for Daily Runoff Simulation in Different Climatic Zones of Peninsular Spain. *Water* 10, 192. https://doi.org/10.3390/w10020192

Jimeno-Sáez, P., Blanco-Gómez, P., Pérez-Sánchez, J., Cecilia, J.M., Senent-Aparicio, J. (2021). Impact Assessment of Gridded Precipitation Products on Streamflow Simulations over a Poorly Gauged Basin in El Salvador. *Water*, 13, 18, 2497. https://doi.org/10.3390/w13182497

Jin, G., Shimizu, Y., Onodera, S., Saito, M., Matsumori, K. (2015). Evaluation of drought impact on groundwater recharge rate using SWAT and Hydrus models on an agricultural island in western Japan. *Proc. IAHS*, 371, 143–148.

Jung, Y., Shin, Y., Won, N.I., Lim, K.J. (2016). Web-Based BFlow System for the Assessment of Streamflow Characteristics at National Level. *Water*, 8, 384.

Kazemi, G.A., Lehr, J.H., Perrochet, P. (2006). Groundwater Age. Wiley, Hoboken, p, 325.

Khosravi, K., Mao, L., Kisi, O., Yaseen, Z.M., Shahid, S. (2018). Quantifying hourly suspended sediment load using data mining models: Case study of a glacierized Andean catchment in Chile. *Journal of Hydrology,* 567, 165–179.

Kilsby, C., Tellier, S., Fowler, H., Howels, T. (2007). Hydrological impacts of climate change on the Tejo and Guadiana Rivers. *Hydrology and Earth System Sciences,* 11, 1175–1189. https://doi.org/10.5194/hess-11-1175-2007

Kim, N.W., Chung, I.M., Won, Y.S., Arnold, J.G. (2008). Development and application of the integrated SWAT-MODFLOW model. *Journal of Hydrology,* 356, 1–16.

Kirtman, B., Power, S.B., Adedoyin, A.J., Boer, G.J., Bojariu, R., Doblas-Reyes, F., Fiore, A.M., Kimoto, M., Meehl, G., Prather, M., Sarr, A., Schär, C., Sutton, R., van Oldenborgh, G.J., Vecchi, G., Wang, H.-J. (2013). Near-term Climate Change: Projections and Predictability, in: Climate Change. The Physical Science Basis. Contribution of Working Group I to the Fifth Assessment Report of the Intergovernmental Panel on Climate Change. Cambridge University Press, Cambridge, UK, New York.

Kitzberger, T., Tiribelli, F., Barberá, I., Gowda, J.H., Morales, J.M., Zalazar, L., Paritsis, J. (2022). Projections of fire probability and ecosystem vulnerability under 21st century climate across a trans-Andean productivity gradient in Patagonia. *Science of The Total Environment,* 839, 156303. https://doi.org/10.1016/j.scitotenv.2022.156303

Kløve, B., Ala-Aho, P., Bertrand, G., Gurdak, J.J., Kupfersberger, H., Kvœrner, J., Muotka, T., Mykrä, H., Preda, E., Rossi, P., Bertacchi, U.C., Velasco, E., Wachniew, P., Pulido-Velázquez, M. (2014). Climate change impacts on groundwater and dependent ecosystems. *Journal of Hydrology,* 518, 250–266.

Koboltschnig, G., Litaor, I., López-Moreno, J., Lorentz, S., Schädler, B., Schreier, H., Schwaiger, K., Vuille, M., Woods, R. (2011). Climate change and mountain water

resources: Overview and recommendations for research, management and policy. *Hydrology and Earth System Sciences,* 15, 471–504.

Kovalevskii, V.S. (2007). Effect of climate changes on groundwater. *Water Resources,* 34, 140–152.

Krause, P., Boyle, D.P., Bäse, F. (2005). Comparison of different efficiency criteria for hydrological model assessment. *Advances Geosciences*, 5, 89–97.

Kuczera, G., Parent, E. (1998). Monte Carlo assessment of parameter uncertainty in conceptual catchment models: the Metropolis algorithm. *Journal of Hydrology,* 211, 69–85.

Kumar, A., Barnston, A., Peng, P., Hoerling, M.P., Goddard, L. (2000). Changes in the spread of the seasonal mean atmospheric states associated with ENSO. *Journal of Climate,* 13, 3139–3151.

Kumar, M., Bhatt, G., Duffy, C.J. (2009). An efficient domain decomposition framework for accurate representation of geodata in distributed hydrologic models. *International Journal of Geographical Information Science,* 23, 1569–1596.

Kumar, N., Dubey, A.K., Goswami, U.P., Singh, S.K. (2022). Modelling of hydrological and environmental flow dynamics over a central Himalayan river basin through satellite altimetry and recent climate projections. Intl Journal of Climatology 42, 8446–8471. https://doi.org/10.1002/joc.7734

Kundzewicz, Z.W., Mata, L.J., Arnell, N.W., Döll, P., Jimenez, B., Miller, K., Oki, T., Sen, Z., Shiklomanov, I. (2008). The implications of projected climate change for freshwater resources and their management. *Hydrological Sciences Journal,* 53, 3–10.

Lahuatte, B., Recalde, M. (2015). Physical-chemical properties of soils as evaluation instruments for restoration strategies implemented in degraded areas of páramos, case study: Catchments in Antisana and Pita. MSc Thesis, *National Polytechnic School*, Quito, 234 pp (in Spanish).

Larrea, O. (2016). Los Acuíferos de Quito, Una Reserva Estratégica [The Aquifers of Quito, A Strategic Reserve]. EPMAPS Repository, Quito, Ecuador.

Larrea, O., Peñafiel, L., Barragán, E., Betancourt, A., Valladares, M., Alulema, R., Pazmiño, E., Palacios, L., Fuertes, E., Chicaiza, S., de la Torre, M.I., Bernal, F., Cadena, V., Gourcy, L., Jakomin, L.M., Alcalá, F.J. (2016). Determinación de

zonas de recarga y dinámica del agua subterránea para una explotación sostenible en los valles orientales del Distrito Metropolitano de Quito [Determination of recharge zones and groundwater dynamics for sustainable exploitation in the eastern valleys of the Metropolitan District of Quito]. IAEA Repository. Scientific Report IAEA-ECU 7/006. Quito, Ecuador, 112 pp.

Lee, J., Kim, J., Jang, W., Lim, K.J., Engel, B.A. (2018). Assessment of Baseflow Estimates Considering Recession Characteristics in SWAT. *Water,* 10, 371.

Legates, D.R., McCabe Jr., G.J. (1999). Evaluating the use of "goodness-of-fit" Measures in hydrologic and hydroclimatic model validation. *Water Resources Research*. 35, 233–241. https://doi.org/10.1029/1998WR900018

Lerner, D.N., Issar, A.S., Simmers, I. (1990). Groundwater recharge. A guide to understanding and estimating natural recharge. IAH International Contributions to Hydrogeology. 8. Heise, Hannover, 345 pp.

Li, Z., Huang, T., Wang, G., Long, Y., Zhang, F., Pang, Z. (2022). A conceptual model for correcting groundwater 14C age. *Applied. Geochemistry*, 50, 222–230.

Lim, K.J., Engel, B.A., Tang, Z., Choi, J., Kim, K., Muthu, K.S., Tripathy, D. (2005). Automated Web GIS Based Hydrograph Analysis Tool, WHAT 1. *Journal of the American Water Resources Association,* 41, 1407–1416.

Litherland, M., Aspden, J., Jemielita, R.A. (1994). The Metamorphic Belts of Ecuador. Nottingham; British Geological Survey. Keyworth, UK, 1–147.

López, S., Wright, C., Costanza, P. (2017). Environmental change in the equatorial Andes: linking climate, land use, and land cover transformations. *Remote Sensing,* 8, 291–303.

López-Ballesteros, A., Senent-Aparicio, J., Martínez, C., Pérez-Sánchez, J. (2020). Assessment of future hydrologic alteration due to climate change in the Aracthos River basin (NW Greece). *Science Total Environment*, 733, 139299. https://doi.org/10.1016/j.scitotenv.2020.139299

López-Moreno, J.I., Vicente-Serrano, S.M., Moran-Tejeda, E., Zabalza, J., Lorenzo-Lacruz, J., García-Ruiz, J.M. (2011). Impact of climate evolution and land use changes on water yield in the Ebro basin. *Hydrology and Earth System Sciences,* 15, 311–322.

Luo, Y., Arnold, J., Allen, P., Chen, X. (2012). Baseflow simulation using SWAT model in an inland river basin in Tianshan Mountains, Northwest China. *Hydrology and Earth System Sciences,* 16, 1259–1267. https://doi.org/10.5194/hess-16-1259-2012

Lyne, V., Hollick, M. (1979). Stochastic time-variable rainfall-runoff modelling. *Institute of Engineers Australia National Conference. Publ*., 79, 89–93.

MAE. (2014). Informative guide of the protected natural areas of Ecuador. Technical Report. Ministry of Environment. Government of Ecuador, Quito 266 pp (in Spanish)

MAG-ORSTOM. (1978). Mapa de Suelos, hoja Quito, escala 1:50.000.

Makowski Giannoni, S., Trachte, K., Rollenbeck, R., Lehnert, L., Fuchs, J., Bendix, J. (2016). Atmospheric salt deposition in a tropical mountain rainforest at the eastern Andean slopes of south Ecuador – Pacific or Atlantic origin? *Atmospheric Chemistry and Physics,* 16, 10241–10261. https://doi.org/10.5194/acp-16-10241-2016

Malo, G., Egdo, L., Díaz, O. (1980). Geological Mapping of Ecuador: Full 85, Píntag (scale 1:100,000). Ed. Dirección General de Geología y Minas (DGGM). Government of Ecuador, Quito (in Spanish).

Mark, B.G., Bury, J., McKenzie, J.M., French, A., Baraer, M. (2010). Climate change and tropical Andean Glacier recession: Evaluating hydrologic changes and livelihood vulnerability in the Cordillera Blanca, Peru. *Annals of the Association of American Geographers,* 100, 794–805.

Martínez, R., Ruiz, D., Andrade, M., Blacutt, L. (2011). Synthesis of the climate of the tropical Andes, in: Climate Change Effects on the Biodiversity of the Tropical Andes: An Assessment of the Status of Scientific Knowledge. IAI-SCOPE, Paris.

Mason, E., Edmonds, M., Turchyn, A.V. (2017). Remobilization of crustal carbon may dominate volcanic arc emissions, *Science*, 357, 290–294.

McDonald, M.G., Harbaugh, A.W. (1988). A modular three-dimensional finite-difference ground-water flow model. US Geological Survey Techniques of Water Resources Investigations Report Book 6, Chapter A1, 528 pp.

Me, W., Abell, J.M., Hamilton, D.P. (2015). Effects of hydrologic conditions on SWAT model performance and parameter sensitivity for a small, mixed land use catchment in New Zealand. *Hydrology and Earth System Sciences,* 19, 4127–4147.

Mejía, L., Morocho, E., Colmet-Daage, F., Zebrowski, C. (1978). Soils Map of Quito (scale 1:200,000). Ed. National Programme for Agricultural Regionalization (PRONAREG) and Overseas Office of Scientific and Technical Research of France (ORSTOM). Ministry of Agriculture and Livestock of Ecuador, Quito (in Spanish).

Menking, K.M., Syed, K.H., Anderson, R.Y., Shafike, N.G., Arnold, J.G. (2003). Model estimates of runoff in the closed, semiarid Estancia basin, central New Mexico, USA. *Hydrological Sciences Journal,* 48, 953–970.

Minga-Leon, S., Gómez-Albores, M., Khalidou, M., Balcázar, L., Manzano-Solis, L., Cuervo-Robayo, A., Mastachi-Loza, A. (2018). Estimation of water yield in the hydrographic basins of southern Ecuador. *Hydrology and Earth System Sciences Discussions*. https://doi.org/10.5194/hess-2018-529

MINTUR. (2014). Bulletin of tourism statistics 2009–2013. Technical Report. Ministry of Tourism. Government of Ecuador, Quito, 160 pp (in Spanish)

MINTUR. (2017). Bulletin of tourism statistics 2012–2016. Technical Report. Ministry of Tourism. Government of Ecuador, Quito, 178 pp (in Spanish)

Mishra, Y., Nakamura, T., Babel, M.S., Ninsawat, S., Ochi, S. (2018). Impact of Climate Change on Water Resources of the Bheri River Basin, Nepal. *Water*, 10, 220. https://doi.org/10.3390/w10020220

Modica, E., Buxton, H.T., Plummer, L.N. (1998). Evaluating the source and residence times of groundwater seepage to streams, New Jersey Coastal Plain. *Water Resources Research*, 34, 2797–2810.

Mook, W.G. (2001). Environmental isotopes in the hydrological cycle: principles and applications. Paris: UNESCO/IAEA; IHP-V Technical Documents in Hydrology; No. 39, Vol. II.

Moriasi, D.N., Arnold, J.G, van Liew, M.W., Bingner, R.L., Harmel, R.D., Veith, T.L. (2007). Model evaluation guidelines for systematic quantification of accuracy in watershed simulations. *Transactions of the ASABE*, 50, 885–900. https://doi.org/10.13031/2013.23153

Moriasi, D.N., Wilson, B.N., Douglas-Mankin, K.R., Arnold, J.G., Gowda, P.H. (2012). Hydrologic and water quality models: Use, calibration, and validation. *Transactions of the ASABE,* 55, 1241–1247, doi:10.13031/2013.42265.

Moriasi, D.N., Gitau, D.N., Pai, N., Daggupati, P. (2015). Hydrologic and Water Quality Models: Performance Measures and Evaluation Criteria. *Transactions of the ASABE* 58, 1763–1785. https://doi.org/10.13031/trans.58.10715

Mothes, P., Hall, M., Janda, R. (1998). The enormous Chillos valley lahar: An ash-flow generated debris flow from Cotopaxi volcano, Ecuador. *Bulletin of Volcanology,* 59, 233–244.

Mothes, P., Hall, M., Andrade, D., Samaniego, P., Pierson, T., Ruiz, G., Yepes, H. (2004). Character, stratigraphy and magnitude of historical lahars of Cotopaxi volcano, Ecuador. *Acta Volcanologica,* 16, 85–107.

Muñoz, P., Orellana-Alvear, J., Célleri, R. (2021). Application of a Machine Learning Technique for Developing Short-Term Flood and Drought Forecasting Models in Tropical Mountainous Catchments, in: Djalante, R., Bisri, M.B.F., Shaw, R. (Eds.), Integrated Research on Disaster Risks, Disaster Risk Reduction. Springer International Publishing, Cham, pp. 11–35. https://doi.org/10.1007/978-3-030-55563-4_2

Muñoz, T. (2016). Contributions of Glacier Melting to the Upper Watershed of the Pita River, Ecuador. MSc Thesis, *Michigan Technological University*, 65 pp.

Nachtergaele, F., van Velthuizen, H., Verelst, L., Batjes, N., Dijkshoorn, K., van Engelen, V., Fischer, G., Jones, A., Montanarella, L., Petri, M. (2008). Harmonized World Soil Database. FAO, United Nations, Rome, Italy.

Narsimlu, B., Gosain, A.K., Chahar, B.R. (2013). Assessment of future climate change impacts on water resources of upper Sind River basin, India using SWAT model. *Water Resources Management,* 27, 3647–3662.

Nash, J.E., Sutcliffe, J.V. (1970). River flow forecasting through conceptual models. Part I: A discussion of principles. *Journal Hydrology*, 10, 282–290. https://doi.org/10.1016/0022-1694(70)90255-6.

Nathan, R.J., MaMahon, T. A. (1990). Evaluation of automated techniques for baseflow and recession analysis, *Water Resources Research,* 26, 1465–1473.

Neitsch, S.L., Arnold, J., Kiniry, J., Williams, J., King, K. (2005). Soil and water assessment tool, theoretical documentation. Version 2005, Blackland Research Center, ARS. Temple, Texas. Texas Water Resources Institute, College Station, Texas TWRI Report TR, 365, 566.

Neitsch, S.L., Arnold, J.G., Kiniry, J.R., Williams, J.R. (2011). Soil and water assessment tool theoretical documentation, version 2009. Grassland, Soil and Water Research Laboratory – Agricultural Research Service. Blackland Research Center – Texas Agricultural Experiment Station. Texas Water Resources Institute Technical Report No. 406, College Station, Texas 77843-2118. Available at https://swat.tamu.edu/docs/

Neitsch, S.L., Arnold, J.G., Kiniry, J.R., Williams, J.R. (2011). SWAT Theoretical Documentation.

Nejadhashemi, A.P., Shirmohammadi, A., Montas, H.J., Sheridan, J.M., Bosch, D.D. (2008). Watershed physical and hydrological effects on baseflow separation. *Journal of Hydrologic Engineering,* 13, 971–980.

Ngor, P.B., Oberdorff, T., Phen, C., Baehr, C., Grenouillet, G., Lek, S. (2018). Fish assemblage responses to flow seasonality and predictability in a tropical flood pulse system. Ecosphere 9, e02366. https://doi.org/10.1002/ecs2.2366

Obuobie, E. (2008). Estimation of groundwater recharge in the context of future climate change in the White Volta River basin, West Africa. Germany. PhD Thesis. *Rheinischen Friedrich-Wilhelms-Universität*, Bonn, Germany, 165 pp.

Ochoa-Tocachi, B.F., Buytaert, W., De Bièvre, B. (2016). Regionalization of land-use impacts on streamflow using a network of paired catchments. *Water Resources Research,* 52, 6710–6729. https://doi.org/10.1002/2016WR018596

Ochoa-Tocachi, B.F., Buytaert, W., Antiporta, J., Acosta, L., Bardales, J.D., Célleri, R., Crespo, P., Fuentes, P., Gil-Ríos, J., Guallpa, M., Llerena, C., Olaya, D., Pardo, P., Rojas, G., Villacís, M., Villazón, M., Viñas, P., De Bièvre, B. (2018). High-resolution hydrometeorological data from a network of headwater catchments in the tropical Andes. Sci Data 5, 180080. https://doi.org/10.1038/sdata.2018.80

Oñate-Valdivieso, F., Bosque-Sendra, J. (2014). Semidistributed Hydrological Model with Scarce Information: Application to a Large South American

Binational Basin. *Journal of Hydrologic Engineering,* 19. https://doi.org/10.1061/(ASCE)HE.1943-5584.0000853

Oñate-Valdivieso, F., Bosque-Sendra, J., Sastre-Merlin, A., Ponce, V.M. (2016). Calibration, validation and evaluation of a lumped hydrologic model in a mountain area in southern Ecuador. *Agrociencia,* 50, 945-963.

Osuch, M., Romanowicz, R., Wong, W.K. (2018). Analysis of low flow indices under varying climatic conditions in Poland. *Hydrology Research*, 49 2, 373–389. https://doi.org/10.2166/nh.2017.021.

Oudin, L., Hervieu, F., Michel, C., Perrin, C., Andréassian, V., Anctil, F., Loumagne, C. (2005). Which potential evapotranspiration input for a lumped rainfall-runoff model? Part 2—Towards a simple and efficient potential evapotranspiration model for rainfall-runoff modeling. *Journal of Hydrology,* 303, 290–306.

Palazón, L., Gaspar, L., Latorre, B., Blake, W.H., Navas, A. (2014). Evaluating the importance of surface soil contributions to reservoir sediment in alpine environments: a combined modelling and fingerprinting approach in the Posets-Maladeta Natural Park. *Solid Earth,* 5, 963–978.

Paniconi, C., Troch, P.A., van Loon, E.E., Hilberts, A.G.J. (2003). Hillslope-storage Boussinesq model for subsurface flow and variable source areas along complex hillslopes: 2. Intercomparison with a three-dimensional Richards equation model. *Water Resources Res*earch, 39, 1317. doi:10.1029/2002WR001730

Parra, V., Arumí, J.L., Muñoz, E. (2019). Identifying a suitable model for low-flow simulation in watersheds of south-central Chile: a study based on a sensitivity analysis. *Water* 11, 1506. https://doi.org/10.3390/w11071506.

Peñafiel, L. (2009). Geology and analysis of the groundwater resource in the southern Quito subbasin. Enginiering Thesis, *National Polytechnic School*, Quito, 158 pp (in Spanish).

Peñafiel, L., Alcalá, F.J., Barragán, E., Larrea. O. (2016a). Evaluación del balance hídrico en un área vulcano-sedimentaria de alta montaña poco monitorizada en la Cordillera de los Andes: acuífero del río Pita, norte de Ecuador. *Revista Latino-Americana de Hidrogeología,* 10, 502–508

Peñafiel, L., Alcalá, F.J., Barragán, E., Toro-Espitia, L., Larrea, O. (2016b). Uso de trazadores químicos e isotópicos para deducir el funcionamiento del acuífero

del río Pita, Cordillera de los Andes, norte de Ecuador. *Revista Latino-Americana de Hidrogeología,* 10, 495–501.

Peñafiel, L.A., Reyes, P.S., Alcalá F. J., Ramírez, M. R., Cabero, A. (2020). Fold-Axis Parallel Extension along the Southern Ending of the Quito (Ecuadorian Andes) Fault System: Implications in River Network and Aquifer Geometry. *Geotectonics*., 54, 256-265.

Peñafiel, L., Alcalá, F.J., Senent-Aparicio, J. (2021). Usefulness of Compiled Geophysical Prospecting Survey in Groundwater Research in the Metropolitan District of Quito in Northern Ecuador. *Applied Sciences*, 11, 11144.

Pérez-Sánchez, J., Senent-Aparicio, J., Martínez Santa-María, C., López-Ballesteros, A. (2020). Assessment of Ecological and Hydro-Geomorphological Alterations under Climate Change Using SWAT and IAHRIS in the Eo River in Northern Spain. *Water,* 12, 1745. https://doi.org/10.3390/w12061745

PETROECUADOR. (2005). Updated mapping of hydrogeological units and hydrographic basins of Ecuador referenced to the Hydrocarbon sector infrastructures (scale 1:1,000,000). Government of Ecuador, Quito (in Spanish).

Plesca, I., Timbe, E., Exbrayat, J.F., Windhorst, D., Kraft, P., Crespo, Vaché, K.B., Frede, H.G., Breuer, L. (2012). Model intercomparison to explore catchment functioning: Results from a remote montane tropical rainforest. *Ecological Modelling,* 239, 3–13.

Poeter, E., Anderson, D. (2005). Multimodel ranking and inference in ground water modeling. *Ground Water,* 43, 597–605.

Ponce-Vega, L.A. (2015). Puquios, qanats y manantiales: gestión del agua en el Perú antiguo. *Agricultura, sociedad y desarrollo,* 12, 279–296.

Pool, S., Francés, F., Garcia-Prats, A., Puertes, C., Pulido-Velazquez, M., Sanchis-Ibor, C., Schirmer, M., Yang, H., Jiménez-Martínez, J. (2021). Hydrological Modeling of the Effect of the Transition From Flood to Drip Irrigation on Groundwater Recharge Using Multi-Objective Calibration. Water Resources Research 57. https://doi.org/10.1029/2021WR029677

Pourrut, P. (1995). El agua en el Ecuador: clima, precipitaciones, escorrentía. Estudios de Geografía, Volumen 7.

Pulido-Velázquez, M., Peña-Haro, S., García-Prats, A., Mocholi-Almudever, A.F., Henriquez-Dole, L., Macian-Sorribes, H., Lopez-Nicolas, A. (2015). Integrated assessment of the impact of climate and land use changes on groundwater quantity and quality in the Mancha Oriental system (Spain). *Hydrology and Earth System Sciences,* 19, 1677–1693.

Pulido-Velazquez, D., García-Aróstegui, J.L., Molina, J.-L., Pulido-Velazquez, M., (2015b). Assessment of future groundwater recharge in semi-arid regions under climate change scenarios (Serral-Salinas aquifer, SE Spain). Could increased rainfall variability increase the recharge rate? *Hydrological Processes*, 29, 828–844. https://doi.org/10.1002/hyp.10191

Pulido-Velazquez, D., Collados-Lara, A.-J., Alcalá, F.J. (2018). Assessing impacts of future potential climate change scenarios on aquifer recharge in continental Spain. *Journal of Hydrology,* 567, 803–819. https://doi.org/10.1016/j.jhydrol.2017.10.077

Quintero, M., Wunder, S., Estrada, R.D. (2009). For services rendered? Modeling hydrology and livelihoods in Andean payments for environmental services schemes. *Forest Ecology and Management,* 258, 1871–1880.

Rahayuningtyas, C., Wu, R.S., Anwar, R., Chiang, L.C. (2014). Stream Flow Simulation by Incorporating Groundwater Recharge Prediction in the Upstream Lesti Watershed, East Java, Indonesia. *Terrestrial, Atmospheric and Oceanic Sciences,* 25, 881–892.

Rangwala, I., Miller, J.R. (2012). Climate change in mountains: a review of elevation-dependent warming and its possible causes. *Climatic Change*, 114, 527–547. https://doi.org/10.1007/s10584-012-0419-3

Raposo, J.R., Dafonte, J., Molinero, J. (2013). Assessing the impact of future climate change on groundwater recharge in Galicia-Costa, Spain. *Hydrogeology Journal,* 21, 459–479.

Refsgaard, J.C., van der Sluijs, J., Højberg, A.L., Vanrolleghem, P.A. (2007). Uncertainty in the environmental modelling process – a framework and guidance. *Environmental Modelling & Software,* 22, 1543–1556.

Ritchie, J.T. (1972). Model for predicting evaporation from a row crop with incomplete cover. *Water Resources Research,* 8, 1204–1213.

Rivadeneira-Vera, J.F., Zambrano-Mera, Y.E., Pérez-Martín, M.Á. (2020). Adapting water resources systems to climate change in tropical areas: Ecuadorian coast. Science Total Environment, 703, 135554. https://doi.org/10.1016/j.scitotenv.2019.135554

Rollenbeck, R., Fabian, P., Bendix, J. 2006. Precipitation dynamics and chemical properties in tropical mountain forests of Ecuador. Advances in Geosciences, 6, 73–76. https://doi.org/10.5194/adgeo-6-73-2006

Rollo, N. (2012). Modélisation des dynamiques de pollution diffuse dans le bassin versant de la rivère d'Auray. Quantification, caractérisation et gestion des apports nutritifs terrigènes. PhD Thesis. *University of Nantes*, France.

Rose, J. (1996). Quaternary Geology and Geomorphology of South America. *Journal of Quaternary Science* 11, 432–433.

Ross, M., Geurink, J., Said, A., Aly, A., Tara, P. (2005). Evapotranspiration Conceptualization in the Hspf-Modflow Integrated Models1. Journal of the American Water Resources Association. 41, 1013–1025. https://doi.org/10.1111/j.1752-1688.2005.tb03782.x

Rozanski, K., Araguás-Araguás, L., Gonfiantini, R. (1993). Isotopic patterns in modern global precipitation. *Geophysical Monograph*, 78, 1.

Ruiz-Pico, A, Cuenca, A.P., Agila, R.S., Criollo, D.M., Leiva-Piedra, J., Salazar-Campos, J. (2019). Hydrochemical characterization of groundwater in the Loja Basin (Ecuador), *Applied Geochemistry*, 104, 1–9. https://doi.org/10.1016/j.apgeochem.2019.02.008

Rutledge, A.T., Mesko, T.O. (1996). Estimated Hydrologic Characteristics of Shallow Aquifer Systems in the Valley and Ridge, the Blue Ridge, and the Piedmont Physiographic Provinces Based on Analysis of Streamflow Recession and Base Flow. U.S. Geological Survey: Reston, VA, USA, 58 pp.

Salmoral, G., Khatun, K., Llive, F., Madrid-López, C. (2018). Agricultural development in Ecuador: A compromise between water and food security? *Journal of Cleaner Production*, 202, 779–791.

Santhi, C., Arnold, J.G., Williams, J.R., Duglas, W.A., Srinivasan, R., Hauck, L.M. (2001). Validation of the SWAT model on a large river basin with point and

nonpoint sources. *Journal of the American Water Resources Association,* 37, 1169–1188.

Scanlon, B.R., Healy, R.W., Cook, P.G. (2002). Choosing appropriate techniques for quantifying groundwater recharge. *Hydrogeology Journal,* 10, 18–39.

Schaefer, L., Fegley, B. (2005). Alkali and halogen chemistry in volcanic gases on Io. *Icarus,* 173 (2), 454–468.

Schuol, J., Abbaspour, K.C. (2007). A daily weather generator for predicting rainfall and maximum–minimum temperature using monthly statistics based on a half-degree climate grid. *Ecological Modelling,* 201**,** 301–311.

Schuol, J., Abbaspour, K.C., Yang, H., Srinivasan, R., Zehnder, A.J.B. (2008). Modeling blue and green water availability in Africa. *Water Resources Research,* 44, 1–18.

Schwank, J., Escobar, R., Girón, G.H., Morán-Tejeda, E. (2014). Modeling of the Mendoza river watershed as a tool to study climate change impacts on water availability. *Environmental Science and Policy,* 43, 91–97.

Seddon, D., Kashaigili, J.J., Taylor, R.G., Cuthbert, M.O., Mwihumbo, C., MacDonald, A.M. (2021). Focused groundwater recharge in a tropical dryland: Empirical evidence from central, semi-arid Tanzania. Journal of Hydrology: Regional Studies 37, 100919. https://doi.org/10.1016/j.ejrh.2021.100919

Senent-Aparicio, J., Pérez-Sánchez, J., Carrillo-García, J., Soto, J. (2017). Using SWAT and Fuzzy TOPSIS to Assess the Impact of Climate Change in the Headwaters of the Segura River Basin (SE Spain). *Water*, 9, 149. https://doi.org/10.3390/w9020149

Senent-Aparicio, J., Alcalá, F.J., Liu, S., Jimeno-Sáez, P. (2020). Coupling SWAT Model and CMB Method for Modeling of High-Permeability Bedrock Basins Receiving Interbasin Groundwater Flow. *Water*, 12, 657. https://doi.org/10.3390/w12030657

Senent-Aparicio, J., George, C., Srinivasan, R. (2021a). Introducing a new post-processing tool for the SWAT+ model to evaluate environmental flows. Environmental Modelling & Software, 136, 563–571. https://doi.org/10.1016/j.envsoft.2020.104944

Senent-Aparicio, J., Jimeno-Sáez, P., López-Ballesteros, A., Giménez, J.G., Pérez-Sánchez, J., Cecilia, J.M., Srinivasan, R. (2021b). Impacts of swat weather generator statistics from high-resolution datasets on monthly streamflow simulation over Peninsular Spain. *Journal of Hydrology: Regional Studies*, 35, 100826. https://doi.org/10.1016/j.ejrh.2021.100826

Senent-Aparicio, J., Blanco-Gómez, P., López-Ballesteros, A., Jimeno-Sáez, P., Pérez-Sánchez, J. (2021c). Evaluating the Potential of GloFAS-ERA5 River Discharge Reanalysis Data for Calibrating the SWAT Model in the Grande San Miguel River Basin (El Salvador). Remote Sensing, 13, (16), 3299. https://doi.org/10.3390/rs13163299

Senent-Aparicio, J., Peñafiel, L., Alcalá, F.J., Jimeno-Sáez, P., Pérez-Sánchez, J. (2024). Climate change impacts on renewable groundwater resources in the andosol-dominated Andean Highland, Ecuador. *Catena*, 236, 107766. https://doi.org/10.1016/j.catena.2023.107766.

Sharpley, A.N., Williams, J.R. (1990). EPIC Erosion/Productivity Impact Calculator: 1. Model Documentation. U.S. Department of Agriculture Technical Bulletin N° 1768.

Silva, O. (2010). Evaluación del modelo hidrológico SWAT en la cuenca media del río Pao en Venezuela. *Revista Facultad Agronomía,* 36, 134–145.

Simpson, M.J., Jazaei, F., Clement, T.P. (2013). How long does it take for aquifer recharge or aquifer discharge processes to reach steady state? *Journal of Hydrology,* 501, 241–248.

Smyth, M., Clapperton, C. (1986). Late Quaternary volcanic debris avalanche at Cotopaxi, Ecuador. *Revista CIAF,* 11, 24–38.

Somers, L.D., McKenzie, J.M., Zipper, S.C., Mark, B.G., Lagos, P., Baraer, M. (2018). Does hillslope trenching enhance groundwater recharge and baseflow in the Peruvian Andes? *Hydrological Processes,* 32, 318–331. https://doi.org/10.1002/hyp.11423

Sophocleous, M., Perkins, S.P. (2000). Methodology and application of combined watershed and ground-water models in Kansas. *Journal of Hydrology,* 236, 185–201.

Spikings, R.A., Seward, D., Winkler, W., Ruiz, G.M. (2000). Low-temperature thermochronology of the northern Cordillera Real, Ecuador: Tectonic insights from zircon and apatite fission track analysis. *Tectonics*, 19, 649–668. https://doi.org/10.1029/2000TC900010

Stadnyk, T., Gibson, J.J., Longstaffe, F.J. (2014). Basin-Scale Assessment of Operational Base Flow Separation Methods. *Journal of Hydrologic Engineering*, 20. doi:10.1061/(ASCE)HE.1943-5584.0001089

Stahl, K., Hisdal, H., Hannaford, J., Tallaksen, L.M., van Lanen, H.A.J., Sauquet, E., Demuth, S., Fendekova, M., Jódar, J. (2010). Streamflow trends in Europe: evidence from a dataset of near-natural catchments. *Hydrology and Earth System Sciences,* 14, 2367–2382.

Stehr, A., Debels, P., Arumi, J.L., Romero, F., Alcayaga, H. (2009). Combining the Soil and Water Assessment Tool (SWAT) and MODIS imagery to estimate monthly flows in a data-scarce Chilean Andean basin. *Hydrological Sciences Journal,* 54, 1053–1067.

Stehr, A., Aguayo, M., Link, O., Parra, O., Romero, F., Alcayaga, H. (2010). Modelling the hydrologic response of a mesoscale Andean watershed to changes in land use patterns for environmental planning. *Hydrology and Earth System Sciences,* 14, 1963–1977.

Suckow, A. (2014). The age of groundwater – definitions, models and why we do not need this term. *Applied Geochemistry*, 50, 222–230.

Sun, H., Cornish, P.S. (2005). Estimating shallow groundwater recharge in the headwaters of the Liverpool Plains using SWAT. *Hydrological Processes*, 19, 795–807.

Szilagyi, J. (2003). Sensitivity analysis of aquifer parameter estimations based on the Laplace equation with linearized boundary conditions. *Water Resources Research,* 39, 1156, doi:10.1029/2002WR001564

Szilagyi, J. (2004). Heuristic continuous base flow separation. *Journal of Hydrologic Engineering*, 9, 311–318.

Tamay, J., Galindo-Zaldívar, J., Ruano, P., Soto, J., Lamas, F., Azañón, J.M. (2016). New insight on the recent tectonic evolution and uplift of the southern Ecuadorian Andes from gravity and structural analysis of the Neogene-

Quaternary intramontane basins. *Journal of South American Earth Sciences,* 70, 340–352.

Tassi, F., Aguilera, F., Darrah, T., Vaselli, O., Capaccioni, B., Poreda, R.J., Huertas, A.D. (2010). Fluid geochemistry of hydrothermal systems in the Arica-parinacota, Tarapacá and Antofagasta regions (northern Chile). *Journal of Volcanology and Geothermal Ressearch*, 192 (1–2), 1–15.

Tassi, F., Aguilera, F., Vaselli, O., Darrah, T., Medina, E. (2011). Gas discharges from four remote volcanoes in northern Chile (Putana, Olca, Irruputuncu and Alitar): a geochemical survey. Ann. Geophys. 54 (2). doi: 10.4401/ag-5173

Taylor, R.G., Scanlon, B., Döll, P., Rodell, M., van Beek, R., Wada, Y., Longuevergne, L., Leblanc, M., Famiglietti, J.S., Edmunds, M., Konikow, L., Green, T.R., Chen, J., Taniguchi, M., Bierkens, M.F.P., MacDonald, A., Fan, Y., Maxwell, R.M., Yechieli, Y., Gurdak, J.J., Allen, D.M., Shamsudduha, M., Hiscock, K., Yeh, P.J.-F., Holman, I., Treidel, H. (2013). Ground water and climate change. Nature Climate Change, 3, 322–329. https://doi.org/10.1038/nclimate1744

Tesfaye, Y.G., Meerschaert, M.M., Anderson, P.L. (2006). Identification of periodic autoregressive moving average models and their application to the modeling of river flows. *Water Resources Research,* 42, W01419, doi:10.1029/2004WR003772.

Tobin, K.J., Bennett, M.E. (2019). Improving Alpine Summertime Streamflow Simulations by the Incorporation of Evapotranspiration Data. *Water,* 11, 112.

Tobón, C., Arroyave, F.P. (2007). Inputs by fog and horizontal precipitation to the páramo ecosystems and their contribution to the water balance. In: Fourth International Conference on 4th International Conference on Fog, Fog Collection and Dew. La Serena, Chile, 233–236.

Tovar, C., Seijmonsbergen, A.C., Duivenvoorden, J.F. (2013). Monitoring land use and land cover change in mountain regions: An example in the Jalca grasslands of the Peruvian Andes. *Landscape and Urban Planning,* 112, 40–49. https://doi.org/10.1016/j.landurbplan.2012.12.003

Trenkamp, R., Kellogg, J.N., Freymueller, J.T., Mora, P. (2002). Wide plate margin deformation, southern Central America and northwestern South America, CASA GPS observations *Journal of South American Earth Sciences* 15, 157–171.

Uribe, N., Quintero, M. (2011). Aplicación del modelo hidrológico SWAT en la cuenca del rio Cañete. Centro Internacional de Agricultura Tropical. Technical Report. Cali, Colombia.

Uribe, N., Corzo, G., Quintero, M., Griensven, A., Solomatine, D. (2018). Impact of conservation tillage on nitrogen and phosphorus runoff losses in a potato crop system in Fuquene watershed, Colombia. *Agricultural Water Management*, 209, 62–72.

Urrutia, R., Vuille, M. (2009). Climate change projections for the tropical Andes using a regional climate model: Temperature and precipitation simulations for the end of the 21st century. *Journal of Geophysical Research Atmospheres,* 114, 1–15. https://doi.org/10.1029/2008JD011021

Urrutia, J., Guimerà, J., Custodio, E., Herrera, C., Jódar, J., Acosta, O., Ansón, I. (2022). Processes explaining the origin and evolution of groundwater composition in the Andean Precordillera and Altiplano of the Tarapacá Region of northern Chile. *Science of The Total Environment*, 805, 149742.

Vaghefi, S.A., Abbaspour, N., Kamali, B., Abbaspour, K.C. (2017). A toolkit for climate change analysis and pattern recognition for extreme weather conditions – Case study: California-Baja California Peninsula. Environmental Modelling & Software, 96, 181–198. https://doi.org/10.1016/j.envsoft.2017.06.033

Vaghefi, S.A., Iravani, M., Sauchyn, D., Andreichuk, Y., Goss, G., Faramarzi, M. (2019). Regionalization and parameterization of a hydrologic model significantly affect the cascade of uncertainty in climate-impact projections. *Climate Dynamics*. 53, 2861–2886. https://doi.org/10.1007/s00382-019-04664-w

Van der Hammen, T., Hooghiemstra, H. (2000). Neogene and Quaternary history of vegetation, climate, and plant diversity in Amazonia, *Quaternary Science Reviews,* 19, 725–742.

Van Griensven, A., Meixner, T. (2006). Methods to quantify and identify the sources of uncertainty for river basin water quality models. *Water Science and Technology*, 53, 51–59.

Velasco-Argüello, P. (2014). Hydrologic responses to climatic change in Paute river basin in Ecuador: A case study comparing SWAT (Solid and Water Assessment Tool) and WaterWorld. MSc Thesis. *University of London*, UK, 103 pp.

Vengosh, A., Hening, S., Ganor, J., Mayer, B., Weyhenmeyer, C.E., Bullen, T.D., Paytan, A. (2007). New isotopic evidence for the origin of groundwater from the Nubian Sandstone Aquifer in the Negev, Israel. *Applied Geochemistry*, 22, 1052–1073.

Vergara, W., Deeb, A.M., Valencia, A.M., Bradley, R.S., Francou, B., Zarzar, A., Grünwaldt, A., Haeussling, S.M. (2007). Economic impacts of rapid glacier retreat in the Andes. *EOS Transactions American Geophysical Union,* 88, 261–268. https://doi.org/10.1029/2007EO250001

Vincent, A., Violette, S., Aðalgeirsdóttir, G. (2019). Groundwater in catchments headed by temperate glaciers: A review. *Earth-Science Reviews,* 188, 59–76. https://doi.org/10.1016/j.earscirev.2018.10.017

Viviroli, D., Dürr, H.H., Messerli, B., Meybeck, M., Weingartner, R. (2007). Mountains of the world, water towers for humanity: Typology, mapping, and global significance. *Water Resources Research,* 43, W07447, doi:10.1029/2006WR005653.

Viviroli, D., Archer, D.R., Buytaert, W., Fowler, H.J., Greenwood, G.B., Hamlet, A. F., Huang, Y., Koboltschning, G., Litaor, M.L., López-Moreno, J.L., Lorentz, S., Schiidler, B., Schreier, B., Schwaiger, K., Vuille, M., Woods, R. (2011). Climate change and mountain water resources: Overview and recommendations for research, management and policy. *Hydrology and Earth System Sciences,* 15, 471–504. https://doi.org/10.5194/hess-15-471-2011

Vuille, M., Bradley, R.S., Werner, M., Keimig, F. (2003). 20th Century Climate Change in the Tropical Andes: Observations and Model Results, in: Diaz, H.F. (Ed.), Climate Variability and Change in High Elevation Regions: Past, Present & Future, Advances in Global Change Research. Springer Netherlands, Dordrecht, pp. 75–99. https://doi.org/10.1007/978-94-015-1252-7_5

Vuille, M., Francou, B., Wagnon, P., Juen, I., Kaser, G., Mark, B.G., Bradley, R.S. (2008). Climate change and tropical Andean glaciers: Past, present and future. *Earth-Science Reviews*, 89, 79–96. https://doi.org/10.1016/j.earscirev.2008.04.002

Vuille, M., Franquist, E., Garreaud, R., Lavado Casimiro, W.S., Cáceres, B. (2015). Impact of the global warming hiatus on Andean temperature: Global Warming Hatus in the Andes. *Journal Geophysical Research Atmospheres*, 120, 3745–3757. https://doi.org/10.1002/2015JD023126

Vuille, M., Carey, M., Huggel, C., Buytaert, W., Rabatel, A., Jacobsen, D., Soruco, A., Villacis, M., Yarleque, C., Elison Timm, O., Condom, T., Salzmann, N., Sicart, J.-E. (2018). Rapid decline of snow and ice in the tropical Andes – Impacts, uncertainties and challenges ahead. *Earth-Science Reviews*, 176, 195–213. https://doi.org/10.1016/j.earscirev.2017.09.019

Were, A., Villagarcía, L., Domingo, F., Alados-Arboledas, L., Puigdefábregas, J. (2007). Analysis of effective resistance calculation methods and their effect on modelling evapotranspiration in two different patches of vegetation in semi-arid SE Spain. *Hydrology and Earth System Sciences*, 11, 1529–1542. https://doi.org/10.5194/hess-11-1529-2007

Willems, P. (2009). A time series tool to support the multi-criteria performance evaluation of rainfall-runoff models. *Environmental Modelling & Software Journal,* 24, 311–321.

Winchell, M., Srinivasan, M., Di Luzio, M., Arnold, J. (2010). ArcSWAT interface for SWAT 2009. User's Guide. Blackland Research Center, Texas Agricultural Experiment Station, Grassland, Soil and Water Research Laboratory, USDA Agricultural Research Service, 490.

Woodward, G., Perkins, D.M., Brown, L.E. (2010). Climate change in freshwater ecosystems: impacts across multiple levels of organisation. *Philosophical Transactions of the Royal Society,* 365, 2093–2106.

Yang, J., Reichert, P., Abbaspour, K.C., Xia, J., Yang, H. (2008). Comparing uncertainty analysis techniques for a SWAT application to Chaohe Basin in China. *Journal of Hydrology,* 358**,** 1–23.

Yang, J.S., Chi, D.K. (2011). Correlation Analysis between Groundwater Level and Baseflow in the Geum River Watershed, Calculated Using the WHAT System. *Engineering Geology Journal,* 21, 107–116.

Young, B.E., Young, K.R., Josse, C. (2011). Vulnerability of Tropical Andean Ecosystems to Climate Change, in: Climate Change and Biodiversity in the

Tropical Andes. Inter-American Institute for Global Change Research (IAI) and Scientific Committee on Problems of the Environment (SCOPE), pp. 170–181.

Zhang, X., Srinivasan, R., Hao, E. (2007). Predicting hydrologic response to climate change in the Luohe River basin using the SWAT model. *Transactions of the ASABE*, 50, 901–910.

Zhiña, D., Montenegro, M., Montalván, L., Mendoza, D., Contreras, J., Campozano, L., Avilés, A. (2019). Climate Change Influences of Temporal and Spatial Drought Variation in the Andean High Mountain Basin. *Atmosphere*, 10, 558. https://doi.org/10.3390/atmos10090558

Zulkafli, Z., Buytaert, W., Manz, B., Rosas, C.V., Willems, P., Lavado-Casimiro, W., Guyot, J.-L., Santini, W. (2016). Projected increases in the annual flood pulse of the Western Amazon. *Environmental Research Letters*, 11, 014013. https://doi.org/10.1088/1748-9326/11/1/014013

IX – APPENDIXES

IX - APPENDIXES

APPENDIX A. ARTICLES PUBLISHED IN JCR JOURNALS

A1. Publication 1

Senent-Aparicio, J., Peñafiel, L., Alcalá, F.J., Jimeno-Sáez, P., Pérez-Sánchez, J. Climate change impacts on renewable groundwater resources in the andosol-dominated Andean highlands, Ecuador. *Catena*, 236, 107766. https://doi.org/10.1016/j.catena.2023.107766

Impact Factor 2022 (JCR): 6.200; Category: GEOSCIENCES, MULTIDISCIPLINARY; Ranking: 17/202 (Q1); Date of publication: 2024.

Catena 236 (2024) 107766

Contents lists available at ScienceDirect

Catena

journal homepage: www.elsevier.com/locate/catena

Climate change impacts on renewable groundwater resources in the andosol-dominated Andean highlands, Ecuador

Javier Senent-Aparicio [a,*], Lilia Peñafiel [a], Francisco Javier Alcalá [b,c], Patricia Jimeno-Sáez [a], Julio Pérez-Sánchez [d]

[a] Department of Civil Engineering, Catholic University of San Antonio, Campus de los Jerónimos s/n, 30107, Guadalupe, Murcia, Spain
[b] Departamento de Desertificación y Geo-Ecología, Estación Experimental de Zonas Áridas (EEZA–CSIC), 04120 Almería, Spain
[c] Instituto de Ciencias Químicas Aplicadas, Facultad de Ingeniería, Universidad Autónoma de Chile, 7500138 Santiago, Chile
[d] Department of Civil Engineering, Universidad de Las Palmas de Gran Canaria, Campus de Tafira, 35017 Las Palmas de Gran Canaria, Spain

ARTICLE INFO

Keywords:
Climate change
Andean highlands
Páramo ecosystem
Andosols
SWAT model
Ecuador

ABSTRACT

Climate change, coupled with adaptive human actions, will affect water resource access and availability for environmental requirements. Hydrological modelling is an effective strategy for forecasting climate and human impacts on water resources. Modelling tools are advised for sparse-data mountainous basins intended to supply densely populated urban areas in the future. In this context, the SWAT model is used to evaluate the impact of climate change on renewable groundwater resources in the Pita River basin (PRB), a representative area of the andosol-dominated *páramo* ecosystem in the Andean highlands projected to meet future water demand in the metropolitan district of Quito (MDQ), Ecuador. Based on data availability, a SWAT model is configured for the PRB over the period 2006–2015 and five regional climate models (RCMs) based on two Representative Concentration Pathway (RCP) emission scenarios (4.5 and 8.5) for the mid- (2040–2069) and long-term (2070–2099) future horizons are implemented. Hydrological modelling demonstrates increases in average temperature and precipitation of + 2 °C and + 3 % in the mid-term and + 4.5 °C and + 20 % in the long term, respectively. All the RCMs indicate less aquifer recharge in the mid-term. However, this pattern is softened, and even reversed, in several scenarios in the long term. Seasonal differences in streamflow and aquifer recharge in the baseline scenario are predicted to increase to + 23 %. The natural hydrological regime determined by thick porous allophane-rich andosols over virtually full moderate-permeability volcanic and volcano-sedimentary aquifers induces high streamflow and low aquifer recharge rates. Future hydrological regime could place the highly sensitive soil–vegetation dynamics of the *páramo* ecosystem at risk of degradation, with negative consequences for habitat preservation, in general, and stream water provision, in particular. Hence, groundwater is the safest option for water provision in the future.

1. Introduction

Climate change, coupled with particular adaptive human actions, will introduce a variety of physical and biological effects that directly impact hydrological processes and indirectly affect water availability for human and environmental requirements (Bovolo et al., 2009; Green et al., 2011, 2007). In mountainous regions, climate change is expected to strongly modify temporal and spatial temperature and precipitation patterns, with significant consequences for freshwater provision in low-lying areas (Kilsby et al., 2007; López-Moreno et al., 2011). According to projected regional climate scenarios, changes in long-term precipitation and temperature regimes are likely to increase the frequency and intensity of extreme rainfall events and dry spells, altering the dynamics of crucial water balance components such as soil moisture, streamflow and infiltration (Blanco-Gómez et al., 2019; Buytaert et al., 2010; Green et al., 2011; Mishra et al., 2018; Pulido-Velazquez et al., 2018) with repercussions for water supply, food provision, hydropower generation and the preservation of dependent ecosystems. In mountainous areas, identifying water resource generation mechanisms and quantifying the extent of renewable groundwater within the water balance are the first steps towards sustainable water policies under a global warming framework.

* Corresponding author.
E-mail address: %20jsenent@ucam.edu (J. Senent-Aparicio).

https://doi.org/10.1016/j.catena.2023.107766
Received 3 January 2023; Received in revised form 25 October 2023; Accepted 18 December 2023
Available online 21 December 2023
0341-8162/© 2023 Elsevier B.V. All rights reserved.

In temperate mid-terrestrial latitudes, mountain regions play a crucial role in regional freshwater supply and are highly sensitive to climate change (Barnett et al., 2005; Bradley et al., 2006; Rangwala and Miller, 2012; Viviroli et al., 2011). High mountain basins, including those partially headed by temperate glacier patches with a base at melting point (Cuffey and Paterson, 2010; Van Vliet-Lanoe, 2014), have been preferentially studied for surface hydrology purposes and soil–vegetation eco-systemic surveys. However, the renewable groundwater component determined by the fraction of precipitation that infiltrates below the soil-root zone and reaches the underground water table (hereafter called aquifer recharge) has rarely been considered, even though evolving groundwater dynamics (recharge, discharge and storage) must be assessed to forecast the evolution of freshwater resources under changing climatic forces and adaptive human actions (Vincent et al., 2019).

The northern Andean highlands roughly extend between the latitudes 11°N and 8°S, from Costa Rica to northern Peru, and lie over 3,000 m above sea level (m a.s.l). This region lies in the Inter-Andean Valley (IAV), the western flank of the Eastern Andean Cordillera (EAC) and the eastern flank of the Western Andean Cordillera (WAC). The *páramo* ecosystem dominates the landscape. This neotropical alpine grassland ecosystem consists of steep, mostly glacier-formed valleys and plains with a large variety of lakes, peat bogs and wet grasslands intermingled with shrublands and low-bearing forest patches (Buytaert et al., 2006). This tropical alpine environment hosts unique flora and fauna, and biodiversity plays an essential role for local communities (Myers et al., 2000). The ensemble formed by thick porous allophane-rich andosols over moderate-permeability volcanic and volcano-sedimentary formations and crystalline rocks determines the hydrological functioning of the *páramo* ecosystem (Clapperton, 1993; Garrison et al., 2011; Rose, 1996; Spikings et al., 2000). As in other high mountain areas, most ecosystem typologies in the Andean highlands are groundwater dependent (Bradley et al., 2006; Buytaert et al., 2006; Ochoa-Tocachi et al., 2018, 2016; Urrutia and Vuille, 2009; Zulkafli et al., 2016) and streamflow is the accessible water source for local communities and densely populated low-lying areas, for hydropower generation and irrigation, because of the difficulty in accessing groundwater (Buytaert et al., 2005b, 2006; Vergara et al., 2007). Hydrological literature on the Andean highlands, as in other mountainous regions, primarily refers to surface hydrology processes preferentially studied in small catchments over short monitoring periods (Buytaert et al., 2006, 2005a, 2004; Célleri and Feyen, 2009; Tovar et al., 2013). Applied studies concerning the renewable groundwater component (recharge, discharge and storage) or more advanced studies focused on the impact of climate change on this resource in large basins are insignificant in number or virtually non-existent (Baraer et al., 2014; Favier et al., 2008; Hemmings et al., 2016; Ruiz-Pico et al., 2019; Vuille et al., 2018). The scant knowledge about groundwater systems in the Andean highlands derives from limited groundwater accessibility, few operational weather and stream-gauging stations, a lack of detailed geological and soil maps and sparse hydraulic and soil–vegetation data. In recent decades, climate records for the Andean highlands have also revealed perturbing changes in precipitation and temperature regimes (Espinoza-Villar et al., 2009), the consequences of which for soil moisture, streamflow and renewable groundwater remain largely unknown.

The Pita River basin (PRB) is a representative area of the *páramo* ecosystem in the northern Andean highlands in Ecuador with relatively high data density and null groundwater abstraction and where the natural state of soils, streams and aquifers is well preserved. This pristine andosol-dominated basin was selected to evaluate the impact of climate change on renewable groundwater resources due to its representativeness, minimum data coverage requirement and potential to supply approximately 400,000 inhabitants in the MDQ in the near future. Hence, this basin is significant for future water resource assessment and management by local water authorities. This situation is similar to that reported in other large urban areas in the Andean highlands due to the expected reduction in renewable water resources and the increasing population's water use habits.

This paper evaluates the impact of climate change on renewable groundwater resources in the PRB. The results intend to illustrate how climate change could modify the regime of this barely known resource, which is destined to meet most future water demand. The methodological route to achieving this aim includes two stages. First, the semi-distributed rainfall–runoff SWAT model (Arnold et al., 1998) is implemented, calibrated and validated over the period 2006–2015. Next, the variables of a climate change prediction ensemble consisting of five RCMs (ESM2M, HadGEM2-ES, IPSL-CM5A-LR, MIROC and NoerESM1-M) using the RPC 4.5 and 8.5 emission scenarios for the mid- (2040–2069) and long-term (2070–2099) future horizons are implemented into the SWAT model to generate future streamflow series, from which the impacts of climate change on the renewable groundwater resources are assessed. This paper is organised as follows: Section 2 describes the characteristics of the selected study area, situated in Ecuador, which serves as a representative area of the páramo ecosystem in the Andean highlands. Section 3 introduces the methodology, and Section 4 analyses and discusses the SWAT model results, projected variations in precipitation and temperature regimes and renewable groundwater resource response to climate change in the mid and long-term future horizons. Section 5 presents the main conclusions and recommendations.

2. Study area

The PRB is located 50 km southeast of Quito city (0°29′–0°41′ S, 78°19′–78°26′ W) in northern Ecuador (Fig. 1a), covers an area of 184.5 km^2 and has a mean elevation of 4,008 m a.s.l. The basin is bounded by the north-eastern flank of the Cotopaxi Volcano and the south-western flank of the Sincholagua Volcano (Fig. 1b) and lies in the IAV between the EAC and WAC. The Pita River is a tributary of the Esmeraldas River in the Pacific Ocean watershed (Fig. 1a).

This area exhibits a neotropical high mountain climate determined by its steep orography, the El Niño–Southern Oscillation oceanographic phenomena and the Humboldt current (Bendix, 2000; Bendix et al., 2004; González-Zeas et al., 2019). The distribution of biozones includes tropical mountain rainforests in low-lying areas, the *paramo* ecosystem in mid-slope areas and highlands, dry and cold scrublands in summit areas and permanent snow cover on volcano peaks (Buytaert et al., 2006). The *páramo* ecosystem dominates most of the PRB landscape.

Most precipitation (P) occurs in February–May, whereas the lowest amount is recorded in July–September (Rollenbeck et al., 2006). Annual mean P is around 1,100 mm with a coefficient of variation of 0.21 over the period 1964–2017. Precipitation follows a decreasing gradient from east to west controlled by the incoming Atlantic cloud fronts and elevation (Garreaud and Falvey, 2008; Makowski Giannoni et al., 2016). Annual mean temperature (T) is around 7.5 °C, with daily minimums in June–September and maximums in February–April; the daily amplitude can be as high as 19 °C in highlands and around 10 °C in low-lying areas. Annual mean potential evapotranspiration is around 1,000 mm.

From a hydrogeological perspective (Fig. 1c), the PRB lies in the IAV, where various Quaternary volcanic and volcano-sedimentary formations from the Sincholagua, Cotopaxi and Chalupas stratovolcanoes are unconformably deposited over a Palaeozoic metapelitic basement, which does not outcrop in the area (Garrison et al., 2011; Spikings et al., 2000), with the following synthetic succession from bottom to top (Hall and Mothes, 2008; Hall and Wood, 1985): (1) early to late Pleistocene andesitic lavas and rhyolitic pyroclastic flows from the Sincholagua (SIVS), Cotopaxi (COVS) and Chalupas (CHVS) volcano sequences; and (2) late Pleistocene to Holocene ash flows, extensive avalanche flows, lahars, andesitic lavas, pumice flows and scoria flows from COVS. The Quaternary sedimentary formations (Clapperton, 1993; Rose, 1996) comprise (1) Pleistocene to Holocene fluvial-glacial deposits, (2) Holocene alluvial deposits filling the Pita River valley, and (3) current glacier

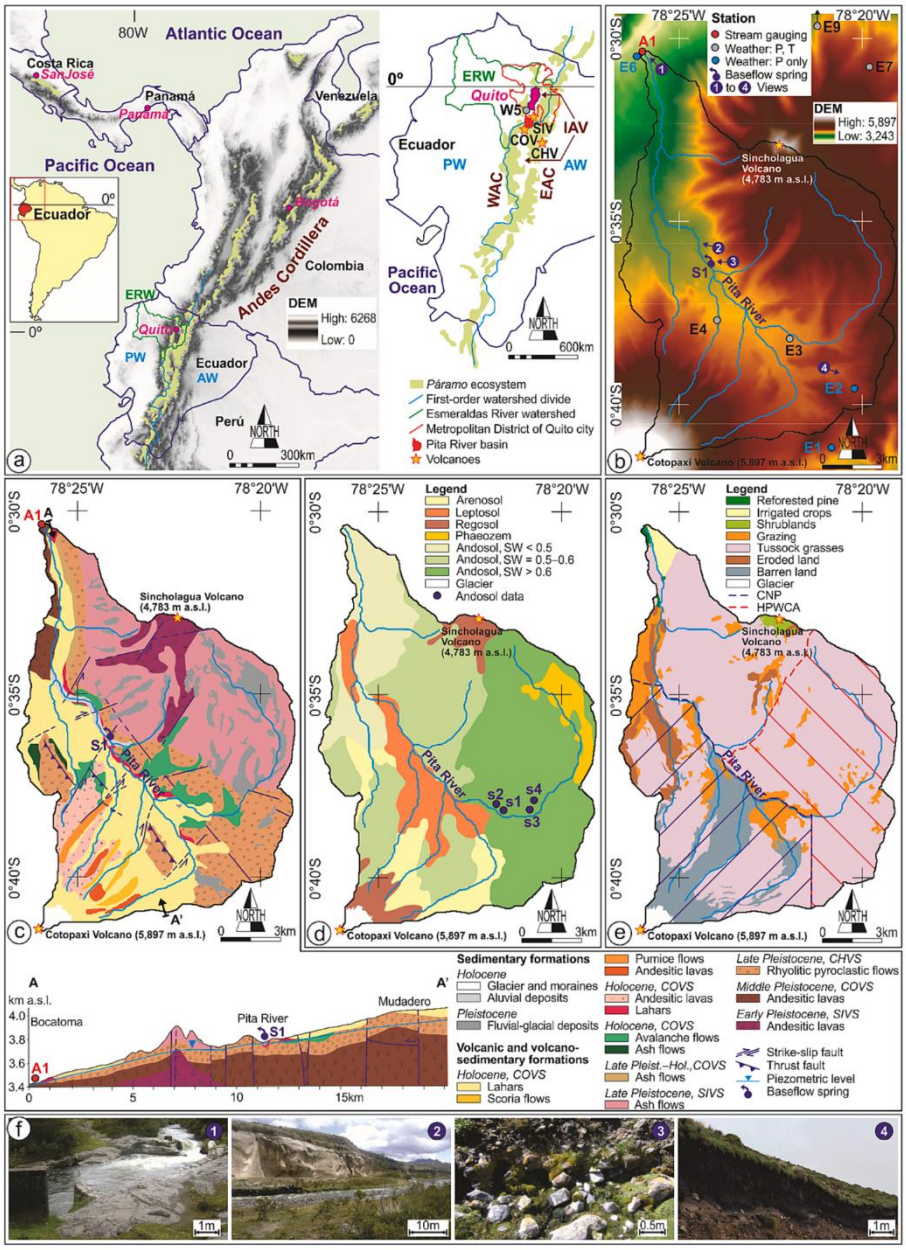

(caption on next page)

Fig. 1. (a) The northern Andean highlands dominated by the páramo ecosystem from Costa Rica to Peru after Buytaert et al. (2006), indicating the PRB's location in northern Ecuador and other sites cited in the text. (b) A 30-m-resolution DEM of the PRB (from the SavGIS website: https://www.savgis.org/ecuador.htm) displaying the location of weather stations and stream-gauging station A1 (as in Table 2) and four illustrative views. (c) Hydrogeological map (scale 1:50,000) of the PRB, after literature data (Clapperton, 1993; Hall and Mothes, 2008) and direct field observations, indicating the location of the permanent Chilcahuayco spring (S1) contributing to baseflow and regional piezometry in the synthetic hydrogeological cross-section A–A′. (d) Soil map (scale 1:200,000) of the PRB after Mejía et al., (1978) and direct field observations, showing the location of soil samples s1 to s4 (as in Table 1) after Lahuette and Recalde (2015). (e) Land-use units of the PRB (scale 1:25,000) after FONAG (2022), aerial photographs and direct field observations, illustrating the surface covered by the Cotopaxi National Park (CNP) and the High Pita Water Conservation Area (HPWCA). (f) Views of 1—Bocatoma gauging station (A1) and andesitic lavas from the Cotopaxi Volcano sequence (COVS) at the PRB outlet; 2—typical leptosol over ash flows from COVS; 3—baseflow spring S1 discharging into the Pita River; and 4—typical andosol of the páramo ecosystem over pyroclastic flows from the Chalupas Volcano sequence (CHVS). IAV—Inter-Andean Valley; EAC—Eastern Andean Cordillera; WAC—Western Andean Cordillera; PW—Pacific watershed; AW—Atlantic watershed; ERV—Esmeraldas River watershed; SIVS—Sincholagua Volcano sequence (SIVS); SW—volumetric soil–water content at saturation ($cm^3\ cm^{-3}$); T—temperature; P—precipitation.

and moraines at the Cotopaxi Volcano peak.

Two moderate-permeability aquifers, separated by aquitards, are located in the PRB. The shallow aquifer is formed by Holocene andesitic lavas and avalanche flows from COVS and late Pleistocene rhyolitic pyroclastic flows from CHVS. The deep aquifer is formed by middle Pleistocene andesitic lavas from COVS and early Pleistocene andesitic lavas from SIVS (Fig. 1c). As in other Andean highlands, a noticeable permeability contrast exists between thick porous soils (predominantly andosols) and volcanic and volcano-sedimentary formations, determining high interflow runoff rates (Buytaert et al., 2005a, 2006; Célleri and Feyen, 2009; Flores-López et al., 2016). However, aquifer recharge to shallow and deep aquifers is possible from (i) direct rainfall and interflow runoff infiltration (and de-icing to a slight extent) in unconfined high-elevation areas (Hemmings et al., 2016; Vuille et al., 2018) and (ii) preferential rainfall and runoff infiltration through shallow fissured geological formations when they are hydraulically connected to the deep aquifer (Alcalá, 2016; Changkuon et al., 1989). Most aquifer discharge occurs where the topography of the incisive valleys intersects the regional piezometry to produce permanent baseflow springs that contribute significantly to streamflow (Fig. 1c).

Organic-carbon-rich andosols predominate in the cold and wet *páramo* ecosystem in the PRB. Andosols are dark, humic and allophane-rich with a porous structure (Flores-López et al., 2016). These features, together with Al-rich clay mineral assemblages and organic-carbon contents of between 10 % and 40 %, determine volumetric soil–water contents at saturation of between 0.5 $cm^3\ cm^{-3}$ and 0.7 $cm^3\ cm^{-3}$, with exceptional values up to 0.9 $cm^3\ cm^{-3}$ (Fig. 1d). This figures induce soil infiltration capacities in the 20–60 mm h^{-1} range that can exceed typical rainfall intensities in the study area (Buytaert et al., 2006, 2005a, 2005b; Célleri and Feyen, 2009).

The PRB's soil typologies include 71.1 % organic-carbon-rich andosols, 9.2 % arenosols on northern slopes, 8.2 % leptosols over lahars and ash flows in the Pita River valley, 7.5 % regosols in summit areas, 3.3 % phaeozems over fluvial-glacial sediments above 4,000 m a.s.l., and less than 1 % is the Cotopaxi Volcano glacier (Fig. 1d) (Mejía et al., 1978). Regarding land use, 73.4 % of the PRB is covered by xerophytic tussock grasses over andosols, arenosols, phaeozems and regosols, 14.4 % by barren and eroded lands over leptosols, regosols and arenosols, 9.3 % by grazing over leptosols at lowlands and andosols at midlands, and 0.8 % by shrubs and small natural low-bearing forest patches over regosols (FONAG, 2022) (Fig. 1e). The PRB hosts two environmentally protected areas: the Cotopaxi National Park and the High Pita Water Conservation Area (Fig. 1e).

The water-dependent economy in the area includes traditional irrigated crops in small farms and extensive livestock in low-lying areas. Irrigated crops, such as cereals (corn, barley and wheat), potatoes and vegetables, and small fields of rain-fed crops are primarily produced for family consumption. Irrigation water collected from headwater springs in lateral catchments is distributed through a network of ancestral ditches, which favour permanent water loss, soil saturation and preferential infiltration (Somers et al., 2018). Water irrigation demand is around 5,000 m^3 per hectare yearly (FONAG, 2022).

3. Methods

3.1. SWAT model

Hydrological modelling of the PRB was performed using the SWAT (Soil and Water Assessment Tool) extension (Arnold et al., 1998) for the QGIS interface, called QSWAT (Dile et al., 2016). The SWAT model is one of the most widely used hydrological models, and numerous previous studies have demonstrated its capability for modelling rainfall–runoff response in basins of different typologies (Gassman et al., 2007). For example, SWAT has been successfully applied to many non-homogeneous high mountain areas after overcoming the difficulties in determining spatial precipitation with sufficient accuracy, monitoring streamflow, and parameterising land attributes and physical properties from available datasets (Ahl et al., 2008; Jain et al., 2017; Liu et al., 2022; Luo et al., 2012; Senent-Aparicio et al., 2020, 2018, 2017). These areas demonstrate similar hydrological complexity and water problems to those existing in the Andean highlands.

SWAT is a continuous, long-term, semi-distributed, physically based hydrological model that operates on monthly, daily or hourly time steps. SWAT considers the basin's spatial heterogeneity by dividing it into multiple sub-basins attending to the river network and topography. Sub-basins are further discretised into hydrologic response units (HRUs), unique soil, land-use and slope combinations of homogeneous hydrological responses not identified spatially within a SWAT simulation (Neitsch et al., 2011). The streamflow generated in each HRU adds to the streamflow at the sub-basin outlet, which contributes to observed streamflow at a given reference gauging station downstream (Zhou et al., 2014).

3.1.1. Input data and model set-up

The SWAT model requires the following inputs: elevation, land use, soil, vegetation cover and meteorological data such as daily precipitation, maximum and minimum air temperature, solar radiation, relative humidity and wind speed. A 30-m-resolution digital elevation model (DEM) of Ecuador (Datum PSA56) was retrieved from the SavGIS website (http://www.savgis.org/ecuador.htm). Soil information included (i) a soil map (1:50,000 scale) obtained from MAG-ORSTOM (1978) (Fig. 1d), (ii) andosol experimental data obtained from Lahuette and Recalde (2015), and (iii) the Harmonized World Soil Database (HWSD), version 1.2 (FAO / UNESCO, 1988). A first comparison of andosol parameters from HWSD and Lahuette and Recalde (2015) revealed differences in the ± 0.05 range (Table 1). Given this low relative error, the HWSD was used to characterise each soil type based on information about soil texture, hydraulic conductivity and available water content, among others. Four soil types are included in the study area (Table 1). A digital land-use map (scale 1:25,000) was obtained from CLIRSEN-EMAAP-Q (2006). The primary land use is *páramo* grassland (over 70 % of the PRB), followed by barren land (around 15 %), as illustrated in Fig. 1e.

Meteorological data (daily precipitation and maximum and minimum air temperature) for the period 2003–2015 was obtained from public repositories such as Quito's public water supply company

Table 1
The Harmonized World Soil Database (FAO / UNESCO, 1988) soil data implemented in the SWAT model and andosol experimental data obtained from Lahuette and Recalde (2015) in the PRB.

	Andosol						Gleysol	Phaeozem	Regosol
	HWSD	Experimental data [a]					HWSD	HWSD	HWSD
HWSD code [b] / sample ID [c]	16,206	s1	s2	s3	s4	RE [d]	16,207	16,197	16,201
Depth, m	0.30	0.40	0.17	0.40	0.36	0.10	0.30	0.30	0.30
Field capacity (FC), mm H_2O	150.0	185.6	84.2	198.3	169.7	0.06	150.0	150.0	150.0
Wilting point (WP), mm H_2O		134.8	61.1	136.0	147.6				
Saturation (SA), mm H_2O		317.2	135.3	289.0	290.7				
pH, H_2O	5.1	5.8	5.6	5.7	5.71	0.11		6.20	8.50
Organic carbon, % weight	13.1	15.3	14.5	13.0	14.5	0.08	0.80	0.88	0.34
Bulk density, g cm^3	0.7	0.85	0.76	0.74	0.76	0.13	1.29	1.36	1.29
Sand fraction, %	27	38	40	38	34	0.28	8	60	48
Silt fraction, %	56	43	43	47	55	−0.19	57	31	49
Clay fraction, %	17	19	17	15	11	−0.10	35	9	3

[a] Andosol experimental data (ED) obtained from Lahuette and Recalde (2015).
[b] Harmonized World Soil Database (HWSD) codes.
[c] Sample ID and location as in Fig. 1d.
[d] For andosol, relative error is expressed as RE = (ED–HWSD): ED, where ED is the average value of the available experimental data.

(EPMAPS), Ecuador's Fund for the Protection of Water (FONAG), and Ecuador's National Institute for Meteorology and Hydrology (INAMHI). These meteorological stations are located inside and around the PRB (Fig. 1b; Table 2). EPMAPS provided the streamflow data recorded at the Bocatoma gauging station (A1) at the PRB outlet. Among the options the SWAT model offers in function of available data, the non-global Hargreaves method (Hargreaves, 1994) was used to estimate potential evapotranspiration.

3.1.2. Model calibration and validation

The SWAT model was calibrated using the SUFI–2 algorithm from SWAT–CUP (Calibration and Uncertainty Programs) (Abbaspour, 2007). The calibration methodology used was based on two steps according to Castellanos-Osorio et al. (2023): (i) First, a monthly-scale calibration was conducted with the objective of better adjusting the water volumes, and (ii) subsequently, a second step involved daily-scale calibration to enhance the temporality of the model flows. Twenty-one widely used calibration parameters and their ranges were selected based on SWAT manuals and scientific literature. Three iterations (each iteration representing 500 simulations) were performed to achieve an acceptable calibration. Each parameter range was updated after each iteration. Streamflow data from gauging station A1 for the periods 2006–2010 and 2011–2015 was used for model calibration and validation, respectively. It is important for a reliable calibration and validation of the model that both periods should include dry, wet and usual values (Arnold et al., 2012; Gan et al., 1997). We considered wet and dry years as the 80th and 20th percentiles of annual cumulative precipitation, respectively, resulting in 1228 mm (80th) and 1033 mm (20th). The calibration period (2006–2010) ranged from 1484 mm to 1025 mm, and the validation values (2011–2015) ranged from 1334 mm to 990 mm, thus fulfilling the above premise. The period 2003–2005 was considered for model warm-up.

3.1.3. Model evaluation

The Kling–Gupta efficiency (KGE) (Gupta et al., 2009) was chosen as the primary objective function to evaluate the SWAT model's efficiency on a daily scale. Further efficiency criteria used to measure the model's goodness-of-fit included the logarithmic Nash-Sutcliffe coefficient efficiency (lnNSE) (Nash and Sutcliffe, 1970), the coefficient of determination (R^2), percent bias (PBIAS), root mean squared error (RMSE) and RMSE relative to the standard deviation of the observations (RSR). The description of these statistics can be found in Moriasi et al. (2007). Krause et al. (2005) advise against using the NSE to evaluate low flow conditions. To better evaluate the behavior of low flows, lnNSE has been adopted as an alternative indicator to NSE. The lnNSE has the advantage of providing a more balanced approach at both extremely low and peak values. Previous studies have successfully applied this lnNSE index (Castellanos-Osorio et al., 2023; Chen et al., 2018; Osuch et al., 2018; Parra et al., 2019; Senent-Aparicio et al., 2021a).

3.2. Climate scenarios and statistical bias correction

After the SWAT model was calibrated and validated using current hydrological conditions, streamflow was simulated for future climate scenarios. Data for the different climate change scenarios was collected from the Climate Change Toolkit (CCT) outlined by Vaghefi et al. (2017). Available at the Water Weather Energy Ecosystems website (https://www.2w2e.com), the CCT enables data extraction and set-up for climate change studies and hydrological applications. Precipitation and temperature data were extracted from the five GCMs available in the CCT (GFDL-ESM2M, HadGEM2-ES, IPSL-CM5A-LR, MIROC and NoerESM1-M) for the historical baseline (1975–2005) and the future (2006–2099). The RCP 4.5 and 8.5 emission scenarios were used to assess the potential changes in hydrological response in the PRB in the mid- (2040–2069) and long-term (2070–2099) future horizons.

Table 2
Description of weather (E) and stream-gauging (A) stations used in this study.

ID	Name	Latitude	Longitude	Elevation (m a.s.l.)	Variable	P [a]	T [a]	Q [a]
E1	Maucatambo	0°40′30″ S	78°20′60″ W	3,845	P	1,049		
E2	Yangahuagra	0°38′53″ S	78°20′24″ W	4,040	P	1,053		
E3	Mudadero	0°37′01″ S	78°24′07″ W	3,866	P, T	721	6.3	
E4	Cotopaxi	0°33′50″ S	78°26′35″ W	3,670	P, T	941	7.2	
E6	Bocatoma	0°29′49″ S	78°26′17″ W	3,360	P	1,217		
E7	El Carmen	0°30′07″ S	78°19′59″ W	4,100	T		4.8	
E9	Gordillo	0°25′05″ S	78°21′25″ W	3,248	T		11.5	
A1	Bocatoma	0°29′49″ S	78°26′08″ W	3,380	Q			2.6

ID as in Fig. 1b.
[a] Average annual values of P—precipitation in mm, T—temperature in °C, and Q—streamflow in m s^{-1} over the period 2003–2015.

Climate change scenarios were modelled in four steps. First, historical baseline and future GCM climate data was extracted from GFDL-ESM2M, HadGEM2-ES, IPSL-CM5A-LR, MIROC and NoerESM1-M models. Next, the GCM products were regionalised to a specific area to obtain a meaningful interpretation of the impacts of climate change on a local scale. In addition, climatic data was corrected to eliminate potential biases (Chen et al., 2013). Statistical downscaling was used to bias-correct the future GCM data against the observed data. Different hydro-climatological studies (Vaghefi et al., 2019) consider this statistical bias correction method satisfactory for downscaling the precipitation and temperature variables from the GCMs. The CCT software was used for data downloading, spatial downscaling and correcting the GCMs for bias.

The third step was to select GCMs according to their ability to reproduce historical baseline climatology in the study area. A comparative analysis of GCM products, previously downscaled and bias corrected, was performed. This task was completed using the methodology for aquifer recharge projections under future climate change scenarios introduced by Pulido-Velazquez et al., (2015a). This method compares the monthly means and standard deviations for an average year of historical and GCM (RCM) precipitation and temperature series over the same period. For this purpose, the index *Id* given by Equation (1) measures the goodness-of-fit obtained for each RCM by adding the changes (increases) in the means and standard deviations of the control series over the historical period 1980–2004 for both climatic variables:

$$Id_i = \sum_{n,m=1}^{2} Id_i(V_nS_m)$$
$$Id_i(V_nS_m) = \sum_{j=1}^{12} \left[(V_nS_m)^j_i - (V_nS_m)^j_{Hist}\right] / (V_nS_m)^j_{Hist}, \quad (1)$$

where the subscript *i* denotes a specific RCM, the superscript *j* represents the months of a mean year, *V1* is mean precipitation, *V2* is mean temperature, and *S1* and *S2* are the monthly mean value and monthly standard deviation for a specific RCMi, respectively.

Once the four *Id* indexes for each RCM were obtained, each corresponding to the mean value and standard deviation of the precipitation and temperature series, the superior models in terms of goodness-of-fit to the observed time series were selected. Finally, the simulation results from the selected RCMs, such as daily precipitation and maximum and minimum air temperature data for both scenarios, were used as SWAT model inputs to generate the streamflow responses in the PRB in the mid- and long-term future horizons.

4. Results and discussion

4.1. Model calibration and validation

The SWAT model was calibrated over the period 2006–2010. Twenty-one widely used calibration parameters and their ranges were selected based on previous knowledge obtained by authors researching temperate and tropical mountainous areas and numerous examples compiled from the scientific literature (Jimeno-Sáez et al., 2021; Senent-Aparicio et al., 2021b, 2020). Calibration focused on those parameters associated with groundwater flow, surface and interflow runoff and soil hydraulics (Table 3). The SWAT parameters were optimised using the SUFI–2 algorithm SWAT–CUP. The calibration involved two stages: (i) the first thirteen parameters allowed the observed water volume to be conformed, so they were used on a monthly basis; and (ii) the remaining eight parameters were used to adjust the streamflow distribution daily. The twenty-one fitted parameters were finally used in the daily model. The ranges of the calibrated parameters presented in Table 3 have been determined physically realistic after the criteria proposed by Eckhardt et al. (2005). Therefore, the model can be used to assess the current hydrological regime in the PRB and predict the impact of future climate change scenarios on streamflow after formal analysis of the performance metrics.

Table 3
Calibration of the SWAT model parameters.

Parameter [a]	Description and units [b]	Range used in calibration	Fitted value
r_CN2.mgt	SCS runoff curve number	–0.1 to 0.1	0.02
v_ALPHA_BF.gw	Baseflow alpha factor (day^{-1})	0 to 0.8	0.63
a_GW_DELAY.gw	Groundwater delay time (day)	–10 to 70	58.60
a_GWQMN.gw	Threshold depth of water in the shallow aquifer for return flow to occur (mm)	–200 to 200	129.50
v_GW_REVAP.gw	Groundwater revap coefficient	0.02 to 0.2	0.10
a_RCHRG_DP.gw	Deep aquifer percolation fraction	–0.01 to 0.03	–0.004
a_REVAPMN.gw	Threshold depth of water in the shallow aquifer for revap or percolation to the deep aquifer to occur (mm)	–250 to 250	185.60
v_CANMX.hru	Maximum canopy storage (mm)	0 to 5	0.15
v_EPCO.bsn	Plant uptake compensation factor	0.3 to 1	0.45
v_ESCO.bsn	Soil evaporation compensation factor	0.3 to 0.8	0.71
r_SOL_AWC.sol	Available water capacity of the soil layer (mm) H_2O/mm soil	–0.02 to 0.02	–0.01
v_LAT_TTIME.hru	Lateral flow travel time (day)	10 to 150	104.01
v_SLSOIL.hru	Slope length for lateral subsurface flow (m)	0 to 50	0.28
r_SLSUBBSN.hru	Average slope length (m)	–0.1 to 0.5	0.41
r_HRU_SLP.hru	Average slope steepness (m/m)	–0.5 to 0.2	0.04
v_OV_N.hru	Manning's (n) value for overland flow	0.1 to 1	0.99
r_CH_S1.sub	Average slope of tributary channels (m/m)	–0.5 to 0.2	–0.48
v_CH_N1.sub	Manning's (n) value for the tributary channels	0.01 to 30	2.08
r_CH_S2.rte	Average slope of main channel along the channel length (m/m)	–0.5 to 0.3	–0.21
v_CH_N2.rte	Manning's (n) value for the main channel	0.02 to 0.2	0.13
v_SURLAG.bsn	Surface runoff lag coefficient	0.05 to 15	3.74

[a] Parameter notation as it appears in SWAT manuals. Prefix r_refers to relative change (i.e., the current parameter must be multiplied by 1 + the value obtained in calibration), Prefix v_means that the existing parameter value must be replaced by the value obtained in calibration, and Prefix a_refers to absolute change (i.e., the fitted value must be added to the existing parameter value).
[b] Units are only included for dimensional parameters; the remaining parameters are dimensionless.

Aside from CN2 and SLSOIL, the most sensitive monthly parameters relate to groundwater (suffix.gw), especially those associated with the shallow aquifer (GW_REVAP, GWQMN, GW_DELAY and ALPHA_BF). Similarly, the relevance of soil hydraulics, vegetation cover, and orography are evident in the PRB, as CN2 emerged as the most influential parameter by far. This observation is consistent with similar findings concerning the high sensitivity of other hydrological models based on the Andean highlands to CN2 (Fernandez-Palomino et al., 2021; Oñate-Valdivieso et al., 2016; Yacoub and Foguet, 2013). The SLSOIL parameter describes the slope length for lateral subsurface flow (interflow runoff) in an HRU. The PRB's steep orography makes this parameter highly sensitive due to its significant dependence on slope (Zaibak and Meddi, 2022). The GW_REVAP parameter indicates the upward capillary movement of shallow groundwater to the soil when it reaches its driest condition (i.e., the wilting point). It was calibrated in the 0.02–0.2 range with a fitted value of 0.1, indicating a high rate of groundwater transfer to the soil in drier periods. The parameters GW_DELAY and GWQMN reflect the delay time for precipitation to reach the shallow aquifer through the soil profile and the subsequent water depth in the shallow aquifer measured from the surface, respectively. As deduced, the

contribution of groundwater to streamflow in the PRB is only possible when the water depth in the shallow aquifer is equal to or greater than GWQMN (Sharma et al., 2022). Furthermore, the baseflow amount is directly related to GWQMN (Kannan et al., 2007). Although the water depth in the shallow aquifer was 129.5 mm, the 58.6-day delay time is close to the maximum range, reflecting the soils' high storage capacity, and the high potential for baseflow. In the PRB, 60 % of the soils are andosols with a WRC $\geq$ 0.5 (Fig. 1d). The parameter ALPHA_BF concerns aquifer recharge mechanisms and subsequent time-delayed aquifer discharge contributing to streamflow (Oñate-Valdivieso and Bosque-Sendra, 2014). The fitted value is 0.63 day^{-1}, indicating a moderate discharge response to aquifer recharge events. Regarding the daily calibrated parameters, the most sensitive are OV_N, CH_S1, SLSUBBSN and HRU_SLP, in this order. All the parameters determine the concentration time and average velocity (Singh and Jha, 2021), which define the hydrograph's shape (Athira and Sudheer, 2021).

Fig. 2 compares simulated streamflow values with their observed counterparts during daily (Fig. 2a) and monthly (Fig. 2b) calibration and validation. The SWAT model generally simulated trends and baseflow well but failed to capture peak flow magnitudes. These differences are much more evident on a daily basis (Fig. 2a); the SWAT model has evidently underestimated peaks above 7 m^3 s^{-1}. This may be caused by the fact that SWAT uses the CN-SCS method to calculate runoff and this method cannot model snowmelt adequately for mountainous regions (such as the area of this study). This limitation has been reported in numerous studies in different regions worldwide (Gassman et al., 2014; Jimeno-Sáez et al., 2018; Liu et al., 2022; López-Ballesteros et al., 2020; Ur Rahman et al., 2020), and SWAT developers still have much to do (Arnold et al., 2012). However, this limitation does not substantially affect the groundwater components evaluation, which is the subject of this paper.

Monthly model calibration resulted in good agreement between simulated and observed streamflow, as indicated by the evaluation statistics given in Table 4. All the evaluation statistics in the monthly streamflow comparison outperformed the equivalent metrics in daily streamflow comparisons. The KGE is based on the decomposition of NSE into correlation, bias and relative variability (Rivas-Tabares et al., 2019). However, it demonstrates less sensitivity to high streamflow values after considering all streamflow levels in a more balanced approach (Radcliffe and Mukundan, 2017). According to Knoben et al.

Table 4
SWAT model evaluation statistics for daily and monthly streamflow.

Model evaluation statistic	Daily streamflow		Monthly streamflow	
	Calibration	Validation	Calibration	Validation
KGE	0.48	0.60	0.73	0.65
lnNSE	0.44	0.52	0.67	0.65
R^2	0.31	0.45	0.66	0.67
PBIAS	1.96	7.43	1.75	7.36
RMSE	1.25	0.95	0.51	0.58
RSR	0.85	0.77	0.58	0.62

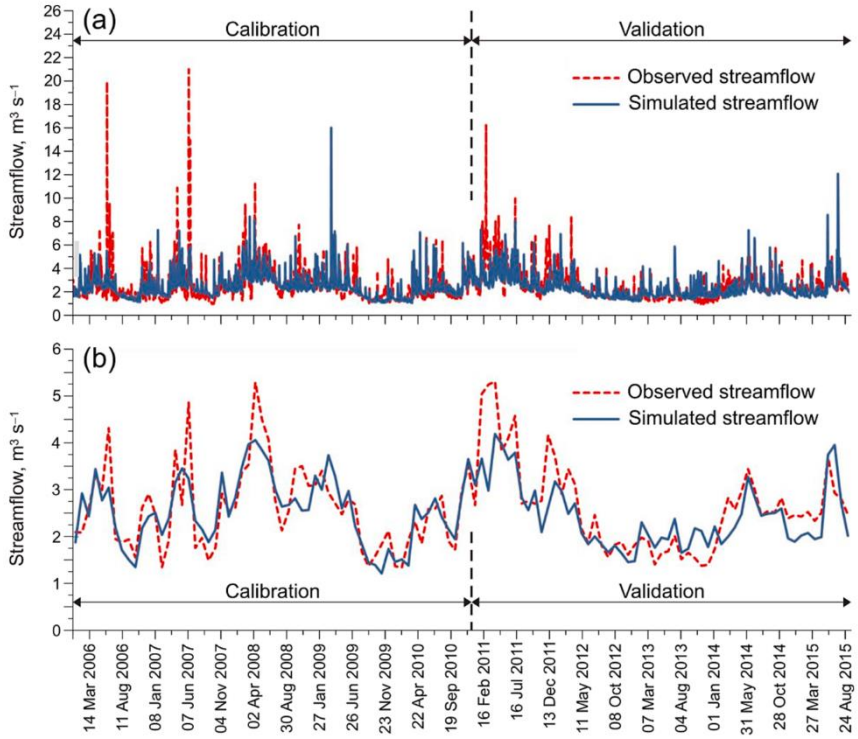

Fig. 2. In the PRB over the period 2006–2015, hydrograph simulated using the SWAT model and compared with the observed streamflow on (a) a daily and (b) a monthly basis. Calibration (2006–2010) and validation (2011–2015) periods are also displayed.

(2019), KGE values below −0.41 should be considered unacceptable, whereas good performance is achieved when KGE > 0.5 (Ekolu et al., 2022). Except for the daily calibration in which KGE = 0.48, on the threshold of a good model, the other daily and monthly results indicate satisfactory SWAT model performance. Logarithmic NSE (lnNSE) was used instead of NSE to assess the model's performance regarding low flows (Cheng et al., 2020) since the former reduces sensitivity to peak flows (Krause et al., 2005). As with the KGE, the 0.44 daily calibration value indicates acceptable performance, although the daily and monthly validation results are above 0.5, indicating satisfactory model fitting (Cheng et al., 2017). The R^2 explains the fraction of variance in observed values in the model. Similar to NSE, R^2 is also moderately sensitive to high flows since it can be significantly affected by outliers, increasing model bias (Legates and McCabe Jr., 1999). Peak flow underestimation could be one reason for daily R^2 values below 0.5 in calibration and validation. Since flow aggregation produces peak flattening, the monthly R^2 values are slightly higher than 0.6 in calibration and validation, indicating satisfactory model performance (Moriasi et al., 2015).

PBIAS checks the model's tendency to overestimate (PBIAS > 0) or underestimate (PBIAS < 0) the observed values (Gupta et al., 1999). The daily and monthly results prove to be somewhat similar. Based on Moriasi et al. (2015), the model's performance was very good during calibration and good during validation, with an overestimation of less than 8 % on a daily and monthly basis. Finally, RMSE and RSR measure the difference between observed and simulated streamflow, although RMSE measures the absolute difference, and RSR standardises the difference by dividing RMSE by the standard deviation of the observations (Moriasi et al., 2007). Despite their different conceptions and interpretations, both statistics point in the same direction. According to Singh et al. (2005), the difference between observed and simulated streamflow can be considered low when RMSE is less than half of the standard deviation of the observations. Table 4 demonstrates that the daily RMSE is two-fold the value obtained monthly. Since the daily RSR values are higher than 0.75, the model can be considered unsatisfactory (Kalin et al., 2010; Moriasi et al., 2015, 2007). Notwithstanding, the monthly model performed in the good-to-satisfactory range during calibration (RSR = 0.58) and validation (RSR = 0.62), respectively.

Statistical analysis revealed limited SWAT model performance on the daily basis, as pointed out previously by Reza Eini et al. (2020). However, the monthly results demonstrate reasonably good prediction capability, permitting further model processing as it is considered in previous studies all over the world (Tan et al., 2021). Moreover, the monthly time resolution is considered sufficiently competent for long-term water resource evaluation and subsequent long-term climate impact forecasting (Georgakakos et al., 2012), which is the subject of this paper.

4.2. Selection of climate change models

As described in Section 3.2, the five RMC models available in the CCT (GFDL-ESM2M, HadGEM2-ES, IPSL-CM5A-LR, MIROC and NoerESM1-M) were analysed to identify those that best reproduce the average year from the mean values and standard deviations. The selection was based on the *Id* index, which is the sum of the absolute value of the relative differences in the historical and control series statistics during the 12 months of an average year. Table 5 presents the *Id* values obtained for the 2006–2015 study period. The higher the *Id*, the worse the goodness-of-fit. Except for the HadGEM2-ES model, the RCM models achieved similar mean *Id* values, $Id(\Delta x)$, for precipitation and temperature. However, greater differences in standard deviations, $Id(\Delta\sigma)$, were observed among the RCM models, especially for temperature, which ranged from 18.78 (model IPSL-CM5A-LR) to 55.64 (model GFDL-ESM2M). The IPSL-CM5A-LR, MIROC and NoerESM1-M models achieved lower *Id* values. This issue is in line with previous similar works (Pulido-Velazquez et al., 2015b; Urrutia and Vuille, 2009). Hence, these three RCM models were selected to assess the impact of climate change on renewable groundwater resources in the PRB.

Table 5
Id index of each RCM model for precipitation and temperature, monthly series.

RCM model		Precipitation		Temperature		*Id* [a]
		$Id(\Delta x)$	$Id(\Delta\sigma)$	$Id(\Delta x)$	$Id(\Delta\sigma)$	
1	GFDL-ESM2M	0.87	11.60	0.61	55.64	68.72
2	HadGEM2-ES	7.97	12.24	7.47	23.12	50.80
3	IPSL-CM5A-LR	0.80	5.92	0.61	18.78	26.11
4	MIROC	1.22	6.10	0.57	30.32	38.21
5	NoerESM1-M	0.92	8.38	0.59	22.65	32.54

[a] *Id*—sum of the absolute values of the mean values, denoted as $Id(\Delta x)$, and standard deviations, denoted as $Id(\Delta\sigma)$, of precipitation and temperature monthly series.

4.3. Changes in projected precipitation and temperature

The implemented ensembles consisted of three RCM models (IPSL-CM5A-LR, MIROC and NoerESM1-M) and RCP emission scenarios 4.5 and 8.5. Table 6 summarises the changes in the average values and standard deviations of the temperature and precipitation (the climate variables) annual series from the implemented ensembles relative to the corresponding values of each RCM baseline period (1976–2005). The changes refer to the mid- (2040–2069) and long-term (2070–2099) future horizons. In addition, the distributions of monthly mean values and standard deviations of temperature and precipitation for the three RCM-RCP 4.5 ensembles and the three RCM-RCP 8.5 ensembles over the baseline period in the mid- and long-term future horizons are displayed in Figs. 3 and 4, respectively.

Regarding average annual temperature (Table 6), the three RCMs predicted increases from + 1.4 °C, in the mid-term, to + 2.5 °C, in the long term, for RCP 4.5 and from + 1.9 °C, in the mid-term, to 4.7 °C, in the long term, for RCP 8.5. These figures indicate increases of + 20–35 % for RCP 4.5 and + 30–65 % for RCP 8.5 regarding the baseline. The NoerESM1-M model predicted lower temperature increases regarding the baseline, with values 10–20 % (depending on the RCP) lower than those obtained in the other two RCMs. This increase in temperature is a proven historical fact corroborated by the 0.1–0.2 °C increase per decade recorded in the last 70–100 years (Buytaert et al., 2014; Sklenář et al., 2021; Vuille et al., 2015), which exceeds the threshold of natural climate variation (Gutiérrez-Salazar and Medrano-Vizcaíno, 2019). These results concur with the average temperature increases of 2 °C and 5 °C predicted in the coastal versant of the WAC (Ilbay-Yupa et al., 2021; Rivadeneira-Vera et al., 2020) and the Andean highlands (Herzog et al., 2012) of Ecuador, respectively. Regarding the average annual temperature standard deviations, the IPSL-CM5A-LR and NoerESM1-M models revealed changes lower than the baseline for RCP. 4.5, whereas the MIROC model predicted increases of more than 100 % for RCP 4.5. The RCP 8.5 ensembles predicted an increase in temperature in the 20–90 % range, depending on the RCM.

At the monthly scale, for RCP 4.5 (Fig. 3) and RCP 8.5 (Fig. 4), the mid- and long-term mean temperature trends are similar to the baseline, regardless of the RCM considered. Only the NoerESM1-M model predicted more pronounced variation between April and July for RCP 8.5 in the long term, with higher temperature increases for the rest of the year. However, the standard deviations for monthly temperature changed significantly depending on the RCM-RCP ensemble. While the baseline remained unvaried in the mid- and long-term RCP 4.5 scenarios, except for the MIROC model, RCP 8.5 revealed an apparent increase in standard deviations for all the RCMs, especially in the long term. Moreover, the dry season exhibited the highest values, except in the NoerESM1-M model. Furthermore, the change in temperature for RCP 4.5 is much greater in the mid-term than in the long term, inversely compared to the RCP 8.5 results. Generally, these projections are consistent with the results previously assessed in similar regions studies (Buytaert et al.,

Table 6
Changes in the average values and standard deviations of annual precipitation and temperature predicted by the implemented RCM-RCP ensembles relative to the corresponding values for each RCM's baseline scenario.

RCM model	Emission scenario	Period	Annual precipitation (mm)				Annual temperature (°C)			
			Mean value	Change relative to baseline [a]	Standard deviation	Change relative to baseline [a]	Mean value	Change relative to baseline [a]	Standard deviation	Change relative to baseline [a]
IPSL-CM5A-LR	Baseline	1976–2005	1091.29	–	91.2	–	7.12	–	0.45	–
	RCP 4.5	2040–2069	1124.11	+ 32.82(+3%)	95.06	+3.88(+4%)	9.08	+1.96(+28 %)	0.31	–0.14(–31 %)
		2070–2099	1143.73	+52.45(+5%)	71.50	–19.68(–22 %)	9.55	+2.43(+34 %)	0.27	–0.18(–39 %)
	RCP 8.5	2040–2069	1141.76	+50.47(+5%)	84.40	–6.78(–7 %)	9.82	+2.71 (+38 %)	0.53	+0.08(+18 %)
		2070–2099	1309.72	+218.43 (+20 %)	104.57	+13.39(+15 %)	11.82	+4.70 (+66 %)	0.69	+0.24(+54 %)
MIROC	Baseline	1976–2005	945.32	–	49.18	–	8.20	–	0.47	–
	RCP 4.5	2040–2069	923.21	–22.12 (–2%)	44.34	–4.84(–10 %)	10.03	+1.83 (+22 %)	1.00	+0.53(+111 %)
		2070–2099	932.08	–13.24 (–1%)	46.16	–3.02(–6 %)	10.67	+2.47 (+30 %)	0.67	+0.20(+41 %)
	RCP 8.5	2040–2069	948.82	+3.50 (+0.4 %)	66.72	+17.54(36 %)	10.69	+2.48 (+30 %)	0.61	+0.14(+29 %)
		2070–2099	1052.05	+106.73 (+11 %)	39.27	–9.91(–20 %)	12.70	+4.50 (+55 %)	0.89	+0.42(+88 %)
NoerESM1-M	Baseline	1976–2005	970.43	–	70.20	–	7.16	–	0.33	–
	RCP 4.5	2040–2069	1160.21	+189.79(+20 %)	89.38	+19.18(+27 %)	8.53	+1.37 (+19 %)	0.29	–0.04(–13 %)
		2070–2099	1149.02	+178.59 (+18 %)	86.31	+16.11(+23 %)	8.84	+1.68 (+23 %)	0.27	–0.06(–19 %)
	RCP 8.5	2040–2069	1197.85	+227.42 (+23 %)	89.81	+19.61(+28 %)	9.02	+1.86 (+26 %)	0.40	+0.07(+22 %)
		2070–2099	1371.91	+401.48 (+41 %)	92.55	+22.34(+32 %)	10.28	+3.12 (+44 %)	0.46	+0.13(+40 %)

[a] Changes are expressed as positive or negative absolute (in the same unit as the variable) and relative (percentages in parentheses) differences.

2011; Cresso et al., 2020; Flores-López et al., 2016a).

Regarding average annual precipitation (Table 6), the MIROC–RCP 4.5 ensemble revealed slight decreases of −2% and −1% in the mid- and long-term horizons, respectively, compared to the baseline. Conversely, the ensembles generated from the other two RCMs predicted increases. Unlike the temperature trend, precipitation covered a wide range of changes regarding the baseline, varying from + 0.4 % to + 41 % depending on the RCM-RCP ensemble, although RCP 8.5 generally demonstrated greater increases. Recent studies agree that regional warming is more evident than future variations in precipitation. For example, several authors have demonstrated a decrease of nearly 15 % in the IAV region (Kirtman et al., 2013; Vuille et al., 2008), while others have suggested increases of around 10 % in the eastern and western flanks (Ilbay-Yupa et al., 2021). Historical precipitation over the last 50 years does not display a definitive trend (Vuille et al., 2003), only a slight reduction at most (Martínez et al., 2011) with few impacts on water resource availability. Regarding the average annual precipitation standard deviation, the changes vary between −20 % and + 35 %, in contrast to the wide variation between −30 % and + 110 % in the average annual temperature standard deviation. Notwithstanding, each RCM-RCP ensemble differs significantly. The IPSL-CM5A-LR model demonstrated a significant decrease (–22 %) for RCP 4.5 in the long term but the opposite (an increase of + 15 %) for RCP 8.5. The NoerESM1-M model achieved increases of approximately 20 % for all the scenarios, whereas the MIROC model revealed precipitation increases and decreases depending on the RCP and time horizon considered.

At the monthly scale, for RCP 4.5 (Fig. 3) and RCP 8.5 (Fig. 4), mean precipitation also exhibits slight seasonal differences. For all RCMS, mean monthly precipitation is similar to the baseline, except in June. This finding is especially relevant for RCP 8.5 in the long term, where the increase reached + 100 % in the IPSL-CM5A-LR and MIROC models. No clear trends are evident concerning the monthly precipitation standard deviation since variations are indistinctly positive or negative depending on the RCM-RCP ensemble, which appear not to be in line with Zhiña et al. (2019) whose study in the southern Ecuadorian Andes points to a higher increase in monthly precipitation, especially in the long-term period.

In the mid- and long-term future, the increase in average temperature combined with the slight increase in average precipitation obtained in most of the RCM-RCP ensembles should result in higher actual evapotranspiration (i.e., the evaporative fraction of precipitation that returns to the atmosphere) and, therefore, a decrease in available water for ecosystems and human uses (i.e., the non-evaporative fraction of precipitation or the water amount that could contribute to streamflow and aquifer recharge after discounting transmission losses), as presented in Table 6. This plausible framework could also be accompanied by changes in the fire regime (Kitzberger et al., 2022) due to warmer temperatures and soil degradation resulting from subsequent low-vegetated patches and changes in the frequency and intensity of rainfall events (Muñoz et al., 2021) and dry spells. This combination could worsen the current hydraulic state of andosols (Young et al., 2011), altering or degrading the *páramo* ecosystem's hydrological functioning and temporal water storage capacity. This alpine ecosystem's sensitivity to climate change (Cuesta et al., 2017) implies a high risk of habitat loss and unsafe water provision, as identified by Anderson et al. (2011).

4.4. Water resources response to climate change

This section analyses and discusses the main water balance components' response to each RCM-RCP ensemble in the mid- (2040–2069) and long-term (2070–2099) future horizons. The results are summarised in Table 7. The changes in the baseline scenario indicate the renewable groundwater resource's expected magnitude and hydrological significance in the future. Different experimental relationships for aquifer recharge predictions under different precipitation fields associated to current and future climate frameworks can be found in the scientific literature (Alcalá et al., 2018, 2011; Ross et al., 2005). For example, Taylor et al. (2013) observed a positive relationship between projected changes in precipitation and subsequent aquifer recharge responses. In the PRB, although increased precipitation typically implies increased streamflow, it does not always correspond with increased aquifer recharge, as presented in Table 7. Therefore, precipitation (P) and aquifer recharge (TA_RCHG) did not follow a linear relationship, and more interdisciplinary information to conceptualise the soil–aquifer

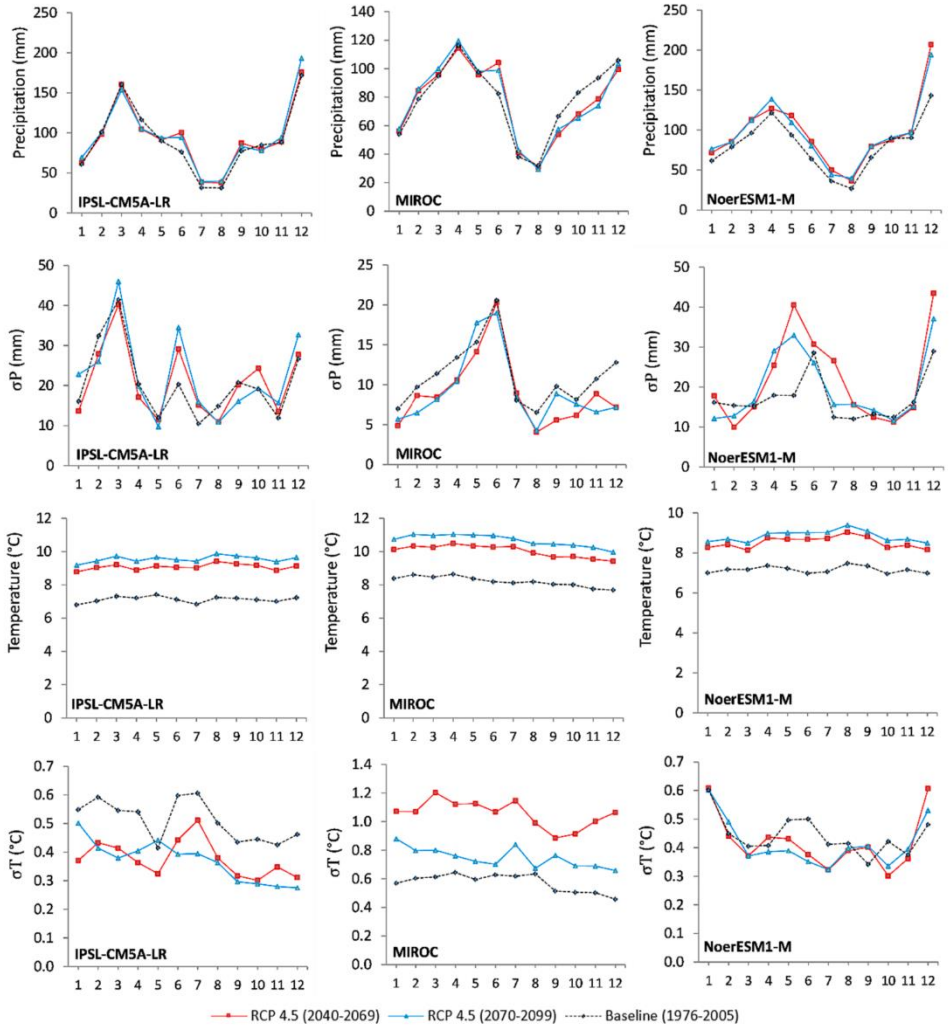

Fig. 3. Distribution of the mean values and standard deviations of monthly temperature and precipitation of the three RCM-RCP 4.5 ensembles for the baseline period (1976–2005) and the mid- (2040–2069) and long-term (2070–2099) future horizons.

relationships is needed to interpret the changes in lower aquifer recharge rates obtained as differences in P and other significant water balance components such as actual evapotranspiration (ET). In most ungauged mountainous areas, ET is typically one of the less certain water balance components, especially when only non-global models, such as Hargreaves (1994) and others, can be used due to data scarcity (Alcalá et al., 2011; España et al., 2013, 2011; Were et al., 2007). This is the case in the PRB, where uncertainty in ET propagates through the model equations to reveal relatively uncertain aquifer recharge rates, which can be uninterpretable when attempting to draw conclusions. Therefore, comparisons of aquifer recharge with the evaporative fraction of P (ET:P ratio) or the non-evaporative fraction of P (1–[ET:P] ratio) instead of P or ET were preferred to analysing changes in streamflow and aquifer recharge. Likewise, other authors (Pool et al., 2021; Seddon et al., 2021) have used similar indices in order to provide more accurate relationships between the parameters implied in the aquifer recharge. When the ET:P and 1–(ET:P) ratios were compared with aquifer recharge, interpretable negative and positive relationships were obtained, respectively, as expected.

After this conceptualisation, the IPSL-CM5A-LR model produced increases lower than 6 % in P and ET for the two RCPs. The exception is RCP 8.5 in the long term, which reached increases of + 20 % and + 15 % in P and ET, respectively. Similar P and ET magnitudes resulted in slight increases in the ET:P ratio below + 2 %, contributing to a gradual

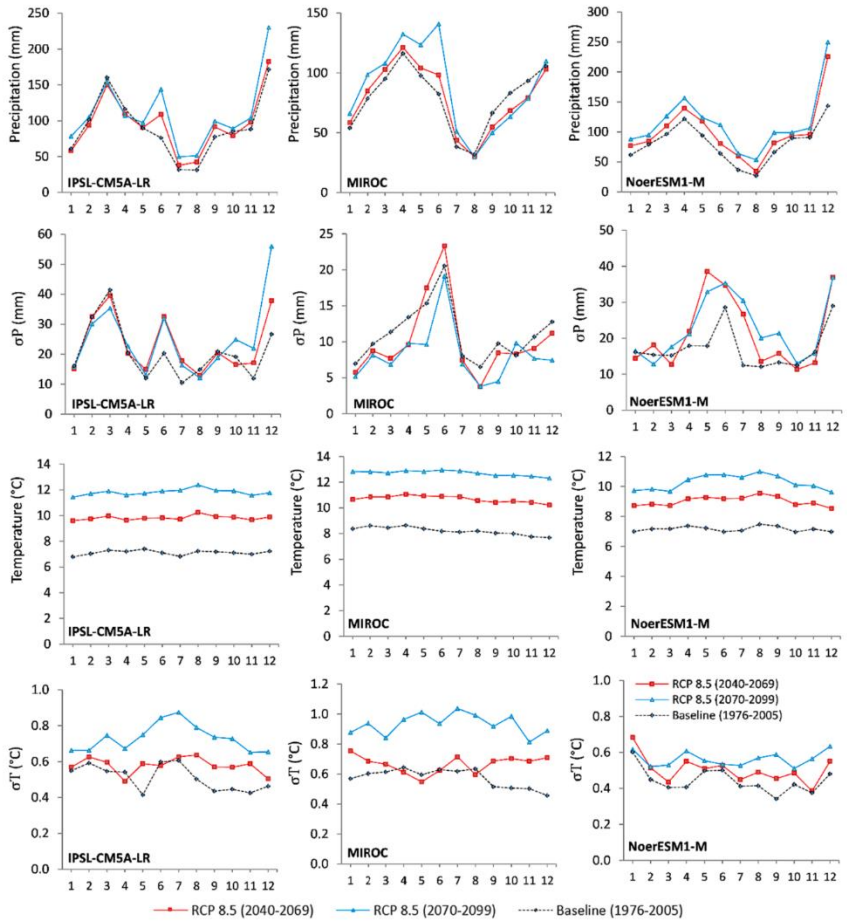

Fig. 4. Distribution of the mean values and standard deviations of monthly temperature and precipitation of the three RCM-RCP 8.5 ensembles for the baseline period (1976–2005) and the mid- (2040–2069) and long-term (2070–2099) future horizons.

increase in streamflow due to the increase in P but a sharp decrease in aquifer recharge of between −14 % and −17 %. In the long term, RCP 8.5 significantly increased P (+20 %) and ET (+15 %). However, the greater difference in P and ET increased the 1–(ET:P) ratio by + 6 %, resulting in significant increases in streamflow (+27 %) and aquifer recharge (+15 %). The NoerESM1-M model produced higher increases in P and ET, significantly increasing the 1–(ET:P) ratio compared with the other two RCMs, reaching + 25 % for RCP 8.5 in the long term. Moreover, the NoerESM1-M model increased aquifer recharge; the observed aquifer recharge increase is two-fold higher than the observed streamflow increase. In fact, the increase in streamflow and aquifer recharge for RCP 8.5 in the long term is + 76 % and + 173 %, respectively. The MIROC model illustrates how the water balance components adjust when P decreases and ET increases. Regarding the IPSL-CM5A-LR model, the ET:P ratios are also positive (in the 1–2 % range), but the other water balance components differ substantially. The decrease in P caused a slight decrease in streamflow (between −3% and −6%), but the diminution of aquifer recharge was significant at approximately −40 % for RCP 4.5 in the long term.

The distributions of the monthly mean values of the water balance components for the three RCM-RCP 4.5 ensembles and the three RCM-RCP 8.5 ensembles, over the baseline period and the mid- and long-term future horizons, are displayed in Figs. 5 and 6, respectively. The variations in monthly aquifer recharge are highly dependent on the RCP. For RCP 4.5, aquifer recharge decreased conspicuously in the mid and long term, except in the NoerESM1-M model. However, RCP 8.5 revealed a significant increase, especially in the second half of the year. The differences in streamflow and aquifer recharge in the NoerESM1-M model increased significantly, especially in the long term. Notwithstanding, the yearly pattern does not differ significantly from the baseline, except in June and July (dry season), as previously identified in monthly variations in temperature and precipitation (climate variables). No significant differences were observed in the average monthly ET:P and 1–(ETP:P) ratios.

Table 7
Average annual SWAT water balance components in the PRB after implementing the RCM-RCP 4.5 and 8.5 ensembles for mid- (2040–2069) and long-term (2070–2099) future horizons.

RCM model	Emission scenario	Period	P (mm) [a]	ET (mm) [a]	ET/P [a]	1–(ET/P) [a]	WYLD (mm) [a]	TA_RCHG (mm) [a]
IPSL-CM5A-LR	Baseline	1976–2005	1091.29	663.57	0.61	0.39	412.23	17.54
	RCP 4.5	2040–2069	1124.11 (+3%)	695.19 (+5%)	0.62 (+2%)	0.38 (-3%)	414.31 (+1%)	14.59 (–17 %)
		2070–2099	1143.73 (+5%)	701.92 (+6%)	0.61 (+1%)	0.39 (-1%)	427.89 (+4%)	14.98 (–15 %)
	RCP 8.5	2040–2069	1141.76 (+5%)	701.21 (+6%)	0.61 (+1%)	0.39 (-2%)	428.34 (+4%)	15.05 (–14 %)
		2070–2099	1309.72 (+20 %)	765.56 (+15 %)	0.58 (–4%)	0.42 (+6%)	523.92 (+27 %)	20.11 (+15 %)
MIROC	Baseline	1976–2005	945.32	657.08	0.70	0.30	283.64	4.05
	RCP 4.5	2040–2069	923.21 (–2%)	651.27 (–1%)	0.71 (+1%)	0.29 (-3%)	267.72 (–6%)	3.08 (–24 %)
		2070–2099	932.08 (–1%)	660.99 (+1%)	0.71 (+2%)	0.29 (-5%)	267.93 (–6%)	2.44 (–40 %)
	RCP 8.5	2040–2069	948.82 (+0.4 %)	669.39 (+2%)	0.71 (+1%)	0.29 (-3%)	275.03 (–3%)	2.86 (–29 %)
		2070–2099	1052.05 (+11 %)	719.31 (+9%)	0.68 (–2%)	0.32 (+4%)	327.44 (+15 %)	4.70 (+16 %)
NoerESM1-M	Baseline	1976–2005	970.43	628.23	0.65	0.35	332.88	8.62
	RCP 4.5	2040–2069	1160.21 (+20 %)	693.67 (+10 %)	0.60 (–8%)	0.40 (+14 %)	452.19 (+36 %)	15.72 (+82 %)
		2070–2099	1149.02 (+18 %)	697.14 (+11 %)	0.61 (–6%)	0.39 (+12 %)	436.94 (+31 %)	14.09 (+63 %)
	RCP 8.5	2040–2069	1197.85 (+23 %)	711.10 (+13 %)	0.59 (–8%)	0.41 (+15 %)	469.32 (+41 %)	16.06 (+86 %)
		2070–2099	1371.91 (+41 %)	765.57 (+22 %)	0.56 (–14 %)	0.44 (+25 %)	585.90 (+76 %)	23.54 (+173 %)

[a] P—average annual precipitation; ET—average annual evapotranspiration; ET/P—evaporative fraction of P as a dimensionless fraction; 1–(ET/P) —non-evaporative fraction of P as a dimensionless fraction; WYLD—average annual maximum amount of water that can contribute to streamflow and aquifer recharge after discounting transmission losses; and TA_RCHG—average annual total aquifer recharge. The percentages of the relative changes in the variables and/or ratios to the corresponding baseline scenarios are given in parentheses.

These findings demonstrate a strong positive relationship between P and streamflow. However, aquifer recharge variations are predominantly related to the ET:P and 1–(ET:P) ratios. This observation supports the rationale that aquifer recharge highly depends on the water available after soil and vegetation water demands have been satisfied (Bhunia, 2020); in the case of andosols is high as described above. The logical increases in streamflow for low (below + 10 %) increases in precipitation are also corroborated by streamflow increases in the 1–3 % range for every + 1 % change in P, as reported globally by Chiew et al. (2006). However, uncertainty propagation in model projections has induced a wide range of aquifer recharge changes, as discussed above and observed by Döll (2009). Notably, small changes in aquifer recharge forecasted by Buytaert et al. (2010) in equivalent humid Andean highlands with similar andosols do not align with our results indicating changes ranging from −40 % to + 173 %. This disparity is not definitive since it can be attributed to a number of factors, such as the different observation scales used, improvability of RCM models over time, and inadequate aquifer recharge estimation as differences in P and ET when data scarcity prevents ET estimation using global models (Alcalá et al., 2011; España et al., 2013, 2011; Were et al., 2007).

As indicated in Table 8 and Figs. 5 and 6, variation in aquifer recharge is greater in the wet season (February to May) than in the dry season (July to September), except in the MIROC model. In the IPSL-CM5A-LR and NoerESM1-M models, aquifer recharge in the dry season is approximately 0.7–0.9-fold the observations during the wet season. However, the magnitude of the relative change in aquifer recharge in wet and dry seasons differs; the change in the wet season is usually greater than that observed in the dry season. This typical aquifer recharge behaviour depends on available soil water, as has been documented in other mountainous areas (Alcalá et al., 2011; Were et al., 2007). However, a discrepancy is observed in the MIROC model: the change is between −15 % and −54 % in the wet season and between −9% and + 47 % in the dry season. Similarly, the sharp increases in aquifer recharge in the NoerESM1-M model are much higher in the wet season than in the dry season. Aquifer recharge rates are typically low, in the 0.43–8.38 mm range. Null groundwater exploitation in the moderate-permeability volcanic and volcano-sedimentary aquifers in the PRB favours high piezometric levels. Hence the aquifer can be considered virtually full, repelling most recharge events, while most soil water excess percolates downwards and contributes interflow runoff to streamflow in the wet season. Consequently, only a minor fraction of the soil water excess during the wet season produces aquifer recharge, delayed, to some extent, when the aquifer marginally empties during the dry season.

Previous studies conducted over a large territory including soils with worse hydraulic conditions (less water storage capacity) in nearby regions (Carvajal et al., 2017) highlight the apparent differences between wet and dry seasons. However, our results in the PRB (where andosols with better hydraulic conditions predominate) do not diverge as much by season. In fact, soil hydraulics tests performed on degraded and well-preserved andosols (Boulanger et al., 2007; Buytaert et al., 2009) also provide different aquifer recharge responses, which diverge from the more similar responses obtained in the implemented RCM-RCP 4.5 and 8.5 ensemble projections. The exception is the NoerESM1-M model projections, which could depend more on specific soil, vegetation cover and climate data for improved results. However, this work is beyond the scope of this study.

The influence of the soil preservation state on aquifer recharge response appears evident. Alcalá (2016) used tracer (chemical, stable isotopes and radioisotopes) and physical techniques to evaluate aquifer recharge in a close IAV catchment with well-preserved andosols over moderate-permeability volcano-sedimentary geological formations (the typical *páramo* ecosystem landscape) similar to those existing in the PRB. This author demonstrated aquifer recharge responses in the three–four-month range after the wet season had ended. Therefore, the soil preservation degree is a determinant for the ET:P and 1–(ET:P) ratios and, thus, controls the magnitude and duration of aquifer recharge events. Climate change could alter (deteriorate) soil hydraulic properties, as reported by Kumar et al. (2022) and, therefore, current surface water–groundwater dynamics in the andosol-dominated Andean highlands, resulting in less soil water storage capacity, more rapid runoff responses and prolonged water-deficit periods.

The magnitude and variability of water resources are critical for conserving natural biodiversity and the stability of aquatic environments (Pérez-Sánchez et al., 2020). The indicators of hydrological alteration included in the IAHRIS (IndicAtors of Hydrological alteration in RIverS) software (Fernández et al., 2012), specific for the evaluation of the alteration of the natural regime of a river in non-coetaneous series, have been used to evaluate the impact of climate change on the magnitude, variability and seasonality of water resources in the PRB. These indexes are: 1) Mean value of the annual volumes (Mean); 2) Extreme variability (EV), which is calculated as the average value of the difference between the maximum and minimum monthly discharge for each year; 3) Difference between the daily mean flows corresponding to the 10th (Q10) and 90th (Q90) percentiles; 4) Maximum/minimum relative frequency of the month (MaxRF/MinRF). As can be seen in

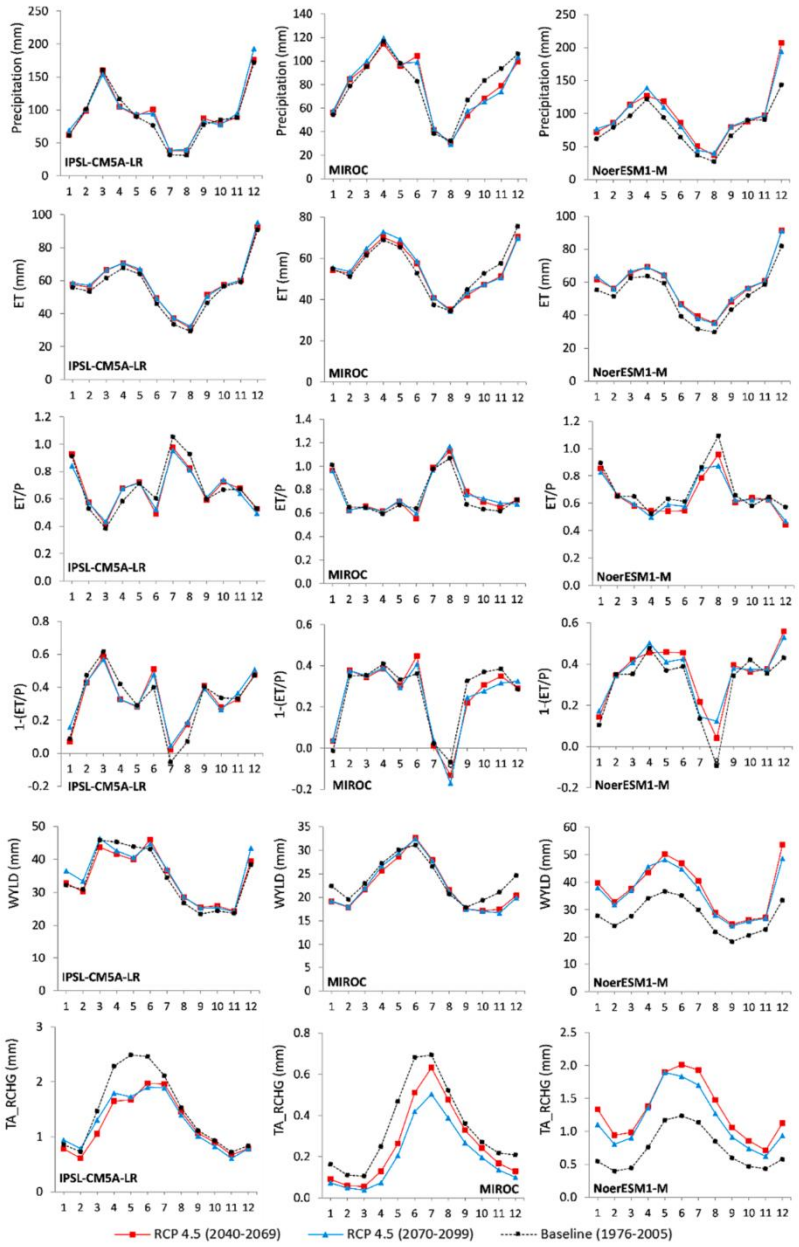

Fig. 5. Distribution of the monthly mean values of the main water balance components predicted by the three RCM-RCP 4.5 ensembles in the PRB for the baseline period (1976–2005) and the mid- (2040–2069) and long-term (2070–2099) future horizons. P—precipitation (mm); ET—evapotranspiration (mm); ET/P—evaporative fraction of P as a dimensionless fraction; 1–(ET/P) —non-evaporative fraction of P as a dimensionless fraction; WYLD—maximum amount of water that can contribute to streamflow and aquifer recharge after discounting transmission losses (mm); and TA_RCHG—total aquifer recharge (mm).

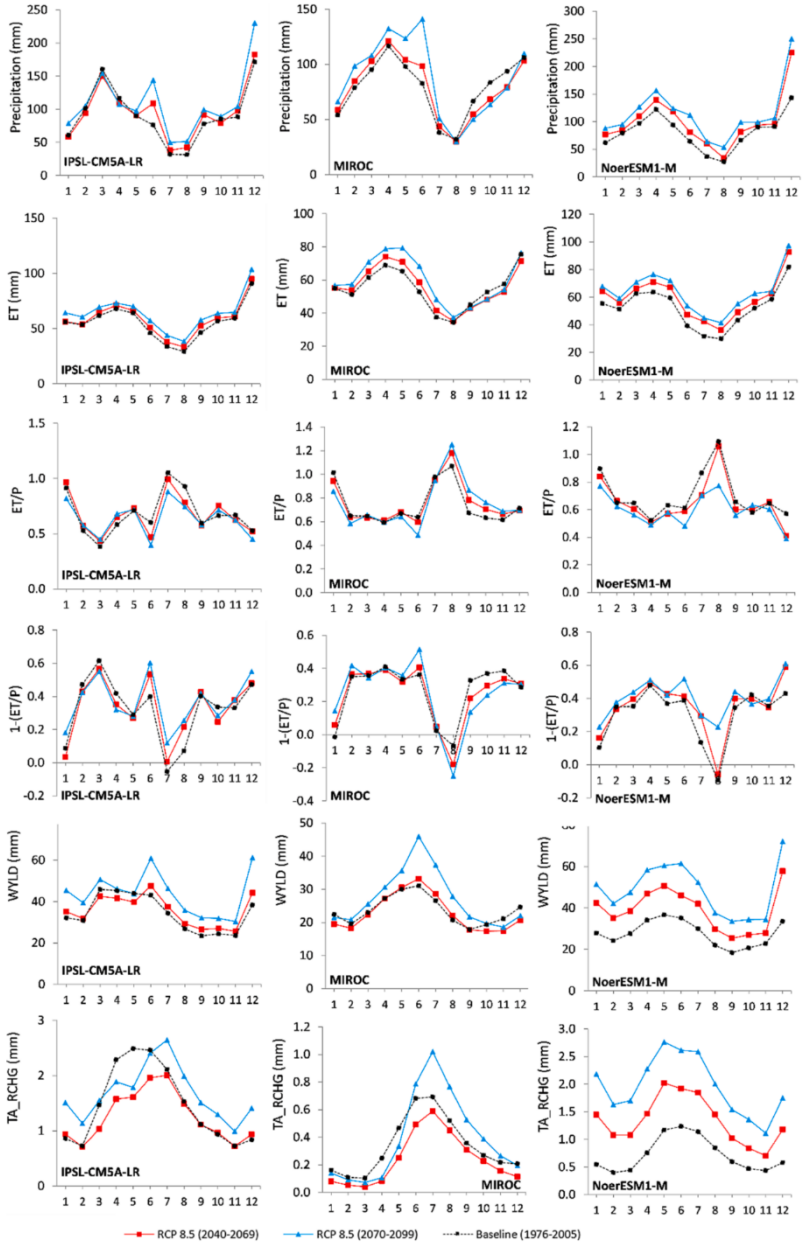

Fig. 6. Distribution of the monthly mean values of the main water balance components predicted by the three RCM-RCP 8.5 ensembles in the PRB for the baseline period (1976–2005) and the mid- (2040–2069) and long-term (2070–2099) future horizons. P—precipitation (mm); ET—evapotranspiration (mm); ET/P—evaporative fraction of P as a dimensionless fraction; 1–(ET/P) —non-evaporative fraction of P as a dimensionless fraction; WYLD—maximum amount of water that can contribute to streamflow and aquifer recharge after discounting transmission losses (mm); and TA_RCHG—total aquifer recharge (mm).

Table 8
Seasonal distribution of predicted aquifer recharge (TA_RCHG) in the PRB after implementing the RCM-RCP 4.5 and 8.5 ensembles for mid- (2040–2069) and long-term (2070–2099) future horizons.

RCM model	Emission scenario	Period	TA_RCHG (mm) [a]	TA_RCHG (wet season fraction, mm) [a]	TA_RCHG (dry season fraction, mm) [a]
IPSL-CM5A-LR	Baseline	1976–2005	17.54	6.97	4.76
	RCP 4.5	2040–2069	14.59 (–17 %)	4.99 (–28 %)	4.49 (–6%)
		2070–2099	14.98 (–15 %)	5.61 (–19 %)	4.30 (–10 %)
	RCP 8.5	2040–2069	15.05 (–14 %)	4.93 (–29 %)	4.61 (–3%)
		2070–2099	20.11 (+15 %)	6.35 (–9%)	6.14 (+29 %)
MIROC	Baseline	1976–2005	4.05	0.93	1.57
	RCP 4.5	2040–2069	3.08 (–24 %)	0.51 (–46 %)	1.44 (–9%)
		2070–2099	2.44 (–40 %)	0.79 (–15 %)	1.16 (–26 %)
	RCP 8.5	2040–2069	2.86 (–29 %)	0.43 (–54 %)	1.35 (–14 %)
		2070–2099	4.70 (+16 %)	0.61 (–35 %)	2.31 (+47 %)
NoerESM1-M	Baseline	1976–2005	8.62	2.77	2.58
	RCP 4.5	2040–2069	15.72 (+82 %)	5.21 (+88 %)	4.47 (+73 %)
		2070–2099	14.09 (+63 %)	4.96 (+79 %)	3.88 (+50 %)
	RCP 8.5	2040–2069	16.06 (+86 %)	5.65 (+104 %)	4.32 (+67 %)
		2070–2099	23.54 (+173 %)	8.38 (+203 %)	6.13 (+137 %)

[a] Changes are expressed as positive or negative absolute (in the same unit as the variable) and relative (percentages in parentheses) differences.

Table 9
Quantification of the impact of climate change on the magnitude and variability.

Parameter	RCM model	Baseline (1976–2005)	RCP 4.5 (2040–2069)	RCP 4.5 (2070–2099)	RCP 8.5 (2040–2069)	RCP 8.5 (2070–2099)
Mean (hm^3)	IPSL-CM5A-LR	74.37	74.01	76.47	76.88	93.23
	MIROC	50.57	47.63	47.88	48.79	58.47
	NoerESM1-M	59.51	81.23	78.39	83.60	105.51
EV (hm^3)	IPSL-CM5A-LR	5.13	4.94	5.58	5.15	7.74
	MIROC	2.66	2.92	3.06	3.07	4.98
	NoerESM1-M	4.36	6.84	5.90	6.88	8.26
Q10% (m^3/s)	IPSL-CM5A-LR	3.33	3.15	3.33	3.31	4.08
	MIROC	2.05	2.03	2.07	2.10	2.67
	NoerESM1-M	2.52	3.60	3.48	3.71	4.75
Q90% (m^3/s)	IPSL-CM5A-LR	1.53	1.63	1.63	1.71	2.03
	MIROC	1.22	1.13	1.11	1.14	1.28
	NoerESM1-M	1.29	1.67	1.65	1.71	2.19

Table 10
Quantification of the impact of climate change on the seasonality.

Parameter	RCM model	Emission scenario	Jan	Feb	Mar	Apr	May	Jun	Jul	Aug	Sep	Oct	Nov	Dec
Max RF	IPSL-CM5A-LR	Baseline (1976–2005)	0.00	0.00	0.38	0.10	0.14	0.21	0.00	0.00	0.00	0.00	0.00	0.17
		RCP 4.5 (2040–2069)	0.03	0.00	0.21	0.07	0.00	0.45	0.00	0.00	0.00	0.00	0.00	0.24
		RCP 4.5 (2070–2099)	0.00	0.00	0.38	0.03	0.00	0.24	0.00	0.00	0.00	0.00	0.00	0.34
		RCP 8.5 (2040–2069)	0.00	0.03	0.10	0.14	0.03	0.45	0.00	0.00	0.00	0.00	0.00	0.24
		RCP 8.5 (2070–2099)	0.03	0.03	0.14	0.00	0.00	0.45	0.00	0.00	0.00	0.00	0.00	0.34
	MIROC	Baseline (1976–2005)	0.00	0.00	0.00	0.00	0.38	0.59	0.03	0.00	0.00	0.00	0.00	0.00
		RCP 4.5 (2040–2069)	0.00	0.00	0.00	0.00	0.10	0.90	0.00	0.00	0.00	0.00	0.00	0.00
		RCP 4.5 (2070–2099)	0.00	0.00	0.00	0.00	0.24	0.76	0.00	0.00	0.00	0.00	0.00	0.00
		RCP 8.5 (2040–2069)	0.00	0.00	0.00	0.00	0.28	0.72	0.00	0.00	0.00	0.00	0.00	0.00
		RCP 8.5 (2070–2099)	0.00	0.00	0.00	0.00	0.38	0.59	0.03	0.00	0.00	0.00	0.00	0.00
	NoerESM1-M	Baseline (1976–2005)	0.00	0.00	0.00	0.14	0.41	0.21	0.07	0.00	0.00	0.00	0.00	0.17
		RCP 4.5 (2040–2069)	0.07	0.00	0.00	0.03	0.28	0.14	0.00	0.00	0.00	0.00	0.00	0.48
		RCP 4.5 (2070–2099)	0.03	0.00	0.00	0.24	0.17	0.21	0.00	0.00	0.00	0.00	0.00	0.34
		RCP 8.5 (2040–2069)	0.03	0.00	0.00	0.10	0.21	0.10	0.07	0.00	0.00	0.00	0.00	0.48
		RCP 8.5 (2070–2099)	0.00	0.00	0.00	0.07	0.07	0.21	0.03	0.00	0.00	0.00	0.00	0.62
Min RF	IPSL-CM5A-LR	Baseline (1976–2005)	0.03	0.14	0.00	0.00	0.00	0.00	0.00	0.03	0.28	0.21	0.31	0.00
		RCP 4.5 (2040–2069)	0.07	0.10	0.00	0.00	0.00	0.00	0.00	0.03	0.10	0.14	0.55	0.00
		RCP 4.5 (2070–2099)	0.03	0.03	0.00	0.00	0.00	0.00	0.00	0.00	0.31	0.21	0.41	0.00
		RCP 8.5 (2040–2069)	0.03	0.10	0.00	0.00	0.03	0.00	0.00	0.03	0.31	0.07	0.41	0.00
		RCP 8.5 (2070–2099)	0.03	0.07	0.00	0.07	0.00	0.00	0.00	0.03	0.10	0.24	0.45	0.00
	MIROC	Baseline (1976–2005)	0.00	0.28	0.00	0.00	0.00	0.00	0.00	0.00	0.66	0.03	0.03	0.00
		RCP 4.5 (2040–2069)	0.00	0.28	0.00	0.00	0.00	0.00	0.00	0.00	0.24	0.24	0.24	0.00
		RCP 4.5 (2070–2099)	0.00	0.17	0.00	0.00	0.00	0.00	0.00	0.00	0.10	0.31	0.41	0.00
		RCP 8.5 (2040–2069)	0.07	0.17	0.00	0.00	0.00	0.00	0.00	0.00	0.21	0.28	0.28	0.00
		RCP 8.5 (2070–2099)	0.00	0.28	0.00	0.00	0.00	0.00	0.00	0.00	0.66	0.03	0.03	0.00
	NoerESM1-M	Baseline (1976–2005)	0.00	0.03	0.00	0.00	0.00	0.00	0.00	0.00	0.90	0.07	0.00	0.00
		RCP 4.5 (2040–2069)	0.00	0.07	0.00	0.00	0.00	0.00	0.00	0.00	0.69	0.10	0.14	0.00
		RCP 4.5 (2070–2099)	0.00	0.07	0.00	0.00	0.00	0.00	0.00	0.03	0.76	0.03	0.10	0.00
		RCP 8.5 (2040–2069)	0.00	0.03	0.00	0.00	0.00	0.00	0.00	0.07	0.66	0.10	0.14	0.00
		RCP 8.5 (2070–2099)	0.00	0.00	0.00	0.00	0.00	0.00	0.00	0.17	0.28	0.21	0.34	0.00

Table 9, there is no significant overall increase in annual flows except in the long term and under the scenario RCP 8.5. Only the RCM Model NoerESM1-M estimates significant increases in annual flows in the short and long term and for RCP 4.5 and 8.5. However, there is a wider consensus in estimating an increase in flow variability. For example, all models estimate that the extreme variability may almost double in the long term and under the RCP 8.5 scenario. It is important to note that this increase in variability can significantly affect the geomorphological and ecological dynamics of the river and thus the diversity of the river (López-Ballesteros et al., 2020). Accordingly, variability based on the 10th and 90th percentiles will also increase, although to a more limited extent than extreme variability.

The seasonality in which maximum and minimum flows occur in a river is an aspect that is closely and synchronously linked to the life cycles of the species (Ngor et al., 2018). As can be seen in Table 10, climate change can significantly affect these life cycles. A delay is observed in the MaxRF, with respect to the maximums that tend to occur in the month of May and which in the future will occur more frequently in June. An increase in the frequency of these MaxRFs is also observed in December. Regarding the MinRFs, all models coincide in concentrating these MinRFs during the months of September-November. There is a clear tendency to delay the occurrence of these minimum values from September to November.

5. Conclusions

This paper has evaluated the impact of projected climate change scenarios on renewable groundwater resources in the PRB. Three selected RCM models (IPSL-CM5A-LR, MIROC and NoerESM1-M) demonstrated a general increase in average annual temperature, ranging from + 2 °C, in the mid-term, to + 4.5 °C, in the long term. However, average annual precipitation increased between + 3 % and + 20 %, and even as high as + 41 % in the RCP 8.5 scenario. Although the increase in precipitation (P) will induce higher streamflow, the increase in temperature (T) is more relevant and could increase actual evapotranspiration (ET), reducing streamflow and aquifer recharge. Aquifer recharge better correlates with the evaporative (ET:P ratio) and non-evaporative (1–[ET:P] ratio) fractions of P rather than P or ET. The IPSL-CM5A-LR and MIROC models revealed a general decrease in aquifer recharge, although this trend was softened, or even reversed, in several long-term scenarios. Conversely, the NoerESM1-M model significantly increased aquifer recharge in the mid and long term, which is consistent with admission of more recharge events as the aquifer empties moderately in a context of lower water resources availability in the future. Furthermore, this final RCM model exhibited greater differences in seasonal aquifer recharge regarding the baseline scenario. The difference was as high as + 23 % during the wet season in the long term.

The satisfactory performance on the monthly scale was a prerequisite for considering the SWAT model suitable for long-term water resources evaluation. However, underestimations of streamflow peaks indicate additional uncertainty extending to streamflow and aquifer recharge predictions in the mid and long term regarding equivalent predictions in the baseline scenario. Similarly, weak performance on the daily scale could limit SWAT model application when predicting extraordinary flood events and rapid groundwater response, expected following soil degradation and higher rainfall intensities induced by global warming in the future.

Regarding the significance of renewable groundwater resources in the PRB, in particular, and the Andean highlands, in general, future research should aim to refine future predictions based on necessary groundwater monitoring to support specific groundwater modelling tools. For example, coupled SWAT-MODFLOW models have proven satisfactory solutions, provided piezometry can be monitored long-term and hydraulic parameters for aquifers and hydraulically connected aquitards can be surveyed accurately. Similarly, uncertainty in RCM results could be reduced by extending the comparison to more data-demanding climate change scenarios, which is currently unfeasible based on existing data.

Despite these unavoidable limitations, the model results are sufficiently confident to provide detailed insights into uncertainties regarding groundwater resources and improve the knowledge base required to enhance decision-making based on sustainability. Furthermore, the model results can help forecast hydrological stress trends and subsequent ecological risks in Andean alpine ecosystems. Although this paper focuses on the PRB, it aims to provide the foundation for studies in other data-scarce basins in the andosol-dominated Andean highlands, where global warming is already affecting traditional freshwater availability.

Declaration of competing interest

The authors declare that they have no known competing financial interests or personal relationships that could have appeared to influence the work reported in this paper.

Data availability

Data will be made available on request.

Acknowledgements

This research was partly supported by the International Atomic Energy Agency Project ECU/7/006, the Ecuadorian Research Project PROMETEO-CEB-014-2015, the EU HORIZON project CiROCCO under Grant Agreement No 101086497 and the Spanish Ministry of Science and Innovation Research Project (PID2021-128126OA-I00). The authors are grateful to the Quito's Public Water Supply Company (EPMAPS), Water Protection Fund of Ecuador (FONAG), Institute for Meteorology and Hydrology of Ecuador (INAMHI), and Ecuador Water Authority (SENAGUA) for the suggestions and information provided. Also, thanks to Scribbr editing services for proofreading the text.

References

Abbaspour, K.C., 2007. User manual for SWAT-CUP. SWAT Calibration and Uncertainty Analysis Programs. Swiss Federal Institute of Aquatic Science and Technology, Eawag, Duebendorf, Switzerland.

Ahl, R.S., Woods, S.W., Zuuring, H.R., 2008. Hydrologic calibration and validation of SWAT in a snow-dominated Rocky Mountain watershed, Montana, USA. J. Am. Water Resour. Assoc. 44, 1411–1430. https://doi.org/10.1111/j.1752-1688.2008.00233.x.

Alcalá, F.J., 2016. Optimization of methods to evaluate the groundwater quantity and quality dynamics in basins of the province of Tungurahua in Ecuador (Scientific Report PROMETEO-CEB-014-2015). Secretary for Higher Education Science, Technology and Innovation of Ecuador (SENESCYT), Quito, Ecuador.

Alcalá, F.J., Cantón, Y., Contreras, S., Were, A., Serrano-Ortiz, P., Puigdefábregas, J., Solé-Benet, A., Custodio, E., Domingo, F., 2011. Diffuse and concentrated recharge evaluation using physical and tracer techniques: results from a semiarid carbonate massif aquifer in southeastern Spain. Environ. Earth Sci. 62, 541–557. https://doi.org/10.1007/s12665-010-0546-y.

Alcalá, F.J., Martín-Martín, M., Guerrera, F., Martínez-Valderrama, J., Robles-Marín, P., 2018. A feasible methodology for groundwater resource modelling for sustainable use in sparse-data drylands: Application to the Amtoudi Oasis in the northern Sahara. Sci. Total Environ. 630, 1246–1257. https://doi.org/10.1016/j.scitotenv.2018.02.294.

Anderson, E.P., Marengo, J., Villalba, R., Halloy, S., Young, B., Cordero, D., Gast, F., Jaimes, E., Ruiz, D., 2011. Consequences of climate change for ecosystems and ecosystem services in the tropical Andes. In: Climate Change and Biodiversity in the Tropical Andes Inter-American Institute for Global Change Research (IAI) and Scientific Committee on Problems of the Environment (SCOPE), pp. 1–18.

Arnold, J.G., Srinivasan, R., Muttiah, R.S., Williams, J.R., 1998. Large Area Hydrologic Modeling and Assessment Part I: Model Development. J Am Water Resources Assoc 34, 73–89. https://doi.org/10.1111/j.1752-1688.1998.tb05961.x.

Arnold, J.G., Moriasi, D.N., Gassman, P.W., Abbaspour, K.C., White, M.J., Srinivasan, R., Santhi, C., Harmel, R.D., van Griensven, A., Van Liew, M.W., Kannan, N., Jha, M.K., 2012. SWAT: Model Use, Calibration, and Validation. Trans. ASABE 55, 1491–1508. https://doi.org/10.13031/2013.42256.

Athira, P., Sudheer, K.P., 2021. Calibration of distributed hydrological models considering the heterogeneity of the parameters across the basin: a case study of

SWAT model. Environ. Earth Sci. 80, 131. https://doi.org/10.1007/s12665-021-09434-8.
Baraer, M., McKenzie, J., Mark, B.G., Gordon, R., Bury, J., Condom, T., Gomez, J., Knox, S., Fortner, S.K., 2014. Contribution of groundwater to the outflow from ungauged glacierized catchments: a multi-site study in the tropical Cordillera Blanca. Peru. Hydrol, Process, p. 21.
Barnett, T.P., Adam, J.C., Lettenmaier, D.P., 2005. Potential impacts of a warming climate on water availability in snow-dominated regions. Nature 438, 303–309. https://doi.org/10.1038/nature04141.
Bendix, J., 2000. Precipitation dynamics in Ecuador and northern Peru during the 1991/92 El Nino: A remote sensing perspective. Int. J. Remote Sens. 21, 533–548. https://doi.org/10.1080/014311600210731.
Bendix, J., Rollenbeck, R., Palacios, W.E., 2004. Cloud detection in the Tropics–a suitable tool for climate-ecological studies in the high mountains of Ecuador. Int. J. Remote Sens. 25, 4521–4540. https://doi.org/10.1080/01431160410001709967.
Bhunia, G.S., 2020. An approach to demarcate groundwater recharge potential zone using geospatial technology. Appl Water Sci 10, 138. https://doi.org/10.1007/s13201-020-01231-1.
Blanco-Gómez, P., Jimeno-Sáez, P., Senent-Aparicio, J., Pérez-Sánchez, J., 2019. Impact of Climate Change on Water Balance Components and Droughts in the Guajoyo River Basin (El Salvador). Water 11, 2360. https://doi.org/10.3390/w11112360.
Boulanger, J.-P., Martinez, F., Segura, E.C., 2007. Projection of future climate change conditions using IPCC simulations, neural networks and Bayesian statistics. Part 2: Precipitation mean state and seasonal cycle in South America. Clim. Dyn. 28, 255–271. https://doi.org/10.1007/s00382-006-0182-0.
Bovolo, C.I., Parkin, G., Sophocleous, M., 2009. Groundwater resources, climate and vulnerability. Environ. Res. Lett. 4, 035001 https://doi.org/10.1088/1748-9326/4/3/035001.
Bradley, R.S., Vuille, M., Diaz, H.F., Vergara, W., 2006. Threats to water supplies in the tropical andes. Science 312, 1755–1756. https://doi.org/10.1126/science.1128087.
Buytaert, W., De Bièvre, B., Wyseure, G., Deckers, J., 2004. The use of the linear reservoir concept to quantify the impact of changes in land use on the hydrology of catchments in the Andes. Hydrol. Earth Syst. Sci. 8, 108–114. https://doi.org/10.5194/hess-8-108-2004.
Buytaert, W., Sevink, J., De Leeuw, B., Deckers, J., 2005a. Clay mineralogy of the soils in the south Ecuadorian páramo region. Geoderma 127, 114–129. https://doi.org/10.1016/j.geoderma.2004.11.021.
Buytaert, W., Wyseure, G., De Bièvre, B., Deckers, J., 2005b. The effect of land-use changes on the hydrological behaviour of Histic Andosols in south Ecuador. Hydrol. Process. 19, 3985–3997. https://doi.org/10.1002/hyp.5867.
Buytaert, W., Célleri, R., De Bièvre, B., Cisneros, F., Wyseure, G., Deckers, J., Hofstede, R., 2006. Human impact on the hydrology of the Andean páramos. Earth-Sci. Rev. 79, 53–72. https://doi.org/10.1016/j.earscirev.2006.06.002.
Buytaert, W., Célleri, R., Timbe, L., 2009. Predicting climate change impacts on water resources in the tropical Andes: Effects of GCM uncertainty. Geophys. Res. Lett. 36 https://doi.org/10.1029/2008GL037048.
Buytaert, W., Vuille, M., Dewulf, A., Urrutia, R., Karmalkar, A., Célleri, R., 2010. Uncertainties in climate change projections and regional downscaling in the tropical Andes: implications for water resources management. Hydrol. Earth Syst. Sci. 14, 1247–1258. https://doi.org/10.5194/hess-14-1247-2010.
Buytaert, W., Cuesta-Camacho, F., Tobón, C., 2011. Potential impacts of climate change on the environmental services of humid tropical alpine regions: Climate change and environmental services. Global Ecology and Biogeography 20, 19–33. https://doi.org/10.1111/j.1466-8238.2010.00585.x.
Buytaert, W., Sevink, J., Cuesta, F., LLambi, L., Posner, J., 2014. Cambio climático: la nueva amenaza para los páramos, in: Avances En Investigación Para La Conservación de Los Páramos Andinos. Condesan, Lima, Peru.
Carvajal, P.E., Anandarajah, G., Mulugetta, Y., Dessens, O., 2017. Assessing uncertainty of climate change impacts on long-term hydropower generation using the CMIP5 ensemble—the case of Ecuador. Climatic Change 144, 611–624. https://doi.org/10.1007/s10584-017-2055-4.
Castellanos-Osorio, G., López-Ballesteros, A., Pérez-Sánchez, J., Senent-Aparicio, J., 2023. Disaggregated monthly SWAT+ model versus daily SWAT+ model for estimating environmental flows in Peninsular Spain. J. Hydrol. 623, 129837 https://doi.org/10.1016/j.jhydrol.2023.129837.
Célleri, R., Feyen, J., 2009. The hydrology of tropical andean ecosystems: Importance, knowledge status, and perspectives. Mt. Res. Dev. 29, 350–355. https://doi.org/10.1659/mrd.00007.
Changkuon, L., Aranyossy, J.F., Oleas, M., Lopoukine, M., 1989. Determination of the geothermal model of the Chillos Valley (Ecuador), based on environmental isotopes. In: Isotope Hydrology Investigations in Latin America. IAEA, Vienna, Austria, pp. 291–303.
Chen, J., Brissette, F.P., Chaumont, D., Braun, M., 2013. Performance and uncertainty evaluation of empirical downscaling methods in quantifying the climate change impacts on hydrology over two North American river basins. J. Hydrol. 479, 200–214. https://doi.org/10.1016/j.jhydrol.2012.11.062.
Chen, Y., Chen, X., Xu, C.Y., Zhang, M., Liu, M., Gao, L., 2018. Toward improved calibration of SWAT using season-based multi-objective optimization: a case study in the Jinjiang Basin in southeastern China. Water Resour. Manag. 32 (4), 1193–1207. https://doi.org/10.1007/s11269-017-1862-8.
Cheng, S., Cheng, L., Liu, P., Zhang, L., Xu, C., Xiong, L., Xia, J., 2020. Evaluation of baseflow modelling structure in monthly water balance models using 443 Australian catchments. J. Hydrol. 591, 125572 https://doi.org/10.1016/j.jhydrol.2020.125572.
Cheng, Y., Ogden, F.L., Zhu, J., 2017. Earthworms and tree roots: A model study of the effect of preferential flow paths on runoff generation and groundwater recharge in steep, saprolitic, tropical lowland catchments. Water Resour. Res. 53, 5400–5419. https://doi.org/10.1002/2016WR020258.
Chiew, F.H.S., Peel, M.C., McMahon, T.A., Siriwardena, L.W., 2006. Precipitation elasticity of streamflow in catchments across the world, in: Climate Variability and Change: Hydrological Impacts, IAHS Publication. In: Press, I.A.H.S. (Ed.), Presented at the 5th FRIEND World Conference. Havana, CUBA, pp. 256–262.
Clapperton, C.M., 1993. Quaternary geology and geomorphology of south america. Elsevier, Amsterdam.
CLIRSEN-EMAAP-Q, 2006. Diagnóstico ambiental de la cuenca del río pita. Memoria Técnica, Quito.
Cresso, M., Clerici, N., Sanchez, A., Jaramillo, F., 2020. Future climate change renders unsuitable conditions for paramo ecosystems in colombia. Sustainability 12, 8373. https://doi.org/10.3390/su12208373.
Cuesta, F., Muriel, P., Llambí, L.D., Halloy, S., Aguirre, N., Beck, S., Carilla, J., Meneses, R.I., Cuello, S., Grau, A., Gámez, L.E., Irazábal, J., Jácome, J., Jaramillo, R., Ramírez, L., Samaniego, N., Suárez-Duque, D., Thompson, N., Tupayachi, A., Viñas, P., Yager, K., Becerra, M.T., Pauli, H., Gosling, W.D., 2017. Latitudinal and altitudinal patterns of plant community diversity on mountain summits across the tropical Andes. Ecography 40, 1381–1394. https://doi.org/10.1111/ecog.02567.
Cuffey, K., Paterson, W.S.B., 2010. The Physics of Glaciers. Academic Press, Burlington and Oxford.
Dile, Y.T., Daggupati, P., George, C., Srinivasan, R., Arnold, J., 2016. Introducing a new open source GIS user interface for the SWAT model. Environ. Modell. Softw. 85, 129–138. https://doi.org/10.1016/j.envsoft.2016.08.004.
Döll, P., 2009. Vulnerability to the impact of climate change on renewable groundwater resources: a global-scale assessment. Environ. Res. Lett. 4, 035006 https://doi.org/10.1088/1748-9326/4/3/035006.
Eckhardt, K., Fohrer, N., Frede, H.-G., 2005. Automatic model calibration. Hydrol. Process. 19, 651–658. https://doi.org/10.1002/hyp.5613.
Ekolu, J., Dieppois, B., Sidibe, M., Eden, J.M., Tramblay, Y., Villarini, G., Peña-Angulo, D., Mahé, G., Paturel, J.-E., Onyutha, C., van de Wiel, M., 2022. Long-term variability in hydrological droughts and floods in sub-Saharan Africa: New perspectives from a 65-year daily streamflow dataset. J. Hydrol. 613, 128359 https://doi.org/10.1016/j.jhydrol.2022.128359.
España, S., Alcalá, F.J., Vallejos, Á., Pulido-Bosch, A., 2011. ArcE: A GIS tool for modelling actual evapotranspiration. Comput. Geosci. 37, 1468–1475. https://doi.org/10.1016/j.cageo.2011.03.008.
España, S., Alcalá, F.J., Vallejos, Á., Pulido-Bosch, A., 2013. A GIS tool for modelling annual diffuse infiltration on a plot scale. Comput. Geosci. 54, 318–325. https://doi.org/10.1016/j.cageo.2013.01.017.
Espinoza-Villar, J.C., Ronchail, J., Guyot, J.L., Cochonneau, G., Naziano, F., Lavado, W., De Oliveira, E., Pombosa, R., Vauchel, P., 2009. Spatio-temporal rainfall variability in the Amazon basin countries (Brazil, Peru, Bolivia, Colombia, and Ecuador). Int. J. Climatol. 29, 1574–1594. https://doi.org/10.1002/joc.1791.
FAO/UNESCO, 1988. Soil map of the world: Revised legend; FAO world resources report 60. Food and Agricultural Organization of the United Nations, Rome, Italy.
Favier, V., Coudrain, A., Cadier, E., Francou, B., Ayabaca, E., Maisincho, L., Pradeiro, E., Villacís, M., Wagnon, P., 2008. Evidence of groundwater flow on Antizana ice-covered volcano, Ecuador / Mise en évidence d'écoulements souterrains sur le volcan englacé Antizana. Equateur. Hydrol. Sci. J. 53, 278–291. https://doi.org/10.1623/hysj.53.1.278.
Fernández, J.A., Martínez, C., Magdaleno, F., 2012. Application of indicators of hydrologic alterations in the designation of heavily modified water bodies in Spain. Environmental Science & Policy 16, 31–43. https://doi.org/10.1016/j.envsci.2011.10.004.
Fernandez-Palomino, C.A., Hattermann, F.F., Krysanova, V., Vega-Jácome, F., Bronstert, A., 2021. Towards a more consistent eco-hydrological modelling through multi-objective calibration: a case study in the Andean Vilcanota River basin, Peru. Hydrological Sciences Journal 66, 59–74. https://doi.org/10.1080/02626667.2020.1846740.
Flores-López, F., Galaitsi, S., Escobar, M., Purkey, D., 2016. Modeling of Andean páramo ecosystems' hydrological response to environmental change. Water 8, 94. https://doi.org/10.3390/w8030094.
FONAG, 2022. Fondo para la protección del agua [WWW Document]. accessed 6.12.22. https://www.fonag.org.ec/web/.
Gan, T.Y., Dlamini, E.M., Biftu, G.F., 1997. Effects of model complexity and structure, data quality, and objective functions on hydrologic modeling. Journal of Hydrology 192, 81–103. https://doi.org/10.1016/S0022-1694(96)03114-9.
Garreaud, R.D., Falvey, M., 2008. The coastal winds off western subtropical South America in future climate scenarios. Int. J. Climatol. 12.
Garrison, J.M., Davidson, J.P., Hall, M., Mothes, P., 2011. Geochemistry and petrology of the most recent deposits from cotopaxi volcano, northern volcanic zone. Ecuador. J. Petrol. 52, 1641–1678. https://doi.org/10.1093/petrology/egr023.
Gassman, P.W., Reyes, M.R., Green, C.H., Arnold, J.G., 2007. The soil and water assessment tool: Historical development, applications, and future research directions. T. ASABE 50, 1211–1250. https://doi.org/10.13031/2013.23637.
Gassman, P.W., Sadeghi, A.M., Srinivasan, R., 2014. Applications of the SWAT model special section: Overview and insights. J. Environ. Qual. 43, 1–8. https://doi.org/10.2134/jeq2013.11.0466.
Georgakakos, A.P., Yao, H., Kistenmacher, M., Georgakakos, K.P., Graham, N.E., Cheng, F.-Y., Spencer, C., Shamir, E., 2010. Value of adaptive water resources management in Northern California under climatic variability and change: Reservoir management. J. Hydrol., Hydrology Conference. https://doi.org/10.1016/j.jhydrol.2011.04.038.
González-Zeas, D., Erazo, B., Lloret, P., De Bièvre, B., Steinschneider, S., Dangles, O., 2019. Linking global climate change to local water availability: Limitations and

prospects for a tropical mountain watershed. Sci. Total Environ. 650, 2577–2586. https://doi.org/10.1016/j.scitotenv.2018.09.309.
Green, T.R., Taniguchi, M., Kooi, H., 2007. Potential impacts of climate change and human activity on subsurface water resources. Vadose Zone J. 6, 531–532. https://doi.org/10.2136/vzj2007.0098.
Green, T.R., Taniguchi, M., Kooi, H., Gurdak, J.J., Allen, D.M., Hiscock, K.M., Treidel, H., Aureli, A., 2011. Beneath the surface of global change: Impacts of climate change on groundwater. J. Hydrol. 405, 532–560. https://doi.org/10.1016/j.jhydrol.2011.05.002.
Gupta, H.V., Sorooshian, S., Yapo, P.O., 1999. Status of automatic calibration for hydrologic models: Comparison with multilevel expert calibration. J. Hydrol. Eng. 4, 135–143. https://doi.org/10.1061/(ASCE)1084-0699(1999)4:2(135).
Gupta, H.V., Kling, H., Yilmaz, K.K., Martinez, G.F., 2009. Decomposition of the mean squared error and NSE performance criteria: Implications for improving hydrological modelling. J. Hydrol. 377, 80–91. https://doi.org/10.1016/j.jhydrol.2009.08.003.
Gutiérrez-Salazar, P., Medrano-Vizcaíno, P., 2019. The effects of climate change on decomposition processes in Andean paramo ecosystem–synthesis, a systematic review. Appl. Ecol. Env. Res. 17, 4957–4970. https://doi.org/10.15666/aeer/1702_49574970.
Hall, M., Mothes, P., 2008. The rhyolitic–andesitic eruptive history of Cotopaxi volcano. Ecuador. Bull. Volcanol. 70, 675–702. https://doi.org/10.1007/s00445-007-0161-2.
Hall, M.L., Wood, C.A., 1985. Volcano-tectonic segmentation of the northern Andes. Geology 13, 203–207. https://doi.org/10.1130/0091-7613(1985)13<203:VSOTNA>2.0.CO;2.
Hargreaves, G.H., 1994. Defining and using reference evapotranspiration. J. Irrig. Drainage Eng.-ASCE 120, 1132–1139. https://doi.org/10.1061/(ASCE)0733-9437(1994)120:6(1132).
Hemmings, B., Whitaker, F., Gottsmann, J., Hawes, M.C., 2016. Non-eruptive ice melt driven by internal heat at glaciated stratovolcanoes. J. Volcanol. Geotherm. Res. 327, 385–397. https://doi.org/10.1016/j.jvolgeores.2016.09.004.
Herzog, S.K., Martínez, R., Jørgensen, P.M., Tiessen, H., 2012. Climate change and biodiversity in the tropical andes [spanish]. – inter-american institute for global change research (IAI). Montevideo and Scientific Committee on Problems of the Environment (SCOPE).
Ilbay-Yupa, M., Ilbay, F., Zubieta, R., García-Mora, M., Chasi, P., 2021. Impacts of climate change on the precipitation and streamflow regimes in equatorial regions: guayas river basin. Water 13, 3138. https://doi.org/10.3390/w13213138.
Jain, S.K., Jain, S.K., Jain, N., Xu, C.-Y., 2017. Hydrologic modeling of a Himalayan mountain basin by using the SWAT mode. Hydrol. Earth Syst. Sc. 1–26 https://doi.org/10.5194/hess-2017-100.
Jimeno-Sáez, P., Senent-Aparicio, J., Pérez-Sánchez, J., Pulido-Velazquez, D., 2018. A comparison of SWAT and ANN models for daily runoff simulation in different climatic zones of peninsular spain. Water 10, 192. https://doi.org/10.3390/w10020192.
Jimeno-Sáez, P., Blanco-Gómez, P., Pérez-Sánchez, J., Cecilia, J.M., Senent-Aparicio, J., 2021. impact assessment of gridded precipitation products on streamflow simulations over a poorly gauged basin in El salvador. Water 13, 2497. https://doi.org/10.3390/w13182497.
Kalin, L., Isik, S., Schoonover, J.E., Lockaby, B.G., 2010. Predicting water quality in unmonitored watersheds using artificial neural networks. J. Environ. Qual. 39, 12.
Kannan, N., White, S.M., Worrall, F., Whelan, M.J., 2007. Sensitivity analysis and identification of the best evapotranspiration and runoff options for hydrological modelling in SWAT-2000. J. Hydrol. 332, 456–466. https://doi.org/10.1016/j.jhydrol.2006.08.001.
Kilsby, C.G., Tellier, S.S., Fowler, H.J., Howels, T.R., 2007. Hydrological impacts of climate change on the Tejo and Guadiana Rivers. Hydrol. Earth Syst. Sci. 11, 1175–1189. https://doi.org/10.5194/hess-11-1175-2007.
Kirtman, B., Power, S.B., Adedoyin, A.J., Boer, G.J., Bojariu, R., Doblas-Reyes, F., Fiore, A.M., Kimoto, M., Meehl, G., Prather, M., Sarr, A., Schär, C., Sutton, R., van Oldenborgh, G.J., Vecchi, G., Wang, H.-J., 2013. Near-term Climate Change: Projections and Predictability, in: Climate Change 2013: The Physical Science Basis. Contribution of Working Group I to the Fifth Assessment Report of the Intergovernmental Panel on Climate Change. Cambridge University Press, Cambridge, UK, New York.
Kitzberger, T., Tiribelli, F., Barberá, I., Gowda, J.H., Morales, J.M., Zalazar, L., Paritsis, J., 2022. Projections of fire probability and ecosystem vulnerability under 21st century climate across a trans-Andean productivity gradient in Patagonia. Science of the Total Environment 839, 156303. https://doi.org/10.1016/j.scitotenv.2022.156303.
Knoben, W.J.M., Freer, J.E., Woods, R.A., 2019. Technical note: Inherent benchmark or not? Comparing Nash-Sutcliffe and Kling-Gupta efficiency scores. Hydrol. Earth Syst. Sci. 23, 4323–4331. https://doi.org/10.5194/hess-23-4323-2019.
Krause, P., Boyle, D.P., Bäse, F., 2005. Comparison of different efficiency criteria for hydrological model assessment. Adv. Geosci. 5, 89–97.
Kumar, N., Dubey, A.K., Goswami, U.P., Singh, S.K., 2022. Modelling of hydrological and environmental flow dynamics over a central Himalayan river basin through satellite altimetry and recent climate projections. Intl Journal of Climatology 42, 8446–8471. https://doi.org/10.1002/joc.7734.
Legates, D.R., McCabe Jr., G.J., 1999. Evaluating the use of "goodness-of-fit" Measures in hydrologic and hydroclimatic model validation. Water Resour. Res. 35, 233–241. https://doi.org/10.1029/1998WR900018.
Liu, S., Pérez-Sánchez, J., Jimeno-Sáez, P., Alcalá, F.J., Senent-Aparicio, J., 2022. A novel approach to assessing the impacts of dam construction on hydrologic and ecosystem alterations. Case study: Castril river basin. Spain. Ecohydrol. Hydrobiol. 22, 598–608. https://doi.org/10.1016/j.ecohyd.2022.08.004.
López-Ballesteros, A., Senent-Aparicio, J., Martínez, C., Pérez-Sánchez, J., 2020. Assessment of future hydrologic alteration due to climate change in the Aracthos River basin (NW Greece). Sci. Total Environ. 733, 139299 https://doi.org/10.1016/j.scitotenv.2020.139299.
López-Moreno, J.I., Vicente-Serrano, S.M., Moran-Tejeda, E., Zabalza, J., Lorenzo-Lacruz, J., García-Ruiz, J.M., 2011. Impact of climate evolution and land use changes on water yield in the ebro basin. Hydrol. Earth Syst. Sci. 15, 311–322. https://doi.org/10.5194/hess-15-311-2011.
Luo, Y., Arnold, J., Allen, P., Chen, X., 2012. Baseflow simulation using SWAT model in an inland river basin in Tianshan Mountains. Northwest China. Hydrol. Earth Syst. Sci. 16, 1259–1267. https://doi.org/10.5194/hess-16-1259-2012.
MAG-ORSTOM, 1978. Mapa de Suelos, hoja Quito, escala 1:50.000.
Makowski Giannoni, S., Trachte, K., Rollenbeck, R., Lehnert, L., Fuchs, J., Bendix, J., 2016. Atmospheric salt deposition in a tropical mountain rainforest at the eastern Andean slopes ofsouth Ecuador – Pacific or Atlantic origin? Atmos. Chem. Phys. 16, 10241–10261. https://doi.org/10.5194/acp-16-10241-2016.
Martínez, R., Ruiz, D., Andrade, M., Blacutt, L., 2011. Synthesis of the climate of the tropical Andes. Climate Change Effects on the Biodiversity of the Tropical Andes: An Assessment of the Status of Scientific Knowledge. IAI-SCOPE, Paris.
Mejía, L., Morocho, E., Colmet-Daage, F., Zebrowski, C., 1978. Soils Map of Quito (scale 1:200,000). National Programme for Agricultural Regionalization (PRONAREG) and Overseas Office of Scientific and Technical Research of France (ORSTOM), Ministry of Agriculture and Livestock of Ecuador, Quito.
Mishra, Y., Nakamura, T., Babel, M.S., Ninsawat, S., Ochi, S., 2018. Impact of climate change on water resources of the bheri river basin. Nepal. Water 10, 220. https://doi.org/10.3390/w10020220.
Moriasi, D.N., Arnold, J.G., Liew, M.W.V., Bingner, R.L., Harmel, R.D., Veith, T.L., 2007. Model evaluation guidelines for systematic quantification of accuracy in watershed simulations. Trans. ASABE 50, 885–900. https://doi.org/10.13031/2013.23153.
Moriasi, D.N., Gitau, D.N., Pai, N., Daggupati, P., 2015. Hydrologic and water quality models: Performance measures and evaluation criteria. Trans. ASABE 58, 1763–1785. https://doi.org/10.13031/trans.58.10715.
Muñoz, P., Orellana-Alvear, J., Célleri, R., 2021. Application of a machine learning technique for developing short-term flood and drought forecasting models in tropical mountainous catchments. In: Djalante, R., Bisri, M.B.F., Shaw, R. (Eds.), Integrated Research on Disaster Risks, Disaster Risk Reduction. Springer International Publishing, Cham, pp. 11–35. https://doi.org/10.1007/978-3-030-55563-4_2.
Myers, N., Mittermeier, R.A., Mittermeier, C.G., da Fonseca, G.A.B., Kent, J., 2000. Biodiversity hotspots for conservation priorities. Nature 403, 853–858. https://doi.org/10.1038/35002501.
Nash, J.E., Sutcliffe, J.V., 1970. River flow forecasting through conceptual models. Part I: A discussion of principles. J. Hydrol. 10, 282–290. https://doi.org/10.1016/0022-1694(70)90255-6.
Neitsch, S.L., Arnold, J.G., Kiniry, J.R., Williams, J.R., 2011. SWAT Theoretical Documentation.
Ngor, P.B., Oberdorff, T., Phen, C., Baehr, C., Grenouillet, G., Lek, S., 2018. Fish assemblage responses to flow seasonality and predictability in a tropical flood pulse system. Ecosphere 9, e02366.
Ochoa-Tocachi, B.F., Buytaert, W., De Bièvre, B., 2016. Regionalization of land-use impacts on streamflow using a network of paired catchments: Regionalization using paired catchments. Water Resour. Res. 52, 6710–6729. https://doi.org/10.1002/2016WR018596.
Ochoa-Tocachi, B.F., Buytaert, W., Antiporta, J., Acosta, L., Bardales, J.D., Célleri, R., Crespo, P., Fuentes, P., Gil-Ríos, J., Guallpa, M., Llerena, C., Olaya, D., Pardo, P., Rojas, G., Villacís, M., Villazón, M., Viñas, P., De Bièvre, B., 2018. High-resolution hydrometeorological data from a network of headwater catchments in the tropical Andes. Sci Data 5, 180080. https://doi.org/10.1038/sdata.2018.80.
Oñate-Valdivieso, F., Bosque-Sendra, J., 2014. Semidistributed hydrological model with scarce information: Application to a large south amerıcan binational basin. J. Hydrol. Eng. 19, 1006–1014. https://doi.org/10.1061/(ASCE)HE.1943-5584.0000853.
Oñate-Valdivieso, F., Bosque-Sendra, J., Sastre-Merlín, A., Ponce, V.M., 2016. Calibration, validation and evaluation of a lumped hydrologic model in a mountain area in southern Ecuador. Agrociencia 50, 945–963.
Osuch, M., Romanowicz, R., Wong, W.K., 2018. Analysis of low flow indices under varying climatic conditions in Poland. Hydrol. Res. 49 (2), 373–389. https://doi.org/10.2166/nh.2017.021.
Parra, V., Arumí, J.L., Muñoz, E., 2019. Identifying a suitable model for low-flow simulation in watersheds of south-central Chile: a study based on a sensitivity analysis. Water 11, 1506. https://doi.org/10.3390/w11071506.
Pérez-Sánchez, J., Senent-Aparicio, J., Martínez Santa-María, C., López-Ballesteros, A., 2020. Assessment of ecological and hydro-geomorphological alterations under climate change using SWAT and IAHRIS in the Eo river in northern spain. Water 12, 1745. https://doi.org/10.3390/w12061745.
Pool, S., Francés, F., Garcia-Prats, A., Puertes, C., Pulido-Velazquez, M., Sanchis-Ibor, C., Schirmer, M., Yang, H., Jiménez-Martínez, J., 2021. Hydrological modeling of the effect of the transition from flood to drip irrigation on groundwater recharge using multi-objective calibration. Water Resources Research 57. https://doi.org/10.1029/2021WR029677.
Pulido-Velazquez, D., García-Aróstegui, J.L., Molina, J.-L., Pulido-Velazquez, M., 2015a. Assessment of future groundwater recharge in semi-arid regions under climate change scenarios (Serral-Salinas aquifer, SE Spain). Could increased rainfall variability increase the recharge rate? Hydrol. Process. 29, 828–844. https://doi.org/10.1002/hyp.10191.
Pulido-Velazquez, D., García-Aróstegui, J.L., Molina, J.-L., Pulido-Velazquez, M., 2015b. Assessment of future groundwater recharge in semi-arid regions under climate

change scenarios (Serral-Salinas aquifer, SE Spain). Could increased rainfall variability increase the recharge rate?: RECHARGE IN SEMI-ARID REGIONS UNDER CLIMATE CHANGE SCENARIOS. Hydrol. Process. 29, 828–844. https://doi.org/10.1002/hyp.10191.

Pulido-Velazquez, D., Collados-Lara, A.-J., Alcalá, F.J., 2018. Assessing impacts of future potential climate change scenarios on aquifer recharge in continental Spain. J. Hydrol. 567, 803–819. https://doi.org/10.1016/j.jhydrol.2017.10.077.

Radcliffe, D.E., Mukundan, R., 2017. PRISM vs. CFSR precipitation data effects on calibration and validation of SWAT models. J. Am. Water Resour. Assoc. 53, 89–100. https://doi.org/10.1111/1752-1688.12484.

Rangwala, I., Miller, J.R., 2012. Climate change in mountains: a review of elevation-dependent warming and its possible causes. Climatic Change 114, 527–547. https://doi.org/10.1007/s10584-012-0419-3.

Reza Eini, M., Javadi, S., Delavar, M., Gassman, P.W., Jarihani, B., 2020. Development of alternative SWAT-based models for simulating water budget components and streamflow for a karstic-influenced watershed. CATENA 195, 104801. https://doi.org/10.1016/j.catena.2020.104801.

Rivadeneira-Vera, J.F., Zambrano-Mera, Y.E., Pérez-Martín, M.Á., 2020. Adapting water resources systems to climate change in tropical areas: Ecuadorian coast. Sci. Total Environ. 703, 135554 https://doi.org/10.1016/j.scitotenv.2019.135554.

Rivas-Tabares, D., Tarquis, A.M., Willaarts, B., De Miguel, Á., 2019. An accurate evaluation of water availability in sub-arid Mediterranean watersheds through SWAT: Cega-Eresma-Adaja. Agric. Water Manage. 212, 211–225. https://doi.org/10.1016/j.agwat.2018.09.012.

Rollenbeck, R., Fabian, P., Bendix, J., 2006. Precipitation dynamics and chemical properties in tropical mountain forests of Ecuador. Adv. Geosci. 6, 73–76. https://doi.org/10.5194/adgeo-6-73-2006.

Rose, J., 1996. Quaternary Geology and Geomorphology of South America. J. Quat. Sci. 11, 432–433. https://doi.org/10.1002/(SICI)1099-1417(199609/10)11:5<432::AID-JQS246>3.0.CO;2-R.

Ross, M., Geurink, J., Said, A., Aly, A., Tara, P., 2005. Evapotranspiration Conceptualization in the Hspf-Modflow Integrated Models1. J. Am. Water Resour. Assoc. 41, 1013–1025. https://doi.org/10.1111/j.1752-1688.2005.tb03782.x.

Ruiz-Pico, Á., Pérez-Cuenca, A., Serrano-Agila, R., Maza-Criollo, D., Leiva-Piedra, J., Salazar-Campos, J., 2019. Hydrochemical characterization of groundwater in the Loja Basin (Ecuador). Applied Geochemistry 104, 1–9. https://doi.org/10.1016/j.apgeochem.2019.02.008.

Seddon, D., Kashaigili, J.J., Taylor, R.G., Cuthbert, M.O., Mwihumbo, C., MacDonald, A. M., 2021. Focused groundwater recharge in a tropical dryland: Empirical evidence from central, semi-arid Tanzania. Journal of Hydrology: Regional Studies 37, 100919. https://doi.org/10.1016/j.ejrh.2021.100919.

Senent-Aparicio, J., Pérez-Sánchez, J., Carrillo-García, J., Soto, J., 2017. Using SWAT and fuzzy TOPSIS to assess the impact of climate change in the headwaters of the segura river basin (SE Spain). Water 9, 149. https://doi.org/10.3390/w9020149.

Senent-Aparicio, J., Liu, S., Pérez-Sánchez, J., López-Ballesteros, A., Jimeno-Sáez, P., 2018. Assessing impacts of climate variability and reforestation activities on water resources in the headwaters of the segura river basin (SE Spain). Sustainability 10, 3277. https://doi.org/10.3390/su10093277.

Senent-Aparicio, J., Alcalá, F.J., Liu, S., Jimeno-Sáez, P., 2020. Coupling SWAT model and CMB method for modeling of high-permeability bedrock basins receiving interbasin groundwater flow. Water 12, 657. https://doi.org/10.3390/w12030657.

Senent-Aparicio, J., George, C., Srinivasan, R., 2021a. Introducing a new post-processing tool for the SWAT+ model to evaluate environmental flows. Environ. Model. Softw. 136, 563–571. https://doi.org/10.1016/j.envsoft.2020.104944.

Senent-Aparicio, J., Jimeno-Sáez, P., López-Ballesteros, A., Giménez, J.G., Pérez-Sánchez, J., Cecilia, J.M., Srinivasan, R., 2021b. Impacts of swat weather generator statistics from high-resolution datasets on monthly streamflow simulation over Peninsular Spain. J. Hydrol.-Reg. Stud. 35, 100826 https://doi.org/10.1016/j.ejrh.2021.100826.

Sharma, A., Patel, P.L., Sharma, P.J., 2022. Influence of climate and land-use changes on the sensitivity of SWAT model parameters and water availability in a semi-arid river basin. CATENA 215, 106298. https://doi.org/10.1016/j.catena.2022.106298.

Singh, A., Jha, S.K., 2021. Identification of sensitive parameters in daily and monthly hydrological simulations in small to large catchments in Central India. J. Hydrol. 601, 126632 https://doi.org/10.1016/j.jhydrol.2021.126632.

Singh, J., Knapp, H.V., Arnold, J.G., Demissie, M., 2005. Hydrological modeling of the Iroquois river watershed using HSPF and SWAT. J. Am. Water Resour. Assoc. 343–360 https://doi.org/10.1111/j.1752-1688.2005.tb03740.x.

Sklenář, P., Romoleroux, K., Muriel, P., Jaramillo, R., Bernardi, A., Diazgranados, M., Moret, P., 2021. Distribution changes in páramo plants from the equatorial high Andes in response to increasing temperature and humidity variation since 1880. Alp Botany 131, 201–212. https://doi.org/10.1007/s00035-021-00270-x.

Somers, L.D., McKenzie, J.M., Zipper, S.C., Mark, B.G., Lagos, P., Baraer, M., 2018. Does hillslope trenching enhance groundwater recharge and baseflow in the Peruvian Andes? Hydrol. Process. 32, 318–331. https://doi.org/10.1002/hyp.11423.

Spikings, R.A., Seward, D., Winkler, W., Ruiz, G.M., 2000. Low-temperature thermochronology of the northern Cordillera Real, Ecuador: Tectonic insights from zircon and apatite fission track analysis. Tectonics 19, 649–668. https://doi.org/10.1029/2000TC900010.

Tan, M.L., Gassman, P.W., Liang, J., Haywood, J.M., 2021. A review of alternative climate products for SWAT modelling: Sources, assessment and future directions. Science of the Total Environment 148915. https://doi.org/10.1016/j.scitotenv.2021.148915.

Taylor, R.G., Scanlon, B., Döll, P., Rodell, M., van Beek, R., Wada, Y., Longuevergne, L., Leblanc, M., Famiglietti, J.S., Edmunds, M., Konikow, L., Green, T.R., Chen, J., Taniguchi, M., Bierkens, M.F.P., MacDonald, A., Fan, Y., Maxwell, R.M., Yechieli, Y., Gurdak, J.J., Allen, D.M., Shamsudduha, M., Hiscock, K., Yeh, P.-J.-F., Holman, I., Treidel, H., 2013. Ground water and climate change. Nature Clim. Change. 3, 322–329. https://doi.org/10.1038/nclimate1744.

Tovar, C., Seijmonsbergen, A.C., Duivenvoorden, J.F., 2013. Monitoring land use and land cover change in mountain regions: An example in the Jalca grasslands of the Peruvian Andes. Landsc. Urban Plan. 112, 40–49. https://doi.org/10.1016/j.landurbplan.2012.12.003.

Ur Rahman, K., Shang, S., Shahid, M., Wen, Y., 2020. Hydrological evaluation of merged satellite precipitation datasets for streamflow simulation using SWAT: A case study of Potohar Plateau. Pakistan. J. Hydrol. 587, 125040 https://doi.org/10.1016/j.jhydrol.2020.125040.

Urrutia, R., Vuille, M., 2009. Climate change projections for the tropical Andes using a regional climate model: Temperature and precipitation simulations for the end of the 21st century. J. Geophys. Res. 114, D02108. https://doi.org/10.1029/2008JD011021.

Vaghefi, S.A., Abbaspour, N., Kamali, B., Abbaspour, K.C., 2017. A toolkit for climate change analysis and pattern recognition for extreme weather conditions – Case study: California-Baja California Peninsula. Environ. Modell. Softw. 96, 181–198. https://doi.org/10.1016/j.envsoft.2017.06.033.

Vaghefi, S.A., Iravani, M., Sauchyn, D., Andreichuk, Y., Goss, G., Faramarzi, M., 2019. Regionalization and parameterization of a hydrologic model significantly affect the cascade of uncertainty in climate-impact projections. Clim. Dyn. 53, 2861–2886. https://doi.org/10.1007/s00382-019-04664-w.

Van Vliet-Lanoe, B., 2014. Les environnements froids: Glaciaire et périglaciaire. Vuibert, Ballan-Miré, France.

Vergara, W., Deeb, A., Valencia, A., Bradley, R., Francou, B., Zarzar, A., Grünwaldt, A., Haeussling, S., 2007. Economic impacts of rapid glacier retreat in the Andes. Eos Trans. AGU 88, 261–264. https://doi.org/10.1029/2007EO250001.

Vincent, A., Violette, S., Aðalgeirsdóttir, G., 2019. Groundwater in catchments headed by temperate glaciers: A review. Earth-Sci. Rev. 188, 59–76. https://doi.org/10.1016/j.earscirev.2018.10.017.

Viviroli, D., Archer, D.R., Buytaert, W., Fowler, H.J., Greenwood, G.B., Hamlet, A.F., Huang, Y., Koboltschnig, G., Litaor, M.I., López-Moreno, J.I., Lorentz, S., Schädler, B., Schreier, H., Schwaiger, K., Vuille, M., Woods, R., 2011. Climate change and mountain water resources: overview and recommendations for research, management and policy. Hydrol. Earth Syst. Sci. 15, 471–504. https://doi.org/10.5194/hess-15-471-2011.

Vuille, M., Bradley, R.S., Werner, M., Keimig, F., 2003. 20th Century Climate Change in the Tropical Andes: Observations and Model Results, In: Diaz, H.F. (Ed.), Climate Variability and Change in High Elevation Regions: Past, Present & Future, Advances in Global Change Research. Springer Netherlands, Dordrecht, pp. 75–99. Doi: 10.1007/978-94-015-1252-7_5.

Vuille, M., Francou, B., Wagnon, P., Juen, I., Kaser, G., Mark, B.G., Bradley, R.S., 2008. Climate change and tropical Andean glaciers: Past, present and future. Earth-Sci. Rev. 89, 79–96. https://doi.org/10.1016/j.earscirev.2008.04.002.

Vuille, M., Franquist, E., Garreaud, R., Lavado Casimiro, W.S., Cáceres, B., 2015. Impact of the global warming hiatus on Andean temperature: GLOBAL WARMING HIATUS IN THE ANDES. J. Geophys. Res. Atmos. 120, 3745–3757. https://doi.org/10.1002/2015JD023126.

Vuille, M., Carey, M., Huggel, C., Buytaert, W., Rabatel, A., Jacobsen, D., Soruco, A., Villacis, M., Yarleque, C., Elison Timm, O., Condom, T., Salzmann, N., Sicart, J.-E., 2018. Rapid decline of snow and ice in the tropical Andes – Impacts, uncertainties and challenges ahead. Earth-Sci. Rev. 176, 195–213. https://doi.org/10.1016/j.earscirev.2017.09.019.

Were, A., Villagarcía, L., Domingo, F., Alados-Arboledas, L., Puigdefábregas, J., 2007. Analysis of effective resistance calculation methods and their effect on modelling evapotranspiration in two different patches of vegetation in semi-arid SE Spain. Hydrol. Earth Syst. Sci. 11, 1529–1542. https://doi.org/10.5194/hess-11-1529-2007.

Yacoub, C., Foguet, A.P., 2013. Slope effects on SWAT modeling in a mountainous basin. J. Hydrol. Eng. 18, 1663–1673. https://doi.org/10.1061/(ASCE)HE.1943-5584.0000756.

Young, B.E., Young, K.R., Josse, C., 2011. Vulnerability of tropical andean ecosystems to climate change. In: Climate Change and Biodiversity in the Tropical Andes Inter-American Institute for Global Change Research (IAI) and Scientific Committee on Problems of the Environment (SCOPE), pp. 170–181.

Zaibak, I., Meddi, M., 2022. Simulating streamflow in the Cheliff basin of west northern Algeria using the SWAT model. J. Earth Syst. Sci. 131, 25. https://doi.org/10.1007/s12040-021-01777-x.

Zhiña, D., Montenegro, M., Montalván, L., Mendoza, D., Contreras, J., Campozano, L., Avilés, A., 2019. Climate Change Influences of Temporal and Spatial Drought Variation in the Andean High Mountain Basin. Atmosphere 10, 558. https://doi.org/10.3390/atmos10090558.

Zhou, J., Liu, Y., Guo, H., He, D., 2014. Combining the SWAT model with sequential uncertainty fitting algorithm for streamflow prediction and uncertainty analysis for the Lake Dianchi Basin. China. Hydrol. Process. 28, 521–533. https://doi.org/10.1002/hyp.9605.

Zulkafli, Z., Buytaert, W., Manz, B., Rosas, C.V., Willems, P., Lavado-Casimiro, W., Guyot, J.-L., Santini, W., 2016. Projected increases in the annual flood pulse of the Western Amazon. Environ. Res. Lett. 11, 014013 https://doi.org/10.1088/1748-9326/11/1/014013.

A2. Publication 2

Peñafiel, L., Alcalá, F.J., Senent-Aparicio, J. Usefulness of Compiled Geophysical Prospecting Survey in Groundwater Research in the Metropolitan District of Quito in Northern Ecuador. *Applied Sciences*, 11, 11144. https://doi.org/10.3390/app112311144

Impact Factor 2021 (JCR): 2.838; Category: PHYSICS, APPLIED; Ranking: 76/161 (Q2); Date of publication: 2021.

applied sciences

MDPI

Article

Usefulness of Compiled Geophysical Prospecting Surveys in Groundwater Research in the Metropolitan District of Quito in Northern Ecuador

Lilia Peñafiel [1,2], Francisco Javier Alcalá [3,4,*] and Javier Senent-Aparicio [1]

[1] Departamento de Ingeniería Civil, Universidad Católica de Murcia, 30107 Murcia, Spain; lapenafiel@alu.ucam.edu (L.P.); jsenent@ucam.edu (J.S.-A.)
[2] Empresa Pública Metropolitana de Agua Potable y Saneamiento de Quito (EPMAPS), Quito 17-03-0330, Ecuador
[3] Departamento de Desertificación y Geo-Ecología, Estación Experimental de Zonas Áridas (EEZA-CSIC), 04120 Almería, Spain
[4] Instituto de Ciencias Químicas Aplicadas, Facultad de Ingeniería, Universidad Autónoma de Chile, Santiago 7500138, Chile
* Correspondence: fjalcala@eeza.csic.es; Tel.: +34-950-281-045

Abstract: As in other large Andean cities, the population in the Metropolitan District of Quito (MDQ) in northern Ecuador is growing, and groundwater is becoming essential to meet the increasing urban water demand. Quito's Public Water Supply Company (EPMAPS) is promoting groundwater research for sustainable water supply, and geophysical prospecting surveys are used to define aquifer geometry and certain transient groundwater features. This paper examines the usefulness of existing geophysical prospecting surveys in groundwater research in the MDQ. A database was built using 23 representative geophysical prospecting surveys compiled from EPMAPS' public repository, official geotechnical research reports, and the scientific literature. Fifteen EPMAPS-promoted surveys used near-surface electrical techniques (seven used electrical resistivity tomography and eight used vertical electrical sounding) to explore Holocene and Pleistocene sedimentary and volcano-sedimentary formations in the 25–500-m prospecting depth range, some of which form shallow aquifers used for water supply. Four other surveys used near-surface seismic techniques (refraction microtremor) for geotechnical research in civil works. These surveys have been reinterpreted to define shallow aquifer geometry. Finally, four surveys compiled from the scientific literature used electromagnetic techniques (magnetotelluric sounding and other very low-frequency methods) to explore Holocene to late Pliocene formations, some of which form thick regional aquifers catalogued as the larger freshwater reservoirs in the MDQ. However, no geophysical prospecting surveys exploring the complete saturated thickness of the Pliocene aquifers could be compiled. Geophysical prospecting surveys with greater penetration depth are proposed to bridge this research gap, which prevents the accurate assessment of the renewable groundwater fraction of the regional aquifers in the MDQ that can be exploited sustainably.

Keywords: geophysical prospecting techniques; groundwater research; urban water supply; Metropolitan District of Quito; Ecuador

check for updates

Citation: Peñafiel, L.; Alcalá, F.J.; Senent-Aparicio, J. Usefulness of Compiled Geophysical Prospecting Surveys in Groundwater Research in the Metropolitan District of Quito in Northern Ecuador. *Appl. Sci.* **2021**, *11*, 11144. https://doi.org/10.3390/app112311144

Academic Editor: Hyung-Sup Jung

Received: 30 October 2021
Accepted: 22 November 2021
Published: 24 November 2021

Publisher's Note: MDPI stays neutral with regard to jurisdictional claims in published maps and institutional affiliations.

Copyright: © 2021 by the authors. Licensee MDPI, Basel, Switzerland. This article is an open access article distributed under the terms and conditions of the Creative Commons Attribution (CC BY) license (https://creativecommons.org/licenses/by/4.0/).

1. Introduction

The Andean Highlands roughly extend between latitudes 11° N and 8° S, are over 3000 m a.s.l., play an important role in regional freshwater supply, and are highly sensitive to climate change [1–3]. As in other high mountain areas, most ecosystem typologies are groundwater dependent [2,4–6]. The combined influence of global driving forces and some anthropogenic activities (e.g., deforestation, overgrazing, soil degradation, and water overdevelopment) is altering river flow and aquifer recharge regimes [4–8], with

negative consequences for human water supply and the preservation of dependent ecosystems [2,5,8]. Rivers and streams have traditionally been the main freshwater source to meet the water demand of downstream urban areas [4,9,10]. Increased demand in many densely populated Andean cities has driven water source diversification [2,4,6,10]. This is the case in the Metropolitan District of Quito city (MDQ) in northern Ecuador, where groundwater from the Andean Highlands and surface water transferred from the Amazonian watershed supplement traditional surface water sources [8,10]. A question arises of how is increasing groundwater extraction affecting reserves and dependent ecosystems? Applied groundwater research aimed at defining the aquifer functioning is yet incipient to answer this question accurately [11,12].

The Ecuador Water Authority and Quito's Public Water Supply Company (EPMAPS) are not immune to this problem. EPMAPS is responsible for prospecting, developing, distributing, and managing potable water in the MDQ, and promotes groundwater research to improve general hydrogeological knowledge as a prerequisite for a sustainable water supply. Hydrogeological studies use geophysical prospecting surveys to define aquifer geometry and certain transient groundwater features. Such studies typically cover two observation scales associated with two aquifer typologies. EPMAPS has used near-surface electrical geophysical techniques, such as electrical resistivity tomography (ERT) and vertical electrical sounding (VES), to explore shallow aquifer geometry and transient groundwater features required for drilling pumping wells intended to supply scattered population nuclei. The water company has also supported other public agencies and academic institutions can apply electromagnetic geophysical techniques for near-surface (very low-frequency electromagnetic methods, VLF-EMs) and deep (low-frequency magnetotelluric sounding, MTS) explorations to deduce the structure of shallow and thick regional geological formations catalogued as the larger freshwater reservoirs in the MDQ. Near-surface seismic prospecting techniques, such as refraction microtremor (REMI), have also been used to explore shallow geotechnical features.

Such geophysical prospecting techniques have proven useful in groundwater research in different hydrogeological environments [13–18]. They are non-invasive, usually inexpensive to apply, and useful when geotechnical sounding data is sparse or unable to provide subsurface information required for detailed groundwater research over multiple observation scales [15–17]. However, most geophysical prospecting surveys of interest in groundwater research are unpublished. Therefore, these experiences must be compiled and may need to be reinterpreted for groundwater research purposes. Such information concerning the aquifer saturated thickness, piezometric level, and spatial distribution of pore-water conductivity is essential to assess the fraction of groundwater that can sustainably supplement the urban water demand in the MDQ.

This paper examines the feasibility of compiled geophysical prospecting surveys in groundwater research in the MDQ, providing findings of interest to improve the hydrogeological conceptualization and identifying research gaps that can be bridged in the near future. Twenty-three representative geophysical prospecting surveys were compiled from EPMAPS' public repository, official geotechnical research reports, and the scientific literature. The compiled information was arranged in a database for interpretation. This paper does not intend to introduce new formulations, produce new data, discuss well-known principles of applied geophysical prospecting techniques, or assess the quality of the interpretations derived from the compiled surveys. This paper is organized as follows. Section 2 briefly describes the study area. Section 3 explains the steps followed to build the database. Section 4 reports the overall findings of the database analysis and gives an example of each geophysical prospecting technique. Section 5 discusses the geophysical prospecting scope, including research findings and gaps. Section 6 presents the main conclusions.

2. Study Area

2.1. Location and Climate

The MDQ is located in northern Ecuador at 0°14′ N to 0°35′ S and 78°10′ W to 78°56′ W (Figure 1), covers a surface area of 4320 km^2, and includes three main geomorphological sectors (Figure 1a). The 40-km-wide northern elongated Inter-Andean Valley (IAV) has an elevation ranging from 2100 to 3500 m a.s.l. and lies between the Western Andean Cordillera (WAC) (peak elevation 4776 m a.s.l., at Guagua-Pichincha Volcano) and Eastern Andean Cordillera (EAC) (peak elevation 4873 m a.s.l., at Sincholagua Volcano) (Figure 1b). The Guayllamba River flows north through the IAV and is the main surface watercourse (Figure 1b).

The MDQ exhibits a neo-tropical high-mountain climate, determined by the El Niño-Southern Oscillation and the Humboldt Current, and a steep orography [8,19,20]. Consequently, it has a marked distribution of biozones and ecosystems at different elevations including tropical mountain rainforests in the lowlands, wet alpine meadows (locally named *páramo*) in mid-slope areas, dry and cold scrublands in the highlands, and permanent snow covers at volcanoes' peaks [4,6,21].

Precipitation (P) follows a decreasing gradient from east to west, controlled by incoming Atlantic cloud fronts and elevation [22,23] and exhibits a positive gradient from low-lying areas to around 3500 m a.s.l. and a negative gradient above that elevation [19,20]. Most P occurs in February–May. In contrast, the lowest amount is recorded in July–September [23]. Annual mean P is around 1100 mm, with a coefficient of variation of 0.21 measured over the period 2003–2019. Annual mean temperature (T) is around 7.5 °C, with daily minimums in June–September and maximums in February–April. The decreasing T gradient with elevation is around 0.6–0.7 °C per 100 m elevation [21,22]. Insolation increases from low-lying areas to summits due to cloudiness induced by the Foehn effect in valleys from incoming Atlantic cloud fronts [7]. Annual mean potential evapotranspiration is around 1000 mm.

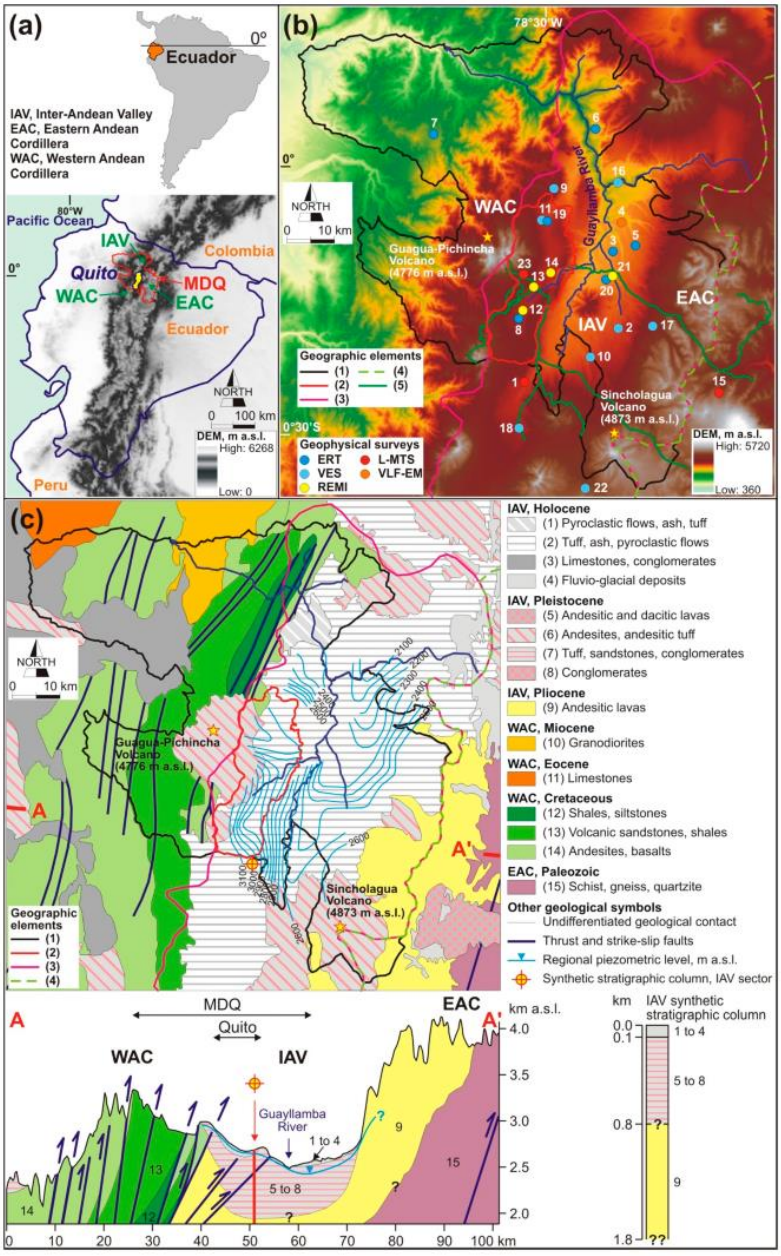

Figure 1. (**a**) Location of the study area. (**b**) The MDQ displayed using the 30 m-resolution Digital Elevation Model from Shuttle Radar Topography Mission (http://srtm.csi.cgiar.org/srtmdata/ (accessed on 11 February 2021), showing the

location and typology of the compiled 23 geophysical prospecting surveys and additional geographical features cited in the text: (1) MDQ, (2) Quito city, (3) Quito-Machachi Hydrogeological Unit [24–26], (4) Cayambe-Rumiñahui Hydrogeological Unit [24–26], and (5) the water transfer system used by EPMAPS to supply the MDQ [8]. ERT—Electrical Resistivity Tomography; VES—Vertical Electrical Sounding; REMI—Refraction Microtremor; L-MTS—Low-frequency Magnetotelluric Sounding; VLF-EM—Very low-frequency Electromagnetic Method. (**c**) Hydrogeological map (scale 1:250,000) of the MDQ, updated and improved from [24–26], showing regional piezometry [24–26], and the location of the hydrogeological cross-section A–A′ and a synthetic stratigraphic column of the IAV sector [18,24–26].

2.2. *Geology and Hydrogeology*

The study area belongs to the Pacific Ring of Fire, a highly active belt of volcanic and seismic activity originating from the subduction of the oceanic Nazca Plate beneath the South American Plate, which is the source of the compressive tectonics and arc magmatism of the Andes Cordillera [27,28]. The MDQ is located in the westernmost part of the NNE-trending fault-bounded Andean compressive structure, which includes the IAV between the WAC and EAC (Figure 1b).

The basement of the MDQ includes a variety of geological formations (Figure 1c). Upper Cretaceous oceanic, arc-island sequences, and volcano-sediments (codes 12–14 in Figure 1c) form the non-metamorphic basement of the WAC, which underlies Paleocene to Eocene marine turbidites and limestones (code 11 in Figure 1c), and is locally intruded by Miocene granodiorites (code 10 in Figure 1c) [29]. Subparallel belts of Paleozoic metapelitic rocks (code 15 in Figure 1c) and other volcanic-arc rocks accreted against the stable craton during the early Cretaceous form the western metamorphic basement of the EAC [30]. At present, the IAV basement depth and typology remain unknown, although Bouguer gravity anomaly data [31] would suggest an east-verging tectonic wedge of the Cretaceous WAC basement [29], which is covered by Pliocene andesitic lavas (code 9 in Figure 1c), and Pleistocene (codes 5–8 in Figure 1c) and Holocene (codes 1–4 in Figure 1c) sedimentary and volcano-sedimentary formations [32].

The IAV and EAC sectors occupy a large portion of the Quito-Machachi Hydrogeological Unit and a small part of the Cayambe-Rumiñahui Hydrogeological Unit (Figure 1b). The WAC sector is officially catalogued as a regional impervious area. In hydrogeological terms, the above geological formations can be classified into five groups attending to the permeability type and effective porosity reported in the consulted literature [25,26,33,34]: (1) the Paleozoic metapelitic EAC basement is a low-permeability formation representing the impervious lower boundary of the eastern aquifers; (2) the Late Cretaceous sedimentary and volcanic WAC basement is assumed to include low- to moderate-permeability formations comprising the impervious lower boundary of the aquifers in the western IAV sector; (3) the Pliocene and Pleistocene andesitic lavas and pyroclastic flows form thick regional compartmentalized aquifers of moderate permeability, with yield dependent upon the degree of fissuring and fracturing; (4) the Pleistocene and Holocene ash, tuff, and lahar are low- to moderate-permeability formations, often confining the above Pliocene and Pleistocene aquifers; and (5) the Pleistocene and Holocene fluvio-glacial formations form high-permeability aquifers with intergranular porosity (Figure 1c). Table 1 summarizes the compiled information regarding the permeability and effective porosity of representative geological formations in the MDQ.

Hydrogeological functioning in the MDQ depends on: (1) the low permeability of the EAC (metapelitic rocks) and WAC (sedimentary and volcanic rocks) basements; (2) the compartmentalization, thickness, and degree of fissuring and fracturing in Pliocene and Pleistocene andesitic lavas, which determine the storage capacity and permeability of these aquifers in the IAV; (3) the extent and thickness of low-permeability Pleistocene and Holocene volcano-sedimentary formations forming aquitards in the IAV; (4) the hydraulic connectivity between Pliocene and Pleistocene aquifers and between Pleistocene and Holocene aquitards, favoring the deep percolation of aquifer recharge and localized aquifer discharge; and (5) the extent and thickness of Pleistocene and Holocene coarse-grained sediments for draining runoff and aquifer discharge [9,11,12,18,26,35,36].

Table 1. Compiled information regarding the permeability and effective porosity of representative geological formations in the MDQ.

Lithology	Age	MDQ Sector [1]	Permeability [2]		Effective Porosity [3]	Reference
			Magnitude	Type		
Metapelites	Paleozoic	EAC	10^{-4}–10^{-2} (nd)	fr,fi	nd	[25,26]
Andesites and basalts	Cretaceous	WAC	10^{-4}–10^{-2} (nd)	fr,fi	nd	[25]
Sandstones and siltstones	Cretaceous	WAC	10^{-2}–10^{-1} (nd)	fr,fi	nd	[25]
Andesitic lavas	early Pleistocene	IAV	10^{-2}–10^{-1} (0.04)	fr,fi	nd	[26]
Andesitic lavas	middle Pleistocene	IAV	10^{-2}–10^{-1} (0.04)	fr,fi	0.02–0.08	[26,33,34]
Pyroclastic flows	middle Pleistocene	IAV	0.13–0.86 (nd)	fr,fi	nd	[25,26]
Ash	middle Pleistocene	IAV	10^{-3}–10^{-1} (0.01)	fr,fi	nd	[25,26]
Ash	late Pleistocene	IAV	10^{-3}–10^{-1} (0.01)	fr,fi	<0.01	[26,33,34]
Fluvio-glacial deposits	late Pleistocene	IAV	0.05–10 (1.02)	fi,ip	0.01–0.03	[25,26]
Ash	Holocene	IAV	10^{-3}–10^{-1} (nd)	fr,fi	nd	[25,26]
Avalanche flows	Holocene	IAV	10^{-2}–10^{-1} (nd)	fr,fi	nd	[25,26]
Lahar	Holocene	IAV	10^{-3}–10^{-2} (0.01)	fr,fi	0.01–0.06	[26,33,34]
Alluvial	Holocene	IAV	0.05–0.18 (0.12)	ip	0.05–0.12	[25,26]
Glacier and moraines	Holocene	IAV	0.05–0.15 (0.09)	ip	0.05–0.15	[25,26]

[1] EAC—Eastern Andean Cordillera, WAC—Western Andean Cordillera, and IAV—Inter-Andean Valley. [2] Permeability in m d^{-1}; magnitude refers to theoretical ranges and experimental values after borehole surveying (in parenthesis); fr—fracturation, fi—fissuration, and ip—intergranular porosity. [3] Effective porosity as a fraction; magnitude refers to experimental values after borehole surveying. nd—no data.

2.3. Urban Water Demand

Quito has historically been supplied from local rivers and streams. Since the 1990s, internal migration has produced rapid population growth in the MDQ, leading to increased water demand and the need to diversify water sources [37]. The MDQ currently has around 2.7 million inhabitants. Groundwater from the highlands (the EAC sector) and surface water transferred from the Amazonian watershed supplement the traditional surface water sources [8,10]. Groundwater exploitation began in the 1960s when the first pumping wells were drilled to supply northern urban districts [37]. Since then, EPMAPS has drilled more than 120 pumping wells to supply the increasing water demand [26]. The water supply system currently covers about 99% of the inhabitants, making the MDQ one of the best-served urban areas in Latin America. Groundwater meets around 16% of the total urban water demand. This figure will undoubtedly increase due to the noticeable population increase projected for the period 2020–2040 [37].

3. Data Compilation

A data search was conducted to examine the feasibility of existing geophysical prospecting surveys in groundwater research in the MDQ. The rationale was to create a database to cover as many geological formations (preferably those catalogued as aquifers), research interests, and prospecting techniques as possible. The selection prioritized geophysical surveys that explored depths of at least 10 m and used external validation data, such as geotechnical soundings logs and/or additional prospecting techniques. The selection also considered those surveys developed or promoted by the EPMAPS in sites where it has (or intends to have) operative water catchments. Therefore, EPMAPS' public repository (information available on request), official geotechnical research reports, and the scientific literature were consulted. Finally, 23 representative surveys covering the abovementioned scopes and priorities were selected to build the database in Table 2. Most of the compiled surveys were performed in the IAV sector (Figure 1b).

Table 2. Database comprising the compiled 23 geophysical prospecting surveys of interest in groundwater research in the MDQ. The data are clustered according to the applied geophysical prospecting technique, explored aquifer typology, deduced transient groundwater features, and additional technical information.

ID	Coordinates		Elevation, m a.s.l.	Geophysical Technique [1]			Geological Environment [2]						Research Interest [3]			Additional Technical Information [4]						Reference
				T1	T2	T3	G1	G2	G3	G4	G5	G6	R1	R2	R3	Variable	AQF	AQT	Profiles	PL	PD	
1	78°32′ W	0°24′ S	3046			b	a,b	a,b,c	a,b,c	c	a		a,b	b	a	ER, Ω m	10–210	220–8010	1	1300	1800	[18]
2	78°22′ W	0°18′ S	2644	a			a,b	a,b		a,b,c	a		a	b	b	ER, Ω m	62–170		10	400–500	250	[38]
3	78°22′ W	0°09′ S	2379	b			b		a,b,c	a,b,c	a		a	b	b	ER, Ω m	80–150		7	504–855	70–160	[39]
4	78°21′ W	0°06′ S	2350			a	b		a,b,c	a,b,c	a		a	b	b	ER, Ω m	15–195	210–280	13	160–750	130	[39]
5	78°20′ W	0°09′ S	2484	b			b		a,b,c	a,b,c	a		a	b	a,b	ER, Ω m	30–75	210–250	2	880	137	[40]
6	78°24′ W	0°04′ N	2064	b			b		a,b,c	b,c	a		a,b	a	a,b	ER, Ω m	10–50		2	303–358	50	[40]
7	78°42′ W	0°03′ N	1823	b			a,b	a,b		b,c		a	a	a	a,b	ER, Ω m	17–198	210–315	1	715	120	[40]
8	78°33′ W	0°17′ S	2860	b			a,b	a,b,c	a,b				a	a	c	ER, Ω m	3–210	215–300	9	250	40	[41]
9	78°29′ W	0°00′ N	2736	a			a,b	a,b	b,c	c			a	b	a	ER, Ω m	20–40		9	600–1000	322	[42]
10	78°25′ W	0°21′ S	2690	a			a		a,b,c		a,b,c		a	a	a,b	ER, Ω m	17–28	215–345	9	600–1000	271	[42]
11	78°30′ W	0°06′ S	2722	a			a,b	a,b,c	a,b,c		a,b,c		b	b	a,b	ER, Ω m	30–98		11	400–1000	200–500	[43]
12	78°32′ W	0°16′ S	2849		a		a,b	a,b,c	a,b,c				a	a	c	VS, m s^{-1}	95–680	95–680	171	8600	40–55	[44]
13	78°31′ W	0°13′ S	2826		a		a,b	a,b,c	c				b	b	c	VS, m s^{-1}	135–1050	135–1050	15	3200	120	[44]
14	78°29′ W	0°12′ S	2777		a		a,b	a,b,c	a,b,c				a	b	c	VS, m s^{-1}	125–710	125–710	171	10,330	40–55	[44]
15	78°11′ W	0°25′ S	4184			b	a,b		c	c	a	b	b	b	d	ER, Ω m	30–215	230–3190	130	15,000	4000	[45]
16	78°22′ W	0°02′ S	2145	a			a			a,b,c	a		a	b	a	ER, Ω m	50–170	218–457	23	600–1000	230	[46]
17	78°18′ W	0°18′ S	3260	a			a	a,b	c	c	a		b	b	a	ER, Ω m	28–56		3	600–800	180	[47]
18	78°33′ W	0°29′ S	2835	a			a,b	a,b,c	a	a,b,c	a		b	b	b	ER, Ω m	45–150	255–400	16	1000	200	[48]
19	78°29′ W	0°06′ S	2693	b			a,b	a,b	a,b				a	a	a,b	ER, Ω m	40–100	220–320	3	715	60	[49]
20	78°22′ W	0°12′ S	2280	b			a			a,b,c			a	a	c	ER, Ω m	20–150		3	110	25	[50]
21	78°22′ W	0°12′ S	2400		a		a		a,b,c				a	a	c	VS, m s^{-1}		720–945	7	120	60	[50]
22	78°25′ W	0°35′ S	3743	a					a,b,c	c	a		b	a	a	ER, Ω m	56–203	225–850	20	1000	150	[51]
23	78°30′ W	0°12′ S	2800			b	a	a,b,c	b,c	c	a	a	b	b	a	ER, Ω m	22–230	235–27,100	3	17,000	1500	[52]

[1] T1—Near-surface electrical techniques: (a) VES and (b) ERT. T2—Near-surface seismic techniques: (a) REMI. T3—Electromagnetic techniques: (a) VLF-EM and (b) Low-frequency MTS. [2] G1—Holocene sedimentary and volcano-sedimentary formations: (a) anthropogenic fillings and soils, and (b) silty and sandy ash. G2—late Pleistocene sedimentary and volcano-sedimentary formations: (a) ash and pumice ash, (b) tuff and paleo-soils, and (c) mud flows. G3—early–middle Pleistocene sedimentary and volcano-sedimentary formations: (a) lacustrine deposits, paleo-soils, peats, tuff, and microbreccias; (b) ash, pyroclastic flows, and tuff; and (c) avalanche flows, volcanic breccias and lavas. G4—early Pleistocene sedimentary and volcano-sedimentary formations: (a) alluvial sand and conglomerates; (b) siltstones and tuff; and (c) lahar, andesitic lavas, and avalanche flows. G5—late Pliocene volcanic formations: (a) andesitic lavas. G6—Basement: (a) Cretaceous WAC and IAV basement, and (b) Paleozoic EAC basement. [3] R1—Aquifer geometry: (a) layer thickness, and (b) fissuring and fracturing. R2—Aquifer dynamics and functioning in natural regime: (a) first groundwater observation, (b) regional piezometric level, (c) high-conductivity areas, and (d) geothermal areas. R3—Other applications: (a) basic research, (b) water supply, (c) civil works, and (d) geothermal energy. [4] AQF—Range of the variables electrical resistivity (ER) and share-wave velocity (VS) in geological formations catalogued as aquifers. AQT—Range of the variables ER and VS in geological formations catalogued as aquitards. PL—Prospecting length of the profiles in m. PD—Prospecting depth of the profiles in m.

Survey information was catalogued according to: (1) the applied prospecting technique; (2) the explored aquifer typology; (3) deduced transient groundwater features; and (4) additional technical information, such as the magnitude of the geophysical variables in geological formations catalogued as aquifers and aquitards, and prospecting length and depth (Table 2). The compiled data were initially checked to ensure a suitable statistical sample of the range of field technical conditions allowed by each geophysical technique. In all surveys, the original interpretations were examined to (i) standardize the age, lithological description, and hydrogeological behavior of the geological formations; (ii) adapt the achieved transient groundwater features to the scope of this paper; and (iii) adjust the drawing style to the scientific editing requirements. In the REMI and low-frequency MTS surveys, the original geotechnical and geodynamic findings were reinterpreted for groundwater research purposes.

Section 4 examines and classifies the compiled 23 surveys into three main groups of techniques (electrical, seismic, and electromagnetic) used to explore two main aquifer typologies (shallow and regional) and deduce two main research interests (aquifer geometry and transient groundwater features). This section also provides a representative survey of each technique. This survey represents an average condition of (i) prospecting depth and length, (ii) prospected geological formations, and (iii) deduced hydrogeological features regarding the compiled surveys of each technique.

4. Results

4.1. Near-Surface Electrical Surveys

Near-surface electrical techniques take voltage measurements between two potential electrodes installed on the land surface once direct current is injected into two current electrodes. Such techniques allow the calculation of subsurface electrical resistivity (ER) [Ω m], reciprocal of subsurface electrical conductivity (EC). Penetration depth and resolution depend on subsurface EC, which is a function of transient pore-water EC and steady ground EC, the input voltage used, and the electrode spacing adopted [53–55].

Fifteen surveys used near-surface electrical techniques; of these, eight surveys used VES for 1D ER models, and seven used ERT for 2D ER models. The VES surveys were part of groundwater research technical reports [38,42,43,46–48,51], whereas the ERT surveys included groundwater research technical reports [40,41,49,50] and scientific documents [39] (Table 2). The VES surveys aimed to define the punctual thickness of Holocene and late Pleistocene shallow aquifers. The ERT surveys aimed to explore the geometry of shallow aquifers and transient groundwater features, such as first groundwater observation, regional piezometric level, and pore-water conductivity. Both the VES and ERT surveys used Schlumberger, Wenner, and dipole–dipole arrays as the typical electrode configuration. The prospecting length range was 400–1000 m for the VES and 110–880 m for the ERT surveys, and the prospecting depth range was 150–500 m for the VES and 25–160 m for the ERT surveys (Table 2). For the geological formations catalogued as aquifers, the ER range was 17–203 Ω m for VES and 3–150 Ω m for ERT. For the geological formations catalogued as aquitards, the ER range was 215–850 Ω m for VES and 210–320 Ω m for ERT.

The ERT survey labelled 19 in Figure 1b and Table 2 was selected (Figure 2). This survey was performed in January 2016 and included three NNE–SSW ERT profiles (Figure 2b) covering a total prospecting length of 715 m [49]. The survey was part of groundwater research promoted by EPMAPS to supply scattered areas in the northern district of Quito city. Research interests were the geometry of shallow geological formations (some forming aquifers) and transient groundwater features, such as first groundwater observation.

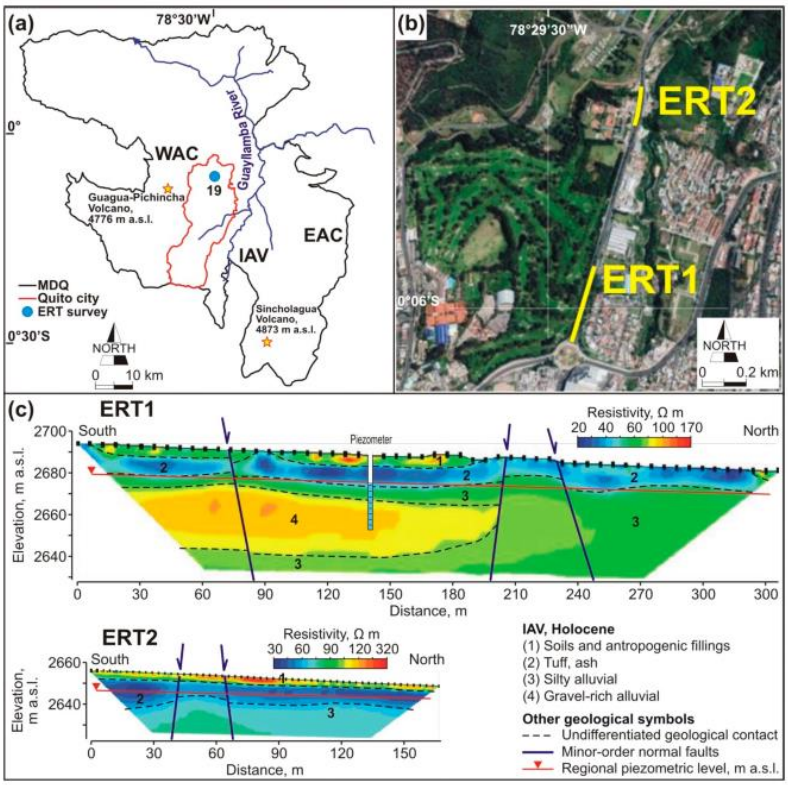

Figure 2. (**a**) General location of the selected ERT survey labelled 19 in Figure 1b and Table 2, updated and reinterpreted from Yautibug and Herrera [49]. (**b**) Detailed location of two selected ERT profiles, here called ERT1 and ERT2. (**c**) ERT1 and ERT2 profiles. The first groundwater observation (in this survey equivalent to the regional piezometric level) is singled out. Hydrogeological reinterpretation of ER models after [49] and local hydrogeological information [26,33,34]. Profiles are topographically corrected, and the vertical-to-horizontal scale ratio is 1:1.

The ER data were acquired using the SuperSting R8/IP eight-channels and the SuperSting R1/IP single-channel Memory Earth Resistivity and IP Meter by Advanced Geosciences Inc., Austin, TX. Fifty-six electrodes were placed along each ERT profile using a variable 3–6-m spacing and applying an input voltage of 200 V. A Schlumberger electrode array was used. See Yautibug and Herrera [49] for further methodological details.

Figure 2b shows the location of selected ERT profiles, here called ERT1 and ERT2. The profile features were prospecting lengths of 330 (ERT1) and 165 m (ERT2), prospecting depths of 59 (ERT1) and 28 m (ERT2), ER in the ranges of 20–175 (ERT1) and 25–330 Ω m (ERT2), and average root-mean-square errors (RMSE) of 1.80 (ERT1) and 2.94 (ERT2). Both ERT1 and ERT2 exposed quite similar horizontal and vertical ER distributions (Figure 2c). The ER values were typical of sedimentary and volcano-sedimentary rocks with a variable degree of saturation [56].

Local hydrogeological information [26,33,34] was used to reinterpret the ER models. From top to bottom, the vertical ER distribution was as follows: (i) 1–5 (ERT1) and 1–8 m (ERT2) of discontinuous porous soils and anthropogenic fillings with ER in the 70–300 Ω m range; (ii) 3–5 (ERT1) and 6–15 m (ERT2) of tuff and ash formation catalogued as aquitard

with ER in the 20–50 Ω m range; (iii) 5–10 (ERT1) and 10–20 m (ERT2) of silty alluvial formation catalogued as aquitard with ER in the 40–80 Ω m range; (iv) 5–50 (ERT1) and 10–50 m (ERT2) of coarse-grained alluvial formation catalogued as aquifer with ER in the 80–120 Ω m range; and (v) 5–10 m (ERT1) of silty alluvial formation catalogued as aquitard with ER in the 40–80 Ω m range. The interbedded coarse-grained alluvial formation between the above silty alluvial formation (which includes items iii and v) is part of a shallow aquifer that provided the first groundwater observation corresponding to the regional piezometric level. Changes in the thickness and spatial continuity in the vertical ER distribution are due to sedimentary processes (e.g., lateral facies changes and erosive channels) and the action of minor-order normal faults described in the area [26,33,34].

4.2. Near-Surface Seismic Surveys

Near-surface seismic techniques respond to the steady shear modulus of subsurface materials, expressing seismic shear-wave velocity (VS) [L T^{-1}], in which the Rayleigh wave fundamental mode dispersion curve and higher modes (if present) are extracted from a shot record and then inverted to generate 1D VS models [57–62]. A succession of geophones records ambient microtremor to generate the Rayleigh waves from which a 2D VS model is obtained [61,62].

REMI was the near-surface seismic technique used to acquire VS data and map 2D VS models in four surveys designed to support geotechnical research in civil works (Table 2). The total prospecting length was 22.2 km, the prospecting depth was 40–120 m, and VS varied in the 95–1050 m s^{-1} range (Table 2).

This paper reinterpreted the 2D VS models for the shallow geological definition following the interpretative criteria reported by Paz et al. [63] and Alcalá et al. [64]. These authors propose that subsurface VS propagation is a site-specific steady property determined by effective compaction and therefore is dependent on the age and depth of each geological material piled vertically [65–68]. The different relationships between VS and age and depth in different lithologies described in the scientific literature [63–71] were used to reinterpret the VS models.

The VS increased in depth according to the increasing age and compaction of geological materials, from less than 200 m s^{-1} in recent anthropogenic fillings and lacustrine formations, 200–550 m s^{-1} in Holocene sedimentary and volcano-sedimentary formations, and more than 550 m s^{-1} in Pleistocene volcano-sedimentary formations. As in other near-surface seismic techniques, REMI cannot disambiguate boundaries of different geological formations with similar VS [63,64,70,71]. This limitation to make inner divisions was solved by using external validation data, such as regional [24,25] and local [26,33,34] geological information, geotechnical soundings logs, and other prospecting techniques [63,64].

The REMI surveys labelled 12 and 14 in Figure 1b and Table 2 were selected (Figure 3). They were performed in November 2011 as part of the Quito Subway geotechnical research, which included 201 REMI profiles grouped into three REMI surveys with prospecting lengths of 8.6 (southern Quito), 3.2 (central Quito), and 10.3 km (northern Quito) [44]. Since these prospecting lengths are too long to be drawn in detail, two 2.5-km sections from the southern- and northern-Quito REMI surveys exploring the most representative geological formations were selected (Figure 3b).

The VS data were acquired using the DAQlink-4 24-channels Compact Seismograph and the 4.5 Hz Geo-Space geophones by Seismic Source Co., Ponca city, OK, USA. The following configuration was applied: a recording array of 24 vertical component geophones, 4-m geophone spacing for a prospecting depth of around 40 m, 10-m displacement between readings, and a sampling rate of 0.25 m s^{-1}. See Cataldi [44] for further details about the data processing and mathematical inversion.

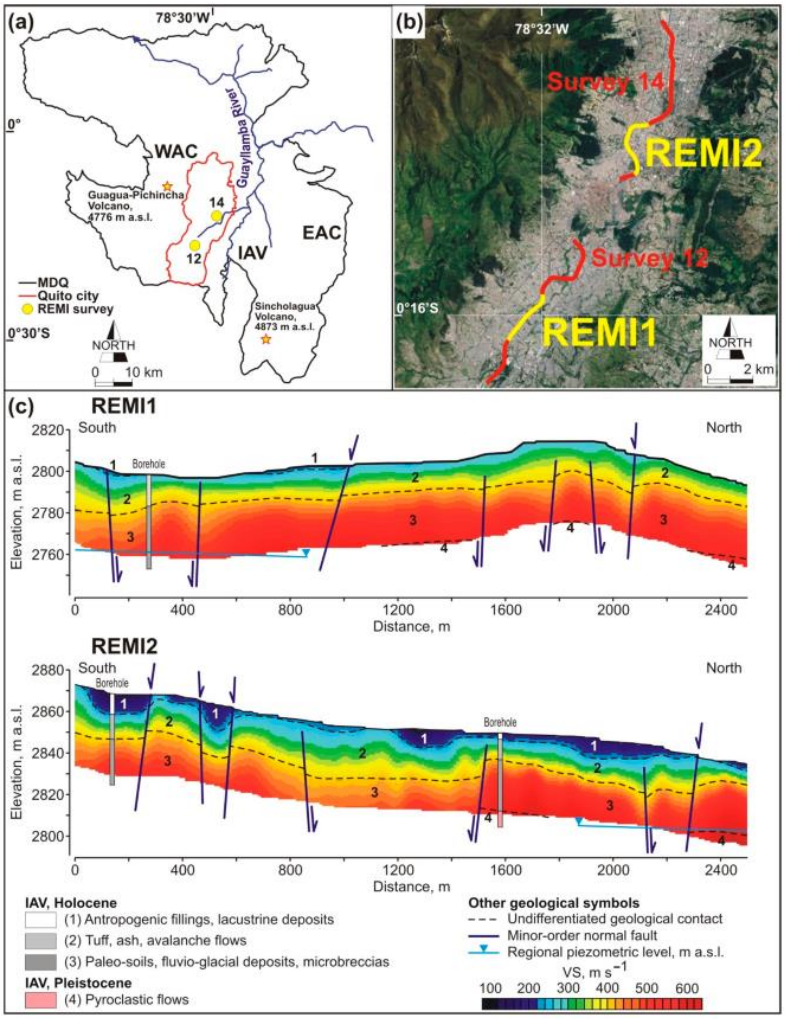

Figure 3. (**a**) General location of the selected southern- and northern-Quito REMI surveys labelled 12 and 14 in Figure 1b and Table 2, updated and reinterpreted from Cataldi [44]. (**b**) Detailed location of two selected 2.5-km sections from REMI surveys 12 and 14, here called REMI1 and REMI2. (**c**) REMI1 and REMI2 profiles' sections. The first groundwater observation (in these surveys equivalent to the regional piezometric level) is singled out. Hydrogeological reinterpretation of the two VS models after [44] and regional [24,25] and local [26,33,34] hydrogeological information. Profiles are topographically corrected, and the vertical-to-horizontal scale ratio is 1:0.13.

Figure 3b shows the location of the two selected REMI surveys sections, here called REMI1 from survey 12 and REMI2 from survey 14. The section features comprised an imposed prospecting length of 2.5 km, a prospecting depth of 40 m, VS in the range of 120–580 (REMI1) and 190–610 m s^{-1} (REMI2), and average RMSEs of 10.83 (REMI1) and 9.42 (REMI2) (Figure 3c). The VS values were typical of sedimentary [63,64] and volcano-sedimentary [72] rocks.

Based on geotechnical soundings logs and regional [24,25] and local [26,33,34] geological information, the vertical VS distribution was reinterpreted from top to bottom as follows: (i) 5–15 (REMI1) and 1–5 m (REMI2) of anthropogenic fillings, soils, and lacustrine deposits with VS less than 200 m s^{-1}; (ii) 10–40 (REMI1) and 10–20 m (REMI2) of Holocene tuff, ash, and avalanche flows with VS in the 200–400 m s^{-1} range; (iii) 1–40 m (REMI1) and less than 10 m (REMI2) of Holocene paleo-soils, fluvio-glacial deposits, and microbreccias with VS in the 400–550 m s^{-1} range; and (iv) 10–50 (REMI1) and 10–30 m (REMI2) of Pleistocene pyroclastic flows with VS higher than 550 m s^{-1}. The Pleistocene formations were only occasionally identified. The horizontal continuity of the vertical VS distribution was frequently interrupted by sedimentary processes (e.g., lateral facies changes and erosive channels) and the action of minor-order normal faults described in the urban area of Quito city [26,33,34].

4.3. Electromagnetic Surveys

Four surveys used electromagnetic techniques, specifically VLF-EM and low-frequency MTS, for the geometry and structure of Holocene to late Pliocene formations resulting from the action of first-order thrusts and strike-slip faults [18,39,45,52]. In general, electromagnetic techniques infer subsurface ER from measurements of natural geomagnetic and geoelectric field variations at the ground surface [73,74]. In particular, VLF-EM and low-frequency MTS use a fixed grounded dipole or horizontal loop as an artificial signal source to determine ER [75,76]. Both natural and controlled-source electromagnetic signals are used to obtain 1D ER models beneath the measurement site [77]. The ER dataset at the corresponding depths and signal-source distances are mathematically inverted to produce a 2D ER model [75,77].

One survey used VLF-EM (<10 Hz) in 13 profiles with a prospecting length in the 160–750 m range, a maximum prospecting depth of 130 m, and ER in the 15–280 Ω m range [39]. Three surveys used low-frequency MTS (>10 Hz) [18,45,52] with a total prospecting length of 33.3 km, a maximum prospecting depth of 4000 m, and ER in the ranges of 10–220 Ω m for geological formations catalogued as aquifers and 220–27,100 Ω m for geological formations catalogued as aquitards (Table 2).

The low-frequency MTS survey labelled 01 in Figure 1b and Table 2 was selected (Figure 4). This survey was performed in 2016 and included 13 measurement sites aligned in an NNE–SSW profile perpendicular to the Saguanchi Gorge strike-slip fault in the southern border of the MDQ (Figure 4b) [18]. Strike-slip faulting produces additional extensional areas disposed perpendicular to the primary shortening tectonic component evidenced by the Quito Fault System, which has implications for the drainage network and the extension and thickness of aquifers in the IAV [18].

The ER data were acquired using the StrataGem EH-4 four-channels Hybrid Source with a TxIM2 transmitter and electric BE-26 and magnetic G100k sensors by Geometrics, Inc., San Jose, CA, USA. The configuration was as follows: 13 measurement sites were set up using a variable 40–170 m array spacing and applying three frequencies in the 10–50 Hz range to record ER from depths of 0.6 to 1.8 km. The recorded ER data were mathematically inverted to obtain a 2D ER model. See Peñafiel et al. [18] for further methodological details.

Figure 4b shows the location of the selected low-frequency MTS profile, here called MTS1 (Figure 4c). The profile features included a prospecting length of 1300 m, a prospecting depth of 1800 m, ER in the 10–8010 Ω m range, and an average RMSE of 14.32. The ER values were similar to that reported for similar volcano-sedimentary rocks with variable degrees of fissuring, fracturing, and saturation [52,56].

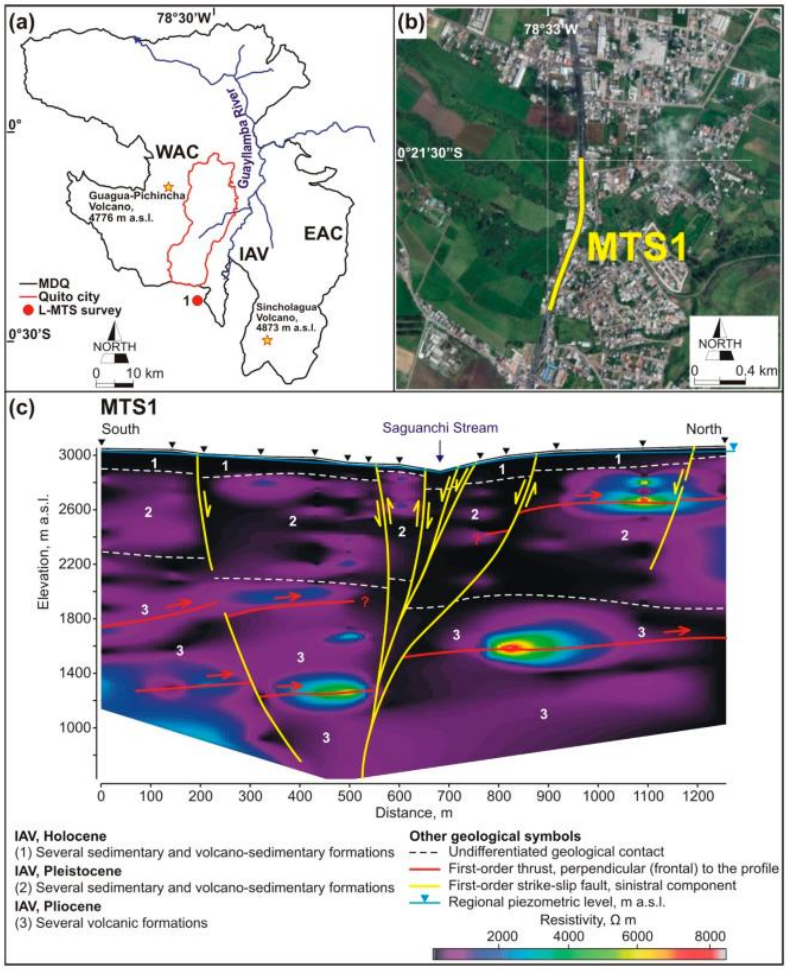

Figure 4. (**a**) General location of the selected low-frequency MTS survey labelled 1 in Figure 1b and Table 2, updated and reinterpreted from Peñafiel et al. [18]. (**b**) Detailed location of the selected low-frequency MTS profile, here called MTS1. (**c**) MTS1 profile. The regional piezometric level is singled out. Hydrogeological reinterpretation of the ER profile after [18] and regional [24,25] and local [26,33,34] hydrogeological information. Profile is topographically corrected, and the vertical-to-horizontal scale ratio is 0.34:1.

The ER model displayed (i) high-resistivity southern and northern sectors with an average ER around 1000 Ω m and several anomalies higher than 3000 Ω m, and (ii) a low-resistivity central sector bounded by strike-slip faults with an average ER lower than 1000 Ω m. In detail, ER values in the 10–50 Ω m range are associated with (i) strongly fractured volcanic rocks of different ages and high saturation degrees within the strike-slip fault zone, and (ii) sub-horizontal contacts within the Pleistocene and late Pliocene formations inferred by first-order thrusts observed at other sites (Figure 4c). ER values in the 50–200 Ω m range are associated with Holocene and Pleistocene volcano-sedimentary formations with moderate degrees of fissuring, fracturing, and saturation. ER values in

the 200–1000 Ω m range are attributed to Pleistocene and late Pliocene volcanic formations with moderate fissuring and fracturing and low to moderate degrees of saturation. ER values higher than 1000 Ω m are interpreted as Pleistocene and late Pliocene volcanic rocks with low fissuring, fracturing, and saturation degrees.

5. Discussion

For the period 2020–2040, climate change projections foresee declining surface water sources in the Andean highlands, while the population in the MDQ could increase from 2.7 to about 4.2 million inhabitants [6,8,10]. The consequence is more groundwater exploitation to supplement the increasing urban water demand [37]. Water Authority of Ecuador and EPMAPS are aware of this problem and have already begun to promote applied groundwater research for sustainable use. Geophysical prospecting surveys can contribute to improve the hydrological conceptualization. However, the existing geophysical surveys explored different observations scales aimed to cover different research interests. So, the geophysical information must be examined and integrated before use in groundwater research. Most geophysical surveys have been performed in the most populated IAV sector (Figure 1b, Table 2), where groundwater exploitation is concentrated and signs of degradation have been reported [36,78].

To examine the usefulness of the subsurface geophysical information in groundwater research in the IAV, the area covered by each geophysical prospecting survey (defined by the corresponding prospecting length and depth) (Table 2) was superimposed onto a synthetic stratigraphic column in the southern border of the MDQ (Figure 1c). Of the compiled 23 geophysical prospecting surveys (Table 2), only the 20 ones located in the IAV (Figure 5) were selected and classified into three methodological groups (electrical, seismic, and electromagnetic) covering two observation scales and two aquifer typologies: shallow Holocene and late Pleistocene aquifers and thick regional middle–early Pleistocene and late Pliocene aquifers.

The VES and ERT surveys were used to define the geometry of shallow Holocene and late Pleistocene aquifers, deduce the regional piezometric level, and qualify pore-water conductivity. The prospecting depth was 150–500 m for the VES and 25–165 m for the ERT surveys (Figure 5). Reinterpretation of the 2D ER models shows that the ER range was 17–203 Ω m for VES and 3–150 Ω m for ERT in those geological formations catalogued as aquifers. These figures agree with the expected EC variability in saturated media associated with variable contributions of natural (e.g., recharge, thermalism, mineral dissolution) and anthropogenic (e.g., domestic, agriculture, industry) salinity sources. Groundwater conductivity deduced in shallow aquifers was higher than in thick regional aquifers. In those geological formations catalogued as aquitards, the ER range was 215–850 Ω m for VES and 210–320 Ω m for ERT. These figures agree with the expected lower variability of conductivity induced by the homogeneous clay content and barely variable lower pore-water content. The regional piezometric level varied depending on the aquifer hydraulic functioning, explored aquifer zone (recharge, transit, and discharge), and topography (Table 2).

REMI surveys were originally performed in geotechnical research for civil works. The 2D VS models were reinterpreted for the geometric definition of shallow Holocene and late Pleistocene aquifers, which is an innovative research application. The prospecting depth was 40 m (Figure 5). The VS values were less than 200 m s^{-1} in recent anthropogenic fillings, soils, and lacustrine formations; 200–550 m s^{-1} in Holocene formations; and more than 500 m s^{-1} in late Pleistocene formations.

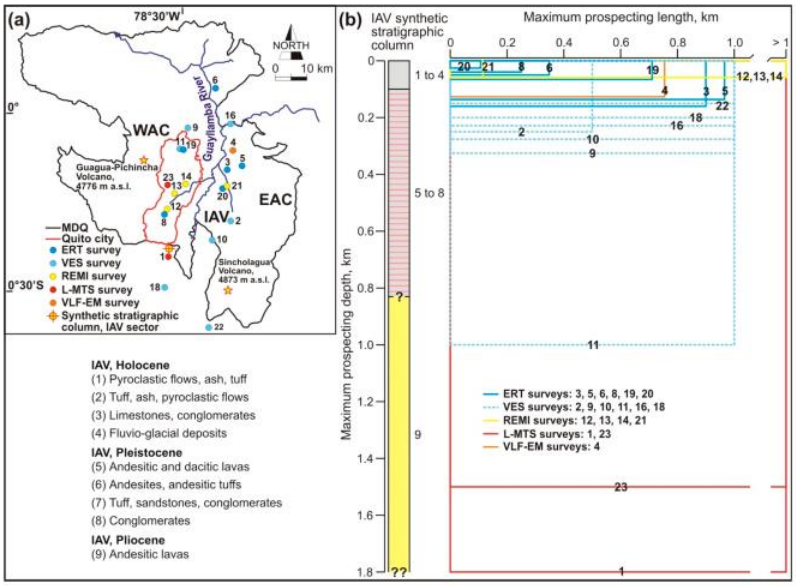

Figure 5. (**a**) General location of the 20 geophysical prospecting surveys in the IAV sector as shown in Figure 1b and Table 2; surveys 15 and 17 in the EAC sector and survey 7 in the WAC sector are excluded from this analysis. (**b**) A synthetic stratigraphic column of the IAV sector, as shown in Figure 1c. The typology and area covered by each geophysical prospecting survey are indicated. Acronyms ERT, VES, REMI, L-MTS, and VLF-EM are defined in Figure 1b.

VLF-EM and low-frequency MTS surveys provided the geometry and structure of Holocene to late Pliocene formations resulting from the action of first-order thrusts and strike-slip faults. The prospecting depths were 130 m for the VLF-EM survey and 1500, 1800, and 4000 m for the three low-frequency MTS surveys, of which only the first two were in the IAV sector (Figure 1b, Table 2). The hydrogeological reinterpretation of these two low-frequency MTS surveys [18,52] provided two significant findings: (i) the delineation of first-order thrusts and strike-slip faults controlling the geometry and stacking structure of Holocene to late Pliocene formations; and (ii) the identification of hitherto unknown disconnections (evidenced as high-resistivity fringes) between aquifers (evidenced as low-resistivity spaces) previously defined as hydraulically connected [26,36], resulting in less groundwater storage than previously known. An example is given in Figure 4c.

Despite the geophysical prospecting findings (Figure 5), three relevant gaps limiting a suitable hydrogeological conceptualization in the IAV sector still remain: (i) identifying the complete saturated thickness of Pliocene formations; (ii) elucidating the existence of older underlying Neogene formations of unknown hydrogeological behavior; and (iii) defining the IAV basement depth and typology, which is assumed to be equivalent to the WAC basement, after Bouguer gravity wedge data [31]. These gaps should be the subject of future research. Geophysical prospecting surveys with greater penetration depth could provide this basic aquifer information to assess the groundwater resource of Pleistocene and Pliocene andesitic lavas catalogued as the larger freshwater reservoirs in the MDQ.

6. Conclusions

The MDQ is a sparse-data area where definition of shallow and thick regional aquifers functioning, as well as their hydraulic relationships, is yet incipient. Different geophysical prospecting surveys originally devoted to different research interests can be integrated

to provide subsurface information of interest in groundwater research. However, the published geophysical information is restricted to some research papers and scientific documents that aimed to investigate the transient groundwater features of shallow aquifers and the structure of deep (but not the deepest) geological formations. The compilation and examination of unpublished geophysical prospecting surveys contribute to improving the hydrogeological conceptualization, as well as to proposing additional research to bridge important gaps, which prevents the implementation of robust hydrological numerical tools to assess the groundwater resource.

A data search was conducted to examine the feasibility of existing geophysical prospecting surveys in groundwater research in the MDQ. Sources of information were the EPMAPS' public repository for near-surface electrical techniques (ERT and VES surveys), official geotechnical research reports in civil works for near-surface seismic techniques (REMI surveys), and scientific documents for electromagnetic techniques (MTS surveys). Finally, 23 representative geophysical prospecting surveys were compiled. Most of the surveys were performed in the IAV sector, where groundwater exploitation is concentrated. The ERT and VES surveys explored aquifer geometry and transient groundwater features of Holocene and late Pleistocene formations (some forming shallow aquifers), such as the aquifer saturated thickness, piezometric level, and spatial distribution of pore-water conductivity. The REMI surveys were reinterpreted to deduce the geometry of Holocene formations and, occasionally, late Pleistocene formations. The VLF-EM and low-frequency MTS surveys provided the structure of Holocene to late Pliocene formations in the IAV sector. No geophysical prospecting surveys exploring the complete saturated thickness of the Pliocene aquifers, other possible older underlying Neogene formations of unknown hydrogeological behavior, and the IAV basement depth and typology could be compiled. However, three surveys partially explored these features in the EAC and WAC sectors. Therefore, this basic information remains unknown, preventing an accurate assessment of the groundwater resource from which to deduce the renewable fraction of thick regional Pleistocene and Pliocene aquifers that can be exploited sustainably. Geophysical prospecting surveys with greater penetration depth could provide this basic information.

This paper demonstrates the need to systematize the use of geophysical prospecting techniques, including the most widely used technique described here to deduce shallow aquifer typologies and transient groundwater features and other specifics to explore the complete saturated thickness of Pleistocene and Pliocene aquifers forming the larger freshwater reservoirs in the MDQ. The above findings and research gaps, together with the generated database, seek to improve the design of geophysical prospecting surveys to explore groundwater resources in the MDQ and other large Andean urban areas.

Author Contributions: Conceptualization, F.J.A.; methodology, F.J.A.; formal analysis, L.P. and F.J.A.; data curation, L.P.; writing—original draft preparation, L.P., F.J.A. and J.S.-A.; writing—review and editing, F.J.A. and J.S.-A.; project administration, F.J.A.; funding acquisition, L.P. and F.J.A. All authors have read and agreed to the published version of the manuscript.

Funding: This research was partly supported by the International Atomic Energy Agency Project ECU/7/006 and the Ecuadorian Research Project PROMETEO-CEB-014-2015.

Institutional Review Board Statement: Not applicable.

Informed Consent Statement: Not applicable.

Data Availability Statement: The data presented in this study are available on request from the corresponding author.

Acknowledgments: The authors are grateful for the information on the geophysical prospecting surveys provided by the EPMAPS. We also wish to express our gratitude to two anonymous reviewers for their valuable advice and comments.

Conflicts of Interest: The authors declare no conflict of interest.

References

1. Barnett, T.P.; Adam, J.C.; Lettenmaier, D.P. Potential impacts of a warming climate on water availability in snow-dominated regions. *Nature* **2005**, *438*, 303–309. [CrossRef]
2. Bradley, R.S.; Vuille, M.; Diaz, H.F.; Vergara, W. Threats to water supplies in the Tropical Andes. *Science* **2006**, *312*, 1755–1756. [CrossRef] [PubMed]
3. Viviroli, D.; Archer, D.R.; Buytaert, W.; Fowler, H.J.; Greenwood, G.B.; Hamlet, A.F.; Huang, Y.; Koboltschning, G.; Litaor, M.L.; López-Moreno, J.L.; et al. Climate change and mountain water resources: Overview and recommendations for research, management and policy. *Hydrol. Earth Syst. Sci.* **2011**, *15*, 471–504. [CrossRef]
4. Buytaert, W.; Célleri, R.; De Bièvre, B.; Cisneros, F.; Wyseure, G.; Deckers, J.; Hofstede, R. Human impact on the hydrology of the Andean páramos. *Earth-Sci. Rev.* **2006**, *79*, 53–72. [CrossRef]
5. Buytaert, W.; Vuille, M.; Dewulf, A.; Urrutia, R.; Karmalkar, A.; Célleri, R. Uncertainties in climate change projections and regional downscaling in the tropical Andes: Implications for water resources management. *Hydrol. Earth Syst. Sci.* **2010**, *14*, 1247–1258. [CrossRef]
6. López, S.; Wright, C.; Costanza, P. Environmental change in the equatorial Andes: Linking climate, land use, and land cover transformations. *Remote Sens.* **2017**, *8*, 291–303. [CrossRef]
7. Flores-López, F.; Galaitsi, S.E.; Escobar, M.; Purkey, D. Modeling of Andean Páramo ecosystems hydrological response to environmental change. *Water* **2016**, *8*, 94–111. [CrossRef]
8. Gonzales-Zeas, D.; Erazo, B.; Lloret, P.; De Bièvre, D.; Steinchneider, S.; Dangles, O. Linking global climate change to local water availability: Limitations and prospects for a tropical mountain watershed. *Sci. Total Environ.* **2019**, *650*, 2577–2586. [CrossRef]
9. Alcalá, F.J.; Toapanta, J.; Peñafiel, L.; Barragán, E.; Yánez, W.; Buenaño, M.; Larrea, O. First data on atmospheric chloride mass balance components in the Andean páramo in central Ecuador: Implications to project climate scenarios of net aquifer recharge and potential groundwater chemical baseline. In *43rd IAH Congress: Groundwater and Society*; IAH: Montpellier, France, 2016; pp. 851–852.
10. Minga-Leon, S.; Gómez-Albores, M.A.; Bâ, K.M.; Balcázar, L.; Manzano-Solis, L.R.; Cuervo-Robayo, A.P.; Mastachi-Loza, C.A. Estimation of water yield in the hydrographic basin of southern Ecuador. *Hydrol. Earth Syst. Sci. Discuss.* **2018**, Preprint. [CrossRef]
11. Peñafiel, L.; Alcalá, F.J.; Barragán, E.; Larrea, O. Evaluación del balance hídrico en un área vulcano-sedimentaria de alta montaña poco monitorizada en la Cordillera de los Andes: Acuífero del río Pita, norte de Ecuador. *Rev. Lat. Hidrogeol.* **2016**, *10*, 502–508.
12. Peñafiel, L.; Alcalá, F.J.; Barragán, E.; Toro-Espitia, L.; Larrea, O. Uso de trazadores químicos e isotópicos para deducir el funcionamiento del acuífero del río Pita, Cordillera de los Andes, norte de Ecuador. *Rev. Lat. Hidrogeol.* **2016**, *10*, 495–501.
13. Paz, C.; Alcalá, F.J.; Carvalho, J.M.; Ribeiro, L. Current uses of ground penetrating radar in groundwater-dependent ecosystems research. *Sci. Total Environ.* **2017**, *595*, 868–885. [CrossRef]
14. Monteiro Santos, F.A.; Sultan, S.A.; Represas, P.; El Sorady, A.L. Joint inversion of gravity and geoelectric data for groundwater and structural investigation: Application to the northwestern part of Sinai, Egypt. *Geophys. J. Int.* **2006**, *165*, 705–718. [CrossRef]
15. Alam, K.; Ahmad, N. Determination of aquifer geometry through geophysical methods: A case study from Quetta Valley, Pakistan. *Acta Geophys.* **2014**, *62*, 142–163. [CrossRef]
16. Binley, A.; Hubbard, S.S.; Huisman, J.A.; Revil, A.; Robinson, D.A.; Singha, K.; Slater, L.D. The emergence of hydrogeophysics for improved understanding of subsurface processes over multiple scales. *Water Resour. Res.* **2015**, *51*, 3837–3866. [CrossRef] [PubMed]
17. Uhlemann, S.S.; Sorensen, J.P.R.; House, A.R.; Wilkinson, P.B.; Roberts, C.; Gooddy, D.C.; Binley, A.M.; Chambers, J.E. Integrated time-lapse geoelectrical imaging of wetland hydrological processes. *Water Resour. Res.* **2016**, *52*, 3. [CrossRef]
18. Peñafiel, L.; Reyes, P.S.B.; Alcalá, F.J.; Ramírez, M.R.; Cabero, A. Fold-axis parallel extension along the southern ending of the Quito (Ecuadorian Andes) fault system: Implications in river network and aquifer geometry. *Geotectonics* **2020**, *54*, 256–265. [CrossRef]
19. Bendix, J. Precipitation dynamics in Ecuador and northern Peru during the 1991/92 El Nino: A remote sensing perspective. *Int. J. Remote Sens.* **2000**, *21*, 533–548. [CrossRef]
20. Bendix, J.; Rollenbeck, R.; Palacios, W.E. Cloud detection in the Tropics–a suitable tool for climate-ecological studies in the high mountains of Ecuador. *Int. J. Remote Sens.* **2004**, *25*, 4521–4540. [CrossRef]
21. Van der Hammen, T.; Hooghiemstra, H. Neogene and Quaternary history of vegetation, climate, and plant diversity in Amazonia. *Quat. Sci. Rev.* **2000**, *19*, 725–742. [CrossRef]
22. Garreaud, R.; Falvey, M. The coastal winds off western subtropical South America in future climate scenarios. *Int. J. Climatol.* **2009**, *29*, 543–554. [CrossRef]
23. Rollenbeck, R.; Fabian, P.; Bendix, J. Precipitation dynamics and chemical properties in the mountain forests of Ecuador. *Adv. Geosci.* **2006**, *6*, 73–76. [CrossRef]
24. Burbano, N.; Becerra, S.; Pasquel, E. *Introduction to the Hydrogeology of Ecuador*; Memory and Appendices; National Institute for Meteorology and Hydrology: Quito, Ecuador, 2015; pp. 1–121.
25. PETROECUADOR. *Updated Mapping of Hydrogeological Units and Hydrographic Basins of Ecuador Referenced to the Hydrocarbon Sector Infrastructures (scale 1:1,000,000)*; Memory and Appendices; Government of Ecuador: Quito, Ecuador, 2005.

56. Ward, S.H. Resistivity and Induced Polarization Methods. In *Geotechnical and Environmental Geophysics*, 2nd ed.; Ward, S.H., Ed.; Society of Exploration Geophysicists: Tulsa, OK, USA, 1990; pp. 147–190.
57. Xia, J.; Miller, R.D.; Park, C.B. Estimation of near-surface shear-wave velocity by inversion of Rayleigh wave. *Geophysics* **1999**, *64*, 691–700. [CrossRef]
58. Xia, J.; Miller, R.D.; Park, C.B.; Hunter, J.A.; Harris, J.B.; Ivanov, J. Comparing shear-wave velocity profiles inverted from multichannel surface wave with borehole measurements. *Soil Dyn. Earthq. Eng.* **2002**, *22*, 181–190. [CrossRef]
59. Park, C.B.; Miller, R.D.; Xia, J. Multi-channel analysis of surface waves. *Geophysics* **1999**, *64*, 800–808. [CrossRef]
60. Park, C.B.; Miller, R.D.; Xia, J.; Ivanov, J. Multichannel analysis of surface waves (MASW)—Active and passive methods. *Lead Edge* **2007**, *26*, 60–64. [CrossRef]
61. Louie, J. Faster, better: Shear-wave velocity to 100 meters depth from refraction microtremor arrays. *Bull Seismol. Soc. Am.* **2001**, *91*, 347–364. [CrossRef]
62. Raines, M.G.; Gunn, D.A.; Morgan, D.J.R.; Williams, G.; Williams, J.D.O.; Caunt, S. Refraction microtremor (ReMi) to determine the shear-wave velocity structure of the near surface and its application to aid detection of a backfilled mineshaft. *Q. J. Eng. Geol. Hydrogeol.* **2011**, *44*, 211–220. [CrossRef]
63. Paz, M.C.; Alcalá, F.J.; Medeiros, A.; Martínez-Pagán, P.; Pérez-Cuevas, J.; Ribeiro, L. Integrated MASW and ERT imaging for geological definition of an unconfined alluvial aquifer sustaining a coastal groundwater-dependent ecosystem in southwest Portugal. *Appl. Sci.* **2020**, *10*, 5905. [CrossRef]
64. Alcalá, F.J.; Martínez-Pagán, P.; Paz, M.C.; Navarro, M.; Pérez-Cuevas, J.; Domingo, F. Combining of MASW and GPR Imaging and Hydrogeological Surveys for the Groundwater Resource Evaluation in a Coastal Urban Area in Southern Spain. *Appl. Sci.* **2021**, *11*, 3154. [CrossRef]
65. García-Jerez, A.; Navarro, M.; Alcalá, F.J.; Luzón, F.; Pérez-Ruiz, J.A.; Enomoto, T.; Vidal, F.; Ocaña, E. Shallow velocity structure using joint inversion of array and h/v spectral ratio of ambient noise: The case of Mula town (SE of Spain). *Soil Dyn. Earthq. Eng.* **2007**, *27*, 907–919. [CrossRef]
66. Mitchell, J.K.; Soga, K. *Fundamentals of Soil Behaviour*, 3rd ed.; Wiley: London, UK, 2005; pp. 1–592.
67. Zimmer, M.A.; Prasad, M.; Mavko, G.; Nur, A. Seismic velocities of unconsolidated sands: Part 1—Pressure trends from 0.1 to 20 MPa. *Geophysics* **2007**, *72*, E1–E13. [CrossRef]
68. McGann, C.R.; Bradley, B.A.; Cubrinovski, M. Investigation of shear wave velocity depth variability, site classification, and liquefaction vulnerability identification using a near-surface Vs model of Christchurch, New Zealand. *Soil Dyn. Earthq. Eng.* **2017**, *92*, 692–705. [CrossRef]
69. Alcalá, F.J.; Espinosa, J.; Navarro, M.; Sánchez, F.J. Propuesta de división geológica de la localidad de Adra (provincia de Almería). Aplicación a la zonación sísmica. *Rev. Soc. Geológica España* **2002**, *15*, 55–66.
70. Martínez-Pagán, P.; Navarro, M.; Pérez-Cuevas, J.; Alcalá, F.J.; García-Jerez, A.; Sandoval-Castaño, S. Shear-wave velocity based seismic microzonation of Lorca city (SE Spain) from MASW analysis. *Near Surf. Geophys.* **2014**, *12*, 739–749. [CrossRef]
71. Martínez-Pagán, P.; Navarro, M.; Pérez-Cuevas, J.; Alcalá, F.J.; García-Jerez, A.; Vidal, F. Shear-wave velocity structure from MASW and SPAC methods. The case of Adra town, SE Spain. *Near Surf. Geophys.* **2018**, *16*, 356–371. [CrossRef]
72. Vanorio, T.; Prasad, M.; Patella, D.; Nur, A. Ultrasonic velocity measurements in volcanic rocks: Correlation with microtexture. *Geophys. J. Int.* **2002**, *149*, 22–36. [CrossRef]
73. Unsworth, M.; Soyer, W.; Tuncer, V.; Wagner, A.; Barnes, D. Hydrogeologic assessment of the Amchitka Island nuclear test site (Alaska) with magnetotellurics. *Geophysics* **2007**, *72*, B47–B57. [CrossRef]
74. Chave, A.D.; Jones, A.G. *The Magnetotelluric Method: Theory and Practice*; Cambridge University Press: New York, NY, USA, 2012; pp. 1–584.
75. McPhee, D.K.; Chuchel, B.A.; Pellerin, L. *Audiomagnetotelluric Data from Spring, Cave, and Coyote Spring Valleys, Nevada*; No. 2006-1164; US Geological Survey: Menlo Park, CA, USA, 2006; pp. 1–43.
76. Zonge, K.L.; Hughes, L.J. Controlled source audio-frequency magnetotellurics. In *Electromagnetic Methods in Applied Geophysics, Volume 2: Application, Parts A and B*; Nabighian, M.N., Ed.; Society of Exploration Geophysics: McLean, VA, USA, 1991; pp. 713–810.
77. Geometrics, Inc. *Operation Manual for Stratagem Systems Running IMAGEM Ver. 2.19*; Geometrics, Inc.: San Jose, CA, USA, 2007.
78. Buytaert, W.; De Bièvre, B. Water for cities: The impacts of climate change and demographic growth in the tropical Andes. *Water Resour. Res.* **2012**, *48*, W08503. [CrossRef]

A3. Publication 3

Peñafiel, L.A., Reyes, P.S., Alcalá F.J., Ramírez, M.R., Cabero, A. Fold-Axis Parallel Extension along the Southern Ending of the Quito (Ecuadorian Andes) Fault System: Implications in River Network and Aquifer Geometry. *Geotectonics*, 54, 256-265. https://doi.org/10.1134/S0016852120020090

Impact Factor 2020 (JCR): 1.121; Category: GEOCHEMISTRY & GEOPHYSICS; Ranking: 75/88 (Q4); Date of publication: 2020.

ISSN 0016-8521, Geotectonics, 2020, Vol. 54, No. 2, pp. 256–265. © Pleiades Publishing, Inc., 2020.

Fold-Axis Parallel Extension along the Southern Ending of the Quito (Ecuadorian Andes) Fault System: Implications in River Network and Aquifer Geometry[1]

L. A. Peñafiel[a, b], P. S. B. Reyes[c, *], F. J. Alcalá[a, d], M. R. Ramírez[e], and A. Cabero[c]

[a] *Department of Civil Engineering, UCAM Catholic University of Murcia, Murcia, P.O. 30107 Spain*
[b] *Empresa Pública Metropolitana de Agua Potable y Saneamiento (EPMAPS-Agua de Quito), Mariana de Jesús, Quito, P.O. 17-03-0330 Ecuador*
[c] *Departamento de Geología, Escuela Politécnica Nacional, Ladrón de Guevara E11-253, Quito, P.O. 17-01-2759 Ecuador*
[d] *Instituto de Ciencias Químicas Aplicadas, Facultad de Ingeniería, Universidad Autónoma de Chile, Santiago, P.O. 7500138 Chile*
[e] *Departamento de Geodinámica, Instituto Espacial Ecuatoriano, Quito, Oe5-61 Ecuador*
**e-mail: pedro.reyes@epn.edu.ec*

Received August 18, 2019; revised November 24, 2019; accepted November 26, 2019

Abstract—Extension parallel to fold axis represents a rarely documented tectonic process that occur in different tectonic settings such as large-scale orogenic belts, mountain ranges, and thrust and fold belts. Along the Ecuadorian Andes, extensional systems have only been reported as tectonic boundaries of local intermontane basins, pull-apart depressions and outer-arc stretching faults along hinge surfaces in compressional antiforms. The Quito fault system shows in planform view a right-stepping en-echelon arrangement which southernmost anticlinal ridge terminates as an arcuate structure locally dissected by the Saguanchi Gorge. Valley hillslopes of this transverse drainage display evidence of tectonic extension featured by several swarms of normal faults commonly dipping towards the valley bottom. Magnetotellurics sounding obtained across a N–S line parallel to the crestline axis reveals three contiguous and distinguishable domains of which the central one shows a wedge-shaped geometry pointing down. This tectonic evidence for ongoing extensional deformation suggests that the process of fold-axis-parallel extension controlled the tectonic development and dissection of the Saguanchi Gorge across the anticlinal ridge. This episode marks a significant change in the groundwater recharge and aquifer storage conditions between the Quito basin and the inter-Andean Depression aquifer systems, currently in production to provide the potable water supply for the Quito city.

Keywords: fold-axis parallel extension, Quito fault system, the aquifer geometry, Ecuador
DOI: 10.1134/S0016852120020090

INTRODUCTION

Oblique convergent motion between Nazca and South America plates through a N83°E horizontal velocity vector [24] drives the NE-ward escape of the North Andean Sliver (NAS) [12, 41]. Dip-slip and strike-slip fault systems control the Neogene uplifting of the Ecuadorian Andes. The dip-slip Quito fault system (QFS) [1], which partially borders the eastern flank of the Andean Western Cordillera, is accommodated by a set of thrust-related anticlinal asymmetric folds verging to the east in response to the ENE shortening imposed at the central Ecuadorian convergent margin. Alvarado et al. [1] pointed out morphological evidences of strike-slip structures related to the QFS motion in Guaylla-bamba area, downstream of the San-Pedro River. In analogous contractional settings, extensional components parallel to the main arc or to the fold-thrust belt structure were described (e.g. the ancient Appalachians [26], Gibraltar-Calabrian arcs [7], Lesser Antilles arc [15], and Tibetan plateau [40]). However, no evidence of tectonic subsidence neither Quaternary extension along the northern Ecuadorian Andes have yet been reported. For instance, along the Northern Himalayan, shortening predominates in a roughly north-south direction [36] whereas the contemporaneous east-west stretching accommodates along north-south striking normal faults [31, 35]. These features suggest that a range-parallel extension characterizes recent deformation in this chain [4, 37, 40, 49].

In various contractional settings such as fold and thrust belts or active orogenic chains, regional extension parallel to fold axes where the minor stress component (sigma 3) is perpendicular to shortening direction, has been rarely described [19, 26] and few studies have described this derivative extensional effect [11]. In this context, along the Ecuadorian Andes, where

[1] The article is published in the original.

compressional and transcurrent regimes are strongly dominant and widely reported (e.g. [13]), only few local extensional settings have been described such as some normal fault systems associated, for example, with the tectonic evolution of the southern Miocene Intermontane Basins [22], the latest Miocene Chota Basin [52] and other local depressions related to strike-slip faults [27, 45]. Thus, in this paper, we investigate the thrusting structure along the southern anticlinal ridge of the dip-slip QFS and the evidence of associated normal faulting cutting through the southernmost anticline. This compressional-extensional setting determines river network and aquifer geometry, as previously reported by [42]. Because the Saguanchi Gorge enable a better exposure of these structures, this area was selected to carry out fieldwork and a sounding campaign by using a magnetotelluric equipment along a north-south profile cutting the structure. The 2D electrical resistivity mapping enables to define local tectonic subsidence, thus leading to alternative tectonic models in order to explain extension in this particular compressional regime.

TECTONIC SETTING

QFS represents the easternmost fault-propagation fold system detached from the N–S trending right-lateral strike-slip Pujilí-Cauca-Patía (PCP) fault system [28, 45]. PCP represents the northwestern branch extension of the Pallatanga fault system [6], which in turn accommodates the southernmost displacement between the North Andean Sliver (NAS) and the South American Plate [2, 12]. The planform geometry of the QFS reveals a right-stepping en-echelon pattern composed of three NNE-trending anticlinal ridges [1, 50] separated by two anticline-syncline fold pair transfer zones [39] between the overlapping blind thrust faults. The southernmost segment of the QFS exhibits a smoothly crestline whose along-strike termination is plunged and deflected southwestward, and locally dissected by various transverse and radial valleys among which Saguanchi Gorge stands out. The QFS anticlinal ridges separate the Quito Basin (QB) from the adjacent Interandean Depression (ID), which in turn is defined as a narrow, elongated, low-topography block, located between the Western and Eastern Andean Cordilleras that together conform the bulk of the Ecuadorian Andes. The QB (Fig. 1) is a NNE-trending piggy-back basin infilled on the back of the QFS overriding structures [21], whose sedimentary filling material is predominantly supplied from the adjacent volcanoes. The QB stratigraphy includes andesitic lavas, pyroclastic and laharitic flows, debris avalanche, alluvial-fan deposits and lacustrine facies, all of them mantled by a roughly massive, structureless silty material of the Cangahua Fm, forming a large, S–N elongated, productive aquifer yielded by EPMAPS [14, 42]. The ID shows similar stratigraphic features to the QB infilling, forming another large, S–N elongated, productive aquifer yielded also by EPMAPS and others [14, 29].

DRAINAGE NETWORK AND AQUIFER GEOMETRY

The southernmost drainage network includes a branching pattern of tributaries that dissects the narrow, gently sloping plain of the QB and coalesces downstream to form the trunk channel of the Machángara River (Fig. 1) before traverse the central QFS anticlinal ridges. Machángara River mainly drains the southern hydrographic basin and flows through the central transfer zone of the QFS until reaching the ID. The Monjas River drains the northern QB (Fig. 1) and flows northward into the NW-flowing Guayllabamba River before it enters the Western Andean Cordillera. Low-steep water divides typically underlain by alluvial-fan landforms separate the hydrographic sub-basins of the QB. Toward the south, the E-flowing Saguanchi Gorge (Fig. 2) and other adjacent entrenched river valleys draining both the foothills of the Atacazo-Ninahuilca volcanic complex and the southernmost QB, coalesce downstream into the N-flowing San-Pedro River (Fig. 1), which flows along the western plain of the ID.

This regional S–N elongated active tectonic setting favors groundwater storage and water flow due to the fractured, fissured and weathered bedrock. Active tectonics and Quaternary sedimentary and volcaniclastic infilling typically favors a secondary shallow groundwater storage. This is the case of the QB and ID (Fig. 2), in which large, productive aquifers develops [14]. The Pita River Basin, located ~12 km southeastward from the Pasochoa volcanic edifice (Fig. 1), outside the study area, is another example on how this tectonic and volcano-sedimentary setting determines drainage network and aquifer geometry [43], which is also under study by this research team.

FIELDWORK EVIDENCE

Geological fieldwork was carried out between 2005 and 2006 during the construction of the Simón-Bolívar highway along the two opposed steeper hillslopes of the Saguanchi Gorge. In a preliminary study, Peñafiel [42] reported several swarms of faults on both sides of the gorge (Fig. 3). Small, closely spaced normal faults with approximately 5 m apart (Fig. 3a, 3b) crop out along the southern hillslope. They often exhibit apparent straight surfaces with dip angles up to 70° in a NW-strike, whose plains are oppositely facing to the valley bottom and show a domino fault-block arrangement. Disposed in a roughly E–W direction, a second set of normal faults dominate the northern hillslope. A well-developed listric normal fault (Fig. 3c, 3d) accommodates a displacement up to 10 m. Antithetic subsidiary normal faults control the local subsidence induced by the hangingwall roll-over tilting upon the

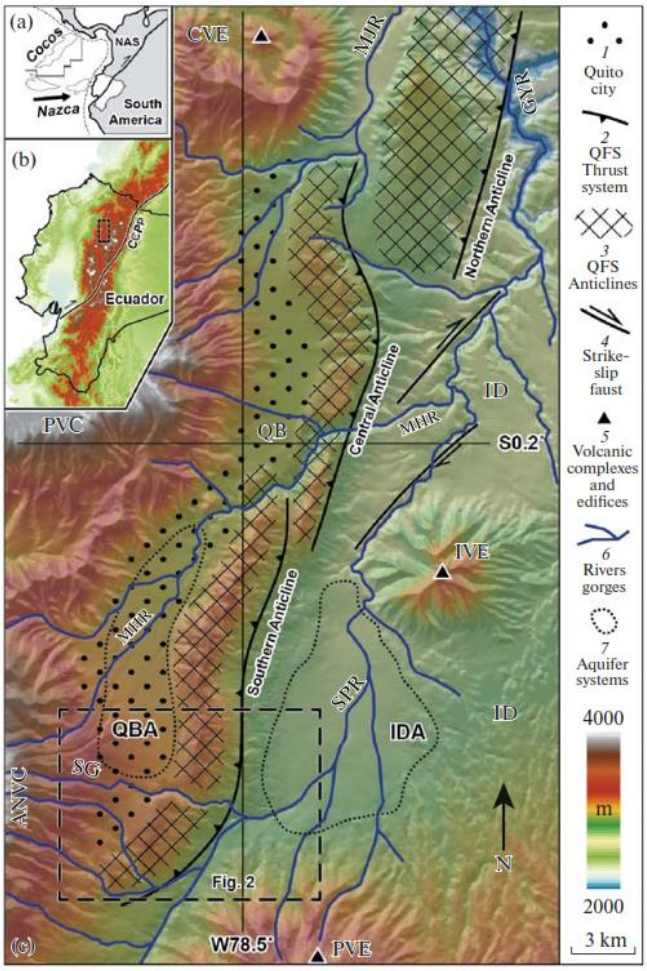

Fig. 1. (a) Regional geodynamic setting including the South American, Nazca, and Cocos Plates, and the Nor-Andean Sliver (NAS). (b) Regional topographic map of the Ecuadorian Andes showing the Chingual-Cosanga-Pallatanga-Puná (CCPP) fault system. (c) Morphotectonic map of the Quito Basin (QB) and the Interandean Depression (ID). Legend: (*1*) Quito city, (*2*) the QFS in a right-stepping en-echelon arrangement, (*3*) the three QFS anticlinal ridges, (*4*) strike-slip fault systems, (*5*) volcanic complexes and edifices as Pichincha Volcanic Complex (PVC), Atacazo-Ninahuilca Volcanic Complex (ANVC), Casitagua Volcanic Edifice (CVE), Pasochoa Volcanic Edifice (PVE), and Ilaló Volcanic Edifice (IVE), (*6*) rivers and gorges as San-Pedro River (SPR), Saguanchi Gorge (SG), Machángara River (MHR), Monjas River (MJR), and Guayllabamba River (GYR), and (*7*) aquifer systems as Quito Basin Aquifer (QBA), and Interandean Depression Aquifer (IDA).

listric fault. Debris-flow mixtures, thepra levels and soil horizons infill the space created by the syntectonic troughs generated upon the hangingwall blocks. Other minor normal faults displace the volcano-sedimentary sequence on the footwall blocks farther away from the gorge (Fig. 3f). E–W-striking isolated horsts remain as tilted blocks close to the Saguanchi valley (Fig. 3c). North-facing footwall backtilting evidenced by gentle dipping fault-truncated layers (Fig. 3d) unconformable overlain by erosional surfaces (Fig. 3g) especially along the northern hillslope. Morphometric planform analysis suggests both around 0.61-km N–S extensional and around 0.27 km E–W lateral offsets along the crestline culmination of the QFS anticline. In summary, fieldwork along the Saguanchi Gorge evidences local tectonic subsidence and N–S extension controlled by bounding normal faults that move away the axial crestline of the southern QFS.

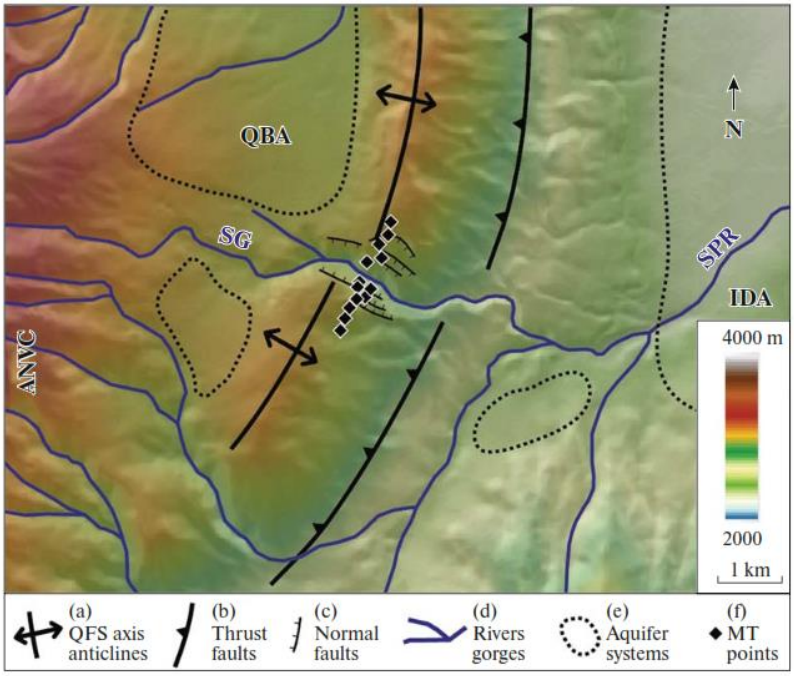

Fig. 2. Morphotectonic map of the southern ending of the QFS anticlinal ridge at the Saguanchi Gorge area. Legend as (a) QFS asymmetric anticlinal axes, (b) QFS thrusting structures, (c) normal faults, (d) river network, (e) aquifer systems boundaries QBA and IDA, (f) MT points of the geophysical profile as in Fig. 4; and the Atacazo-Ninahuilca Volcanic Complex (ANVC).

MAGNETOTELLURIC SURVEY

Magnetotellurics (MT) is a passive frequency-domain electromagnetic sounding technique that uses a fixed grounded dipole or horizontal loop as an artificial signal source to determine electrical resistivity of subsurface media [34, 54]. The Geometrics Strata-Gem EH-4 system (Geometrics, San Jose, CA, USA) uses both natural and controlled-source electromagnetic signals to obtain a continuous electrical sounding of the media beneath the measurement site [18]. Electrical responses in the 50, 20, and 10 Hz frequencies are typically obtained for near-surface (shallow) explorations. Penetration depth may range from few meters to more than one kilometer [18]. Along a perpendicular line to the Saguanchi Gorge downstream direction, 13 arrays (Fig. 2, measuring points) were surveyed. In each measurement point, three low frequencies to accomplish a penetration depth from 0.6 to 1.8 km were used. At each point of the sounding profile, resistivity (Ω m) at the corresponding depth (m) and signal-source distance (m) was recorded. The Stratagem Resistivity Plotter software [18] enables to implement a 2D inversion algorithm for data inversion [34]. The result is a 2D grid that represents continuous resistivity on vertical (depth) and horizontal (distance) axes. A color bar scale categorizes the results in the 0–10000 Ω m range.

RESULTS

MT data were acquired along an N-S orientated line through Saguanchi Gorge (Fig. 2). This line consists of 13 sounding points measuring electrical resistivity in function of depth and distance. The 2D resistivity mapping was based on spatial interpolation of data from south to north (Fig. 4a). Results display a high-resistivity domain HRD-1 with mean values about 1000–2000 Ω m featured by scarcely distributed values higher than 3000 Ω m. To the center of the profile just beneath the Saguanchi Gorge a wedge-shaped block LRD-2, which points vertically down, differs from those of the adjacent domains by having values less than 1000 Ω m. To the north, a high-resistivity domain HRD-3 shows again some scarcely distributed high

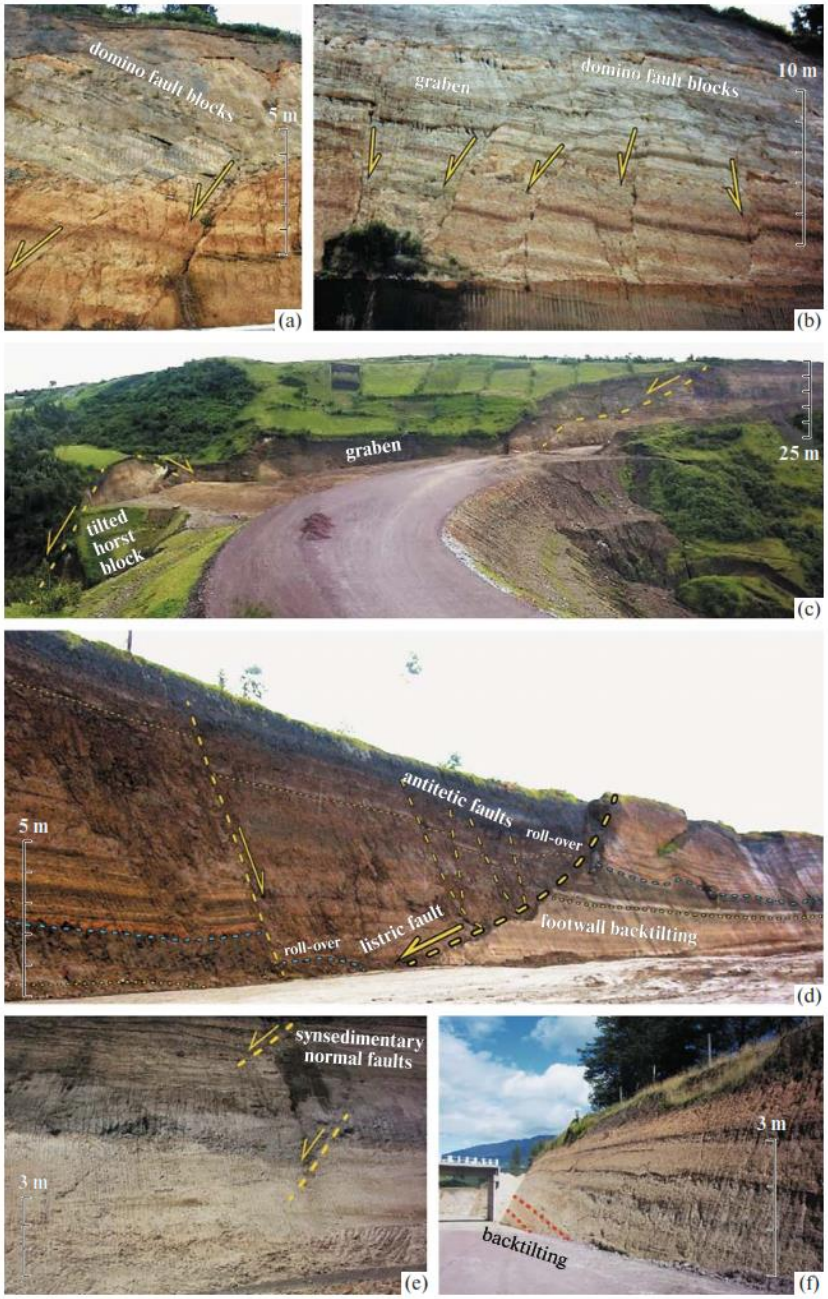

Fig. 3. (a, b) Domino fault block arrangement along the southern hillslope of the Saguanchi Gorge. (c) Tilted horst block and graben development along the northern hillslope of the Saguanchi Gorge. (d) Listric normal fault showing all the associated elements as antithetic faults roll-over anticlines, footwall backtilting and half-graben infilling. (e) Synsedimentary normal faults occurring along the footwall sequence away from the gorge. (f) Backtilting along the northern footwall block beneath a local discordance.

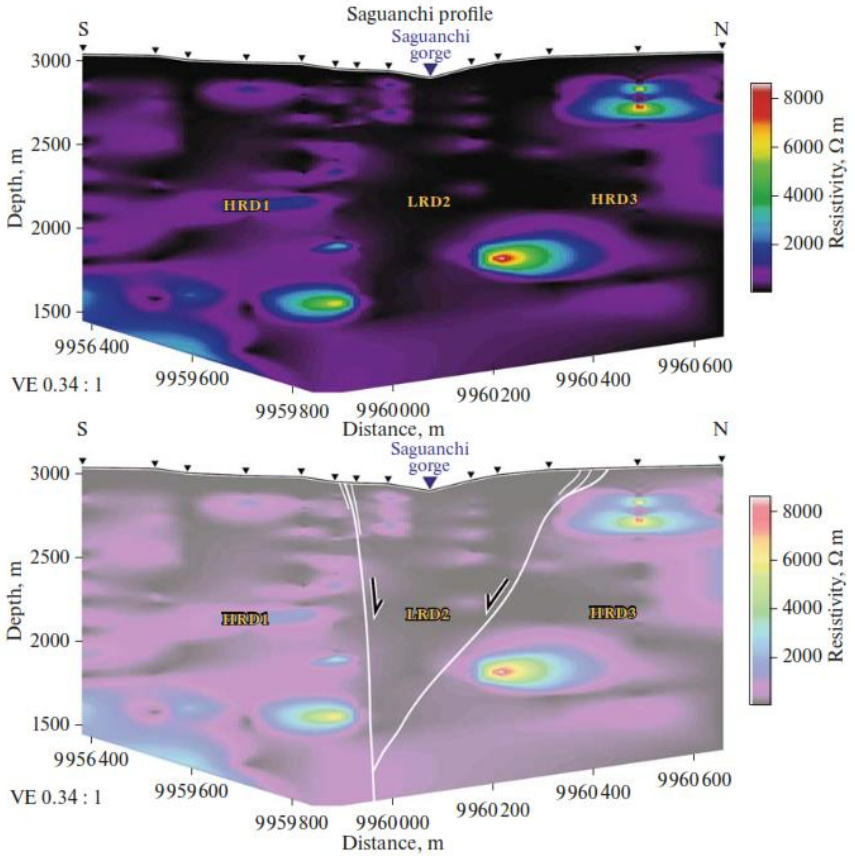

Fig. 4. Electrical resistivity 2D section derived by two-dimensional inversion from a MT sounding (a) electrical resistivity 2D section and (b) tectonic interpretation of the resistivity model where white lines indicate bounding normal faults. Legend as high-resistivity domain 1 (HRD1), low-resistivity domain 1 (LRD2), and high-resistivity domain 2 (HRD3); vertical exaggeration (VE); and inverted solid triangles, the magnetotelluric measurement stations. Note that the LRD2 coincides with the Saguanchi Gorge valley bottom.

values >3000 Ω m with mean values around 1500 Ω m. A roughly structural interpretation of this resistivity profile may be resolved in Fig. 4b by two bounding normal faults. A southern steepened fault plain juxtaposes the wedge-shaped domain (LRD-2) upon the HRD-1. A northern fault with a moderately southward-dipping plain puts in contact LRD-2 upon the HRD-3. This interpreted fault plain arrangement is structurally coherent with the tectonic style of normal faulting as observed in surface (Fig. 3b, 3d) with steepened normal faults to the south and gentle listric faults to the north. Therefore, the highly dissected stream channel of the Saguanchi Gorge develops upon the downthrown block represented by a tectonically subsided wedge actually disposed perpendicularly to the southernmost termination of the QFS anticlinal ridge. The asymmetric geometry of the downthrown block as defined along the resistivity profile (Fig. 4b) forms a subsiding structure such as a wedge-shaped graben block pointing down.

Distinctive hydrogeological features from electrical resistivity values stand out the internal geometry in the upsection of the three blocks. HRD-1 represents a poorly connected aquifer system with an apparent secondary porosity featured by fractures or secondary faults associated to the folding process during QFS activity on very compacted sediments. LRD-2 show the geometric architecture of a highly conductive aquifer system with apparent homogenic distribution of resistivity values which may include both primary and sec-

ondary porosity. HRD-3 displays some characteristics rather of a shallow productive aquifer system associated with stratified and poorly consolidated sediments.

DISCUSSION

Saguanchi Gorge Development

Transverse drainage and river gorges that cut across geological structures and prominent topographic barriers [3, 47] are typically attributed to antecedence, superposition or headward erosion-stream capture [3, 46, 47]. Valley hillslopes adjacent to the Saguanchi Gorge lack of any preserved flights, strath remnants or ancient stream terraces frequently formed during tectonically induced downcutting of streams flowing through progressive growing folds, thereby discarding an antecedence processes. Superposition process requires the drainage system to remove the sedimentary cover burying an ancient folded structure, which results incompatible with the ongoing active thrusting process of the QFS. A fluvial mechanism of headward erosion and stream piracy [46] through a transverse weakened zone induced by tectonic subsidence across an uplifted bedrock appears to be appropriated to explain the Saguanchi Gorge development.

Fold-Axis Parallel Extension

In largely dominant compressional settings and orogenic mountain belts, extensional structures may develop perpendicular to the principal shortening directions involving radial or arc-parallel stretching [4, 10, 23, 33, 44] even at micro-scale fabrics [9, 17]. Although, fold-axis parallel extension may occur during folding process or being superimposed on already formed folds [11], however in arcuate belts or oroclinal bending areas the extensional component may be significant [44]. Along the southern QFS anticlinal structure, the extension parallel to fold axis is associated to normal fault activity which has produced an N–S offset of around 0.61-km in the crestline axis. Nevertheless, the arcuate fault termination of the QFS and fold-axis parallel extension are not enough to explain by itself all the deformation observed. Strike-slip tectonics may also provide for additional extensional zones often disposed roughly perpendicular to the principal shortening component [16, 48]. Morphological measure of the E–W offset of about ~0.27 km that displace the crestline in a roughly S70°E direction suggests a local strike-slip displacement across the anticlinal ridge.

Strain Partitioning along the QFS

The most significant factor driving subsidence along a strike-slip fault is the bending geometry of the fault trace favoring a releasing bend zone where divergent strike slip is accompanied by stretching, subsidence and pull-apart formation [48]. Kingma [25] recognizes that localized subsiding areas along fault-zone terminations may be induced by tensional stress during lateral transcurrent motion thus deriving in a throw away from the virtually no broken stable area. Normal faults may often intersect the tip termination of a strike-slip fault with slip azimuths mostly parallel to the lateral movement [38]. Along the southwestern termination of the QFS, tectonic extension appears to be concentrated along radially dissected deeper gorges (Fig. 2) which stretches the anticlinal tip. However, the additional E–W offset that locally displace the crestline suggest a more complex kinematics including a pure extensional regime and a local strike-slip component. Evidence for a strike-slip component along the whole QFS may come from both morphological and geodetic approaches. On one hand, the morphological planform geometry of "en-echelon" structuration is often associated to strike-slip (wrench) zones [51]. Thus, the right-stepping en-echelon arrangement of the QFS [1, 50], which is composed by three overstepping anticlinal ridges (Fig. 1), may suggest a significantly component of lateral movement occurring simultaneously within the overall compressive system. On the other hand, although the GPS horizontal velocity field data presented by [1] indicate a mean velocity vector closely perpendicular to the regional strike of the QFS (~N17°E), however, Alvarado et al. [2] show a GPS horizontal velocity field data referenced to the Interandean Depression, which rather suggests a mean N82°E velocity vector, thereby implying a minor right-lateral strike-slip component for the QFS may extended in a NNE direction. Therefore, the fault kinematics along the QFS may be partitioned in two components: a pure vertical movement associated to the thrust-related anticlinal uplifting and minor lateral movements associated to the planform geometry in right-stepping en-echelon arrangement of the QFS that drives the fault throw away from the southwestern termination tip.

Extensional Normal Faulting Models

To explain both the ~N–S fold-axis parallel extension and the local ~E–W transverse offset along the southernmost termination of the QFS anticline we present herein three possible extensional models (Fig. 5) for accommodating the normal fault systems through the entrenched valley of the Saguanchi gorge. A first model (Fig. 5a) considers a termination model [38] produced by normal faults intersecting the trailing edge of a strike-slip fault on a tectonic escape system or open tail cracks in the extensional fault termination [5]. The second model (Fig. 5b) contemplates a local releasing stepover with local pull-apart development [8, 30]. The third model (Fig. 5c) considers an ESE-trending right-bending strike-slip fault parallel to the thrust transport direction of the QFS anticline with an associated oblique negative flower structure [20, 32, 53] developed into a divergent low-angle releasing bend

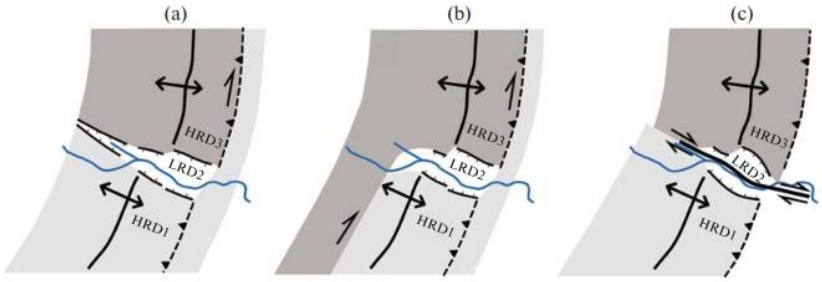

Fig. 5. Extensional Normal Faulting Models prepared to explain fold-axis parallel extension along the southernmost termination of the QFS. (a) Termination model with open tail cracks. (b) Right-lateral strike-slip pull-apart model. (c) Oblique strike-slip tear fault depicted by two couple of arrows with a local releasing bend depression zone.

depression. Due to a lack of structural fieldwork evidence to support a pull-apart depression along the southwestern boundary of the strike-slip fault, we suggest a mixed model that combines the N–S offset of the first scenario and the E–W offset of the third one. Thus, a NNE-ward escape tectonic regime of the HRD-3 (Fig. 5a) controlled by the minor strike-slip component associated to the QFS kinematics causes N-S extension as an open tail crack. The E–W offset may be resolved by a local transfer fault [32] of right-lateral strike-slip movement that separates HRD-3 from HRD-1 through a short and oblique releasing fault bend (Fig. 5c) that occur when the HRD-3 thrust front move further east toward the ID in relation to HRD-1 by an increasing amount of shortening to the north of the QFS.

Tectonic Implications in Drainage Network and Aquifer Geometry

The weakened zone created by the tectonic subsidence of the LRD-2 (Fig. 4) during the extensional event parallel to the fold axis has changed the drainage network configuration of the southern QB. The Saguanchi Gorge valley favors that both, the groundwater flow and the stormwater runoff to converge to the axis bottom. The QBA, which receives much of its recharge comes mostly from the adjacent southern watersheds of the QB catchments, actually discharges a significant volume of its stored groundwater to the IDA and other minor aquifer systems of the ID (Fig. 2) through the Saguanchi valley axis. Thus, the natural groundwater recharge and shallow aquifer storage conditions of the southern QBA has been modified by tectonic controls in favor of the IDA system.

CONCLUSIONS

The fold-axis parallel extension process has been determined by fieldwork evidence and magnetotellurics survey along the arcuate, southernmost anticlinal structure of the Quito fault system where the wedge-shaped downthrown graben block has driven the E-flowing direction of the Saguanchi Gorge into the inter-Andean Depression whose kinematics has been resolved by the NNE escaping block and by the transfer-fault mechanism.

Strain partitioning, as was evidenced along the Quito fault system, may be resolved by two simultaneous processes: (1) the main thrusting process manifested as NNE striking asymmetric anticlinal structures, and (2) the subsidiary strike-slip process whose NNE movement has displaced the southernmost termination and controls the right-stepping en-echelon pattern of the Quito fault system.

ACKNOWLEDGMENTS

We are thankful to Coronel Iván Jarrín and Mayor José Yépez from the Instituto Espacial Ecuatoriano (Quito, Ecuador) for providing us the Geometrics equipment. We grateful to Vicente Condolo (Quito, IEE, Ecuador) for logistics and Mayelin Cabascango (Quito, EPN, Ecuador) for software assistance. The valuable comments and suggestions by Professor Valery S. Imaev and an anonymous reviewer are greatly appreciated.

FUNDING

This work was supported by the Escuela Politécnica Nacional through the Project PII-DG-02-2016.

REFERENCES

1. A. Alvarado, L. Audin, J. M. Nocquet, S. Lagreulet, M. Segovia, Y. Font, G. Lamarque, H. Yepes, P. Mothes, F. Rolandone, P. Jarrín, and X. Quidelleur, "Active tectonics in Quito, Ecuador, assessed by geomorphological studies, GPS data, and crustal seismicity," Tectonics **33**, 67–83 (2014).
2. A. Alvarado, L. Audin, J. M. Nocquet, E. Jaillard, P. Mothes, P. Jarrín, M. Segovia, F. Rolandone, and D. Cisneros, "Partitioning of oblique convergence in the Northern Andes subduction zone: Migration histo-

ry and the present-day boundary of the North Andean Sliver in Ecuador," Tectonics **35**, 1048–1065 (2016).

3. W. Alvarez, "Drainage on evolving fold-thrust belts: A study of transverse canyons in the Apennines," Basin Res. **11**, 267–284 (1999).
4. R. Armijo, P. Tapponnier, J. L. Mercier, and T. L. Han, "Quaternary extension in southern Tibet: Field observations and tectonic implications," J. Geophys. Res., [Solid Earth Planets] **91**, 13803–13872 (1986).
5. A. Aydin and A. Nur, "Evolution of pull-apart basins and their scale independence," Tectonics **1**, 91–105 (1982).
6. S. Baize, L. Audin, T. Winter, A. Alvarado, L. Pilatasig, M. Taipe, P. Reyes, P. Kauffmann, and H. Yepes, "Paleoseismology and tectonic geomorphology of the Pallatanga fault (Central Ecuador), a major structure of the South-American crust," Geomorphology **237**, 14–28 (2015).
7. J. C. Balanyá, A. C. Blanc, M. D. Azpiroz, I. Expósito, F. Torcal, V. P. Peña, and G. B. Rea, "Arc-parallel vs back-arc extension in the Western Gibraltar arc: Is the Gibraltar forearc still active?," Geol. Acta. **10**, 249–263 (2012).
8. B. C. Burchfiel and J. H. Stewart, "Pull-apart origin of the central segment of Death Valley, California," Geol. Soc. Am. Bull. **77**, 439–442 (1966).
9. J. P. Burg, M. Brunel, D. Gapais, G. M. Chen, and G. H. Liu, "Deformation of leucogranites of the crystalline Main Central Sheet in southern Tibet (China)," J. Struct. Geol. **6**, 535–542 (1984).
10. A. Chauvet and M. Séranne, "Extension-parallel folding in the Scandinavian Caledonides: Implications for late-orogenic processes," Tectonophysics **238**, 31–54 (1994).
11. D. Dietrich, "Fold-axis parallel extension in an arcuate fold-and thrust belt: The case of the Helvetic nappes," Tectonophysics **170**, 183–212 (1989).
12. O. Egbue and J. Kellogg, "Pleistocene to present North Andean escape," Tectonophysics **489**, 248–257 (2010).
13. A. Egüez, A. Alvarado, and H. Yepes, *Map of Quaternary Faults and Folds of Ecuador and its Offshore Regions* (U.S. Geol. Surv., Denver, Colo., 2003).
14. *EMAAP-Q: Mapa Hidrogeológico del Distrito Metropolitano de Quito*, No. 19 of *Empresa Metropolitana de Alcantarillado y Agua Potable de Quito, Tec. Rep.* (2009).
15. N. Feuillet, I. Manighetti, P. Tapponnier, and E. Jacques, "Arc parallel extension and localization of volcanic complexes in Guadeloupe, Lesser Antilles," J. Geophys. Res.: Solid Earth **107** (2002). https://doi.org/10.1029/2001JB000308
16. H. Fossen, C. Teyssier, and D. L. Whitney, "Transtensional folding," J. Struct. Geol. **56**, 89–102 (2013).
17. D. Gapais, A. Pêcher, E. Gilbert, and M. Ballèvre, "Synconvergence spreading of the higher Himalaya crystalline in Ladakh," Tectonics **11**, 1045–1056 (1992).
18. *Operation Manual for Stratagem Systems Running IMAGEM, Ver. 2.19* (Geometrics, Inc., San Jose, Calif., 2007).
19. D. Grujic and N. S. Mancktelow, "Folds with axes parallel to the extension direction: An experimental study," J. Struct. Geol. **17**, 279–291 (1995).
20. T. P. Harding, "Seismic characteristics and identification of negative flower structures, positive flower structures, and positive structural inversion," AAPG Bull. **69**, 582–600 (1985).
21. C. Hibsch, A. Alvarado, H. Yepes, V. H. Perez, and M. Sébrier, "Holocene liquefaction and soft-sediment deformation in Quito (Ecuador): A paleoseismic history recorded in lacustrine sediments," J. Geodyn. **24**, 259–280 (1997).
22. D. Hungerbühler, M. Steinmann, W. Winkler, D. Seward, A. Egüez, D. E. Peterson, U. Helg, and C. Hammer, "Neogene stratigraphy and Andean geodynamics of southern Ecuador," Earth Sci. Rev. **57**, 75–124 (2002).
23. M. J. Jessup, D. L. Newell, J. M. Cottle, A. L. Berger, and J. A. Spotila, "Orogen-parallel extension and exhumation enhanced by denudation in the trans-Himalayan Arun River gorge, Ama Drime Massif, Tibet-Nepal," Geology **36**, 587–590 (2008).
24. E. Kendrick, M. Bevis, R. Smalley, B. Brooks, R. B. Vargas, E. Lauria, and L. P. S. Fortes, "The Nazca-South America Euler vector and its rate of change," J. South Am. Earth Sci. **16**, 125–131 (2003).
25. J. T. Kingma, "Possible of Piercement structures, local unconformities, and secondary basins in the Eastern Geosyncline, New Zealand," N. Z. J. Geol. Geophys. **1**, 269–274 (1958).
26. D. Kirkwood, M. Malo, P. St-Julien, and P. Therrien, "Vertical and fold-axis parallel extension within a slate belt in a transpressive setting, northern Appalachians," J. Struct. Geol. **17**, 329–343 (1995).
27. A. Lavenu, T. Winter, and F. Davila, "A Pliocene-Quaternary compressional basin in the Interandean depression, central Ecuador," Geophys. J. Int. **121**, 279–300 (1995).
28. M. Litherland and J. A. Aspden, "Terrane-boundary reactivation: A control on the evolution of the Northern Andes," J. South Am. Earth Sci. **5**, 71–76 (1992).
29. C. Manciati, PhD Thesis (Montpellier, France, 2014).
30. P. Mann, M. R. Hempton, D. C. Bradley, and K. Burke, "Development of pull-apart basins," J. Geol. **91**, 529–554 (1983).
31. J. G. Masek, B. L. Isacks, E. J. Fielding, and J. Browaeys, "Rift flank uplift in Tibet: Evidence for a viscous lower crust" Tectonics **13**, 659–667 (1994).
32. K. R. McClay, "Glossary of thrust tectonics terms," in *Thrust Tectonics*, Ed. by K. R. McClay (Chapman & Hall, London, 1992), pp. 419–433.
33. J. A. McDermott, K. X. Whipple, K. V. Hodges, and M. C. Van Soest, "Evidence for Plio-Pleistocene north-south extension at the southern margin of the Tibetan Plateau, Nyalam region," Tectonics **32**, 317–333 (2013).
34. D. K. McPhee, B. A. Chuchel, and L. Pellerin, *Audiomagnetotelluric Data from Spring, Cave, and Coyote Spring Valleys, Nevada*, No. 2006–1164 of *U.S. Geol. Surv. Open-File Rep.* (2006).
35. P. Molnar and P. Tapponnier, "Cenozoic tectonics of Asia: Effects of a continental collision," Science **189** (4201), 419–426 (1975).
36. P. Molnar and P. Tapponnier, "Active tectonics of Tibet," J. Geophys. Res., B **83**, 5361–5375 (1978).

37. D. R. Montgomery and D. B. Stolar, "Reconsidering Himalayan river anticlines," Geomorphology **82**, 4–15 (2006).
38. V. Mouslopoulou, A. Nicol, T. A. Little, and J. J. Walsh, "Terminations of large strike-slip faults: An alternative model from New Zealand," in *Tectonics of Strike-Slip Restraining and Releasing Bends*, Vol. 290 of *Geol. Soc. London, Spec. Publ.*, Ed. by W. D. Cunningham and P. Mann (London, 2007), pp. 387–415.
39. A. R. Moustafa and S. M. Khalil, "Control of compressional transfer zones on syntectonic and post-tectonic sedimentation: Implications for hydrocarbon exploration," J. Geol. Soc. (London, U. K.) **174**, 336–352 (2017).
40. J. Ni and J. E. York, "Late Cenozoic tectonics of the Tibetan plateau," J. Geophys. Res., B **83**, 5377–5384 (1978).
41. J. M. Nocquet, J. C. Villegas-Lanza, M. Chlieh, P. A. Mothes, F. Rolandone, P. Jarrín, D. Cisneros, A. Alvarado, L. Audin, F. Bondoux, X. Martin, Y. Font, M. Régnier, M. Vallée, T. Tran, et al., "Motion of continental slivers and creeping subduction in the northern Andes," Nat. Geosci. **7**, 287–291 (2014).
42. L. A. Peñafiel, Thesis in Engineering Geology (Quito, Ecuador, 2009).
43. L. A. Peñafiel, F. J. Alcalá, E. Barragán, and O. Larrea, "Evaluación del balance hídrico en un área vulcano-sedimentaria de alta montaña poco monitorizada en la Cordillera de los Andes: Acuífero del río Pita, norte de Ecuador," Rev. Latino-Am. Hidrogeol. **10**, 502–508 (2016).
44. L. Seeber and A. Pêcher, "Strain partitioning along the Himalayan arc and the Nanga Parbat antiform," Geology **26**, 791–794 (1998).
45. J.-P. Soulas, A. Egüez, H. Yepes, and H. Pérez, "Tectónica activa y riesgo sísmico en los Andes Ecuatorianos y el extremo sur de Colombia," Bol. Geol. Ecuatoriano **2**, 3–11 (1991).
46. M. Stokes and A. E. Mather, "Tectonic origin and evolution of a transverse drainage: The Río Almanzora, Betic Cordillera, Southeast Spain," Geomorphology **50**, 59–81 (2003).
47. M. Stokes, A. E. Mather, A. Belfoul, and F. Farik, "Active and passive tectonic controls for transverse drainage and river gorge development in a collisional mountain belt (Dades Gorges, High Atlas Mountains, Morocco)," Geomorphology **102**, 2–20 (2008).
48. A. G. Sylvester, "Strike-slip faults," Geol. Soc. Am. Bull. **100**, 1666–1703 (1988).
49. P. Tapponnier, J. L. Mercier, R. Armijo, H. Tonglin, and Z. Ji, "Field evidence for active normal faulting in Tibet," Nature **294**, 410 (1981).
50. D. Villagómez, Thesis in Engineering Geology (Quito, Ecuador, 2003).
51. R. E. Wilcox, T. T. Harding, and D. R. Seely, "Basic wrench tectonics," AAPG Bull. **57**, 74–96 (1981).
52. W. Winkler, D. Villagómez, R. Spikings, P. Abegglen, and A. Egüez, "The Chota basin and its significance for the inception and tectonic setting of the inter-Andean depression in Ecuador," J. South Am. Earth Sci. **19**, 5–19 (2005).
53. N. H. Woodcock and M. Fischer, "Strike-slip duplexes," J. Struct. Geol. **8**, 725–735 (1986).
54. K. L. Zonge and L. J. Hughes, "Controlled source audio-frequency magnetotellurics," in *Electromagnetic Methods in Applied Geophysics*, Vol 2: *Application, Parts A and B*, No. 3 of *Inv. Geophys.*, Ed. by M. N. Nabighian (Soc. Explor. Geophys., 1991), ch. 9, pp. 713–810.

Reviewer: V.S. Imaev

APPENDIX B. BRIEF DESCRIPTION OF SWAT MODEL

B1. SWAT model performance statistics

For SWAT model efficiency criteria, this Thesis used the following performance statistics: Nash–Sutcliffe efficiency (NSE), logarithm form of the NSE (ln NSE), coefficient of determination (R2), percent bias (PBIAS), root-mean-square error relative to standard deviation ratio (RSR) and Kling–Gupta efficiency (KGE).

Nash–Sutcliffe efficiency (NSE) (Nash and Sutcliffe, 1970) is the normalized relative magnitude of the residual variance relative to the observed data variance. NSE is dimensionless and can theoretically vary from -∞ for a very poor fit to 1 for an optimal linkage between observed and simulated streamflow values (Gupta et al., 1999). It is expressed as:

$$NSE = 1 - \frac{\sum_{i=1}^{n}(Q_{ob,i} - Q_{si,i})^2}{\sum_{i=1}^{n}(Q_{ob,i} - \bar{Q}_{ob})^2} \quad (1)$$

where n is the number of observations, Q_{ob} and Q_{si} are observed and simulated streamflow for observation i, respectively, and $\overline{Q}_{ob}$ is the mean of the n observed data over the simulation period.

The logarithm form of the NSE (ln NSE) is used to reduce the problem of the squared differences and the resulting sensitivity to extreme values calculated with NSE. This logarithmic transformation flat the high flows while the low flows keep the magnitude at the same level. As a result, sensitivity of lnNSE to the model overprediction or underprediction increases. It is expressed as:

$$lnNSE = 1 - \frac{\sum_{i=1}^{n}(lnQ_{ob,i} - lnQ_{si,i})^2}{\sum_{i=1}^{n}(lnQ_{ob,i} - \overline{lnQ}_{ob})^2} \quad (2)$$

Coefficient of determination (R^2) indicates the degree of linear relationship between observed and simulated data. R^2 ranges from 0 to 1, the latter being for a perfect model. It is expressed as:

$$R^2 = 1 - \frac{\left[\sum_{i=1}^{n}\left(Q_{ob,i} - \bar{Q}_{ob}\right)\left(Q_{si,i} - \bar{Q}_{si}\right)\right]^2}{\sum_{i=1}^{n}(Q_{ob,i} - \bar{Q}_{ob})^2 \sum_{i=1}^{n}(Q_{si,i} - \bar{Q}_{si})^2} \quad (3)$$

where $\overline{Q}_{si}$ is the mean of the n simulated data over the simulation period.

Percent BIAS (PBIAS) (Legates and McCabe, 1999) measures the dimensionless average tendency of simulated data to be higher or smaller than their observed counterparts (Gupta et al., 1999). The optimal value of PBIAS is 0, so positive and negative values identify the model underestimation and overestimation biases, respectively. It is expressed as a percentage as:

$$PBIAS = \frac{\sum_{i=1}^{n}(Q_{ob,i} - Q_{si,i})}{\sum_{i=1}^{n}(Q_{ob,i})} . 100 \quad (4)$$

The root-mean-square error relative to standard deviation ratio (RSR) varies from an optimal value of 0 to large positive values for a poor fit. It is expressed as:

$$RSR = \frac{\sqrt{\sum_{i=1}^{n}(Q_{ob,i} - Q_{si,i})^2}}{\sqrt{\sum_{i=1}^{n}(Q_{ob,i} - \bar{Q}_{ob})^2}} \quad (5)$$

NSE includes three distinctive components: correlation, bias, and the relative variability in observed and simulated streamflow. Kling-Gupta efficiency (KGE) reduces the deterioration of the model when optimizing NSE, assigning equal weighting of the three components (Gupta et al., 2009). It is expressed as:

$$KGE = 1 - ED \quad (6a)$$

$$ED = ((R-1)^2 + (\alpha - 1)^2 + (\beta - 1^2)^{\frac{1}{2}} \quad (6b)$$

where ED is the Euclidian distance between observed and simulated data, $\alpha = \frac{S_{si}}{S_{ob}}$ is relative variability in simulated and observed data expressed as their standard deviations, $\beta = \frac{\overline{Q}_{si}}{\overline{Q}_{ob}}$ is mean simulated to mean observed streamflow data ratio, and R is coefficient of between Q_{ob} and Q_{si} data pairs. Table B.1 shows used evaluation criteria for a monthly simulation model performance.

Table B.1. Evaluation criteria for a monthly simulation model performance.

Performance Rating	NSE [a]	RSR [a]	PBIAS (%) [b]	R^2 [c]
Very good	0.75<NSE≤1.00	0.00≤RSR<0.50	PBIAS<±10	0.75<R^2≤1.00
Good	0.65<NSE≤0.75	0.50≤RSR<0.60	±10≤PBIAS<±15	0.60<R^2≤0.75
Satisfactory	0.50<NSE≤0.65	0.60≤RSR<0.70	±15≤PBIAS<±25	0.40<R^2≤0.60
Unsatisfactory	NSE≤0.50	RSR≥0.70	PBIAS≥±25	R^2≤0.40

[a] After Moriasi et al. (2007)

[b] After Gupta et al. (1999)

[c] After Santhi et al. (2001)

B2. Brief description of SWAT model calibration parameters

r_ CN2.mgt, It´s the initial SCS runoff curve number for soil moisture condition II. The SCS curve number is a function of the soil's permeability, land use, and antecedent soil moisture condition. Typical curve numbers for soil moisture condition II over different land cover, soil type and slope are listed in SCS Engineering Division (SCS, 1986). The curve number may be updated in plant, tillage, and harvest / kill operations. If CNOP (SCS runoff curve number for moisture condition II) is never defined for these operations, the value set for CN2 will be used throughout the simulation. If CNOP is defined for an operation, the model only uses operation CNOP value. From that point on, the model only uses operation CNOP values to define the curve number for moisture condition II. Values for CN2 and CNOP should be entered for pervious conditions. In HRUs with urban areas, the model will adjust the curve number to reflect the impact of low-permeability areas.

v_ALPHA_BF.gw, It´s baseflow alpha factor (1 day^{-1}). The baseflow recession constant, a_{gw}, is a directed index of groundwater flow response to changes in recharge (Smedema and Rycroft, 1983). Values vary in the 0.1–0.3 and 0.9–1.0 ranges for land with slow and quickly response to recharge, respectively. Although

the baseflow recession constant may be calculated, the best estimates are obtained by analyzing measured streamflow during periods of no recharge in the watershed.

a_GW_DELAY.gw. It´s groundwater delay time (day), δ_{gw}, which cannot be directly measured. It can be estimated by simulating aquifer recharge using different values for δ_{gw} and comparing the simulated variations in water table level with observed values. Johnson (1997) developed a simple program to iteratively test and statistically evaluate different delay times for a watershed. Sangrey et al. (1984) noted that monitoring wells in the same area had similar values for δ_{gw}, so once a delay time value for a geomorphic area is defined, similar delay times can be used in adjoining watersheds within the same geomorphic province.'

a_GWQMN.gw. Threshold depth of water in the shallow aquifer required for return flow to occur (mm H_2O). Groundwater flow to the reach is allowed only if the depth of water in the shallow aquifer is equal to or greater than GWQMN.

v_CANMX.hru. Maximum canopy storage (mm H_2O). The plant canopy can significantly affect infiltration, surface runoff and evapotranspiration. As rain falls, canopy interception reduces the erosive energy of droplets and traps a portion of the rainfall within the canopy. The influence the canopy exerts on these processes is a function of the density of plant cover and morphology of the plant species.

v_EPCO.bsn. Plant uptake compensation factor. The amount of water uptake that occurs on a given day is a function of the amount the water required by the plant for transpiration, E_t, and the amount of water available in the soil, SW. If upper layers in the soil profile do not contain enough water to meet the potential water to meet the potential water uptake, users may allow lower layers to compensate. The plant uptake compensation factor can vary in the 0.01–1 range. As the EPCO value is increased (up to 1), the model allows more of the water uptake demand to be met by lower layers in the soil. As the EPCO value is decreased (up to 0), the model allows less variation from original depth distribution to take place. If no value for EPCO is entered, the model will set EPCO = 1. The value for EPCO may be set at the watershed or HRU level.

v_ESCO.bsn. Soil evaporation compensation factor. This coefficient has been incorporated to allow the user to modify the depth distribution used to meet the soil evaporative demand to account for the effect of capillary action, crusting and

cracks. ESCO must vary in the 0.01–1 range. As the ESCO value is reduced, the model can extract more of the evaporative demand from lower levels.

v_GW_REVAP.gw. Groundwater 'revap' coefficient. Water may move from the shallow aquifer into the overlying undersaturated zone. In periods when the material overlying the aquifer is dry, water in the capillary fringe that separates the saturated and unsaturated zones will evaporate and diffuse upward. As water is removed from the capillary fringe by evaporation, it is replaced by water from the underlying aquifer. Water may also be removed from the aquifer by deep-rooted plants which are able to uptake water directly from the aquifer. This process is significant in watersheds where the saturated zone is not very far below the surface or where the saturated zone is not very far below the surface or where deep-rooted plants are growing. Because the type of plant cover will affect the importance of revap in the water balance, the parameters governing revap can be varied by land use. As GW_REVAP approaches 0, movement of water from the shallow aquifer to the root zone is restricted. As GW_REVAP approaches 1, the rate of transfer from the shallow aquifer to the root zone approaches the rate of potential evapotranspiration. The value for GW_REVAP should be between 0.02 and 0.20.

a_RCHRG_DP.gw. Deep aquifer percolation fraction. The fraction of percolation from the root zone which recharges the deep aquifer. The value for RCHRG_DP should be between 0.0 and 1.0.

a_REVAPMN.gw. Threshold depth of water in the shallow aquifer for 'revap' or percolation to the deep aquifer to occur (mm H2O). Movement of water from the shallow aquifer to the unsaturated zone is allowed only if the volume of water in the shallow aquifer is equal to or greater than REVAPMN. This variable, along with GW_REVAP, is the reason a different groundwater file is created for each HRU rather than each subbasin.

r_SOL_AWC.sol. Available water capacity of the soil layer (mm H2O/mm soil). The plant available water, also referred to as the available water capacity, is calculated by subtracting the fraction of water present at permanent wilting point from that present at field capacity, AWC=FC-WP where AWC is the plant available water content, FC is the water content at field capacity, and WP is the water content at permanent wilting point. Available water capacity is estimated by determining the amount of water released between in situ field capacity (the soil water content

at soil matric potential is -0.033 MPa) and the permanent wilting point (the soil water content at soil matric potential is -1.5 MPa).

v_LAT_TTIME.hru. Lateral flow travel time (days). Setting LAT_TTIME = 0 will allow the model to calculate the travel time based on soil hydraulic properties. This variable should be set to a specific value only by hydrologists familiar with the base flow characteristics of the watershed.

v_SLSOIL.hru. Slope length for lateral subsurface flow (m). If no value is entered for SLSOIL, the model sets SLSOIL = SLSUBBSN. The GIS interfaces will assign the same value to this variable for all HRUs within a subbasin. However, some users like to vary this value by soil type and land cover.

B3. Parameters used for daily SWAT model calibration

r_SLSUBBSN.hru. Slope length is a parameter that is commonly overestimated. As a rule of thumb, 90 meters is considered a very long slope length. If no value for SLSUBBSN is entered, the model will set SLSUBBSNC = 50. The GIS interfaces will assign the same value to this variable for all HRUs within a subbasin. However, some users like to vary this value by soil type and land cover.

r_HRU_SLP.hru. Average slope steepness ($m\ m^{-1}$). The GIS interfaces will assign the same value to this variable for all HRUs within a subbasin. However, some users like to vary this value by soil types and land cover.

v_OV_N.hru. Manning's 'n' value for overland flow.

r_CH_S1.sub. Average slope of tributary channels ($m\ m^{-1}$). The average channel slope in computed by taking the difference in elevation between the subbasin outlet and the most distant point in the subbasin and dividing by CH_L.

v_CH_N1.sub. Manning's 'n' value for the tributary channels.

r_CH_S2.rte. Average slope of main channel along the channel length ($m\ m^{-1}$).

v_CH_N2.rte. Manning's 'n' value for the main channel.

v_SURLAG.bsn. Surface runoff lag coefficient. In large subbasins with a time of concentration greater than 1 day, only a portion of the surface runoff will reach the main channel on the day it is generated. SWAT. Incorporates a surface runoff storage feature to lag a portion of the surface runoff release to the main channel.

SURLAG controls the fraction of the total available water that will be allowed to enter the reach on any one day. Note that for a given time of concentration, as surlag decreases in value more water is held in storage. The delay in release of surface runoff will smooth the streamflow hydrograph simulated in the reach (Athira and Sudheer, 2021). If no value for SURLAG in entered, the model will set SURLAG=4.

B4. Additional remarks on the interpretation of calibrated parameters

The first step monthly SWAT model calibration used thirteen parameters. The parameter Soil Conservation Service (SCS) curve number for soil moisture condition II (CN2) had to be increased 2% in all HRUs. Average CN2 was in the 82.26–87.91 range in the 7 sub-basins. For the entire basin, the average surface-weighted CN2 was 85.47. These values identify a noticeable capability of the PRB to generate surface and interflow runoff, which is associated with steep orography (Figure 1b) and the predominance of moderate- to low-permeability geological formations (Figure 1c).

The parameter baseflow alpha factor (ALFA _BF) was 0.63 day^{-1}, indicating rapid to moderate response of baseflow to changes in aquifer recharge. This means that groundwater discharge is preferably produced from shallow aquifers, which in turn should be almost full. This suggests an undisturbed state that limits the entry of new recharge events and favors the groundwater discharge from shallow aquifers to be the predominant baseflow component.

The parameter groundwater delay time (GW_DELAY) for shallow aquifers is 90 days. This figure agrees with the preliminary conceptualization of the rapid mechanisms of shallow aquifer recharge and discharge observed in the PRB (Peñafiel et al., 2016b) and other IAV areas (Alcalá et al., 2016).

The parameter threshold groundwater depth in the shallow aquifer for return flow to occur (GWQMN) is 1.30 m. This low magnitude supports the idea that the shallow aquifer is almost full, and its discharge occurs along streambeds when the incisive topography intercepts piezometry.

The parameter groundwater revap coefficient (GW_REVAP), i.e., the depth for soil water to percolate from the lower level of the soil to the shallow aquifer, is 0.10 m. This figure indicates the different hydraulic behavior of organic-matter-rich

porous soils and moderate- to low-permeability underlaying geological formations, thus favoring interflow runoff.

The parameter deep aquifer percolation fraction (RCHRG_DP) is around 0.05. This figure confirms that the deep aquifer is confined, is probably full, and has predominant upward groundwater flow paths that limit a relevant contribution from the shallow aquifers.

The parameter threshold groundwater depth in the shallow aquifer for revap or percolation to the deep aquifer to occur (REVAPMN), i.e., the depth for groundwater to percolate from the lower level of the shallow aquifer to the deep aquifer, is 0.94 m. Since REVAPMN is less than GWQMN, it can be assumed that the deep aquifer (i) contributes groundwater to the shallow aquifer, (ii) must be confined, and (iii) its transference to the shallow aquifers occurs preferentially through faults or where the topography is very incisive and can intercept the deep geological formations to produce localized hot (hydrothermal) permanent springs. Preliminary findings showed that the deep aquifer storage could reach several km^3 (Peñafiel et al., 2021) and its average groundwater turnover time could be greater than a few hundred years at least (Peñafiel et al., 2016b).

The parameter maximum canopy storage (CANMX) was 0.15 mm. This low value is due to the predominance of shrubby vegetation and grass in most of the PRB, with some patches of arborous vegetation restricted to low-lying areas.

The parameter lateral flow travel time (LAT_TTIME) was 104 days. This figure indicates rapid circulation of groundwater through the soil-bedrock boundary and through the shallowest weathered geological formations. Preliminary findings showed lateral flow travel times in the 2–4-month range for weathered geological formations underlying degraded and natural soils, respectively (Alcalá et al., 2016).

The parameter slope length for lateral subsurface flow (SLSOIL) was as low as 0.28 m. This figure corroborates the predominant natural soil state in the PRB.

The parameter plant uptake compensation factor (EPCO) was 0.45, showing that the model has allowed the lower layers of the soil to satisfy the vegetation water demand. This imposition was based on direct soil observations and soil hydraulic tests (Peñafiel, 2009).

The parameter soil evaporation compensation factor (ESCO) was 0.71, thus indicating that the evaporation demand is offset at shallower soil levels. The high atmospheric humidity and the dense vegetation cover do not allow direct evaporation from deeper soil levels, thus favoring the water accumulation in the soil-bedrock boundary.

The parameter available water capacity of the soil layer (SOL_AWC) was in the 0.142–0.165 mm H_2O·mm $soil^{-1}$ range, thus indicating soil water deficit. This relevant finding indicates that the soil water storage capacity is decreasing as soil degradation progresses due to global climate forces and human actions, with consequences on the observed decreasing of water traditional supply in the Andean Highland.